



# THÈSE

**En vue de l'obtention du**

## **DOCTORAT DE L'UNIVERSITÉ DE TOULOUSE**

**Délivré par :**

Institut Supérieur de l'Aéronautique et de l'Espace

---

**Présentée et soutenue par :**  
**William THOLLET**

**le** mardi 18 juillet 2017

**Titre :**

Modélisations simplifiées de turbomachines pour l'analyse par la simulation  
des installations motrices complexes d'avions

Body force modeling of fan-airframe interactions

---

**École doctorale et discipline ou spécialité :**

ED MEGeP : Dynamique des fluides

**Unité de recherche :**

Équipe d'accueil ISAE-ONERA EDyF

**Directeur(s) de Thèse :**

M. Xavier CARBONNEAU (directeur de thèse)  
M. Guillaume DUFOUR (co-directeur de thèse)

**Jury :**

M. Zoltan SPAKOVSKY, Professeur Massachusetts Institute of Technology - Président  
M. Tony ARTS, Professeur Von Karman Institute for Fluid Dynamics - Rapporteur  
M. Florian BLANC, Ingénieur Airbus Opérations SAS  
M. Xavier CARBONNEAU, Professeur ISAE-SUPAERO - Directeur de thèse  
M. Guillaume DUFOUR, Professeur Associé ISAE-SUPAERO - co-Directeur de thèse  
M. Cesare HALL, Professeur Associé University of Cambridge  
M. Paul TUCKER, Professeur University of Cambridge - Rapporteur

## Abstract

Future commercial aircraft concepts feature strong aerodynamic interactions between fan and airframe. In a practical design environment, fast and accurate numerical capabilities are thus required to capture and characterize these interactions. This thesis explores a non axisymmetric throughflow methodology often referred to as “body force modeling”, in which turbomachinery blade rows are replaced by source terms that reproduce flow turning and losses. The thesis presents an improved body force modeling framework that offers an effective way of capturing fan–airframe interactions on both short intake and Boundary Layer Ingestion (BLI) configurations.

In existing models from the literature, the body force source terms are usually expressed as a normal-to-the-flow force, which produces the turning and thus work exchange, and a parallel force, which generates the losses. Some of these models are reviewed, and possible improvements are proposed. In addition, a new formulation based on a lift and drag analogy is proposed, which offers a good compromise between accuracy and calibration cost. For all the models investigated, it is shown that the addition of specific source terms to capture metal blockage greatly enhances the accuracy of the flow prediction in transonic blade rows, both in terms of work coefficient and choke mass flow rate.

The new formulation is applied to nacelle–fan configurations and to conceptual BLI test cases. The results are validated against high-fidelity full-annulus unsteady simulations, and in some cases against experimental data. On nacelle–fan configurations, it is shown that this new formulation reproduces the effect of decreased intake length on inlet–fan coupling. In particular, the model captures the upstream influence of the fan on the intake lips, which is shown to delay flow separation at high angles of attack in short inlet designs. In addition, this body force formulation qualitatively captures the in-plane forces on the fan that result from the unevenly distributed loading around the annulus. Then, it is found that in presence of a BLI-type inlet distortion, the model captures the upstream redistribution of the flow and the distortion transfer through the blade rows. Finally, the model is applied to a conceptual fan–fuselage BLI test case, which allows to evaluate the qualitative evolution of BLI benefits when the amount of ingested fuselage boundary layer is varied.

## Remerciements

Ce travail de thèse a avant tout été un effort collaboratif, et je suis très heureux d'avoir eu l'opportunité de travailler avec toutes les personnes qui m'ont accompagné jusqu'à la soutenance.

En premier lieu, je tiens à souligner que le résultat aurait été très différent si je n'avais pas pu bénéficier d'un encadrement excellent, tant au niveau académique qu'au niveau industriel. Merci Guillaume, pour ta patience, pour ta pédagogie, pour avoir toujours su te rendre disponible quand j'en avais besoin, et pour t'être autant impliqué dans ce projet. Merci Florian pour ton enthousiasme, pour tout ce que tu m'as appris, tant en termes de méthodes de travail qu'en façons de penser, et pour tous les efforts que tu as fournis en amont et au début de ma thèse pour que je sois le plus efficace possible dès mon arrivée. Merci Xavier pour ton soutien moral tout au long de la thèse, mais surtout pour m'avoir donné envie de m'intéresser aux turbomachines pendant mes études, car c'est toute l'énergie positive que tu projette autour de toi qui m'a donné envie de rejoindre l'équipe TMP. Merci enfin Marie-Jo, pour tout le temps que tu m'as consacré et pour tous les efforts que tu as fournis pour que je me retrouve là où je suis aujourd'hui.

Je dois également des remerciements particuliers aux Professeurs Zoltan Spakovszky et Edward Greitzer, qui m'ont donné l'opportunité unique de passer quelques mois au Gas Turbine Lab du MIT, en prenant le temps de m'encadrer comme n'importe lequel de leurs étudiants. Ce séjour a sans aucun doute été le plus enrichissant qu'il m'ait été permis de vivre. Merci à David Hall, qui m'a beaucoup aidé pendant ces 5 mois, à préparer mes points hebdomadaires, à m'adapter à la façon de travailler du Gas Turbine Lab, et à progresser dans mon travail de recherche. Ce séjour n'aurait pas eu lieu sans David Hills et Florent Laporte à Airbus, et je tiens à les remercier pour avoir rendu cela possible.

Je tiens à remercier toutes les personnes qui m'ont aidé à progresser et à avancer pendant la thèse. Merci en particulier à Simon, pour avoir largement contribué à mes résultats et pour tous les coups de main que tu m'as donné sur elsA ou flowsim. Merci également à Marc et Thierry, pour avoir suivi ce travail de près et pour m'avoir conseillé sur la bonne direction à prendre à de nombreuses reprises.

Pour terminer, je tiens à remercier toutes les autres personnes qui ont fait de ces trois ans une période très joyeuse. Suk-Kee, Pierre-Thomas, Aurélie et Valentina, je suis très heureux d'avoir pu progresser en même temps que vous dans le monde impitoyable des turbomachines. Nico B, merci pour tes conseils très avisés (notamment en matière de littérature, scientifique ou non !). A toute l'équipe de l'ISAE, merci de m'avoir donné envie de rester parmi vous après l'ENSICA, par votre bonne humeur et la bonne ambiance qui règne chez vous. Ne changez pas. A toute l'équipe EGDC à Airbus, merci pour m'avoir intégré parmi vous ! Enfin, à toutes les personnes que j'ai rencontré au CTL, il a été très enrichissant de travailler à vos côtés. Merci Andras pour l'installation (et la maintenance) de mon PC, et merci Yuan-Kang pour m'avoir initié à la cuisine Singapourienne !

# Contents

<b>Introduction</b>	<b>16</b>
<b>1 Review of fan-airframe aerodynamic interactions</b>	<b>21</b>
1.1 Inlet-fan interaction background . . . . .	21
1.1.1 Max climb conditions . . . . .	22
1.1.2 Crosswind operation . . . . .	23
1.1.3 Toward UHBR engines: short nacelle framework . . . . .	23
1.2 Boundary layer ingestion . . . . .	26
1.2.1 Upstream influence and distortion transfer . . . . .	26
1.2.2 Loss, fan stability and aeromechanical constraints . . . . .	28
1.3 Simulation of fan-airframe interactions . . . . .	28
<b>2 Body force modeling</b>	<b>30</b>
2.1 Literature review . . . . .	30
2.1.1 2D Throughflow modeling . . . . .	31
2.1.2 Actuator Disk Approach . . . . .	32
2.1.3 3D Throughflow modeling . . . . .	33
2.1.4 Other approaches . . . . .	35
2.1.5 Summary and discussion . . . . .	36
2.2 Body force implementation . . . . .	38
2.2.1 Quasi-steady assumption . . . . .	38
2.2.2 Equations of motion . . . . .	39
2.2.3 Coupling between CFD solver and body force module . . . . .	40
2.2.4 Metal blockage implementation . . . . .	41
2.3 Body force model formulations . . . . .	44
2.3.1 Test case . . . . .	44
2.3.2 Extraction of a body force field from a blade computation . . . . .	45
2.3.3 Gong's model . . . . .	52
2.3.4 Lift / drag model . . . . .	60
2.3.5 Hall's model . . . . .	64
2.4 Summary and conclusions . . . . .	72
<b>3 Intake-fan interactions on short nacelle configurations</b>	<b>75</b>
3.1 Description and assessment of the fan geometry . . . . .	75
3.2 Fan-intake interactions at max climb . . . . .	77

3.2.1	Upstream influence: flow field in the air intake . . . . .	79
3.2.2	Upstream influence: effect of the fan on inlet flow separation . . . . .	82
3.2.3	In-plane-forces acting on the fan . . . . .	85
3.2.4	Fan-OGV interactions . . . . .	87
3.2.5	Summary . . . . .	87
3.3	Inclusion of the bifurcation and exhaust in the computational domain . . . . .	88
3.3.1	Effect of the bifurcation on the intake flow field at max climb . . . . .	89
3.3.2	Effect of the bifurcation on IP forces . . . . .	90
3.3.3	Distortion transfer in the bypass flow . . . . .	90
3.4	Experimental validation . . . . .	94
3.4.1	Intake flow field with vertical wind against lateral wind . . . . .	96
3.4.2	Effect of bifurcation and flow separation on total pressure rise . . . . .	97
3.5	Summary and conclusions . . . . .	97
<b>4</b>	<b>Boundary layer ingestion</b>	<b>99</b>
4.1	R4 fan stage response to BLI inlet distortion . . . . .	99
4.1.1	Description of the test case and computational approach . . . . .	99
4.1.2	Upstream redistribution and distortion transfer . . . . .	101
4.1.3	Parametric study of fan–distortion interactions . . . . .	110
4.1.4	Summary . . . . .	115
4.2	RAPRO experiment . . . . .	116
4.2.1	Description of the RAPRO configuration . . . . .	116
4.2.2	Amount of ingested boundary layer versus power saving . . . . .	117
4.3	Summary and conclusion . . . . .	119
<b>Conclusion and future work</b>		<b>120</b>
<b>A</b>	<b>Loss modeling for compressor cascades</b>	<b>131</b>
A.1	Motivation and objective . . . . .	131
A.2	Parametric linear cascades generation . . . . .	133
A.3	Construction of loss metrics and loading parameter . . . . .	133
A.3.1	Loss metrics . . . . .	134
A.3.2	Loading metric . . . . .	136
A.3.3	Local vs global metrics . . . . .	137
A.4	Correlation of loss metrics against the loading parameter . . . . .	138
A.4.1	Effect of aspect ratio . . . . .	138
A.4.2	Effect of camber, stagger, and solidity . . . . .	138
A.4.3	Effect of thickness . . . . .	139
A.4.4	Effect of tip clearance . . . . .	140
A.4.5	Effect of Mach number . . . . .	140
A.4.6	Other effects . . . . .	141
A.5	Summary and way forward . . . . .	142

<b>B</b>	<b>Circumferentially averaged Navier Stokes Equations</b>	<b>144</b>
B.1	Derivation of the equations . . . . .	144
B.2	Blade force and blockage contribution . . . . .	149
B.3	Blade camber surface and metal angles definition . . . . .	149
B.4	Circumferential stresses . . . . .	151
<b>C</b>	<b>Body force interpolation from database</b>	<b>152</b>
<b>D</b>	<b>Endwall treatment for Hall's model</b>	<b>155</b>

# List of Figures

1	Comparison of the B707 and the A350. . . . .	17
1.1	IDC measurement device . . . . .	22
1.2	Illustration of the behavior of an air intake at max climb. . . . .	23
1.3	Illustration of the behavior of an air intake at crosswind. . . . .	24
1.4	Illustration of the length to diameter ratio of an air intake . . . . .	24
1.5	Illustration of In-Plane forces acting on a fan. . . . .	25
1.6	Illustration of some aerodynamic interactions between fan and airframe in UHBR engines. . . . .	25
1.7	Illustration of the Boundary Layer Ingestion concept . . . . .	26
1.8	Sketch of the flow redistribution upstream of a BLI fan . . . . .	27
2.1	Body force modeling concept: the blades are replaced by source term distributions to capture turning, losses, and blade metal blockage. . . . .	30
2.2	Reduced order models for turbomachinery. . . . .	36
2.3	Illustration of the blade metal blockage parameter and the normal and parallel forces. . . . .	40
2.4	Coupling between the elsA solver and a body force generator via FlowSimulator	41
2.5	Simple stator test case. . . . .	42
2.6	Comparison of direct CFD computations on a simple stator geometry (blade) and body force computations with blockage source terms. Meridional view for two values of the outlet static pressure (contours of Mach number). . . . .	42
2.7	Comparison of direct CFD computations on a simple stator geometry and body force computations with blockage source terms. Mach number evolution at mid-span for two values of the outlet static pressure. . . . .	43
2.8	Comparison of direct CFD computations on a simple stator geometry and body force computations with blockage source terms. Total pressure loss with a normal shock in the meridional plane. . . . .	43
2.9	NASA/GE R4 test case. . . . .	44
2.10	NASA/GE R4 body force computational grid. . . . .	48
2.11	R4 stage performance map (50%, 75% and 100% RPM). Comparison of blade and extracted body force computations (BFA and thermodynamics-based). The BFA gives a better estimation of the global performance than the thermodynamics-based approach. . . . .	49

2.12	Spanwise profiles at 50% RPM (top) and 100% RPM (bottom) downstream of the R4 fan stage. Operating points near max efficiency (left) and near stall (right). Off-design efficiency profiles are not well captured, especially with the BFA. . . . .	49
2.13	R4 stage performance map (50%, 75% and 100% RPM). Comparison of frozen body force approaches based on the extraction of thermodynamic quantities (frozen $f_x$ , $f_r$ , $f_t$ or frozen $f_n$ and $f_p$ or frozen entropy and tangential velocity gradients). . . . .	50
2.14	Spanwise profiles at 50% RPM (top) and 100% RPM (bottom) downstream of the R4 fan stage, near max efficiency (left), and near stall (right) (frozen $f_x$ , $f_r$ , $f_t$ or frozen $f_n$ and $f_p$ or frozen entropy and tangential velocity gradients). Directly imposing the normal and parallel force or the gradients significantly improves the prediction of efficiency. . . . .	50
2.15	The flow field in the blade to blade plane can locally be analyzed as a fluid in a periodic straight channel [39]. . . . .	52
2.16	NASA/GE R4 speed line (90% RPM). Comparison of Gong's baseline model with $K_n = 4.2 - 3.3\beta_m$ , $K_p = 0.02$ , and Gong's improved model with calibrated coefficients. Metal blockage effects are not taken into account in both approaches. . . . .	55
2.17	NASA/GE R4 speed line (90% RPM). Comparison of Gong's improved model, with and without offset on the cross channel velocity $W_\xi$ . Metal blockage effects are not taken into account in both approaches. . . . .	55
2.18	NASA/GE R4 speed line (90% RPM). Comparison of Gong's improved model, with an offset on the cross channel velocity $W_\xi$ , or with the blockage source terms (with and without the pressure-gradient based term). . . . .	56
2.19	R4 fan stage performance map (50%, 75% and 100% RPM). The parallel force either depends on local relative Mach number (one calibration for each speed line), or on local flow coefficient (one calibration for all speed lines, performed at 90% RPM). Using the flow coefficient allows to evaluate the global performance for various rotational speeds. . . . .	57
2.20	R4 fan stage: Spanwise profiles at 50% RPM (top) and 100% RPM. Operating points near max efficiency (left) and near stall (right). The prediction remains accurate at different rotational speeds when the flow coefficient is used for calibration. . . . .	57
2.21	R4 performance map at 100% RPM with $+/-5^\circ$ inlet swirl. The parallel force either depends on the local relative Mach number (calibration performed at 100% RPM), or on the local flow coefficient (calibration performed at 90% RPM). The effect of inlet swirl on the global efficiency is not captured. . . . .	59
2.22	Spanwise profiles at 100% RPM with $5^\circ$ counter-swirl. Operating points near max efficiency (left) and near stall (right). Using the flow coefficient to calibrate the parallel force yields better results than using the relative Mach number. . . . .	59
2.23	R4 speed line at 100% RPM, with and without the offset $C(x)$ in the lift/drag normal force formulation. Adding the offset is required to capture the choke mass flow rate of the fan stage, but it leads to underestimated peak efficiency. . . . .	61

2.24	R4 performance map (50%, 75% and 100% RPM). In blue, the model is re-calibrated for each speed line, in red the model is calibrated from the 75% RPM speed line. The global performance can be evaluated with only one set of calibration coefficients. . . . .	63
2.25	Spanwise profiles at 50% RPM (top) and 100% RPM (bottom) downstream of the R4 fan stage. Operating points near max efficiency (left) and near stall (right). The local off-design efficiency decrease is not well captured. . . . .	63
2.26	NASA/GE R4 operating line at 100% RPM, with $+/-5^\circ$ inlet swirl. The global performance is well captured, but the peak efficiency with co-swirl is underestimated. . . . .	64
2.27	Spanwise profiles at 100% RPM with $5^\circ$ inlet counter-swirl downstream of the R4 fan stage. Operating points near max efficiency (left) and near stall (right). The efficiency profile with inlet swirl near stall is not captured. . . . .	64
2.28	R4 stage performance map at 50% and 100% RPM. Comparison of Hall baseline model and blade computations. . . . .	65
2.29	Compressibility correction applied to the normal force model and contours of tangentially averaged relative Mach number in the R4 fan stage near design. . . . .	67
2.30	Performance map of the R4 fan stage (50% and 100% RPM). Metal blockage decreases the work coefficient predicted by Hall's model but including a compressibility correction in the normal force allows to improve the results. . . . .	67
2.31	R4 fan stage 100% RPM speed line. Illustration of the two-step procedure to capture off-design loss with Hall's model. . . . .	68
2.32	R4 performance map (50%, 75% and 100% RPM). In blue, a $\delta\eta_{max}$ distribution is extracted from the design point at 100% RPM and used to compute all speed lines. In red, a new $\delta\eta_{max}$ distribution is generated for all speed lines, which improves the global accuracy. . . . .	70
2.33	Spanwise profiles at 50% RPM (top) and 100% RPM (bottom) downstream of the R4 fan stage. Operating points near max efficiency (left) and near stall (right). The model gives encouraging results near maximum efficiency when it can be re-calibrated but profiles of efficiency are not captured near stall. . . . .	70
2.34	NASA/GE R4 operating line at 100% RPM, , with $+/-5^\circ$ inlet swirl. The global performance is well captured, but the efficiency is in general overestimated. . . . .	71
2.35	Spanwise profiles at 100% RPM with $5^\circ$ inlet counter-swirl downstream of the R4 fan stage. Operating points near max efficiency (left) and near stall (right). As for the lift/drag model, the profile of efficiency near stall is not captured. . . . .	71
2.36	Total to static pressure ratio in the R4 fan stage (100% RPM). The lift drag model captures the onset of positive slope on the left of the characteristic. . . . .	73
3.1	Performance maps of the fan rotor with $5^\circ$ positive and negative inlet swirl. The overall work coefficient and rotor efficiency are well captured by the BF models. . . . .	76

3.2	Spanwise profiles downstream of the fan rotor (relative error as compared to blade computations). Operating point near maximum efficiency (left) and near stall(right) without swirl (top) and with 5° counter-swirl (bottom). The work and efficiency are captured within 10% on most of the span for a wide range of operating points. . . . .	77
3.3	Illustration of the three intake geometries used to highlight the effect of inlet length on intake-fan interactions. . . . .	78
3.4	Contours of Mach number in a plane near the inlet throat. $AOA_{stall}^{P/O} - 1^\circ$ . The fan-distortion interactions lead to flow redistribution inside the air intake. . . . .	80
3.5	Circumferential evolution of the isentropic Mach number on the inlet lips, near the inlet throat. $AOA_{stall}^{P/O} - 1^\circ$ . The static pressure distributions on the intake lips are altered by the fan on the short intake, which is well captured by the BF models. . . . .	80
3.6	Axial evolution of isentropic Mach number on the lower lip. $AOA_{stall}^{P/O} - 1^\circ$ . The position of the shock is moved upstream and its strength reduced in powered computations. . . . .	81
3.7	Contours of Mach number in a plane at the fan face. $AOA_{stall}^{P/O} - 1^\circ$ . The flow redistribution due to the fan upstream influence is well captured in BF computations. . . . .	81
3.8	Circumferential evolution of absolute and relative Mach numbers and flow angles at mid-span at the fan face (short intake). $AOA_{stall}^{P/O} - 1^\circ$ . The peak-to-peak variations in the relative frame are attenuated by the fan, which is well captured in BF computations. . . . .	82
3.9	Circumferential distortion index at the fan face versus air intake AOA for the long (blue), intermediate (green) and short (red) intake. The onset of separation is delayed by 0.5° on the intermediate intake and 1.5° on the short intake in powered computations. . . . .	83
3.10	Contours of Mach number on the lower lip (left) and at the fan face (right) on the short intake. $AOA_{stall}^{P/O}$ . The flow is separated in the power-off computation but remains attached in URANS and BF computations. . . . .	83
3.11	Circumferential distribution of isentropic Mach number on the short intake lips (left) and axial evolution of isentropic Mach number on the lower lip (right). $AOA_{stall}^{P/O}$ . . . . .	84
3.12	Contours of Mach number on the lower lip (left) and at the fan face (right) on the short intake. $AOA_{stall}^{URANS}$ . The size of the separated region is reduced by the fan upstream influence, which is qualitatively captured by the BF models. . . . .	85
3.13	Circumferential distribution of isentropic Mach number on the short intake lips (left) and axial evolution of isentropic Mach number on the lower lip (right). $AOA_{stall}^{URANS}$ . The beneficial effect of the fan on the separated region is overestimated by Hall's model. . . . .	85
3.14	Contours of Mach number on the lower lip (left) and at the fan face (right) on the long intake. $AOA = AOA_{stall}^{P/O}$ . The separated region is not affected by the fan. . . . .	86

3.15	In-plane forces acting on the fan for the short (red), intermediate (green) and long (blue) intake. The phase is computed relatively to the external flow direction ( $0^\circ$ means that the force is vertical, i.e. aligned with the external flow). The magnitude of the force increases when the air intake is shorter, which is qualitatively captured by the BF models. . . . .	86
3.16	In-plane forces acting on the fan with (purple), and without (red) the OGVs. The phase of the force is shifted when the OGVs are included in the simulation. . . . .	87
3.17	Sketch of the short intake configuration with fully simulated bypass flow. . . . .	88
3.18	Axial evolution of the isentropic Mach number on the lower lip. Effect of the bifurcation on the flow field (a) and ability of the models to capture this effect (b). $AOA = 30^\circ$ . . . . .	89
3.19	Effect of increased AOA on the mass flow rate in the air intake with fully simulated bypass flow. The mass flow rate is normalized by the mass flow rate predicted in URANS computations at $0^\circ$ AOA. . . . .	90
3.20	In-plane forces acting on the fan with (orange), and without (purple) the bifurcation (OGVs included in both cases). . . . .	91
3.21	In-plane forces acting on the OGVs with (orange), and without (purple) the bifurcation. The modulus is normalized by the thrust acting on the OGVs. . . . .	91
3.22	Contours of Mach number and stagnation pressure downstream of the OGVs (station 4). $AOA_{stall}^{URANS} - 1^\circ$ . Distortion transfer is qualitatively captured by the models. . . . .	92
3.23	Circumferential distributions of Mach number and stagnation pressure at 75% span, downstream of the OGVs (station 4). $AOA_{stall}^{URANS} - 1^\circ$ . . . . .	92
3.24	Contours of entropy at the fan face and work coefficient downstream of the fan rotor (station 3). $AOA_{stall}^{URANS}$ . The location and amplitude of flow separation varies slightly between URANS and BF computations, but the impact on the work coefficient downstream of the rotor is well captured. . . . .	93
3.25	Contours of Mach number and stagnation pressure downstream of the OGVs (station 4). $AOA_{stall}^{URANS}$ . The stagnation pressure distortion is attenuated by the fan. . . . .	94
3.26	Circumferential distributions of Mach number and stagnation pressure at 75% span, downstream of the OGVs (station 4). $AOA_{stall}^{URANS}$ . . . . .	94
3.27	Experimental setup for the simulation of fan-intake interactions at high AOA. . . . .	95
3.28	Axial evolution of isentropic Mach number on the intake lips (last attached WTT AOA). Comparison between WTT and lift/drag computations. . . . .	96
3.29	Axial evolution of isentropic Mach number on the intake lips (first separated AOA in lift/drag computations). Comparison between WTT and lift/drag computations. . . . .	97
3.30	Circumferential evolution of stagnation pressure at 75% span downstream of the OGVs. Comparison between WTT and lift/drag computations. . . . .	98
4.1	BLI computational domain for URANS computations. . . . .	100
4.2	Parametric inlet distortion patterns: contours of absolute total pressure. . . . .	100

4.3	Effect of the moving average on circumferential profiles of axial velocity. The result does not depend on the position of the rotor blades, but sharp peaks are attenuated. . . . .	102
4.4	Contours of radial flow angle at the fan face (station 1). The radial redistribution of the flow upstream of the rotor is well captured by the BF models. . . . .	102
4.5	Contours of absolute swirl angle at the fan face (station 1). The top-to-bottom redistribution of the flow upstream of the rotor is well captured by the BF models. . . . .	103
4.6	Circumferential profiles of radial and swirl angles at the fan face (station 1). There is a good quantitative agreement between URANS and body force computations. . . . .	103
4.7	Circumferential profiles of relative Mach number and flow angle at the fan face. . . . .	104
4.8	Contours of work coefficient downstream of the rotor (station 2). The non-uniform work input in the rotor is well captured by the BF models. . . . .	105
4.9	Contours of mass flux coefficient downstream of the rotor (station 2). The mass flow redistribution in the rotor is well captured by the BF models. . . . .	106
4.10	Circumferential profiles of work coefficient and mass flux coefficient downstream of the rotor (station 2). There is a good quantitative agreement between BF and URANS computations. . . . .	106
4.11	Contours of absolute total pressure (normalized by clean inlet total pressure) downstream of the OGVs (station 3) for two inlet flow distributions. . . . .	107
4.12	Circumferential profiles of absolute total pressure (normalized by clean inlet total pressure) downstream of the OGVs (station 3). . . . .	108
4.13	Discrete Fourier transform of a circumferential profile of mass flux at 75% span downstream of the OGVs (station 3). W1 inlet distortion case. . . . .	108
4.14	Discrete Fourier transforms of circumferential profiles of mass flux, from inlet to outlet of the computational domain: stations 1 (top), 2 (middle), 3 (bottom). There is no significant filtering effect in the body force computations. . . . .	109
4.15	Definition of the spatial extent of a bucket $\Delta\theta_{80\%}$ and position of the minimum $\theta_{min}$ . . . . .	111
4.16	Distortion intensity $E_{P_i}^*$ from inlet to outlet for five inlet distortion patterns. The distortion is reduced at 75% span but increased at 25% span, which is well captured by the BF models. . . . .	111
4.17	Position of the total pressure minimum $\theta_{min}$ , from inlet to outlet for five inlet distortion patterns (decreasing values mean that the minimum goes in the same direction as the fan rotation). There is a good agreement between BF and URANS computations. . . . .	112
4.18	Relative range of the total pressure bucket $\Delta\theta_{80\%}$ , from inlet to outlet for five inlet distortion patterns (positive values mean that the bucket is wider than it was at inlet). . . . .	113
4.19	Modulus normalized by thrust and phase of IP forces acting on the R4 rotor and OGVs (negative phase means the vertical force points downward). The impact of each distortion on the modulus of the force is qualitatively captured by the BF models. . . . .	114

4.20	Efficiency decrease relatively to clean inlet flow. The effect of BLI on the fan stage efficiency is qualitatively captured by the models. . . . .	115
4.21	Sketch of principle and photo of the RAPRO2 experimental set-up (credits ONERA [2]) . . . . .	116
4.22	Illustration of the different types of computations conducted on the RAPRO configuration. . . . .	117
4.23	Experimental measurements (WTT) of power saving against body force computations (lift/drag model). . . . .	118
4.24	Portion of ingested fuselage boundary layer in body force computations (lift/drag model). BLI benefits fall to only 2 – 3% when 30% of the fuselage boundary layer is ingested. . . . .	118
A.1	Illustration of the parametric linear cascade geometry. . . . .	132
A.2	Meridional contours of pitch-averaged entropy gradients. The red lines are streamlines computed with the pitch-averaged axial and radial velocities. . . . .	135
A.3	Spanwise distribution of entropy downstream of the cascade blade. . . . .	135
A.4	Computation of a mean loading coefficient on a circumferential sector in a body force computation. A mean loading coefficient can be computed at the tip for each circumferential sector, and the corresponding loss can be applied on the desired fraction of the span from leading to trailing edge, on the same sector. . . . .	137
A.5	Effect of aspect ratio on the 3D loss. . . . .	138
A.6	Loss coefficient $\xi_{3D}$ and loss extent $H_{3D}$ against mean loading factor $\bar{f}_n^*$ for a range of camber, stagger, and solidity. A correlation seems to emerge between the loss metrics and the loading metric. . . . .	139
A.7	Loss coefficient $\xi$ and loss extent $H_{3D}$ against mean loading factor $\bar{f}_n^*$ for three different thickness to chord ratios. The effect of thickness is decoupled from the effect of the loading. . . . .	140
A.8	Tip clearance effect on 3D loss . . . . .	141
A.9	Mach number effect on 3D loss . . . . .	141
B.1	Distributions of blade metal angle from leading to trailing edge on the R4 fan rotor, taken at constant span. Comparison of the blade metal angle directly computed from the camber surface definition in equation (B.17) and of a corrected distribution based on the leading and trailing edge angles. . . . .	150
C.1	Performance prediction with interpolated body forces . . . . .	153
D.1	Spanwise profiles of work coefficient and deviation angle near the hub, downstream of the R4 fan rotor. Comparison of Hall's model with blade computations at the design operating point. . . . .	156

# List of Tables

2.1	NASA R4 fan stage geometry and design operating point . . . . .	44
3.1	9-inch fan stage geometry. . . . .	76
3.2	Length to diameter ratios of each air intake. . . . .	78
4.1	Inlet distributions characteristics. . . . .	101
4.2	RAPRO, non axisymmetric body force computations: distance between fan and fuselage axis, relatively to the fan radius (greater than one means that the fuselage axis is outside of the fan). . . . .	117
A.1	Preliminary cascade computations parameters. . . . .	139

# Nomenclature

## Abbreviations

CFD Computational Fluid Dynamics

RANS Reynolds Averaged Navier-Stokes

BF Body Force

URANS Unsteady Reynolds Averaged Navier-Stokes

LES Large Eddy Simulation

SA Spalart-Allmaras

FPR Fan Pressure Ratio

BPR Bypass Ratio

UHBR Ultra High Bypass Ratio

OGV Outlet Guide Vane

CROR Contra-Rotating Open Rotor

BLI Boundary Layer Ingestion

AD Actuator Disk

LPC Low Pressure Compressor

AOA Angle of Attack

AOSS Angle of SideSlip

RPM Rotation Per Minute

MFR Mass Flow Rate

IP In-Plane

AR Aspect Ratio

WTT Wind Tunnel Test

BFA Blade Force Average

IDC Circumferential Distortion Index

TPS Turbine Powered Simulator

## Coordinates

$x, y, z$  Cartesian coordinates

$x, r, \theta$  Cylindrical coordinates

$\eta, \xi$  Blade passage coordinates

$n, p$  Normal and parallel to the flow

## Greek Symbols

$\alpha$  Angle of attack

$\beta$  Relative flow angle

$\beta_m$  Blade camber angle

$\delta$  Deviation angle

$\eta$  Efficiency

$\lambda$  Blade lean angle

$\nu$  Dynamic viscosity

$\Omega$  Rotational speed

$\Phi$  Mass flux coefficient

$\phi$  Flow coefficient

$\psi$  Work coefficient

$\sigma$  Solidity

$\tau$  Shear stress tensor

$\vec{\tau}_p$  Friction vector

## Operators

$\bar{X}$  Average of  $X$

$|X|$  Absolute value of  $X$

$\hat{X}$  Fourier transform of  $X$

$\tilde{X}$  Favre average of  $X$

## Roman Symbols

$F$  Force

$\vec{f}$  Body force vector per unit mass

$\vec{F}$  Body force vector per unit volume

$\vec{V}$  Absolute velocity vector

$\vec{W}$  Relative velocity vector

$U$  Rotor velocity

$\dot{m}$  Mass flow rate

$\rho$  Density

$T$  Static Temperature

$P$  Static Pressure

$P_i$  Total Pressure

$q$  Dynamic Pressure

$S$  Entropy per unit mass

$h_t$  Total enthalpy per unit mass

$e_t$  Total energy per unit mass

$\vec{q}$  Heat flux

$M$  Mach number

$Re$  Reynolds number

$C_f$  Friction coefficient

$C_L$  Lift coefficient

$b$  Blockage factor

$s$  Blade pitch

$c$  Blade chord

$h$  Blade to blade staggered spacing

$Z_{blade}$  Number of blades

$\vec{n}$  Vector normal to the camber surface

$R$  Radius

## Superscripts and Subscripts

$ss$  Suction side

$ps$  Pressure side

$LE$  Leading edge

$TE$  Trailing edge

$m$  Meridional, Mean, Metal

$l$  Along a streamline

$a$  Absolute

$r$  Relative

$0$  Value at inlet

$ref$  Reference value

$edge$  At the edge of the boundary layer

$P/O$  Power-Off

$t$  Transposed

# Introduction

## Background

It is now a common knowledge that the commercial aircraft industry is putting a lot of efforts toward the reduction of aircraft fuel burn and pollutant emissions. The research that is conducted in this regard is of particular importance to respect environmental constraints and to keep producing competitive airplanes. One of the first successful commercial aircraft was the Boeing 707, whose first flight occurred in 1957, and the most striking thought when one looks at more recent airplanes such as the A350 or the B787 is that they all use the same paradigm (one fuselage, two wings, engines podded under the wing), sixty years later. This does not mean that no efforts have been made to improve commercial airplanes, but rather that this configuration constitutes some local optimum for the whole aircraft system.



**Figure 1:** Comparison of the B707 and the A350.

As a matter of fact, the average commercial aircraft fuel efficiency has approximately doubled between 1960 and 2010 [77]. This can be explained by a number of factors, among which improved aircraft aerodynamics at transonic Mach numbers, improved materials, and better engines. Although further progress may be achieved both in terms of external aerodynamics (laminar wings / fuselage, riblets) or in terms of systems and structure (electric deicing, composite materials), large improvements will be obtained by working on the powerplant and its integration to the aircraft. For instance, the propulsive efficiency of a single stream turbojet engine can be written:

$$\eta_{prop} = \frac{2}{1 + \frac{u_e}{u_0}} \quad (1)$$

where  $u_e$  is the engine exhaust velocity and  $u_0$  is the external flow velocity. The propulsive efficiency is maximum when the exhaust velocity is as close as possible to the external flow velocity. Thrust can be written:

$$F = \dot{m}(u_e - u_0) \quad (2)$$

The analysis of both equations shows that, for a given thrust requirement, it is more efficient to give a small acceleration  $u_e - u_0$  to a large amount of fluid  $\dot{m}$ . In practice, the exhaust velocity decreases with the Fan Pressure Ratio (FPR), and higher mass flow rates can be obtained with larger fan diameters. This explains the current efforts to increase the bypass ratio (BPR) of civil aircraft engines, hence the “Ultra High Bypass Ratio” (UHBR) denomination for future turbofan engines [67]. However, a larger fan diameter also results in a larger casing, which leads to increased nacelle weight and drag penalties.

To take advantage of the future generation of turbofan engines, innovative nacelle designs must thus be examined. For instance, one possibility is to consider shorter and thinner inlet lips. However, this approach leads to increased aerodynamic interactions between the air intake and the fan, which is no longer shielded from the external flow. To ensure a proper operation of both fan and air intake in the whole flight envelope of the aircraft these interactions must be mastered early in the design process of both components. On the long term, new propulsion paradigms must be envisioned to further decrease fuel burn. For instance, the Boundary Layer Ingestion (BLI) concept consists in embedding the engines and the airframe together so that the engines ingest a portion of the airframe boundary layer, which decreases wake drag penalties. In this kind of configuration, the aircraft and the engines are fully coupled, as the fans operate under distorted inflow, and as the pressure distributions on the airframe are affected by the fans. Designing such an aircraft requires a characterization of these interactions, and affordable and robust numerical capabilities that capture the effect of each component on the others.

From the numerical standpoint, it is possible to capture fan–airframe interactions with a full annulus unsteady representation of the fan. However, this kind of approach remains too expensive for quick design loops. In addition, it requires a detailed geometry of the fan blades, which is in general not available to the airframe manufacturers. Another solution could be to replace the fan with an Actuator Disk (AD), but this kind of representation misses important flow features, such as choke and mass flow redistribution within the blade row. In this context, this PhD study focuses on a non-axisymmetric throughflow method in which turbomachinery blade rows are replaced by source terms that reproduce flow turning and stagnation pressure rise (“Body force modeling”). This approach was initially proposed by Marble [62] and has since been adapted for various applications, ranging from compressor stability [40, 15] to noise prediction [23, 87], to name a few. In particular, the relevance of the approach in the frame of fan–airframe integration was demonstrated several times, as it was successfully used to capture intake–fan–exhaust interactions [70], intake–fan interactions under high incidence [11, 50] or fan–distortion interactions on BLI configurations [71, 49]. However, some limitations of the body force formulations that were implemented in past contributions were highlighted by their authors, such as the lack of a model for metal blockage and a heavy calibration process [69], or a restriction to incompressible flows [48].

## Objectives and challenges

The goal of this PhD study is to propose a source term formulation that addresses the limitations reported in previous contributions, and which can be used to design an airframe in an industrial context. In particular, the following objectives are used as guidelines:

- The body force formulation must capture fan–airframe interactions on short intake and BLI configurations.
- The body force formulation must be robust and simple enough to be implemented within an existing CFD solver.
- The body force formulation must be as general as possible and avoid calibration, or the calibration process must be robust enough to be completely automated.

Modeling the effect of modern fan blades, which are highly three-dimensional, is challenging. The body force model must capture the behavior of the fan over a large range of rotational speeds, including high rotational speeds where the fan blades operate under transonic conditions. To capture the interaction of the fan with inlet distortion, the model must capture the non-uniform work input due to varying inlet conditions. Furthermore, the model must capture the choke mass flow rate of the fan to obtain the correct mass flow at high rotational speeds, on installed configurations. While the inviscid effect of the blades may be captured with rather simple approaches, modeling the losses that occur in turbomachinery blade rows is especially complex and has already been a very wide area of research in the past. Finally, adding source terms to the RANS equations can lead to convergence issues, especially at high rotational speeds where flow turning and blockage effects are important.

## Methodology

The contributions of Gong [39], Peters [69] and Hall [48] are used as a basis for the present work. A modified version of Gong’s formulation is first applied to a fan–OGV test case and its main shortcomings are identified. Based on these findings, two formulations are proposed. The first is obtained in analogy with the lift and drag of a wing. The second is an improved version of Hall’s formulation. The relevance of each formulation is assessed based on performance maps and radial profiles downstream of the isolated fan–OGV configuration. As a second step, the two formulations are applied to the following configurations:

- A nacelle–fan configuration with three inlet designs of varying length.
- An intake–fan–OGV interaction test case with a range of prescribed inflow conditions representative of BLI inlet distortion.
- A fuselage–engine test case on which the portion of boundary layer ingested by the engine can be modified and for which experimental data is available.

For each configuration, the ability of the models to capture some of the key physical mechanisms related to fan–distortion interactions is investigated. All the results are validated against full annulus unsteady simulations or wind tunnel experiments.

## Findings and contributions

From a modeling perspective, two body force formulations that respect the constraints given above are proposed. The first formulation is based on a lift/drag analogy and can only be used when detailed computations of the fan are available. The second formulation is obtained by adding a compressibility correction to Hall's model [48]. It is slightly less accurate than the first one, but it only requires the definition of a blade geometry and the knowledge of the maximum efficiency mass flow rate for a given rotational speed. One formulation or the other can thus be used depending on the amount of available data. A simple model for the loss is proposed and implemented in both formulations, which allows to evaluate the off-design efficiency decrease of a fan stage without manual calibration. It is found that for both formulations, modeling metal blockage is required to capture the choke mass flow rate of a fan stage.

From a more practical standpoint, the application of the models to various configurations leads to the following findings:

- An increase of intake operating range of  $1.5^\circ$  angle of attack out of a range of about  $30^\circ$  is observed at max climb conditions on a nacelle configuration with an intake length to diameter ratio  $L/D = 0.277$ , thanks to the fan–intake interactions. On the same configuration, the in-plane forces acting on the fan are increased from 1% of the thrust for an intake with  $L/D = 0.65$  to about 5% of the thrust for an intake with  $L/D = 0.277$  at  $30^\circ$  AOA.
- Fan stage efficiency penalties of up to 3.5 points are found for the NASA R4 fan stage operating with inlet conditions representative of BLI. In-plane forces reach 6% of the thrust for the same inlet conditions.
- BLI benefits on fuel burn of about 12% are observed on an ideal engine-fuselage configuration in which all the fuselage boundary layer is ingested by the fan. These benefits fall to only 2 – 3% when 30% of the fuselage boundary layer is ingested.

## Outline

The first chapter of this thesis is dedicated to the review of fan–airframe interactions. The aerodynamics of air intakes are discussed and the main physical mechanisms related to the interaction of a fan with distortion are listed. The second chapter describes the body force modeling framework and its applications in the literature. The new formulations are presented and compared to an improved version of Gong's model [39] on an isolated fan test case. In the third chapter, these models are applied to three air intakes of varying length. The beneficial effect of the fan on inlet flow separation is quantified, and the mechanisms of interaction between fan, OGVs and bifurcation are explored. Finally, the fourth chapter focuses on the application of these models to BLI-type interaction test cases. First, a study of the interaction of the NASA R4 fan stage with parametric total pressure inlet distortions is conducted. Then, one of the new body force formulations is applied to the Airbus/ONERA RAPRO configuration and used to quantify the BLI benefits on the required power to achieve a given thrust.

# Chapter 1

## Review of fan-airframe aerodynamic interactions

The purpose of this chapter is to describe the engine–airframe aerodynamic integration challenges that will be encountered on future aircrafts. Because engines are often designed independently from the airframe, the conventional aircraft configuration with under-wing podded engines reduces integration efforts. In practice, an engine is isolated from the rest of the aircraft by a nacelle, which is considered part of the airframe in the present work. An important part of the nacelle is the air intake that delivers air to the engine. The first part of this chapter shortly describes the internal aerodynamics of conventional air intakes, and the potential interactions that occur between fan and intake when the length of the latter is reduced. Then, the BLI concept is presented and its implications in terms of engine integration are discussed.

### 1.1 Inlet–fan interaction background

From the aerodynamic point of view, the main role of the air intake is to provide the adequate mass flow rate to the fan and Low Pressure Compressor (LPC) stages, with minimum loss and with low-distortion inflow. The amount of distortion at the fan face is in general characterized by a criterion that depends on the engine manufacturer. Two different criteria are used in the present thesis. The  $DC_{60}$  criterion, which is one of the most commonly used in the literature, is defined as:

$$DC(\theta) = \frac{\overline{P}_i - \overline{P}_{i,\theta}}{\bar{q}} \quad (1.1)$$

where  $\overline{P}_i$  is the average total pressure at the fan face,  $\overline{P}_{i,\theta}$  the average total pressure in the most distorted sector of size  $\theta$  and  $\bar{q}$  the average dynamic pressure at the fan face. This criterion is used in chapter 4 to quantitatively describe inlet distortion in BLI configurations.

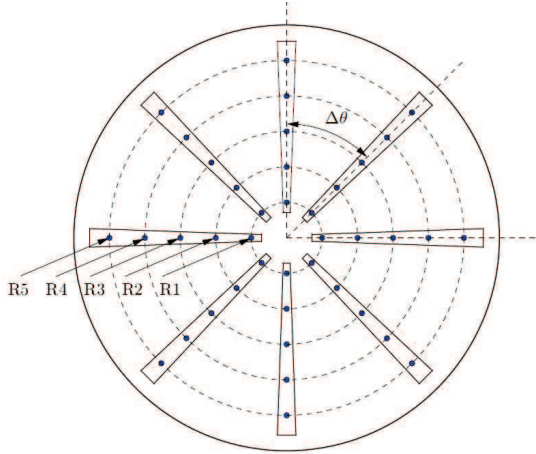


**Figure 1.1:** IDC measurement device (from Colin [18]): eight rakes of five Pitot probes give a spatial discretization of the total pressure at the fan face.

The IDC criterion is based on experimental total pressure rakes, as shown in figure 1.1, and is defined as:

$$IDC = \max_{1 \leq r \leq 5} 0.5 \left( \frac{\overline{P}_{i,r} - P_{i,r}^{\min} + \overline{P}_{i,r+1} - P_{i,r+1}^{\min}}{\overline{P}_i} \right) \quad (1.2)$$

where  $\overline{P}_i$  is the average stagnation pressure in the measurement plane,  $\overline{P}_{i,r}$  the average stagnation pressure on the  $r^{th}$  radius, and  $P_{i,r}^{\min}$  the minimum stagnation pressure on the  $r^{th}$  radius. In the present work, the IDC criterion is used in the short intake framework as it is particularly useful to detect flow separation on the intake lips. For each engine, a specification in terms of maximum distortion level is given by the engine manufacturer to the intake designer, which must not be exceeded. Two particularly challenging aircraft operating conditions for aerodynamic intake design are presented below.

### 1.1.1 Max climb conditions

In some situations an aircraft must be able to quickly gain altitude, to avoid an obstacle for instance. In these conditions, the aircraft AOA is close to its  $C_{L_{max}}$  conditions and the engine is operated at maximum RPM and maximum mass flow rate. Due to the upstream deflection of the wing, the air intake is locally subject to high AOA, which could lead to flow separation on the lower intake lip, as shown in figure 1.2. As the flow goes around the lower lip, it is accelerated until a normal shock appears. If this shock is strong enough, i.e. if the AOA or the mass flow rate are too high, it triggers flow separation in the air intake. As a consequence, the distortion upstream of the fan may be high enough to strongly deteriorate the fan and LPC performance and reduce their stall margin. The intake is therefore designed to avoid separation up to the aircraft  $C_{L_{max}}$  conditions.

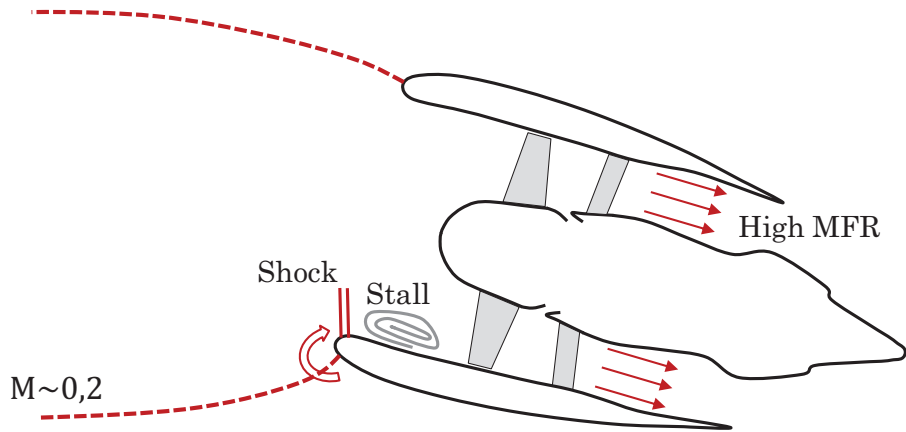


**Figure 1.2:** Illustration of the behavior of an air intake at max climb.

### 1.1.2 Crosswind operation

When the aircraft is operated on the ground before take-off, severe cross wind conditions may impact the operation of the engine, as shown in figure 1.3. At low mass flow rates, the flow has not enough momentum to follow the lip curvature and the intake flow is separated. As the mass flow rate increases, the stall region disappears and the distortion level becomes lower. Finally, at high mass flow rates, a normal shock appears on the lip, which can lead to flow separation and high distortion levels at the fan face, similarly to what happens at max climb.

At low mass flow rates, the presence of flow separation is not critical for the operation of the engine. However, the air intake must maintain low distortion levels just before take-off, when the engine RPM is increasing to provide the required thrust. In particular, the reattachment of the flow must occur before a critical mass flow rate given by the engine manufacturer, above which aeromechanical instabilities may occur. The prediction of the range of mass flow rates for which the intake is not stalled is therefore of particular importance.

### 1.1.3 Toward UHBR engines: short nacelle framework

Future turbofan engines will feature larger fan diameter and lower FPR to reach higher propulsive efficiency, but this comes at the expense of increased casing diameters and thus increased nacelle drag and weight. To mitigate drag and weight penalties, one solution is to reduce the length of the air intake, or more specifically its length to diameter ratio  $\frac{L}{D}$ , illustrated in figure 1.4. However, reducing the length of an air intake is not trivial, as it decreases the potential for aeroacoustic shielding and reduces the room available for critical systems such as anti icing devices. Furthermore, the aerodynamics of both intake and fan are affected. In particular, avoiding flow separation at high AOA and cross wind conditions with short lips is especially challenging, as the curvature of the flow is hard to accommodate. Yet, it was found in previous studies [59, 70, 32] that the fan has a strong upstream influence on distortion. For instance, it was shown that the fan reduces upstream distortion and delays the onset of separation for high AOA conditions. It was also shown that the presence of

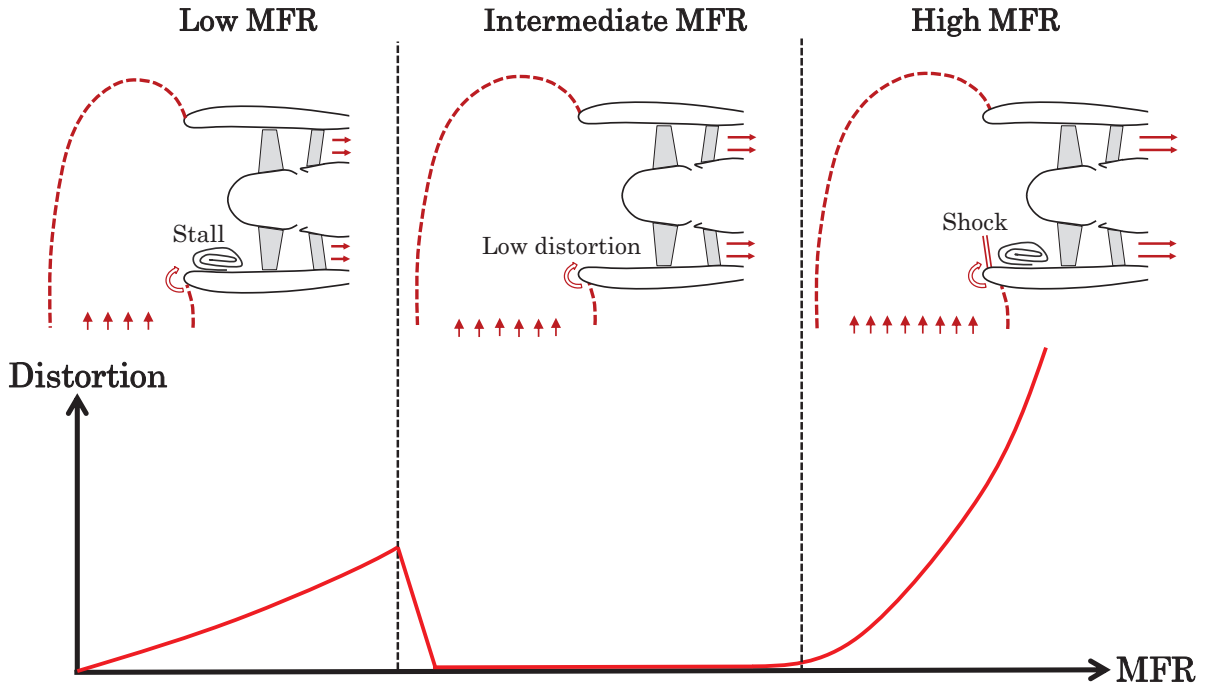


**Figure 1.3:** Illustration of the behavior of an air intake at crosswind.

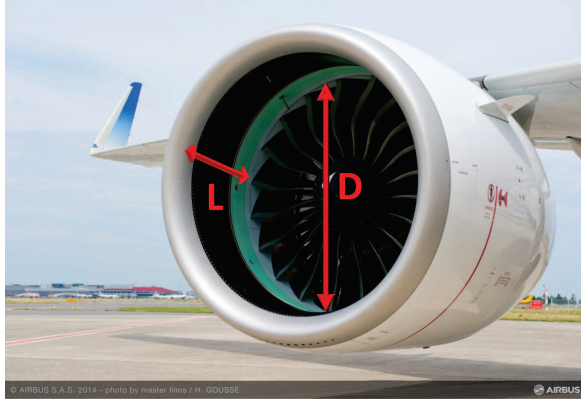


**Figure 1.4:** Illustration of the length to diameter ratio of an air intake (PW1100G, A320 NEO).

the fan extends the separation free region in terms of engine mass flow rate for cross wind conditions [78]. On the other hand, a short intake design does not completely suppress the velocity distortion at the fan face, which decreases the fan efficiency. Furthermore, the residual distortion in the air intake leads to new aeromechanical challenges. In particular, the uneven loading of the blades around the annulus results in what is often referred to as “in plane forces” (IP forces), which are forces acting on the shaft, in the plane orthogonal to the rotation axis, as illustrated in figure 1.5. As will be shown in chapter 3, these forces can

become significant at high AOA for short intake designs and should therefore be accounted for in the structural design of the shaft and its bearings.

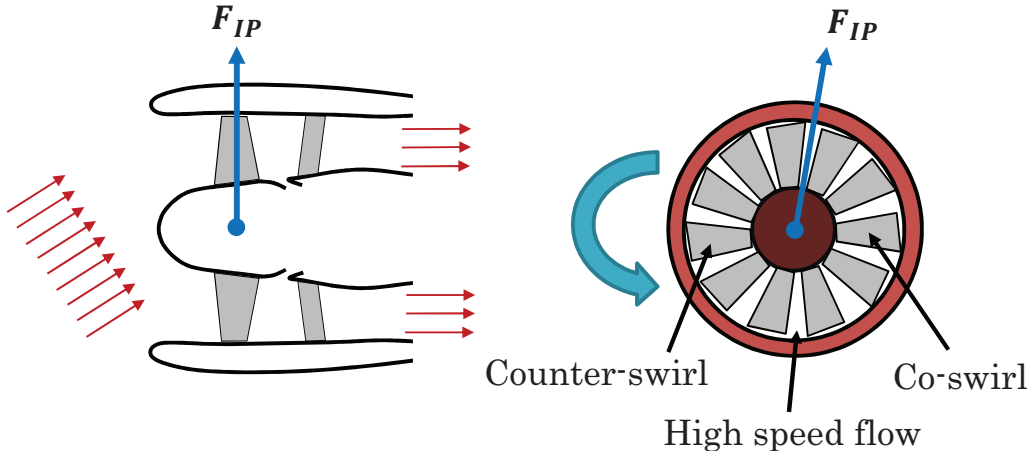


**Figure 1.5:** Illustration of In-Plane forces acting on a fan.

Ultimately, as the need for compact engines will become higher to limit weight and drag penalties, the distance between fan, OGV, bifurcation and exhaust may be reduced, leading to increased interactions between those elements. Figure 1.6 summarizes the aerodynamic challenges that may be faced on these engines. Because of the decrease in FPR, it is more likely that the fan nozzle will be unchoked even at maximum mass flow rate, enabling some interactions between the fan and downstream airframe components such as the wings and flaps.

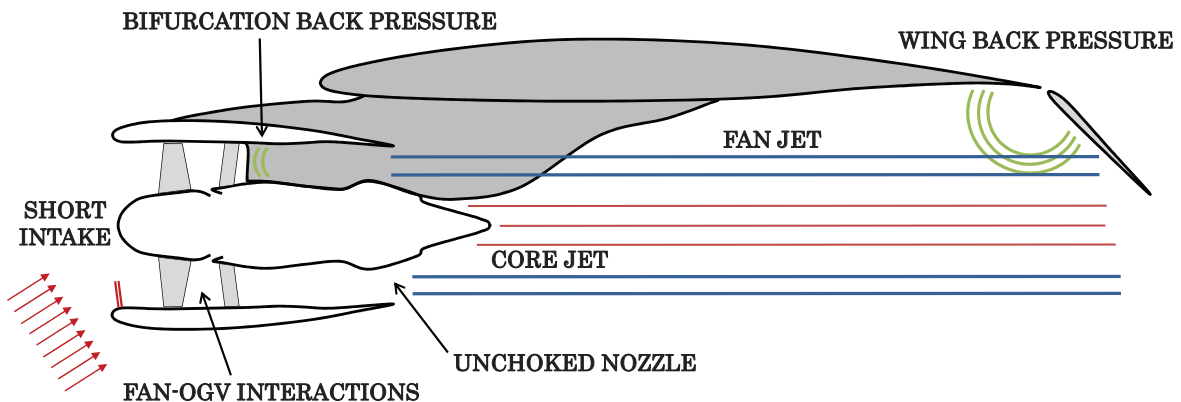


**Figure 1.6:** Illustration of some aerodynamic interactions between fan and airframe in UHBR engines.

Legacy “long” nacelle designs were designed based on CFD simulations using mass flow or static pressure boundary conditions to generate the mass flow rate inside the intake, and

inlet conditions downstream of the fan. This approach was reasonably accurate, given the limited interactions between fan, intake, and exhaust. However, for future designs, accurate CFD predictions of intake separation, intake efficiency, and fan efficiency or stability will require an integrated simulation of all the relevant components.

## 1.2 Boundary layer ingestion

While short nacelles allow to mitigate the drawbacks of larger engines, unconventional concepts are needed to further decrease the fuel consumption of commercial aircrafts. Boundary layer ingestion is a promising concept that consists in ingesting the airframe boundary layer with the engines rather than free stream air, to reduce wake drag penalties and increase the propulsive efficiency. The concept, pictured in figure 1.7, has theoretically been shown to reduce fuel burn by up to 15% compared with conventional engines [88, 2, 47, 31].

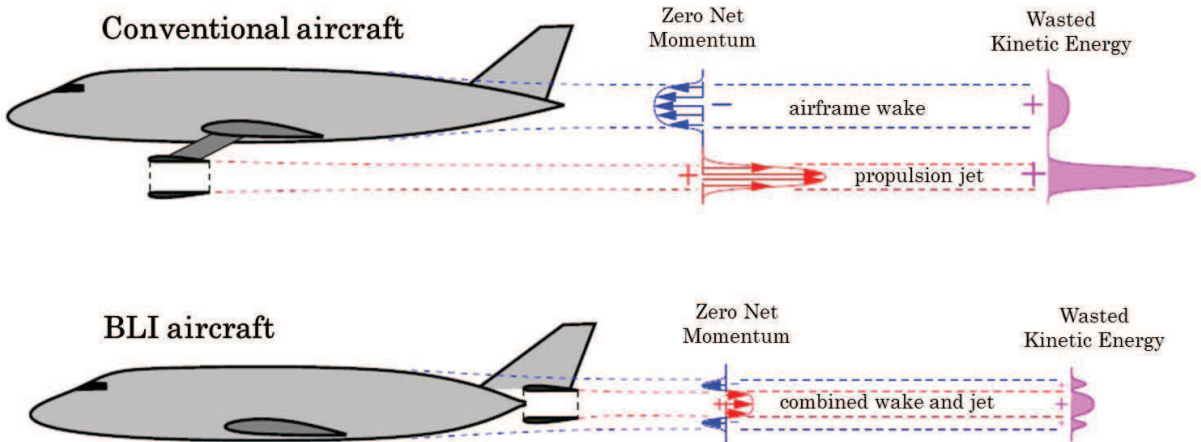


**Figure 1.7:** Illustration of the Boundary Layer Ingestion concept (from Drela [28]).

An important challenge for the practical application of this concept is that the fans and the airframe strongly interact with each other. The fans alter the pressure distributions on the airframe, which modifies lift and drag and thus thrust requirements. Reciprocally, because of the boundary layer ingestion, the fans receive distorted inflow, which locally shifts their operating point toward off-design conditions and reduces their efficiency and stall margin. In practice, fan efficiency reductions of about 1% to 2% relatively to uniform inflow operation were found in [44] for a modern, conventional, fan design. On the other hand, an estimated increase in 0.8% fuel burn per 1% decrease in fan cruise efficiency was found in [48], which is small compared to the potential benefits of BLI on fuel burn.

### 1.2.1 Upstream influence and distortion transfer

The mechanisms leading to the redistribution of the flow upstream of a fan in the presence of distortion are studied thoroughly in references [32, 49, 44] and sketched in figure 1.8. This redistribution is due to the non-axisymmetric work input to the flow in presence of a

non-axisymmetric inlet flow field. In fact, regions in which the flow velocity is lower result in locally higher work input. The low momentum fluid in low stagnation pressure regions is accelerated because of the rotor suction, which creates a circumferential and radial static pressure gradient upstream of the fan blades, which in turns leads to the flow redistribution. The rotor blades experience both swirling and counter-swirling flow regions as they rotate around the annulus, resulting in locally increased or decreased blade incidence. It was found in [44] that this redistribution does not occur further than one casing diameter upstream of the fan face, which implies that the flow is essentially decoupled from the fan upstream of that.

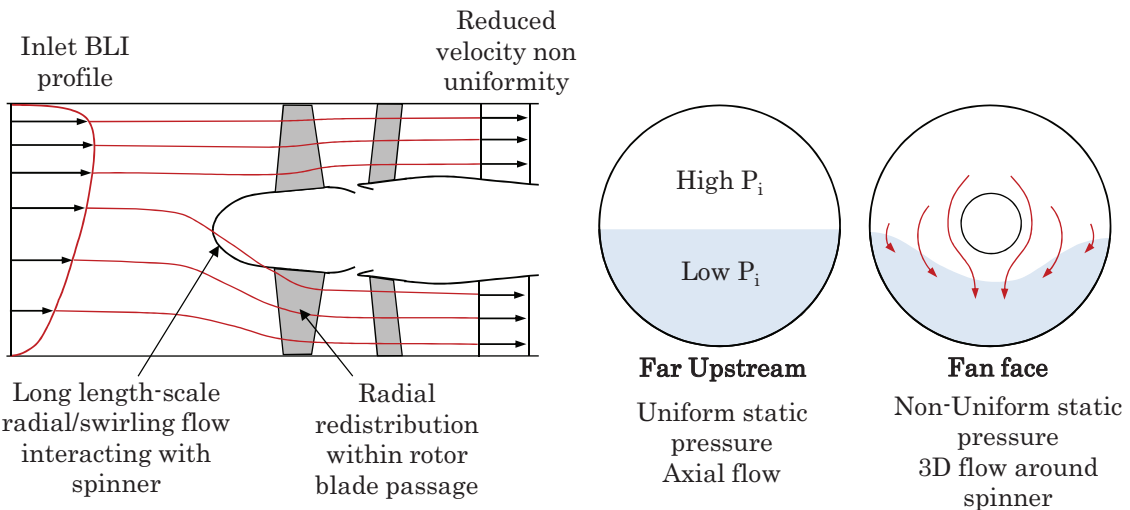


**Figure 1.8:** Sketch of the flow redistribution upstream of a BLI fan (adapted from [44]).

In both the rotor and the stator, the circumferential redistribution of the flow is limited to one blade pitch. However Gunn et al. [44] found that the nature of the BLI distortion, which is both radial and circumferential, leads to radial redistribution in the rotor. A first consequence of this radial redistribution is that the azimuthal distortion is reduced near the tip but increased close to the hub. A second consequence is that the radial component of the distortion is reduced in the blade passage. The radial flow also leads to modified diffusion in the blade passage and to non-uniform radial flow angles upstream of the stator. Finally, the axial velocity is not uniform at the rotor exit, although the relative flow angle does not vary much, so that the stator also experiences non uniform inlet swirl angles.

### 1.2.2 Loss, fan stability and aeromechanical constraints

The description of the redistribution mechanisms in the previous section highlights the strong coupling between the inlet flow field, the spinner, the rotor and the stator. The redistribution upstream of the rotor could lead to increased spinner losses, which must be designed to accommodate the top-to-bottom flow migration. In addition, the local increase in blade incidence near the shroud in the distorted region was shown to result in flow separation on the blades [44], with a significant impact on the rotor efficiency. The non-uniform flow field at the stator inlet leads to corner separation in some regions, although it reduces the diffusion in other regions. While increasing the losses, these phenomena also decrease the stall margin and increase the aeromechanical constraints on the fan blades. For instance, it was shown in [44, 24] that, for a transonic blade row, the shock structure on a rotor blade moves as the blade travels around the annulus, which implies high-frequency shock strength and location variations. All these effects could be amplified by additional airframe elements interacting with the engines, such as the pylon fairing and bifurcation. It is therefore important to design these elements while taking into account their effect on the fan stage operation.

## 1.3 Simulation of fan–airframe interactions

Full annulus unsteady computations with a sliding interface or chimera mesh are required to capture *all* the details of the interaction of rotating blade rows with upstream and downstream components. This approach has already been used a number of times and sometimes validated against experimental data. For instance, Fidalgo et al. [32] studied the aerodynamics of the NASA rotor 67 stage operating with total pressure distortion. Carnevale et al. [12] used this approach to examine the effect of the fan on inlet lip separation at high AOA and found that the fan increases the stall-free range of AOA by up to 5°. Sadoudi [78] simulated intake-fan configurations at crosswind and found that the fan increases the separation-free range of mass flow rates inside the air intake. Guegan et al. [43] conducted a high resolution aeroacoustic simulation of intake, fan, OGV and bypass duct including struts and bifurcation. Pullan and Adamczyk developed a filtering mixing plane approach that eliminates short length scales perturbations and only retains the low reduced frequencies [72]. This approach allows to use coarse time steps in unsteady simulations while capturing the low frequency interactions of interest.

The main limitation of the full annulus unsteady approach is its computational cost, especially if acoustic waves need to be captured, but also the complex pre/post-processing tools that are required to effectively run and analyze the simulations. More affordable solutions based on phase-lagged methods can be envisioned for the simulation of complex fan-airframe configurations. This category of methods offers a good alternative to full annulus computations as only one blade channel is in general needed, which decreases CPU cost and memory requirements. Further reduction of CPU time and complexity for the user can be obtained with a time integration using a Fourier-Based approach. A good example is the Non Linear Harmonic method [66], in which only a steady simulation is involved. For instance, Purwanto et al. [73] presented an intake–fan–OGV simulation at crosswind with the ground effect. Similarly Sharma et al. [80] computed the aerodynamics of a fan under distorted

inflow and found good agreement with full annulus unsteady simulations at one fifth of the cost in terms of CPU and one tenth in terms of memory requirements. Even with significant time reductions as compared to full annulus computations, phase-lagged approaches remain expensive in a design context. In addition, the effectiveness of these methods decreases in configurations with multiple rows, as the inclusion of multiple frequencies is complex and lacks robustness. Because none of these “high” fidelity methods is suitable for design, the next chapter explores reduced order methods in which the computational cost is further reduced.

# Chapter 2

## Body force modeling

The body force modeling concept is depicted in figure 2.1: turbomachinery blade rows are replaced by source terms distributions that reproduce turning, losses, and metal blockage. In particular, these effects are smeared-out in the tangential direction, which eliminates the natural unsteadiness in rotating blade rows. This chapter is dedicated to the review of existing body force models and to the presentation of the formulations that were developed in the context of this PhD research. First, a literature review of throughflow modeling is proposed. Then, the general aspects of the body force implementation that was set up for this study are presented. Finally, different body force models are proposed and assessed on an isolated fan-OGV configuration.

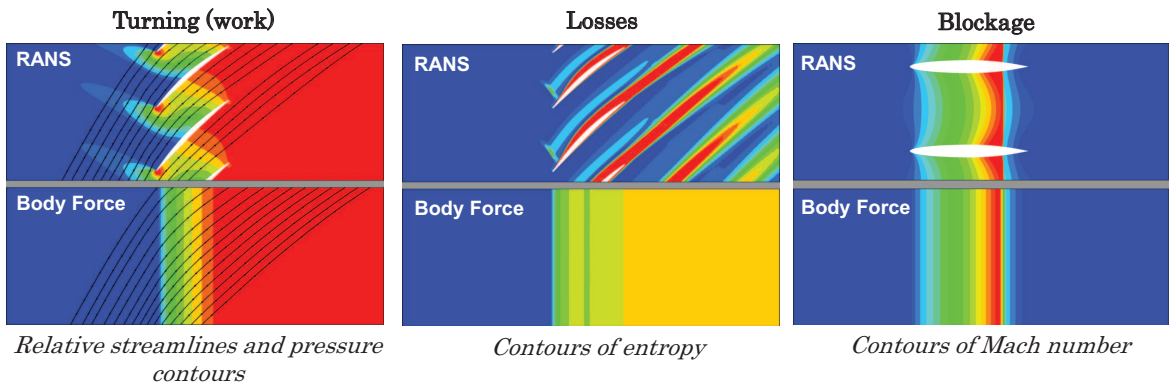


**Figure 2.1:** Body force modeling concept: the blades are replaced by source term distributions to capture turning, losses, and blade metal blockage.

### 2.1 Literature review

Finding efficient ways to capture the aerodynamic flow in turbomachinery blade rows has long been a concern for designers and has lead to the development of multiple reduced order approaches. This section reviews methods in which the blades are not directly included in the CFD simulation, but taken into account using work and loss forcing terms. These methods

are arbitrarily separated into different groups. In particular, non axisymmetric throughflow methods are separated into:

- Explicit, physics-based body-force models.
- Interpolation-based models.
- Semi-explicit models, intermediate between both previous approaches.
- Implicit approaches based on deviation and loss correlations.

Based on the literature review, the explicit body force approach will be selected for the remainder of the study.

### 2.1.1 2D Throughflow modeling

In 1964, Marble [62] built an axisymmetric representation of a blade row, assuming an infinite number of blades, and taking their effects into account by adding body forces to the equations of motion. Using this representation, Marble derived thermodynamic relations linking the blade forces to the total enthalpy change and to the production of entropy within the blade row.

#### Streamline curvature

The first computational approach based on Marble's throughflow representation of a blade row is the Streamline Curvature approach (SLC), which is still widely used nowadays during the early steps of turbomachinery design. This method solves the Euler equations expressed in the form of the full radial equilibrium, using a space marching method along streamlines. In general, the turning is created by forcing the mean flow path to follow the blade camber surface, with some specified deviation profile. Then, the losses are estimated using experimental correlations, based on diffusion factor for instance. The main limitation of this approach is that it is not compatible with transonic designs as the mass flow rate must be specified and as the space marching algorithm is not able to deal with the presence of both subsonic and supersonic zones. In addition, the SLC approach is not able to capture regions of reverse flow, which limits its validity for operating points near stall. Despite these limitations, good results could be obtained on subsonic designs, for instance with the code developed by Denton [25] and improved several times by Gallimore [35].

#### Axisymmetric Euler/NS throughflow

To overcome SLC limitations, two dimensional throughflow codes based on the axisymmetric Euler equations and using a time-marching technique were developed, one of the first examples of this approach being that of Spurr [85] in 1980. Despite the significant improvement of the time-marching approach as compared to SLC, Euler throughflow solvers still strongly rely on empirical correlations for deviation, viscous losses and aerodynamic blockage effects. Baralon et al. [4, 5] focused on these different aspects, proposing a new formulation for the

blade blockage factor and using the eddy viscosity representation of Gallimore and Cumpsty [36, 37] to capture spanwise mixing. More recently, Simon [82] emphasized the necessity for throughflow solvers to capture the aerodynamic blockage due to the enwalls boundary layers, which is usually estimated using empirical correlations and may have a strong impact on transonic designs. He developed a throughflow solver based on the viscous form of the Navier Stokes equations to directly compute these boundary layers and therefore reduce the need for empiricism.

### High order throughflow

The main issue in axisymmetric throughflow codes is that they do not account for the effect of non-uniformities on the mean flow field. In fact, the 3D flow field within a blade row can be seen as the superimposition of a uniform flow field and a circumferential variation. As for the Reynolds ensemble averaging operator, averaging this 3D flow tangentially leads to “perturbation stresses”, also called “circumferential stresses” in the equations for the averaged quantities. Baralon et al. [6] extracted these stresses from 3D computations, and introduced them in a throughflow solver, which allowed to capture spanwise mixing and to accurately reproduce results obtained from pitch-averaged 3D solutions. Following this idea, Simon [82] applied a succession of averaging operators (time averaging, Reynolds averaging, passage-to-passage averaging, and circumferential averaging) to the Navier Stokes equations as described by Adamczyk [1], to form a mathematically exact set of equations that describes the flow field in a blade row. These equations contain several stress terms, each arising from one of the averaging steps, that should be modeled to close the problem. As reported by Simon, that would be a tremendous task, and he preferred to study the importance of each term separately by extracting them from 3D unsteady computations. Simon found that the predominant terms are the inviscid and viscous blade forces, and the circumferential stresses, showing the importance to model each of these terms accurately.

#### 2.1.2 Actuator Disk Approach

A widely used method is the Actuator-Disk (AD) representation, based on the Rankine–Froude Blade-Element momentum theory. In this approach, blade rows are replaced by surfaces of discontinuity across which the flow is altered. Different AD implementations of varying complexity can be found [90, 21, 65]. In particular, the AD may impose uniform turning and losses, or change these inputs depending on local flow conditions. Furthermore, the changes applied to the flow may be applied with boundary conditions, or with surface source terms. Joo and Hynes [53] used the AD aproach to simulate an Intake–Fan–OGV configuration and obtained encouraging results. Recently, Marquez and Stuermer [63] applied a sophisticated AD approach included in the DLR Tau Code to a semi-mounted CROR configuration, finding good agreements with URANS computations. Wiart et al. [91] used an AD condition to analyze the performance of an aircraft with BLI. Zadeh et al. [93] proposed to use a variable static pressure boundary condition to capture the upstream redistribution in an air intake. They obtained encouraging results but the approach did not allow to study distortion transfer.

The main drawback of AD approaches is that they do not account for phenomena occurring within the blade rows, such as mass flow redistribution, choking due to blockage effects, or shocks within the blade passage. In addition they are often highly limited by the quality of the prescribed jumps of total quantities for given conditions, which do not respond to changes in the flow on a physical basis. Finally, the application of the actuator disk to blade rows with high pressure ratios can lead to convergence issues and wave reflection on the discontinuity plane, especially for “short” blades with lower diameter to chord ratios than propeller or helicopter blades, for which the method was initially developed.

### 2.1.3 3D Throughflow modeling

While all the contributions presented in section 2.1.1 focused on the study of turbomachinery internal flows, they are limited to non-distorted inflow due to the axisymmetric assumption. This section presents 3D throughflow approaches that were developed to handle non axisymmetric inflows.

#### Coupling of a 3D solver with an Euler / SLC solver

In 1994, Escuret and Garnier [30] presented a CFD solver that combines a 3D unsteady Euler solution in blade-free volumes with several Euler throughflow solutions within the blade rows. They used the solver to predict the growth of 3D compressible long length scale instabilities. In 1998, Hale and O’Brien [46] presented a 3D code (TEACC) that consists of an Euler solver to which source terms are added to take the blade effects into account. These source terms are computed using a SLC code that is applied on several sectors to obtain a full annulus representation of the turbomachinery stage. The code was applied with success to reproduce the response of an axial compressor to inlet distortion. The same code was later applied by Hale et al. [45] to evaluate the effect of inlet distortion on a three-stage military fan.

#### Explicit body force models

Most 2D throughflow codes were based on empirical models for the deviation and the loss, and body forces were added to the equations of motion to constrain the flow to the calculated deviation and loss values. Another solution consists in directly modeling the blade forces: the deviation and the loss then become a result of the computation rather than an input. An important contribution is that of Gong et al. [40] in 1998, who presented a computational model for low-speed axial compressor stall inception. In his PhD dissertation, Gong [39] extended the model to compressible flows and applied it to study the response of the NASA stage 35 to inlet distortion. The main advantage of Gong’s method is that the body forces depend on the local flow field, allowing the model to respond to flow perturbations on a physical basis. In his model, the blade forces are divided into two components: a flow turning component and a loss component, respectively orthogonal and parallel to the relative flow field. Both components rely on calibration coefficients that Gong estimated with empirical correlations. The model was calibrated by Chan [13] using body forces extracted from SLC computations and applied to an eleven-stage compressor. Hsiao et al. [50] later applied

Gong's formulation to a powered nacelle, focusing on the effect of the fan on inlet flow separation. Plas et al. [71] used Gong's model to assess the performance of an embedded propulsion system in the presence of distortion due to boundary layer ingestion. Kim and Liou [55] assessed a modified version of the model, in which the pressure-gradient based loading term was replaced by a blade camber dependent term, on a wing body aircraft with embedded engines. More recently, Peters et al. [70] used an improved version of Gong's model to find an optimal air-intake length. The modifications of the model consisted in the inclusion of off-design losses in the parallel force and the addition of a radial component to the normal force. The model was calibrated using RANS mixing-plane computations and was able to accurately reproduce results obtained with full annulus unsteady computations. Later, Hall [48] proposed an inviscid (normal force only), first-principle based incompressible body force model that does not rely on empirical coefficients. The model was used to study the interaction of a fan with a BLI-type inlet distortion. The formulations developed in the present work are mainly based on these last contributions.

### Interpolation from database

Another modeling approach consists in generating a body-force database from which a response surface or a look-up table can be defined. In 2001, Choi [17] used single passage RANS computations to build a body-force database and used the relative Mach number as interpolation variable to locally adapt the body forces. Kiwada [56] established the notion of "Blade Force Average", which allows to extract a body force field from 3D RANS computations, and extrapolated its body-force database to mass flow rates beyond the stability limit of the compressor using SLC computations. Benneke [7] applied a similar approach to estimate the stability limit of a centrifugal compressor. Patel [68] proposed to link the body forces extracted from the previous method to the local flow coefficient times the overall flow coefficient to avoid repeated values. Reichstein [74] compared body force distributions extracted from SLC and 3D RANS computations and found that the extracted force fields mainly differ near stall conditions, especially in the tip region, due to tip leakage and reverse flows. Walker [89] studied the effect of changes in an extracted force field on the stall point, and found that it mainly depends on the axial force distribution. Kerner [54] studied the effect of tip clearance on compressor stability, and established the "force flow reconciliation" concept, which allows to ensure consistency between a force field and the flow field it induces.

### Semi-explicit models

The models presented below are intermediates between fully explicit models and response-surface based approaches, as they use physics-based formulations in which the physical sources of turning and losses are extracted from available data. Chima [15] developed a 3D Euler code (CSTALL) which can run in three modes: axisymmetric to quickly draw performance maps, steady 3D to study inlet distortion, and unsteady 3D to study rotating stall. The solver is calibrated with radial profiles of deviation and entropy that are used to compute body forces using Marble's formulation [62]. The main limitations of Chima's approach are that the deviation and entropy elevation are assumed to vary linearly through the blade row. In addition, Chima scales the body forces to operating points different from the one

input to the solver with normalized characteristics maps, which decreases the generality of the method. Chima et al. [16] later combined CSTALL with another code to reproduce the interactions between a serpentine inlet and a fan, obtaining mixed results as compared to experimental data, but finding that inlet distortion reduces the fan's performance and that it is not completely eliminated through the fan. In 2013, Brand [8] presented a body force formulation for axial compressors that addresses some limitations of Gong's model [69]. One shortcoming of his approach is that it is highly dependent on calibration data: the entropy and deviation gradients within blade rows must be known for different operating points and are correlated against flow coefficient. Kottapalli [58] presented another model dedicated to centrifugal compressors, but failed to obtain converged results for 3D test cases. A similar approach that included terms for centrifugal effects and aerodynamic blockage was developed by Sorensen for inducer geometries [84], again with convergence difficulties on a realistic 3D case.

### Immersed Boundary Method with Smeared Geometry

One key idea of Gong's model and body-force database approaches is to explicitly formulate the blade force rather than model deviation and entropy elevation. Cao et al. [10] presented a 3D throughflow modeling approach in which the turning is prescribed by forcing the flow to follow the camber surface plus some imposed deviation, as was done in most 2D throughflow modeling codes. One interesting aspect of his approach is that it can easily be implemented in an existing 3D solver. Furthermore, all the correlations that were developed in the past for 2D throughflow modeling may be used to capture deviation and thus turning. However, it also means that the method must deal with the same numerical issues that were faced in 2D codes, such as the leading edge discontinuity, well described in [3]. An explicit loss model was proposed along with Cao's turning formulation. The approach was applied to a fan-distortion interaction test case and showed good agreement with experimental data and high fidelity full annulus unsteady computations. The model was also used to capture intake-fan interactions under high incidence, and gave good results [11].

#### 2.1.4 Other approaches

For some particular applications, none of the methods presented above is suitable, the steady nature of the turbomachinery blade rows representation, the absence of wakes, or the reduced accuracy of the models being at fault. This section presents some methods that were developed to reduce the computational cost as compared to full annulus unsteady computations while maintaining a high level of fidelity.

Xu [92] proposed to perform full annulus unsteady computations without the resolution of the viscous effects on the blade walls. Instead, these effects are modeled using body forces, with a drag relationship between the forces and the flow velocity. This approach allows to keep some of the accuracy of a fully resolved simulation, as the amplitude of the viscous forces is low compared to that of the inviscid forces, while reducing the computational cost since the mesh is coarser and the time step can therefore be increased.

Defoe et al. [23, 24] studied the propagation of Multiple Pure Tone (MPT) noise in a serpentine inlet using Gong's compressible body force model [39]. To Gong's mean force field

were added a rotor locked disturbance field periodic over a blade passage, which generates shocks, and a rotating disturbance field with a once-per-revolution periodicity that induces variations in the shocks and thus MPT noise. Loiodice et al. [61] analyzed an idealized open rotor engine in tractor configuration. To improve the prediction given by the model on the open rotor blades, they generated wakes by localizing the loss component near the blades, using square waves functions. The same approach was used by Tyacke et al. [87] in a hybrid RANS-LES solver, to assess the effect of internal geometries on a turbofan jet noise. In particular, the OGV blades and the gearbox shaft were modeled with the wake body force model of Loiodice to generate correct turbulence levels at the nozzle inlet, and LES was used to resolve the large scale jet turbulence.

Another approach, known as the actuator line model, was developed by Sorensen and Shen [83] and has been extensively used to study the wake development and the wake-turbine interactions in wind-turbine fields. In this approach, the blade forces are distributed along 3D lines representing the blades. An extension of this approach called the actuator surface was proposed by Shen and Sorensen [81], where the blade forces are distributed along the airfoil chord following empirical correlations.

### 2.1.5 Summary and discussion

An organization of the reduced order methods described above is proposed in figure 2.2.

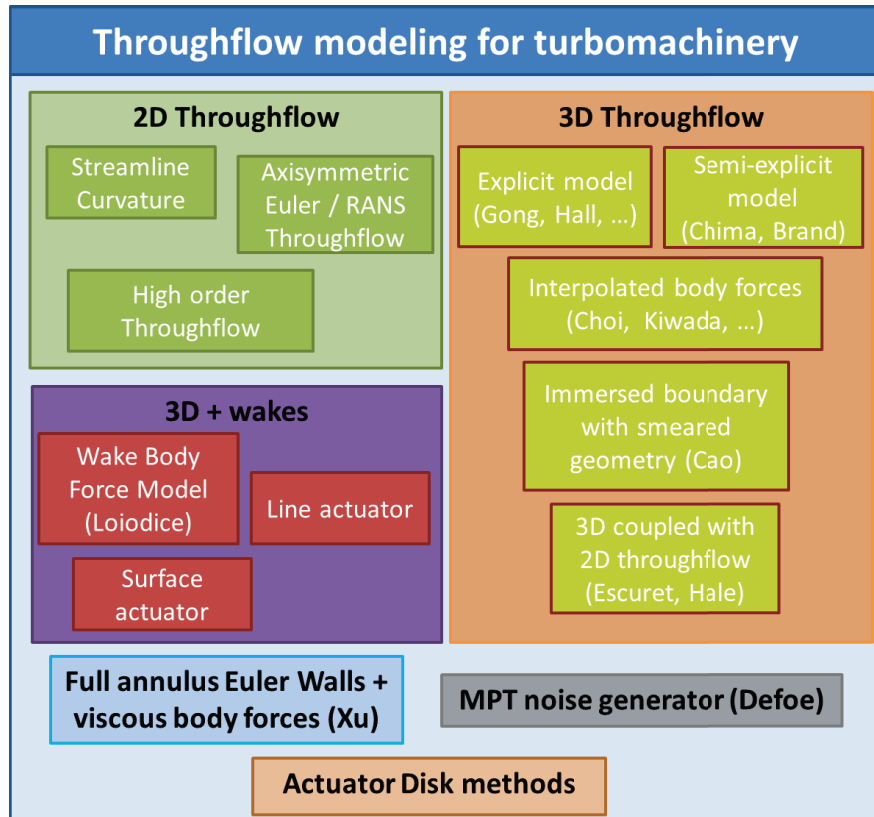


Figure 2.2: Reduced order models for turbomachinery.

Omitting the early methods based on a coupling between a 3D CFD solver and a 2D throughflow solver, 3D throughflow methods can be clustered in the following categories:

- (1) In explicit body force approaches such as Gong's, a physics-based model is derived for the blade force. The deviation and the losses are then a result of the computation. The blade force is usually computed locally and only depends on the local flow conditions. The effect of inlet distortion is thus naturally captured.
- (2) Interpolation based approaches assume a dependency between the body forces and local flow variables such as the flow coefficient or the relative Mach number. Then, a response surface or a look-up table is built from a body-force database, which allows the body forces to locally respond to varying inflow conditions.
- (3) Semi-explicit approaches involve a physics based relationship between the body forces and key quantities such as the gradient of entropy or the gradient of tangential velocity. However, these quantities are not modeled but retrieved using, as for the interpolated body force approach, a look-up table or a response surface.
- (4) The immersed boundary with smeared geometry proposed by Cao does not explicitly link the body force responsible for turning to the flow field. As in 2D SLC solvers, the blade force is computed at each iteration to force the streamlines along a mean flow path that is defined using the blade camber surface and a deviation distribution.

The explicit body force approach is explored in the present thesis, using Gong's and Hall's models [39, 48] as a basis for improved formulations. One of the key features of these models is that they are completely *local*. This is especially important when dealing with distorted inflow, as the streamlines experience strong radial and circumferential shifts, reducing the meaning of deviation and loss correlation that are often based on 2D blade profiles and only valid for uniform inlet flows. These models are thus easy to implement in an existing 3D flow solver. In addition, the blade to blade details are smeared out in the circumferential direction so that a steady approach can be used, reducing the computational cost of the simulations. Another good property of Gong's and Hall's models is that they are robust: in both model, the flow is brought back toward the blade when the deviation increases, which has a stabilizing effect. Finally, both models are able to capture the evolution of work input with varying operating conditions, which is required to capture the interaction of a turbomachinery blade row with inlet distortion.

However, some limitations of the models were reported in previous contributions. Peters [69] proposed an improved version of Gong's model, but the process to calibrate the model was heavy and required a manual intervention. He had to include an offset in the normal force equation to avoid singularities in the normal force coefficient, and the parallel force was computed using the relative Mach number at the inlet of the blade row rather than the local relative Mach number. While this approach can be implemented without too much efforts in a structured solver, it may be inconvenient in an unstructured solver running in parallel. Finally, Peters showed that Gong's formulation does not allow to capture the local streamline curvature in a blade passage, and he mentioned the lack of a model for metal blockage in Gong's body force approach. It will indeed be shown later that modeling metal

blockage is required to capture the choke mass flow rate of a transonic fan stage, which is desired at max climb conditions. Hall [48] later proposed a new formulation, which does not require any calibration from single-passage computations. However, his formulation did not include any model for the loss, and it was restricted to incompressible flows only.

In the present work, an attempt is made to propose modeling approaches that address those limitations. Additional source terms [58] are added to the RANS equations to capture metal blockage, and improved formulations for the blade force are presented. The “lift/drag” formulation is proposed to replace Gong’s model. This formulation requires calibration coefficients but the calibration process is thought to be more robust than for Gong’s model with Peters’ modifications. In addition, the model is completely local, so that its implementation in an existing solver is easier. Then, Hall’s model is modified to capture compressibility effects and stagnation pressure losses, using only first principles to preserve the generality of the model and avoid calibration from single-passage computations. Both models are validated in chapters 3 and 4 on installed configurations. It is useful to have access to different modeling approaches, depending on the amount of available data when the body force computations are performed. In particular, it will be shown that thanks to the calibration, the lift/drag model is slightly more accurate than the modified version of Hall’s model. However, the latter can be useful at a conceptual level when there is no detailed geometry of the blades available and thus no CFD computation nor experimental data to calibrate the model.

In the next sections, the general aspects of the present body force implementation are discussed, then the body force formulations are themselves presented and assessed on an isolated fan stage.

## 2.2 Body force implementation

This section describes the present implementation of the body force framework in an existing solver. The key points of this implementation are:

- A quasi-steady assumption allows to perform steady computations.
- The blade force that produces turning and losses can be computed with the different formulations mentioned before.
- Metal blockage effects are taken into account with specific source terms [58].
- The source terms are computed within an independent Python module and a coupling is set up with the CFD solver to take into account these source terms.

### 2.2.1 Quasi-steady assumption

An important assumption for the methodologies developed further is that the flow field is quasi steady in the blade rows relative frame of reference. This assumption implies that circumferential perturbations have a long time-scale compared to the aerodynamic through-flow time, which is acceptable for distortions such as those encountered in BLI or short intake configurations. As a consequence, short length scale phenomena such as rotor-stator interactions are filtered, but phenomena associated to distortions of length scale much larger

than one blade pitch may be captured. The assumption was translated in previous contributions [42, 22, 69] by a condition on a reduced frequency, defined by:

$$f = \frac{2\pi r \Omega c}{\lambda V_x} \quad (2.1)$$

$f$  compares the time scale associated with the unsteadiness due to distortion  $\frac{\lambda}{2\pi R\Omega}$ , where  $\lambda$  is the distortion wavelength, with the time scale associated to the convection time through a blade row  $\frac{c}{V_x}$ . The quasi-steady assumption is only valid for a reduced frequency below unity. It allows to perform steady body force computations in which the forces react instantaneously to the flow field. A specialized form of the RANS equations and unsteady simulations would be needed to capture short length scale phenomena like short-wavelength stall inception [39].

### 2.2.2 Equations of motion

The CFD solver *elsA* [9], developed by ONERA, is employed for this study. The source terms applied on the right hand side of the RANS equations in blade rows are similar to those in the circumferentially-averaged Navier-Stokes equations derived in Appendix B. Because altering the flux computation in an existing solver can be tricky, metal blockage effects are taken into account with a source term on the right hand side of the RANS equations. In the present implementation, the blockage contribution of the viscous terms  $\tau_{ij}$  is neglected. In addition, the circumferentially-averaged static pressure is supposed to be equal to the average of pressure and suction-side static pressure, ie  $\bar{P} = \frac{P_{ss} + P_{ps}}{2}$ , which is a common approximation in throughflow solvers [3, 82]. Finally, all the circumferential stresses are neglected, which implies that aerodynamic blockage and radial mixing are not directly taken into account. This yields the following set of equations:

$$\frac{\partial \rho}{\partial t} + \operatorname{div}(\rho \vec{V}) = -\frac{1}{b}(\rho \vec{V} \cdot \nabla b) \quad (2.2)$$

$$\frac{\partial \rho \vec{V}}{\partial t} + \operatorname{div}(\rho \vec{V} \vec{V}^t - \vec{\tau}) + \vec{\nabla} P = \rho \vec{f} - \frac{1}{b}(\rho \vec{V} \cdot \nabla b) \vec{V} \quad (2.3)$$

$$\frac{\partial \rho e_t}{\partial t} + \operatorname{div}(\rho h_t \vec{V} - \vec{\tau} \cdot \vec{V} + \vec{q}) = \rho \Omega r f_\theta - \frac{1}{b}(\rho h_t \vec{V} \cdot \nabla b) \quad (2.4)$$

where  $b$  is the blockage factor defined in Fig. 2.3a and  $\vec{f}$  is the blade force. Marble [62] showed that the change in tangential velocity and entropy along a streamline can be related to the blade force using equations (2.5) and (2.6):

$$V_m \frac{\partial r V_\theta}{\partial m} = r f_\theta \quad (2.5)$$

$$V_m \frac{\partial s}{\partial m} = -\frac{W}{T} f_p \quad (2.6)$$

where

$$V_m \frac{\partial}{\partial m} = V_x \frac{\partial}{\partial x} + V_r \frac{\partial}{\partial r} \quad (2.7)$$

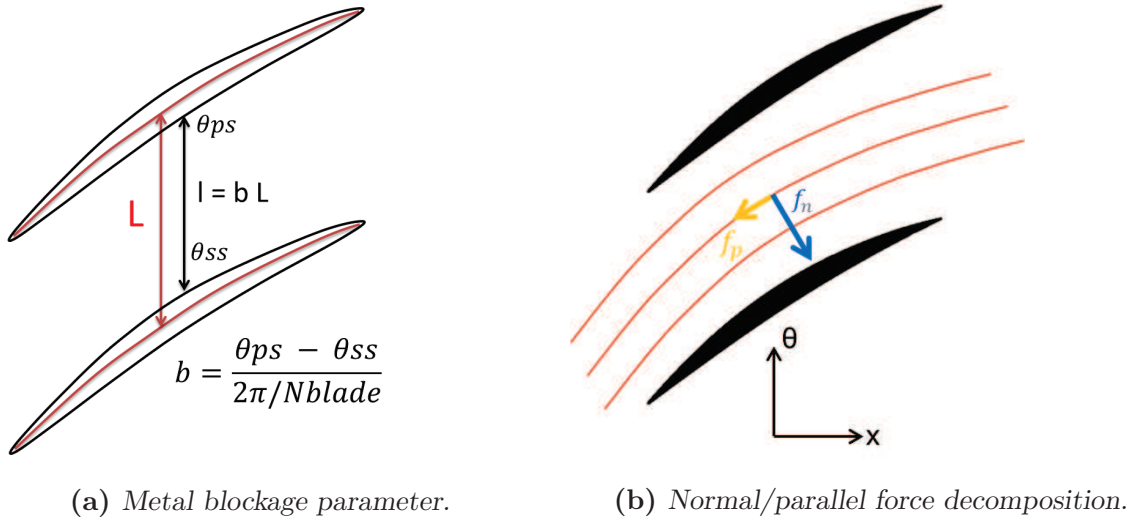


**Figure 2.3:** Illustration of the blade metal blockage parameter and the normal and parallel forces.

In equation (2.6),  $f_p$  is the force parallel to the relative flow field. This highlights the fact that only this component of the force contributes to the losses. It is then convenient to divide the blade force into two components, one orthogonal to the relative flow field, which provides reversible flow turning, and one parallel to the relative flow field, which generates the losses, as shown in figure 2.3b. Using the Euler turbine equation in a rotor, equation (2.5) can be rearranged to yield:

$$V_m \frac{\partial h_t}{\partial m} = \Omega r f_\theta \quad (2.8)$$

This relation implies that the rate at which stagnation enthalpy is rising is equal to the work produced by the blade's torque. This can be seen as a simple application of the first law of thermodynamics when heat transfer is neglected. However, an important implication of this relation is that both the parallel and normal forces contribute to the amount of work added to the flow.

### 2.2.3 Coupling between CFD solver and body force module

A coupling is set up between the solver and an external Python module that computes the source terms, as shown in figure 2.4. The coupling is realized in the framework of the Flowsimulator environment [64]. Arrays that store flow variables and source terms at the cell centers are shared by both entities. After each CFD solver iteration, the flow variables are read by the Python module to compute source term distributions, which are then used for the next solver iteration. To improve the stability of the solver, a relaxation factor is applied to the axial, radial and tangential body force components, but no other special treatment is applied (such as source term implicitation for instance).

This approach gives a lot of flexibility, as external packages dedicated to scientific computing such as [Numpy](#) and [Scipy](#) can be used to perform complex operations, such as in-

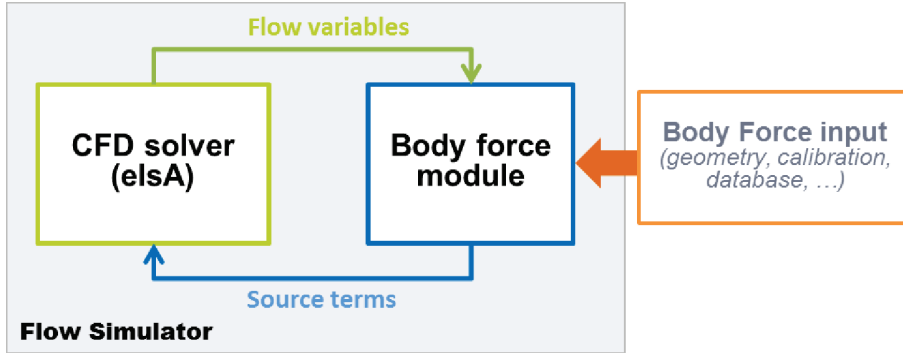


**Figure 2.4:** Coupling between the *elsA* solver and a body force generator via *FlowSimulator*

terpolations for the computation of the source terms. Furthermore, in a multidisciplinary context, this implementation also allows to couple the body force solver with other modules, such as an engine modeling software for instance.

#### 2.2.4 Metal blockage implementation

The present metal blockage implementation exclusively relies on source terms on the right hand side of the RANS equations [58] rather than on a modification of the conservative variables or the mesh metrics, as can be found in [3, 7]. The values of the blockage factor are directly extracted from the blade geometry at the cell centers of the meridional mesh used in body force computations, and the blockage derivatives are computed using a second order centered finite difference scheme. To check the implementation of the metal blockage source terms, Euler computations are conducted on a simplified stator geometry without stagger and camber, and with axial inflow. A uniform pressure is imposed at the outlet of the domain and periodic boundaries are used in the circumferential direction. The test case is shown in figure 2.5. Body force computations are performed on the same domain with the same inlet and outlet conditions, but with the blockage source terms instead of the blade geometry. Since viscous effects are neglected in the Euler equations, the parallel force is equal to zero. In addition, there is no pitch-averaged turning and thus the normal force is also equal to zero. The blockage source terms are active in the whole volume enclosed between the leading and trailing edges of the blade, and in two cell rows just after and before this zone. This is due to the fact that blockage derivatives are estimated using a finite difference method, which results in non zero values in the cells lying on the other side of the leading and trailing edges. The comparison between the body force results and the reference CFD is done for different mass flow rates to simulate both subsonic and supersonic regimes. The results from the reference CFD computations are tangentially averaged and compared to the body force simulations, which directly provide axisymmetric flow fields.

The comparison presented in figures 2.6 and 2.7 shows that the approach captures well metal blockage effects. When the outlet static pressure is small enough, a sonic throat appears, followed by a shock, whose position and strength are well captured by the approach. In particular, the shock losses are captured, as shown in figure 2.8. The shock capturing properties of axisymmetric throughflow solvers are well described by Baralon [3]. Shocks

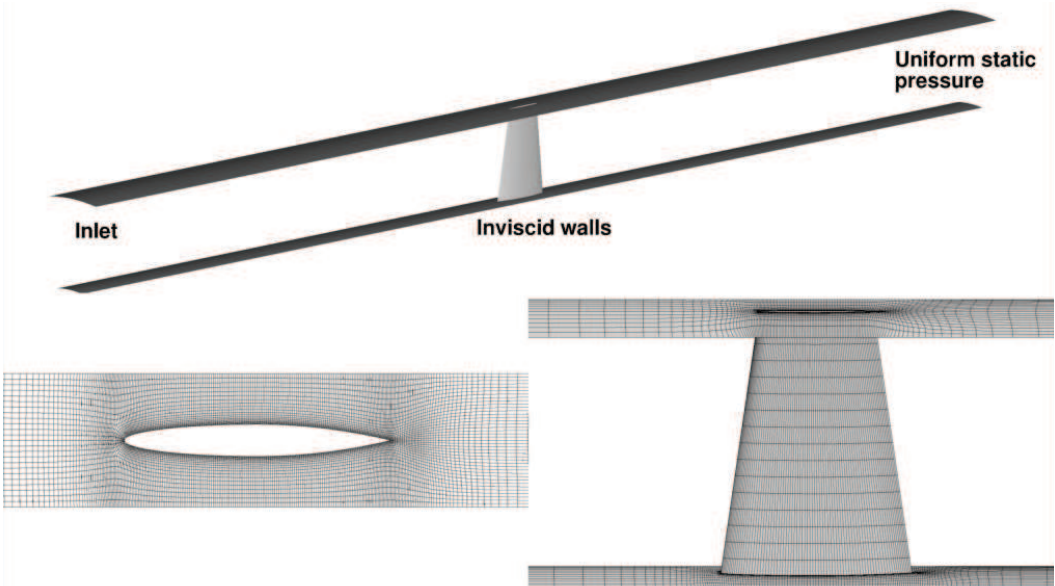


**Figure 2.5:** Simple stator test case.

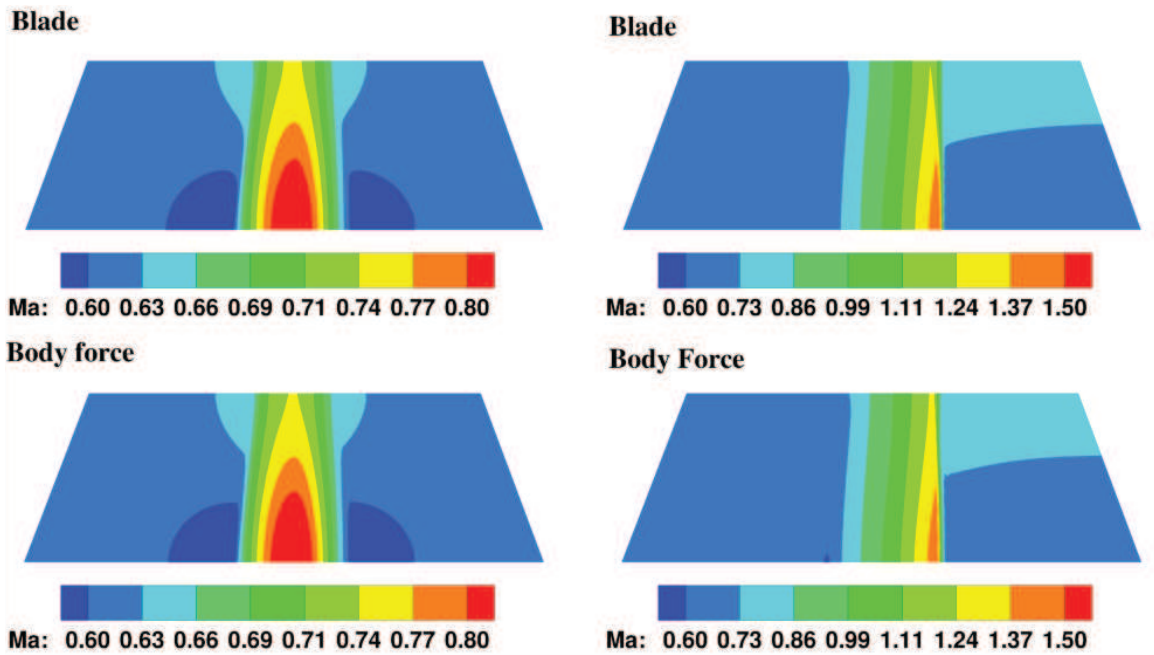


**Figure 2.6:** Comparison of direct CFD computations on a simple stator geometry (blade) and body force computations with blockage source terms. Meridional view for two values of the outlet static pressure (contours of Mach number).

orthogonal to the rotation axis are seldom met in practice, although normal shocks in OGVs downstream of a fan may be almost axial. While these shocks and their associated loss can be captured directly with the metal blockage source terms, normal shocks occurring in highly staggered passages and leading edge shocks are smeared out in the meridional plane, and

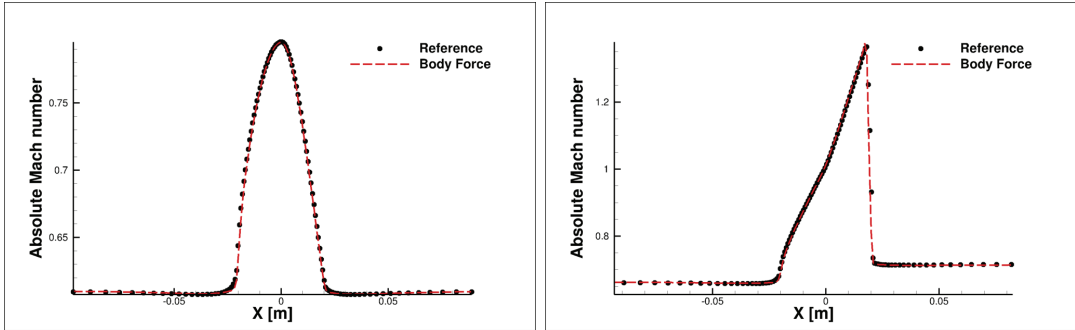


**Figure 2.7:** Comparison of direct CFD computations on a simple stator geometry and body force computations with blockage source terms. Mach number evolution at mid-span for two values of the outlet static pressure.

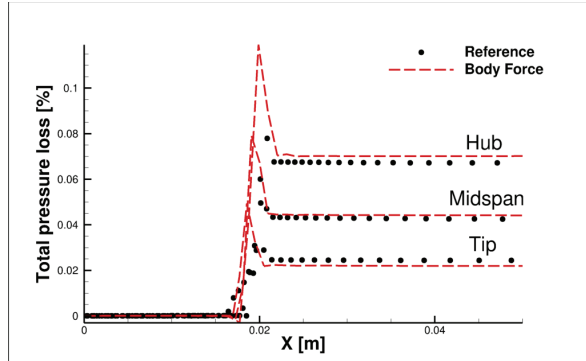


**Figure 2.8:** Comparison of direct CFD computations on a simple stator geometry and body force computations with blockage source terms. Total pressure loss with a normal shock in the meridional plane.

the associated loss must in general be modeled. Baralon [3] introduced a “normal” blockage factor, as opposed to the “standard” blockage used in the present work, taken orthogonal to the camber surface, that aimed at capturing the “real” blockage felt by the flow within a blade passage. With this blockage factor, he greatly improved the value of the choke mass flow rate predicted by his approach, and he obtained interesting shock patterns on the NASA rotor 67 geometry that allowed to capture some of the shock loss produced at the tip of the blade. In the present study, this modification was not necessary, as the choke mass flow rate predicted with the approaches presented below is fairly accurate as compared to what Baralon obtained with the “standard” blockage factor. It is thought that this difference is due to the blade mean surface flow tangency condition of his throughflow method, as opposed to the explicit and interpolated body force models used in this work. Another important point is that the addition of a source term to the density equation does not violate the conservative property of the solver. In the present case, the relative difference between the outlet and inlet mass flow rates was less than 0.05%, although it could reach values up to 0.1% on the more realistic geometries used in the next parts of this study.

## 2.3 Body force model formulations

Several explicit formulations for the blade force  $\vec{f}$  are presented and analyzed in this section. These formulations are assessed on an isolated fan stage and the results are validated against mixing plane computations. It is thought that the models must be able to reproduce the performance of an isolated fan stage for varying operating conditions to accurately capture fan-airframe interactions in an installed configuration. Based on these results, two models are thus selected and applied to more realistic configurations in Chapters 3 and 4.

### 2.3.1 Test case

The assessment of existing and newly developed body force models is done on the NASA/GE R4 fan stage [51]. The characteristics of this model-scale fan are summarized in Table 2.1.

Nb of fan blades	22	Corrected design RPM (100%)	12657
Nb of OGV blades	54	Stage Pressure Ratio	1.47
Fan tip diameter	0.56 m	Corrected design mass flow rate	45.6 kg/s
Fan hub to tip ratio	0.3	Tip relative Mach number	1.26

**Table 2.1:** NASA R4 fan stage geometry and design operating point

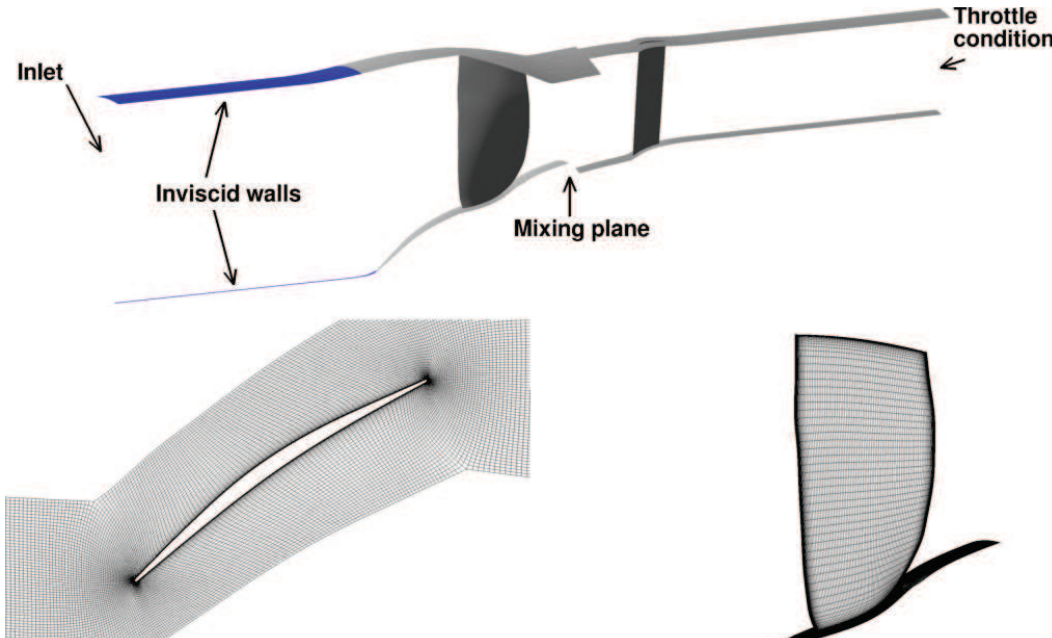


**Figure 2.9:** NASA/GE R4 test case.

CFD computations of the fan are performed on a 3.6 million cells mesh shown in figure 2.9. The simulations are carried out using an implicit pseudo-time marching method with the one-equation turbulence model of Spalart-Allmaras. The convective fluxes are determined using a second-order Roe scheme with the Van Albada limiter.  $y^+$  values are close to unity

everywhere at the walls. The total quantities are imposed at the inlet, and a throttle condition with radial equilibrium is used at the outlet [86]. A mixing-plane is used at the interface between stationary and rotating frames. As most body force models are calibrated from—or built on—CFD data, it is reasonable to use these computations as reference during the assessment process of the different body force models. To avoid confusion, the computations with the blade geometry are denoted as *blade computations*, as opposed to *body force computations*. The validation of the different body force approaches is carried-out with global data (performance maps) and radial profiles downstream of the fan stage. The performance maps are expressed in terms of work coefficient versus flow coefficient and total-to-total isentropic efficiency versus normalized mass flow rate, the latter computed with respect to the design point. This choice is especially useful to isolate the impact of the normal force, which mainly impacts the work coefficient, and that of the parallel force, which drives the efficiency with low effect on work coefficient.

### 2.3.2 Extraction of a body force field from a blade computation

An important feature related to body force modeling is the extraction of a force field from a blade computation. This feature allows to qualitatively and quantitatively examine the body force distribution within a blade row, to calibrate analytic models, or to feed a database used to perform interpolations. Different procedures to extract a body force field were found in the literature. These approaches are described in the next sections.

#### Force field extraction from blade wall pressure and shear stress distributions

One way to extract a body force field from a blade computation is to use the blades pressure and shear stress distributions, which allows to conserve the force acting on the blades. In [69], Peters develops a methodology that allows to directly extract the body force normal to the relative flow field, but the procedure employed is complex and requires to compute intersections between normals to the average flow field and the blade walls. Another way to obtain the blade force is to use the circumferentially averaged form of the RANS equation in a blade passage (see Appendix B), which directly gives the exact relationships between the blade force components and the wall pressure, shear stress, and geometry distribution:

$$F_x = \frac{(P_{ss} - P_{ps})}{\Delta\theta} \frac{\partial\theta_m}{\partial x} + \frac{\tau_{p,x}^{ps} + \tau_{p,x}^{ss}}{r\Delta\theta} \quad (2.9)$$

$$F_r = \frac{(P_{ss} - P_{ps})}{\Delta\theta} \frac{\partial\theta_m}{\partial r} + \frac{\tau_{p,r}^{ps} + \tau_{p,r}^{ss}}{r\Delta\theta} \quad (2.10)$$

$$F_\theta = \frac{(P_{ps} - P_{ss})}{r\Delta\theta} + \frac{\tau_{p,\theta}^{ps} + \tau_{p,\theta}^{ss}}{r\Delta\theta} \quad (2.11)$$

The blade pressure and suction surfaces are defined as functions  $\theta_{ps,ss}(x, r)$  of the axial and radial coordinates.  $\Delta\theta$  is the angular extent between the pressure and suction side, and  $\theta_m$  is the mean camber surface defined by  $\theta_m = 0.5(\theta_{ss} + \theta_{ps})$ . One drawback of this approach is that the pressure and friction distributions on the blade walls must be interpolated carefully

on the body force grid. In addition, the derivatives of the blade camber surface must be computed accurately to avoid any error on the force direction.

### Force field extraction using the Blade force average

Another approach is to extract body forces from a blade computation using the notion of “Blade force average” (BFA) first introduced by Kiwada [56]. In Kiwada’s work, the flux variables  $\rho V_x$ ,  $\rho V_r$ ,  $\rho V_x V_x$ ,  $\rho V_x V_r$ ,  $\rho V_x V_\theta$ ,  $\rho V_r V_r$ ,  $\rho V_r V_\theta$ ,  $\rho V_\theta V_\theta$ ,  $P$ , and  $\rho$  are circumferentially averaged using a surface weighting, then the steady axisymmetric Euler equations are inverted to retrieve the blade force. The main interest of averaging directly the flux variables rather than the velocity components is that it prevents the circumferential stresses and thus ensures that the force acting on the blade is conserved. The BFA is therefore theoretically equivalent to the extraction based on the blade pressure and friction distribution. The main limitation of the approach as originally presented by Kiwada is that it includes viscous effects near the end walls in the blade force. To overcome this limitation, the components of the shear stress tensor  $\tau$  are averaged along with the flux variables, and the steady circumferentially averaged RANS equations are inverted to retrieve the blade force:

$$F_x = \frac{\partial b \overline{\rho V_x V_x + P - \tau_{xx}}}{b \partial x} + \frac{\partial r b \overline{\rho V_x V_r - \tau_{xr}}}{b r \partial r} - \overline{P} \frac{\partial b}{b \partial x} \quad (2.12)$$

$$F_r = \frac{\partial b \overline{\rho V_x V_r - \tau_{xr}}}{b \partial x} + \frac{\partial r b \overline{\rho V_r V_r + P - \tau_{rr}}}{b r \partial r} - \frac{\overline{\rho V_\theta V_\theta + P - \tau_{\theta\theta}}}{r} - \overline{P} \frac{\partial b}{b \partial r} \quad (2.13)$$

$$F_\theta = \frac{\partial b \overline{\rho V_x V_\theta - \tau_{x\theta}}}{b \partial x} + \frac{\partial r b \overline{\rho V_r V_\theta - \tau_{r\theta}}}{b r \partial r} + \frac{\overline{\rho V_r V_\theta - \tau_{r\theta}}}{r} \quad (2.14)$$

### Force field extraction from thermodynamic quantities

A third possibility to extract body forces from a blade computation is to apply Marble’s relationships, which relate the parallel and tangential force to the entropy gradient and to the tangential velocity gradient respectively, as shown in equations (2.5) and (2.6). In several contributions, this approach is used to retrieve the parallel component of the force [8, 58, 55]. The entropy is then assumed to vary linearly between the leading and trailing edge of the blade, and the streamlines to remain at constant relative span, which allows to approximate the entropy gradient by:

$$\frac{\partial S}{\partial m} = \frac{\Delta S}{\Delta m} = \frac{S_{TE} - S_{LE}}{\sqrt{(X_{TE} - X_{LE})^2 + (R_{TE} - R_{LE})^2}} \quad (2.15)$$

This allows to simplify the parallel force extraction process and to smooth the parallel force distribution. It also allows to define a body force model for the parallel force calibrated with radial profiles of total pressure and total temperature upstream and downstream of the blade row, either from experimental or CFD data. In the present case, the entropy, tangential velocity and relative flow angle are circumferentially mass-averaged and used to retrieve the axial and tangential force components. A third relationship is needed to retrieve

the radial component of the normal force, which can be based on the knowledge of the lean angle of the blade:

$$f_{n,r} = -\tan \lambda f_{n,\theta} \quad (2.16)$$

The main advantage of this thermodynamics-based approach is its ability to capture all the mechanisms responsible for deviation and loss, including wakes and secondary flows. However, its main drawback is that it can lead to spurious variations of the axial blade force near the hub and the shroud. In fact, to retrieve the axial component of the blade force, the following relationship must be used (the lean angle is neglected):

$$f_x = f_{px} - (f_\theta - f_{p\theta}) \frac{W_\theta}{W_x} \quad (2.17)$$

When the relative flow is almost tangential, equation (2.17) gives spurious oscillations for the axial force. Another limitation is that the approach captures the entropy elevation due to the friction on both the blade walls and the endwalls. In a RANS body force computation, the losses on the endwall are already captured, which leads to an overestimation of the losses in the hub and tip regions. The same issue arises when normal shocks appear, as the loss produced by that shock may already be captured in the body force computation. Finally, it should be kept in mind that this approach does not conserve the forces acting on the blades. Instead, it allows to conserve the energy and the entropy added to the flow.

### Force field extraction validation

The blade force average procedure and the thermodynamics-based approaches described above are compared on the R4 fan stage. The extraction using the blade pressure and friction repartition is not kept as it theoretically gives the same result as the BFA. All the operating points obtained from mixing plane computations are pitch averaged, and a force field is extracted for each operating point. Spatial derivatives are computed using a second order centered finite difference method at the cell centers, where the flux variables and thermodynamic quantities have been averaged. The main advantage of this approach is that it can easily be implemented within an existing software that computes pitch-averaged flows. In addition, it is consistent with the present blockage implementation, in which blockage derivatives are computed using the same finite difference scheme. “Frozen” axial, radial and tangential forces per unit mass extracted with the BFA and the thermodynamics based approaches are directly imposed in body force computations. The pseudo-axisymmetric body force computational domain is shown in figure 2.10.

For each operating point, the same boundary conditions are applied in body force and blade computations. Due to the central finite difference discretization used to compute the blade force and the blockage source terms, the body force field is active in the cell rows just upstream / downstream of the leading / trailing edge of each blade row. The endwalls are treated as in the blade computations, with an inviscid shroud portion and a rotating spinner. To avoid convergence issues with the thermodynamics-based approach, the body force fields had to be kept constant over a small fraction of the span near the hub and shroud (up to 4% span for highly loaded cases). Near the rotor tip gap especially, regions of reverse flow may appear at low mass flow rates, with locally low axial velocities, leading to spurious values of

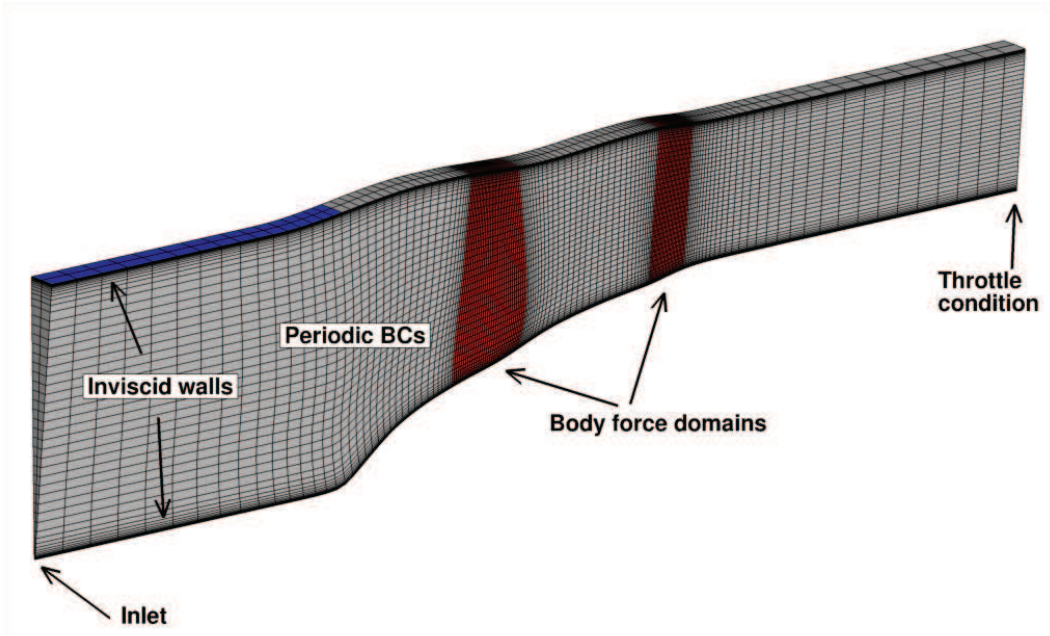


**Figure 2.10:** NASA/GE R4 body force computational grid.

the axial body force, as explained in the previous section. However, this modification also limits the duplication of the losses in the endwalls boundary layers. The performance map obtained with these approaches is shown in figure 2.11. The global performance of the fan stage is well captured by both approaches, although the work coefficient is overestimated at 100% RPM with the thermodynamics-based approach. Spanwise profiles of work coefficient and efficiency downstream of the fan stage are shown in figure 2.12. Significant discrepancies are visible, especially in terms of efficiency distributions. To investigate the origin of these discrepancies, different body force simulations based on the thermodynamic quantities extraction were compared:

- The computations shown in figures 2.11 and 2.12, where the axial, radial and tangential component of the force are directly imposed.
- Computations in which the normal and parallel force are imposed, then projected on each spatial direction at each iteration.
- Computations in which the entropy and tangential velocity gradients are imposed, and where the body forces are thus recomputed at each iteration using Marble equations (2.5) and (2.6).

The resulting performance map is shown in figure 2.13. There are almost no differences between the three approaches at low speed, but significant improvements are obtained at 100% RPM when the parallel and normal force or entropy and tangential velocity gradients are imposed. In particular, the prediction of the work coefficient is better when the gradients are imposed and the prediction of efficiency is improved in both cases. Spanwise profiles of work coefficient and efficiency are shown in figure 2.14. Imposing the normal and parallel

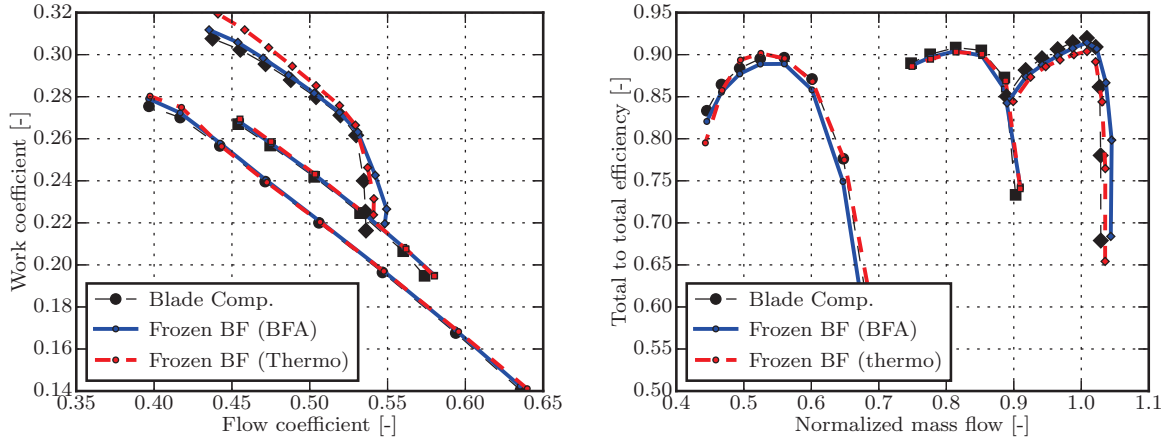


**Figure 2.11:** R4 stage performance map (50%, 75% and 100% RPM). Comparison of blade and extracted body force computations (BFA and thermodynamics-based). The BFA gives a better estimation of the global performance than the thermodynamics-based approach.

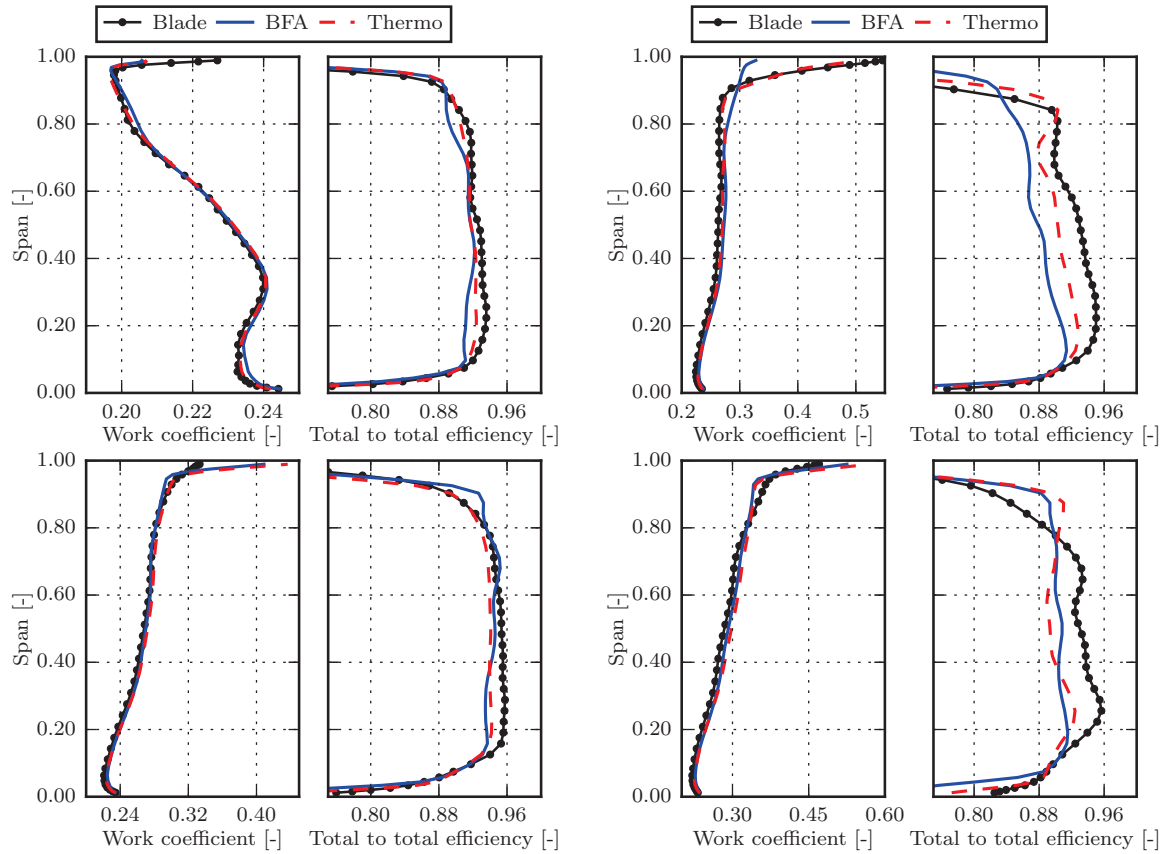


**Figure 2.12:** Spanwise profiles at 50% RPM (top) and 100% RPM (bottom) downstream of the R4 fan stage. Operating points near max efficiency (left) and near stall (right). Off-design efficiency profiles are not well captured, especially with the BFA.

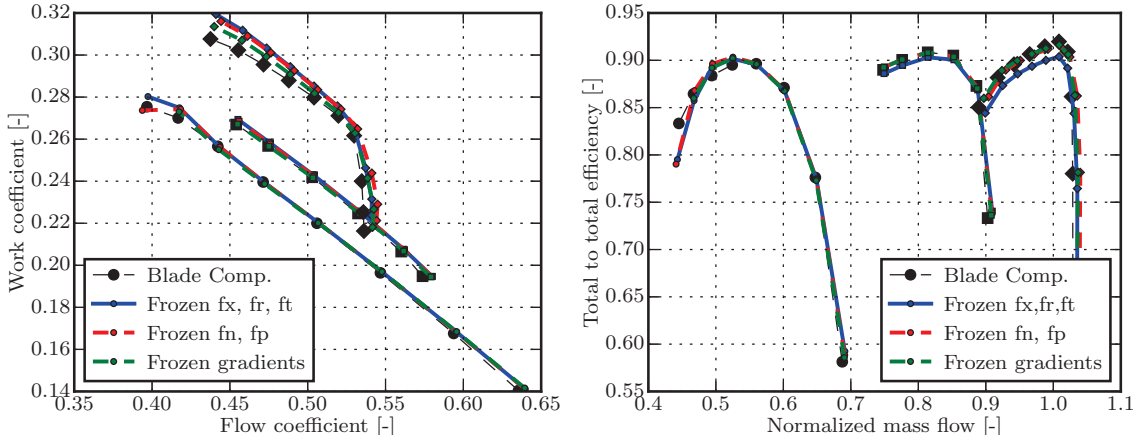


**Figure 2.13:** R4 stage performance map (50%, 75% and 100% RPM). Comparison of frozen body force approaches based on the extraction of thermodynamic quantities (frozen *fx, fr, ft* or frozen *fn and fp* or frozen entropy and tangential velocity gradients).

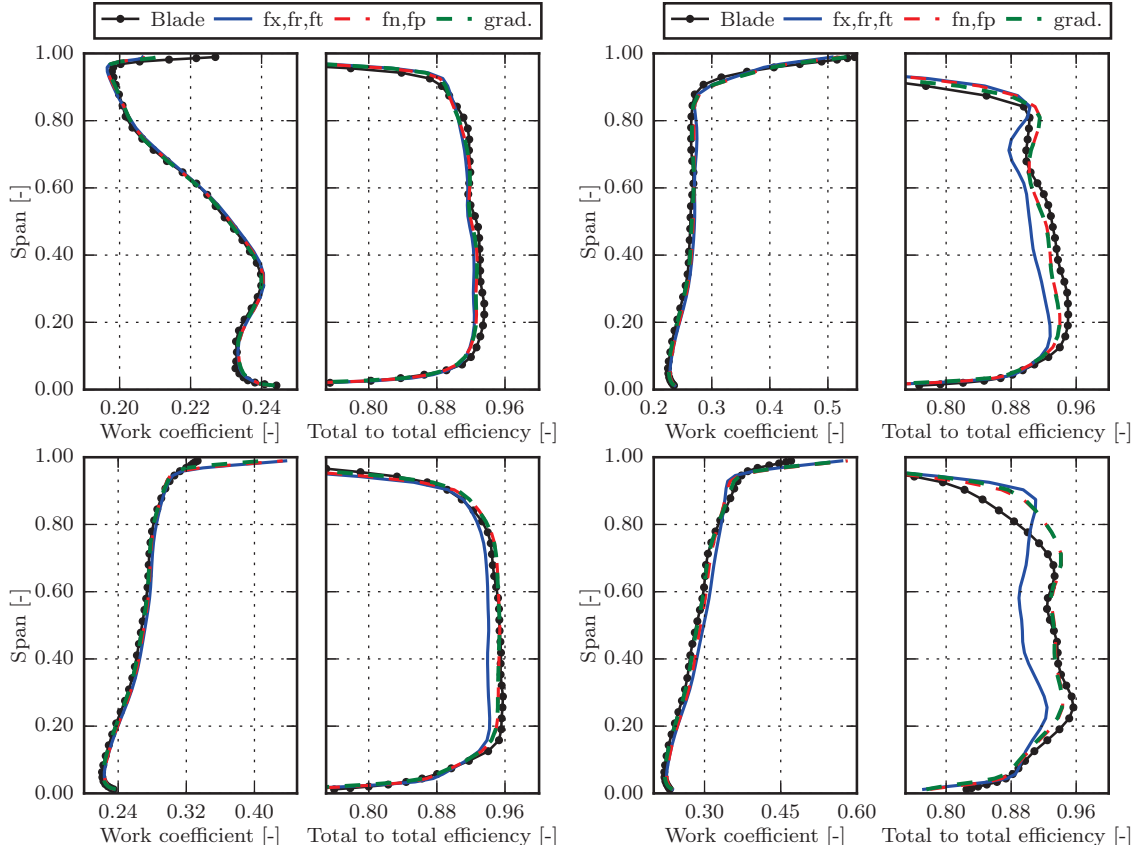


**Figure 2.14:** Spanwise profiles at 50% RPM (top) and 100% RPM (bottom) downstream of the R4 fan stage, near max efficiency (left), and near stall (right) (frozen *fx, fr, ft* or frozen *fn and fp* or frozen entropy and tangential velocity gradients). Directly imposing the normal and parallel force or the gradients significantly improves the prediction of efficiency.

force or the tangential velocity and entropy gradients yields much better results than directly imposing all body force components. Although this is hard to see in the profiles, imposing the gradients also gives a slightly better estimation of work coefficient along the span than imposing the normal and parallel forces, which explains the good agreement on the global performance. Some discrepancies remain near the shroud, which are due to the duplication of the body forces in this region.

The discrepancies between body force and blade results when all spatial body force components are directly imposed are due to small differences between the body force solution and the tangentially averaged blade computations. In particular, when all spatial components are directly imposed, small differences in terms of flow angle can increase the magnitude of the parallel force, which in turn increases the losses. This issue can also lead to errors when interpolating body forces against local flow variables or when calibrating a model. It was reported by Kerner [54] who introduced the “force–flow reconciliation” concept to minimize these errors. Kerner’s solution was to calibrate models or to build body force databases from frozen body force or frozen gradients computations, but this adds another step in the calibration or database generation process. Directly imposing the tangential velocity and entropy gradients yields the best results, as it ensures that the right amount of turning and losses will be added to the flow whatever the flow angle and velocities effectively are.

This observation raises a more general question about the comparison of body force solutions to pitch-averaged blade computations. In particular, a body force simulation does not allow to replicate all the pitch-averaged quantities of an equivalent blade computation. In the BLI context, where notions of energy and entropy are more useful than notions of thrust and drag, conserving the mass-averaged energy and entropy may be more important than conserving the blade force. The thermodynamics-based approach gives a normal and a parallel force component with few manipulations and allows to obtain satisfying results, as compared to the BFA for which new projections would be required. Another advantage of this approach is that a body force solution can be built using only spanwise profiles of work and entropy, if some assumptions are made about the axial distributions of both quantities. This approach is thus used hereafter for the calibration of the models. The calibration is done directly using the pitch-averaged blade computations and Kerner’s force–flow reconciliation concept is not applied.

### 2.3.3 Gong's model

Gong's body force model for high speed compressors [39] is the foundation of this work. One key idea of this approach is that the body forces locally react to perturbations in the flow field. To derive the model, Gong used Marble's decomposition of the blade force into a normal and a parallel component. The normal component is itself divided into a pressure gradient based term, which represents the blade loading, and a deviation-based term, which responds to the local deviation. The first term is found with an analysis of the flow in a periodic, staggered channel as illustrated in figure 2.15. The second term reduces the local deviation and is found by dimensional analysis, based on the projection of the momentum equation on the channel in-passage coordinate. The parallel component of the blade force uses a simple drag relationship.

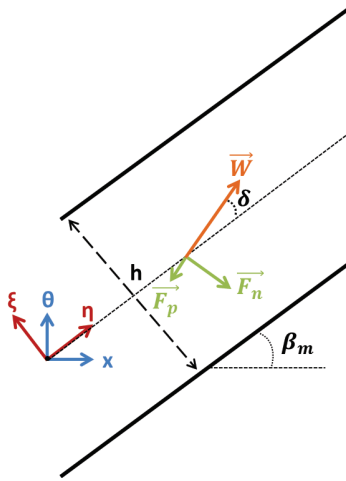


**Figure 2.15:** The flow field in the blade to blade plane can locally be analyzed as a fluid in a periodic straight channel [39].

First, the baseline model equations are given, and Peters' improvements [69] are presented. Then, the following modifications are added to the model:

- The  $K_p$  coefficient in the parallel force is now local and varies with local relative Mach number or local flow coefficient.
- The model is used along with the metal blockage source terms to improve the prediction of work and choke mass flow rate.
- The pressure gradient based term in the normal force is removed.

#### Baseline model and Peters' contribution

The normal and parallel force equations as presented in Gong's PhD thesis are [39]:

$$f_n = \frac{1}{\rho} \frac{\partial P}{\partial x} \sin \beta_m + \frac{K_n}{h_\sigma} W_\eta W_\xi \quad (2.18)$$

$$f_p = \frac{K_p}{h_\sigma} W^2 \quad (2.19)$$

$$h_\sigma = \frac{2\pi r \sqrt{\sigma} \cos \beta_m}{Z_{blade}} \quad (2.20)$$

In equations (2.18) and (2.19),  $\beta_m$  is the blade metal angle,  $h_\sigma$  is the blade to blade staggered spacing computed with equation (2.20), and  $K_n$  and  $K_p$  are calibration coefficients.  $W_\eta$  and  $W_\xi$  are the projections of the relative velocity along the in-passage and cross-passage coordinates, as shown in figure 2.15. Using loss and deviation data from Lieblein's work [60], Gong found the following values for  $K_n$  and  $K_p$  for the Rotor 35 geometry :

$$K_n = 4.2 - 3.3\beta_m \quad (2.21)$$

$$K_p = 0.04 \quad (2.22)$$

The main limitations of the model were the neglection of the radial component of the normal blade force, and the constant value of  $K_p$  along an operating line, the latter leading to an underestimation of the off-design loss generation. Peters [69] later corrected the normal force component representing blade loading and found that the normal force component reacting to deviation can be recast in terms of local deviation angle  $\delta$ :

$$f_n = \frac{1}{\rho} \frac{\partial P}{\partial x} \frac{\sin \beta_m}{\cos^2 \beta_m} + \frac{K_n}{h_\sigma} W^2 \frac{1}{2} \sin(2\delta) \quad (2.23)$$

with

$$\delta = \beta - \beta_m \quad (2.24)$$

He also added a radial component to the normal force using the blade lean angle, and calibrated the model using data from blade computations. The pressure distributions on the blade walls were used to compute the normal force, then relation (2.23) was inverted to retrieve  $K_n$ . However, Peters found that the dependency of the normal force on the deviation angle leads to spurious oscillations of  $K_n$ . To avoid this, he added an offset to the flow velocity component orthogonal to the blade camber:

$$W_\xi = W_x \sin \beta_m + W_\theta \cos \beta_m + CW_{ref}$$

where  $W_{ref}$  is the free stream velocity and  $C$  is a constant between  $0.5 - 0.75$ .

Finally, he introduced a dependency of the coefficient  $K_p$  on the relative Mach number at the blade row inlet  $M_{r,0}$ , so as to form a loss bucket and account for off-design losses:

$$f_p = \frac{K_{p1}}{h_\sigma} [M_{r,0} + K_{p2}(M_{r,0} - M_{ref})^2] W^2$$

where  $M_{ref}$  is the averaged relative Mach number at the blade row inlet at peak efficiency.  $K_{p1}$  and  $K_{p2}$  were found with a trial and error approach, by adapting the coefficients to match the reference CFD data. While the resulting model gave accurate results, some limitations were highlighted by Peters, among which the heavy calibration process and the lack of a model for metal blockage.

## Additional modifications

In the present work, exactly reproducing Peters's results was unsuccessful as the modification of the pressure gradient based term systematically lead to convergence issues. In fact, dividing this term by  $\cos^2 \beta_m$  strongly increases its values and triggers instabilities, which was already reported in [29]. A similar behavior was also met in [8, 58], where the pressure gradient based term was recast in terms of influence coefficients and body forces using a compressible swirling flow analysis to avoid the issue. However, this manipulation is complex and generates a dependency of the normal force to the inverse of  $1 - M_r^2$ , requiring an additional offset to avoid instabilities. All simulations including the pressure gradient based term were therefore run with Gong's original formulation, i.e.  $f_n^{\partial p} = \frac{\partial P}{\partial x} \sin \beta_m$ .

In this work, to avoid introducing a trial and error calibration process and remove the dependency of the parallel force on non-local flow conditions, the calibration coefficient  $K_p$  was expressed as a function of local relative Mach number only, with a loss-bucket shape based on a second order polynomial:

$$K_p = K_{p1}M_r^2 + K_{p2}M_r + K_{p3} \quad (2.25)$$

The main difference with Peter's approach is that the  $K_p$  coefficients vary in space, so that losses are captured locally. The second order polynomial is determined by fitting the  $K_p$  coefficients on an entire speed line. In addition, rather than adding an offset to the cross passage velocity  $W_\xi$ , the coefficient  $K_n$  is determined at each meridional mesh point with the following process:

- First, the  $K_n$  coefficient is computed for each operating point on the speed line. As reported by Peters, this leads to spurious values of  $K_n$  when the deviation angle delta becomes too small.
- Unacceptable values of  $K_n$  are eliminated from the process by specifying an arbitrary maximum allowed value of 40 when the pressure gradient based term is taken into account and 60 when it is not.
- The coefficient  $K_n$  is then determined by averaging all the remaining  $K_n$  less than this maximum value on the speed line. In the case where, for a given grid point, all the computed  $K_n$  are greater than this maximum, the missing data is filled with a nearest neighbor interpolation method.

Applying this calibration methodology without the blockage source terms provides mixed results, as shown in figure 2.16. Although the modification of the parallel force and the calibration of the normal coefficient improve the precision of the model, the work and the choke mass flow rate are globally overestimated. The main reason explaining the discrepancies far from choke is that metal blockage effects impact both the amount of work added to the flow, and the values of the local relative Mach number. The calibration of the parallel force coefficient can therefore not be accurate, as the local relative Mach number distributions in blade computations will not match those in body force computations. Applying an offset to the cross passage velocity as suggested by Peters allows to reduce both the singularities of  $K_n$  and the discrepancies on the work added to the flow, as shown on figure 2.17. The

discrepancies could be further reduced with re-calibration loops for the parallel force, but in any case it would not allow to fully capture the choke mass flow rate, which is significantly affected by metal blockage.

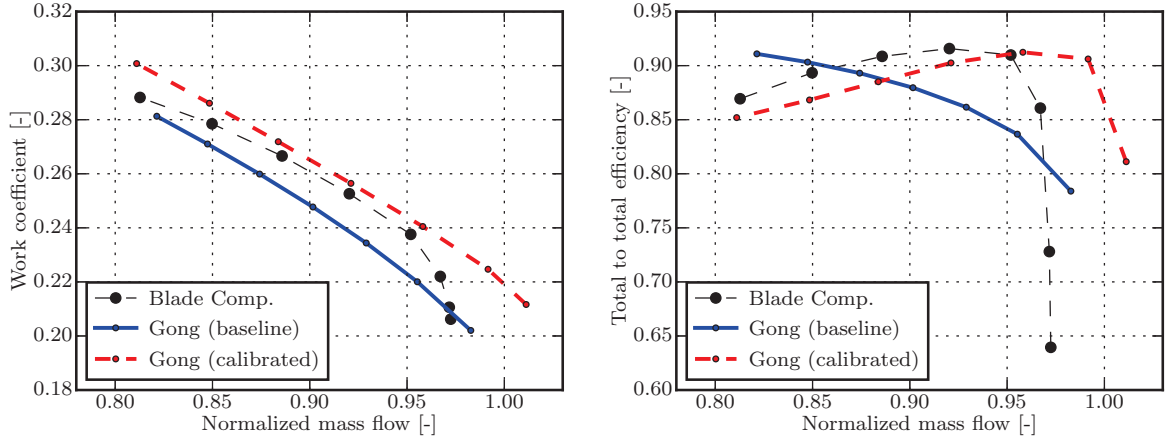


**Figure 2.16:** NASA/GE R4 speed line (90% RPM). Comparison of Gong's baseline model with  $K_n = 4.2 - 3.3\beta_m$ ,  $K_p = 0.02$ , and Gong's improved model with calibrated coefficients. Metal blockage effects are not taken into account in both approaches.

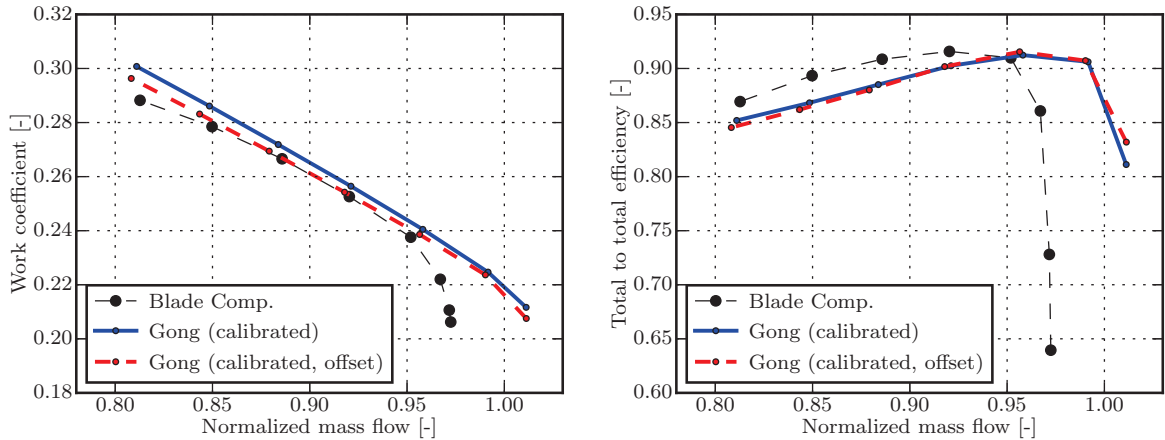


**Figure 2.17:** NASA/GE R4 speed line (90% RPM). Comparison of Gong's improved model, with and without offset on the cross channel velocity  $W_\xi$ . Metal blockage effects are not taken into account in both approaches.

From these results, it follows that including the blockage source terms is necessary to automate the calibration of the model and to correctly capture choked flows. Figure 2.18 shows the results obtained with Gong's model, when blockage source terms are included. The prediction of the model is improved along the speed line, except for the operating points near choke where it can be seen that the model now underestimates the choke mass flow rate. An analysis of the body force distributions at choke revealed that the pressure gradient based

term was responsible for this discrepancy. Near choke, the pressure gradient takes negative values near the leading edge, which decreases the amount of work added to the flow before the sonic throat is reached, and thus decreases choke mass flow rate. Removing this term from the model improves its behavior near choke, at the cost of a slightly decreased fidelity near stall, as shown in figure 2.18. In addition, it improves the stability of the model as, near choke, high pressure gradient values may lead to convergence issues.

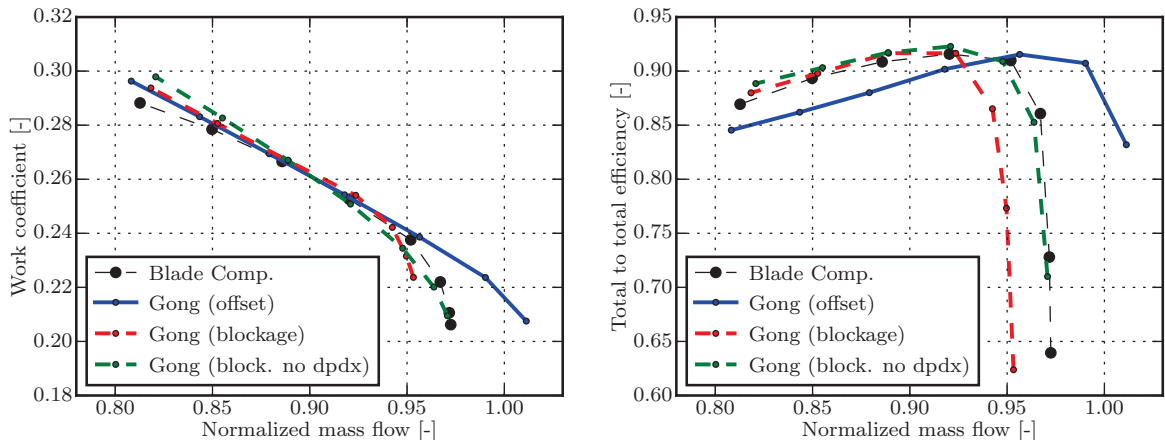


**Figure 2.18:** NASA/GE R4 speed line (90% RPM). Comparison of Gong’s improved model, with an offset on the cross channel velocity  $W_\xi$ , or with the blockage source terms (with and without the pressure-gradient based term).

One remaining issue with this version of Gong’s model is that it must be re-calibrated for each speed line, since the parallel force coefficient depends on the relative Mach number, which varies a lot from one rotational speed to another. To limit errors when applying the model to a different speed line, one solution is to express the parallel force coefficient in terms of local flow coefficient:

$$K_p = K_{p1}\phi^2 + K_{p2}\phi + K_{p3} \quad (2.26)$$

where

$$\phi = \frac{W_m}{U}$$

### Performance map and off-design assessment

A performance map is shown in figure 2.19, in which speed lines obtained with a parallel force that depends on either Mach number or flow coefficient are compared. In the first case, the model is re-calibrated for each speed line, while, in the second case, the model is calibrated once and for all from a speed line at 90% RPM. If the overall accuracy of the flow coefficient based calibration is degraded compared with the Mach number based calibration, the performance trend is still well captured over a large range of rotational speeds, at a lower calibration cost. Spanwise profiles of work coefficient and efficiency downstream of the fan stage are shown in figure 2.20. The profiles of work coefficient are well captured

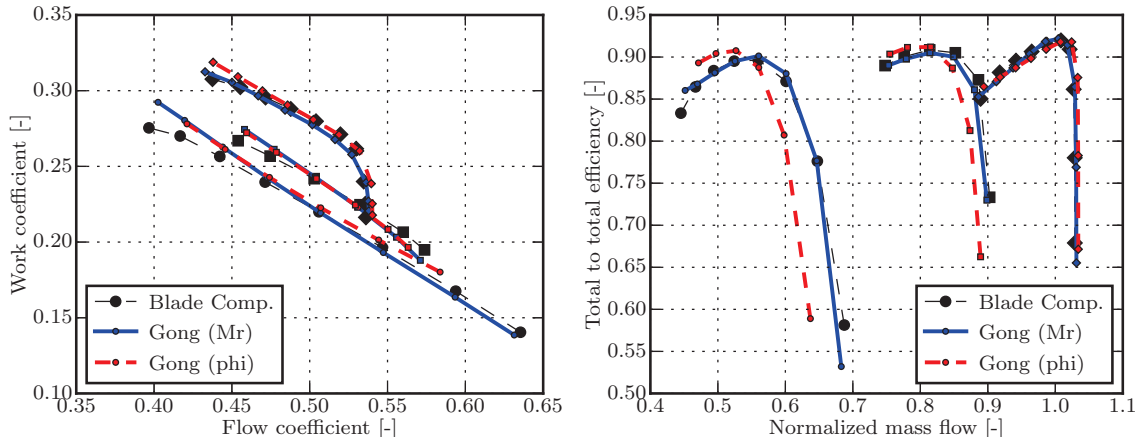


**Figure 2.19:** R4 fan stage performance map (50%, 75% and 100% RPM). The parallel force either depends on local relative Mach number (one calibration for each speed line), or on local flow coefficient (one calibration for all speed lines, performed at 90% RPM). Using the flow coefficient allows to evaluate the global performance for various rotational speeds.

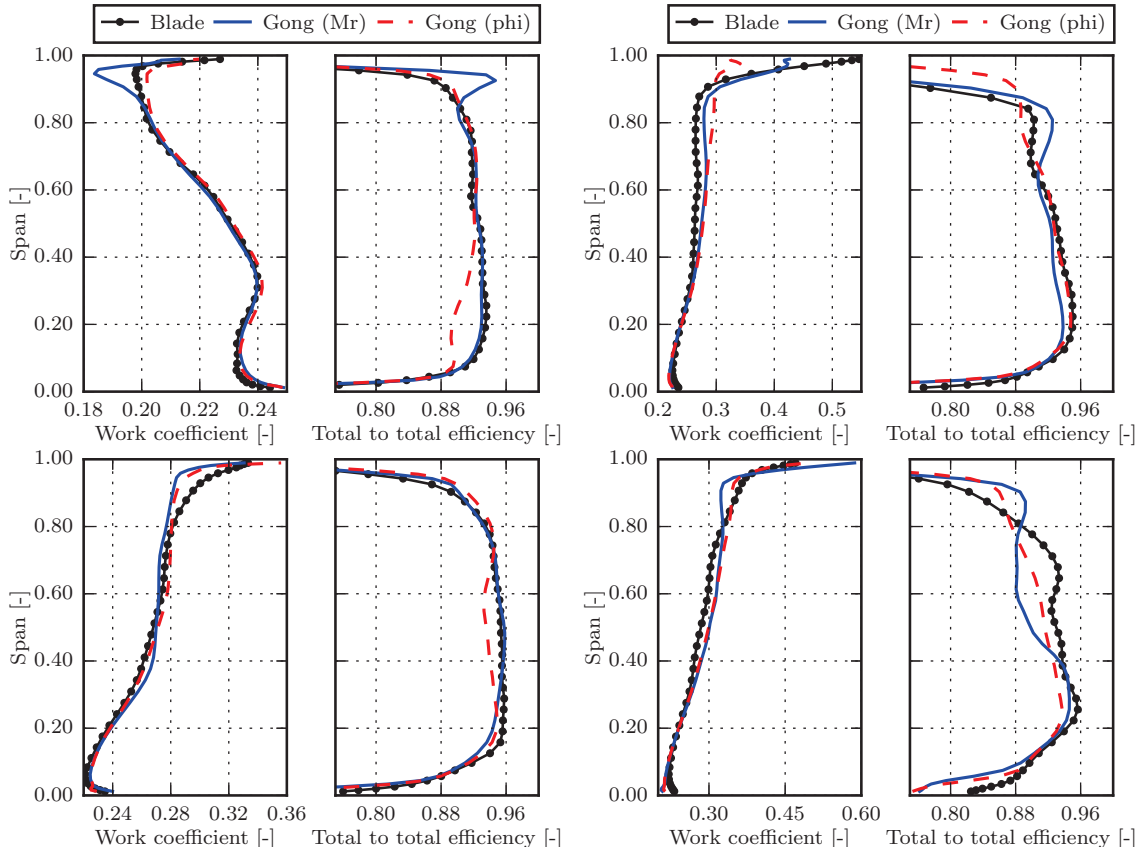


**Figure 2.20:** R4 fan stage: Spanwise profiles at 50% RPM (top) and 100% RPM. Operating points near max efficiency (left) and near stall (right). The prediction remains accurate at different rotational speeds when the flow coefficient is used for calibration.

despite a spike at 50% RPM, which is likely due to fitting errors, but some discrepancies appear on the efficiency profiles, especially near stall. In particular, at 50% RPM, the model calibrated from the 90% RPM speed line with the flow coefficient does not capture the drop in efficiency near 85% span. This is because the physical phenomena leading to off-design loss are different at 50% RPM and 90% RPM. Additional losses at low speed are localized in the tip region and are due to flow separation on the shroud, whereas additional losses at high speed are mainly due to increased shock losses in the supersonic region of the rotor blade. One solution to reach higher overall accuracy could be for instance to use two calibrations for the model, one for low speeds and one for high speeds.

To further assess the off-design capability of the model, computations with positive and negative inlet swirl angles were performed at 100% RPM. The results, shown in figure 2.21, are not very good, both for a Mach number or flow coefficient based calibration and especially for the prediction of the loss: the model is not able to capture the changes in efficiency due to inlet swirl. Although better results were found by Peters [69], it is thought that his manual calibration of the parallel force and its dependency on the Mach number at the fan face rather than on the *local* Mach number allowed to obtain better results. However, it is unclear whether his formulation captured local loss variations or only the bulk change in efficiency. Spanwise profiles downstream of the fan stage are shown in figure 2.22. The spanwise distributions of work coefficient are well captured, but the parallel force formulation does not capture accurately changes in efficiency along the blade span. It is interesting to note that the flow coefficient based calibration seems to give slightly better results than the one with the Mach number. These results suggest that a bivariate formulation for the  $K_p$  coefficient may be necessary to capture loss variations accurately.

## Summary

With the modifications proposed above, the normal and parallel forces of Gong's model are given by:

$$f_n = \frac{K_n}{h_\sigma} W^2 \frac{1}{2} \sin(2\delta) \quad (2.27)$$

$$f_p = \frac{K_{p1} M_r^2 + K_{p2} M_r + K_{p3}}{h_\sigma} W^2 \quad (2.28)$$

$K_n$  and  $K_p$  are defined at each meridional grid point. The local Mach number  $M_r$  in the parallel force equation can be interchanged with the local flow coefficient  $\phi$  if the model is used at different rotational speeds with only one set of calibration coefficients. From the previous analysis it appears that this version of Gong's model suffers from two limitations:

- The calibration process is not robust and sometimes leads to localized errors. For the normal force component, this is due to the inversion of the normal force equation to find  $K_n$ . For the parallel force component, this is due to the second order polynomial fitting of  $K_p$  for each meridional point in the blade domains.
- A simple dependency of  $K_p$  on local relative Mach number or local flow coefficient is not enough to accurately capture off-design losses.

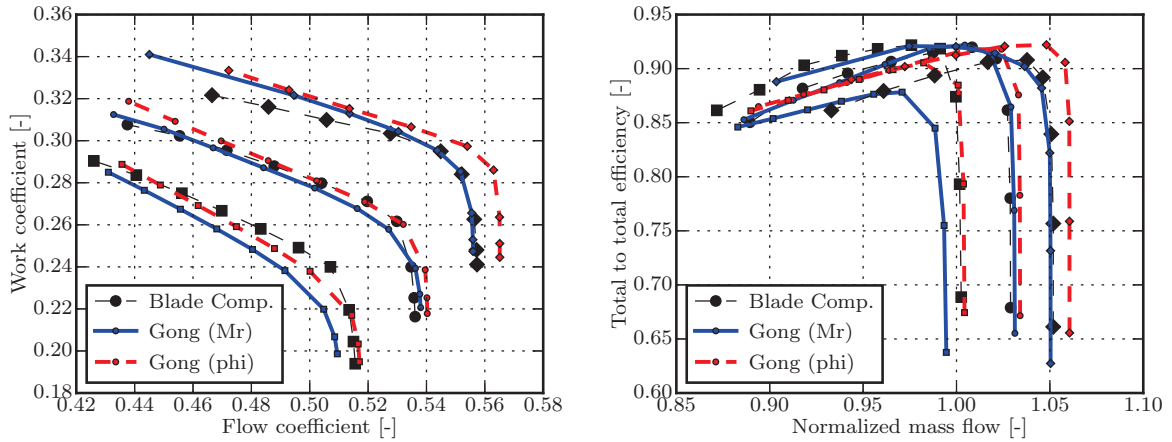


**Figure 2.21:** R4 performance map at 100% RPM with  $\pm 5^\circ$  inlet swirl. The parallel force either depends on the local relative Mach number (calibration performed at 100% RPM), or on the local flow coefficient (calibration performed at 90% RPM). The effect of inlet swirl on the global efficiency is not captured.

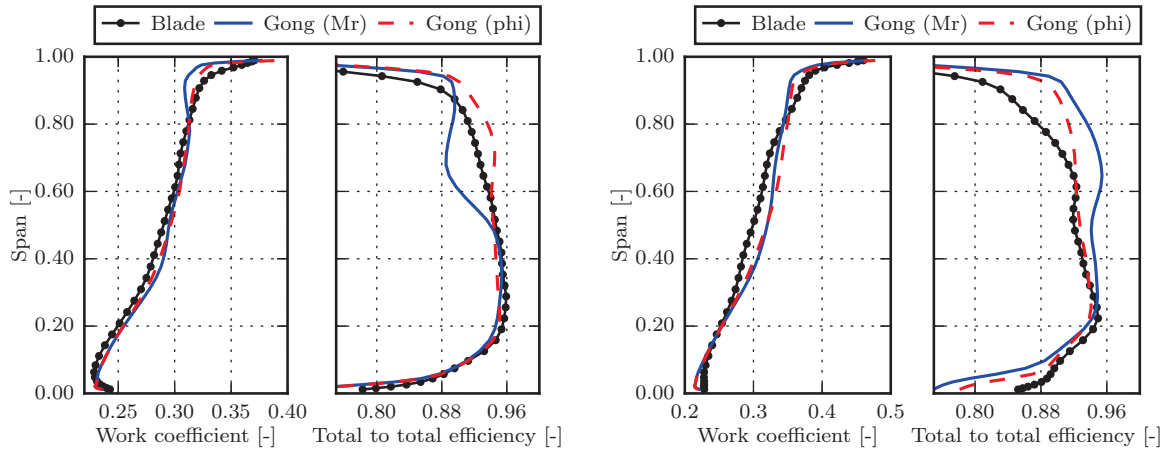


**Figure 2.22:** Spanwise profiles at 100% RPM with  $5^\circ$  counter-swirl. Operating points near max efficiency (left) and near stall (right). Using the flow coefficient to calibrate the parallel force yields better results than using the relative Mach number.

### 2.3.4 Lift / drag model

A different modeling approach was sought to address Gong's model limitations. The approach developed in this section is derived based on a lift/drag analogy for the normal and parallel force components respectively:

$$f_n = \frac{2\pi\sigma}{h} W^2 (\beta - \beta_0) \quad (2.29)$$

$$f_p = \frac{K_p}{h} W^2 \quad (2.30)$$

with

$$K_p = K_p^{\eta_{max}} + 2\pi\sigma(\beta - \beta^{\eta_{max}})^2 \quad (2.31)$$

and

$$h = \frac{2\pi r \cos \beta_m}{Z_{blade}} \quad (2.32)$$

$\sigma$  is the local solidity of the blade row,  $\beta_0$  is a calibration coefficient for the normal force, and  $K_p^{\eta_{max}}$  and  $\beta^{\eta_{max}}$  are respectively the local loss coefficient and relative flow angle at maximum efficiency. To remain consistent with the lift/drag analogy of a wing profile, the normal and parallel forces are canceled in the tip gap. The lift coefficient of a thin airfoil  $2\pi(\alpha - \alpha_0)$  appears in the normal force equation, and the off-design loss component is similar to that of a drag polar. The normal force can be seen as a linearized version of Gong's model as, for low deviation angles  $\delta$ , Gong's model gives:

$$f_n = \frac{K_n}{h} W^2 \delta = \frac{K_n}{h} W^2 (\beta - \beta_m)$$

A practical motivation for this formulation is that the results given by Gong's model are more sensitive to variations of the blade metal angle than to variations of  $K_n$ . The expression of the lift/drag model normal force can be understood as a means to geometrically set the coefficient  $K_n$ , and to base the calibration of the model upon finding the blade angle the most adapted to reproduce the blade loading.  $\beta_0$  can therefore be seen as a local zero-lift relative angle, which comprises both local metal angle and camber effects. This model does not exhibit Gong's limitations regarding the calibration of the normal force.

In addition, the parallel force component contains a term that aims at naturally capturing off-design losses, with the idea that high deviation angles correspond to thick boundary layers and to cases with separated regions that generate large amounts of losses. With this approach, the coefficient  $K_p^{\eta_{max}}$  sets the minimum amount of losses, i.e the maximum efficiency losses, and off-design losses are triggered by flow angle deviations from this operating point. The model can therefore be calibrated for each speed line from the operating point at peak efficiency only, from which the following quantities must be extracted at each meridional grid point:

- The zero lift relative angle  $\beta_0$ , found with equation (2.29)
- The drag coefficient at max efficiency  $K_p^{\eta_{max}}$ , computed from equation (2.30)
- The distribution of relative flow angle at max efficiency  $\beta^{\eta_{max}}$

## Application of an offset in the normal force

An issue was found when applying the model at high rotational speeds, as shown in figure 2.23. With the formulation proposed above, the model overestimates the choke mass flow rate and the work coefficient in the rotor. This happens because the flow turning is too high near the leading edge of the rotor. A solution to avoid this issue consists in applying a shape function that offsets the  $\beta_0$  distribution near the leading edge of the rotor. The function is equal to  $1 + C_0$  at the leading edge, then decreases linearly to 1 at mid-chord and remains constant afterwards, where  $C_0$  is the offset constant with values between 0.01 and 0.05, depending on the case.

$$f_n = \frac{2\pi\sigma}{h} W^2 (\beta - C(x)\beta_0) \quad (2.33)$$

with

$$C(x) = \max \left\{ 1 + C_0 \left( 1 - 2 \frac{x - x_{LE}}{x_{TE} - x_{LE}} \right), 1 \right\} \quad (2.34)$$

The offset is applied during the body force simulations but is not taken into account when  $\beta_0$  is retrieved from a blade computation. This modification improves the prediction of work coefficient over the speed line and allows to capture the choke mass flow rate more accurately, but a trial and error procedure is required to find the value of  $C_0$  that gives the correct choke mass flow rate. In addition, the maximum efficiency is slightly underestimated when the offset is applied, as the flow angle distribution in the body force simulation differs from the one in the blade computation at maximum efficiency.

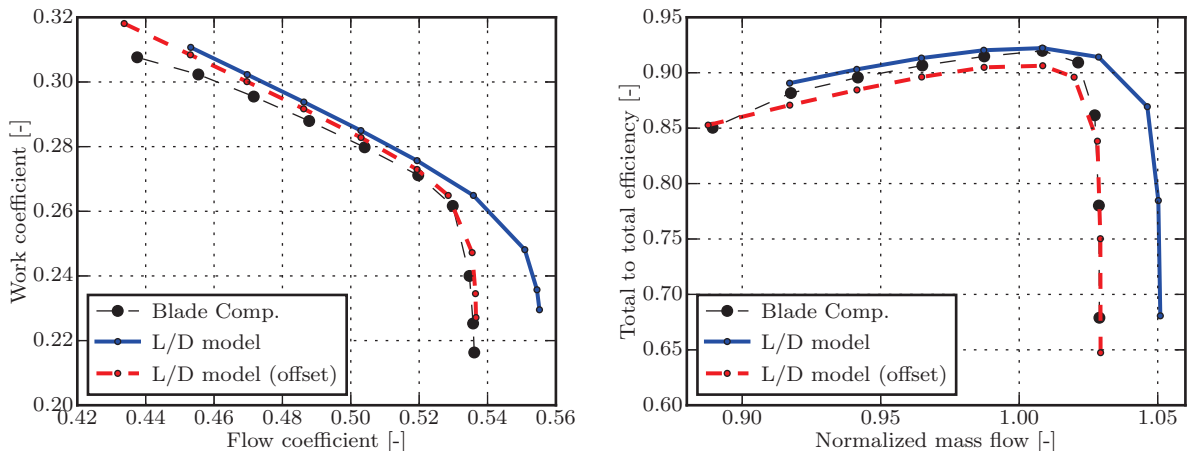


**Figure 2.23:** R4 speed line at 100% RPM, with and without the offset  $C(x)$  in the lift/drag normal force formulation. Adding the offset is required to capture the choke mass flow rate of the fan stage, but it leads to underestimated peak efficiency.

## Performance map and off-design assessment

A performance map obtained with the model is shown in figure 2.24. The model can be calibrated from one speed line and is then able to capture the global performance over a wide range of rotational speeds. The efficiency at 100% RPM is underestimated when the model is calibrated from the 75% RPM speed line, because the design point is on the 100% RPM speed line. As for Gong's model, if a minimum calibration effort is sought, the prediction of efficiency could be refined by using a set of calibration coefficients for low speeds and another set for high speeds.

Spanwise profiles downstream of the fan stage are shown in figure 2.25. The work coefficient is well captured, even with a calibration from a different speed line, which confirms that the functional form chosen for the normal force is physically consistent. However, large discrepancies are visible on the profiles of efficiency, especially near stall. In particular, the off-design loss is uniformly distributed along the span, which implies that the off-design term in the parallel force should be refined to capture the local loss generation. At 100% RPM, a good part of the off-design loss occurs near the tip of the blade, and is due to increased shock losses in the rotor and to corner flow separation in the OGVs. One first improvement of the model could thus be to include a Mach number dependency in the off-design term of the parallel force to improve the prediction of the shock loss in the rotor.

A performance map obtained with inlet swirl is shown in figure 2.26. The global performance with inlet swirl is well captured, although the peak efficiency with co-swirl is underestimated. This may be avoided if the model was calibrated from the “best” possible operating point of the fan stage, i.e. an operating point for which all spanwise stations of both the fan and OGV would be operating at the maximum possible efficiency on all the performance map. Spanwise profiles for 5° counter-swirl are shown in figure 2.27. The profiles of work coefficient are well captured, but the profile of efficiency near stall is not reproduced, which was expected given the previous results without inlet swirl.

## Summary

The expression for the normal and parallel forces in the lift/drag model are:

$$f_n = \frac{2\pi\sigma}{h} W^2 (\beta - C(x)\beta_0) \quad (2.35)$$

$$f_p = \frac{K_p^{\eta_{max}} + 2\pi\sigma(\beta - \beta^{\eta_{max}})^2}{h} W^2 \quad (2.36)$$

$C(x)$  is computed using equation 2.34. The model captures the performance of the R4 fan stage within 5% for the work coefficient and 4 points for the global efficiency, for most operating points. The calibration process is robust and only requires a single operating point, whereas multiple points are needed for Gong's model. Its main limitations are the need for a manual calibration of  $C(x)$  in the normal force to capture the choke mass flow rate, and the lack of physics-based modeling in the parallel force that only allows to capture the bulk off-design loss but not the spanwise profiles of efficiency.

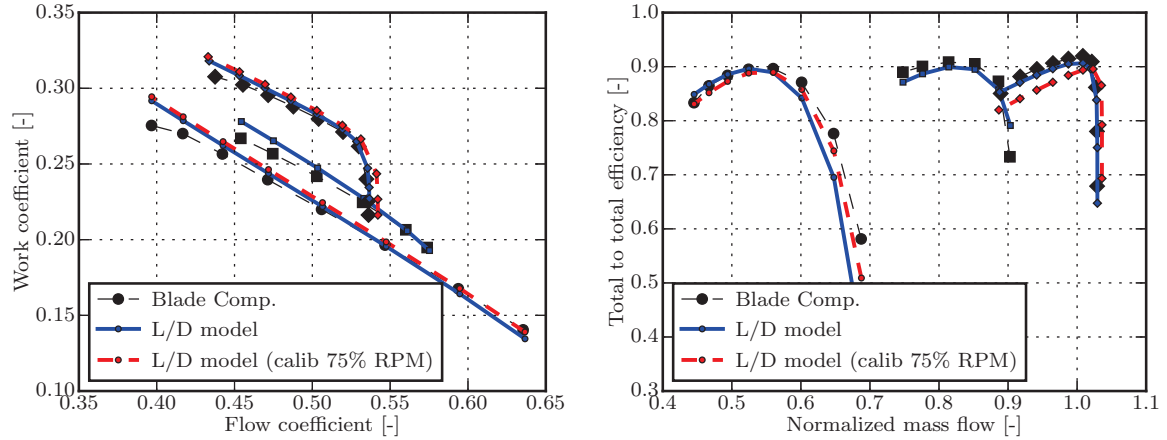


**Figure 2.24:** R4 performance map (50%, 75% and 100% RPM). In blue, the model is re calibrated for each speed line, in red the model is calibrated from the 75% RPM speed line. The global performance can be evaluated with only one set of calibration coefficients.

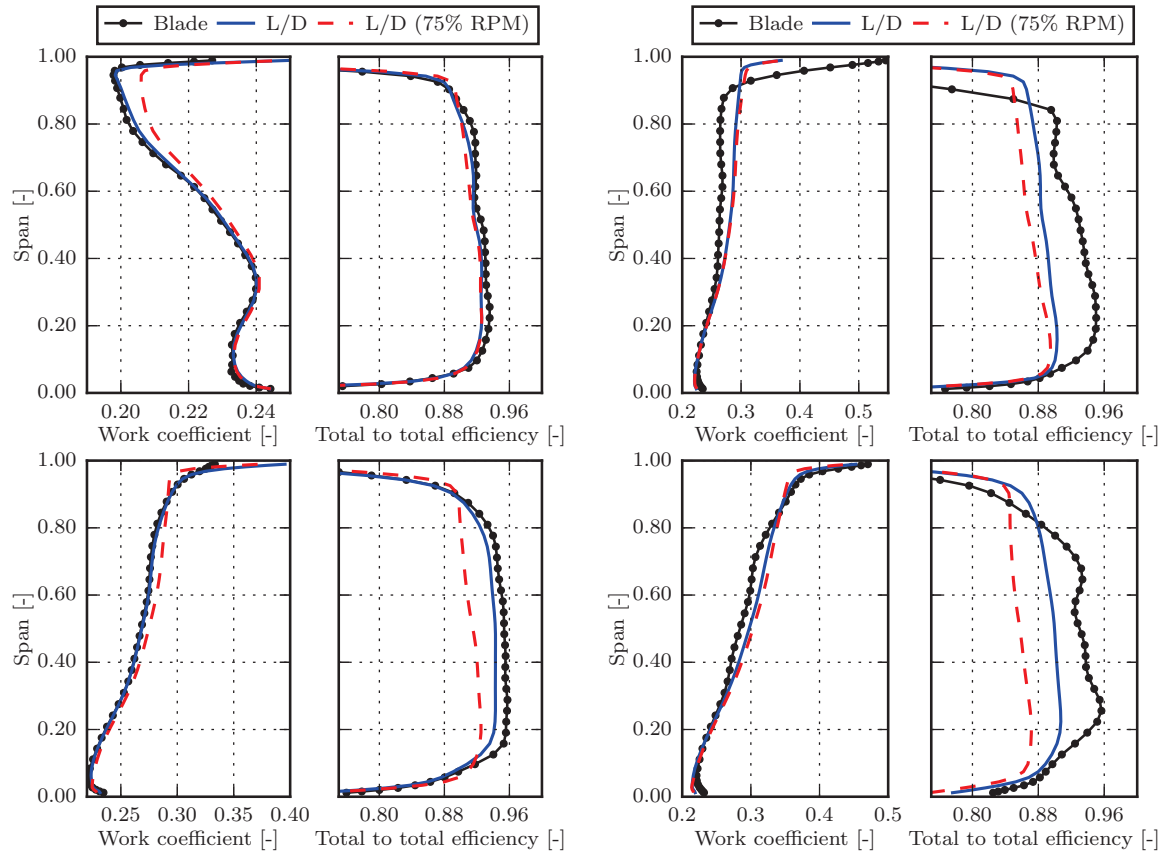


**Figure 2.25:** Spanwise profiles at 50% RPM (top) and 100% RPM (bottom) downstream of the R4 fan stage. Operating points near max efficiency (left) and near stall (right). The local off-design efficiency decrease is not well captured.

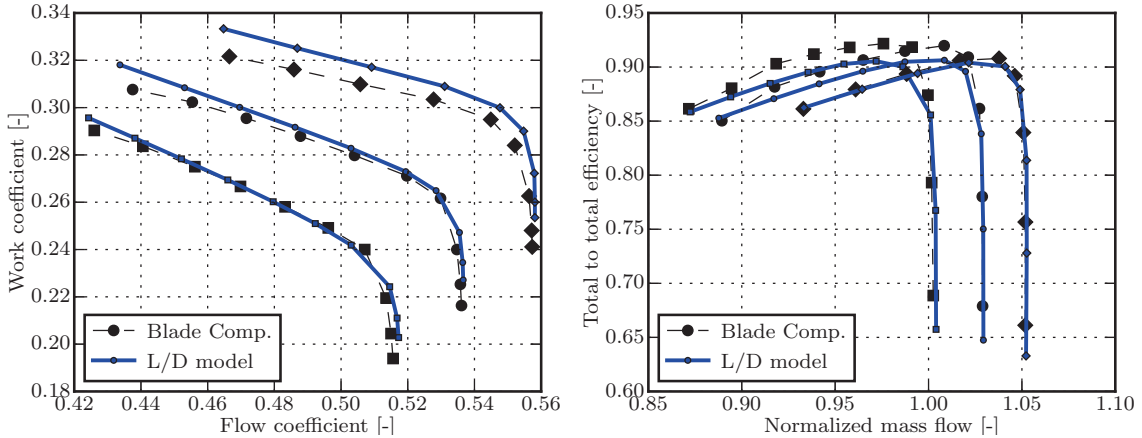


**Figure 2.26:** NASA/GE R4 operating line at 100% RPM, with  $\pm 5^\circ$  inlet swirl. The global performance is well captured, but the peak efficiency with co-swirl is underestimated.

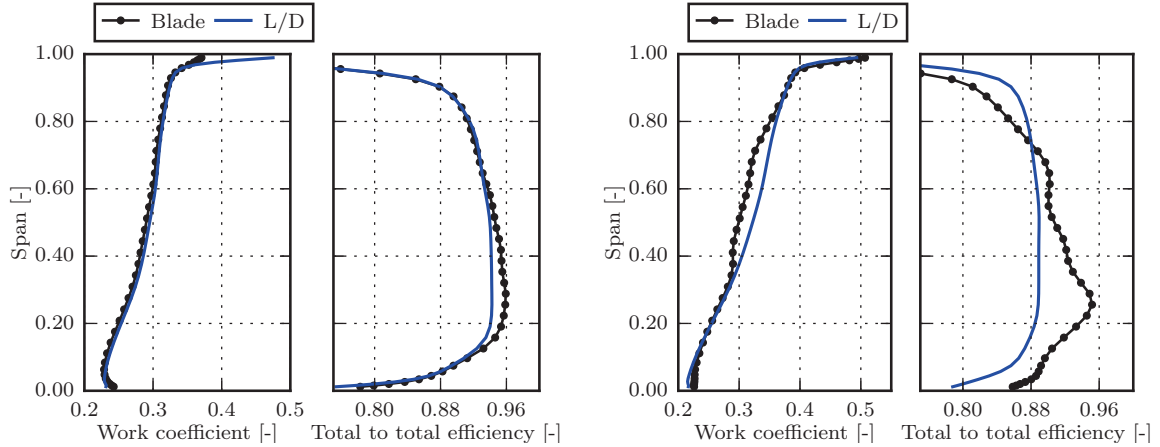


**Figure 2.27:** Spanwise profiles at 100% RPM with  $5^\circ$  inlet counter-swirl downstream of the R4 fan stage. Operating points near max efficiency (left) and near stall (right). The efficiency profile with inlet swirl near stall is not captured.

### 2.3.5 Hall's model

In this section, an inviscid (normal force only) and incompressible model that was originally proposed by Hall [48] and that does not require any calibration from a blade computation or from experimental data is presented. Then, some modifications are proposed, to improve the behavior of the model at high rotational speeds and to capture the loss.

#### Baseline formulation

The expression of the normal force as given by Hall [48] is:

$$f_n = 0.5W^2 2\pi \delta \frac{1}{s|n_\theta|} \quad (2.37)$$

where  $s$  is the local blade pitch and  $\delta$  a local 3D deviation angle.

In equation (2.37),  $n_\theta$  is the tangential component of the vector locally normal to the blade camber surface. The model gives the theoretical lift coefficient for an isolated flat plate ( $2\pi\delta$ ) and has a physically consistent behavior in the infinite solidity limit (the flow is instantaneously turned toward the blade so that  $\delta \rightarrow 0$ ). The deviation angle  $\delta$  is computed with respect to the 3D plane locally tangent to the blade camber surface. In addition, the normal force is projected in the plane shared by the normal to the camber surface and the relative velocity, so that radial force components are naturally captured. In particular the model can be used for both axial and radial turbomachines without any special modification. In fact, although this is not shown here, the model was applied to a centrifugal compressor geometry and gave encouraging results. Finally, the normal force is set to zero in rotor tip gaps to capture some of the undeturning in this region.

Hall validated the model on incompressible test cases, without blockage source terms. Because the parallel force was not modeled, diffusion factor was used as a surrogate for the losses. Applying this baseline model to the R4 fan stage at 100% RPM yields mixed results, as shown in figure 2.28. In particular, without the blockage source terms the choke mass flow rate is overestimated.

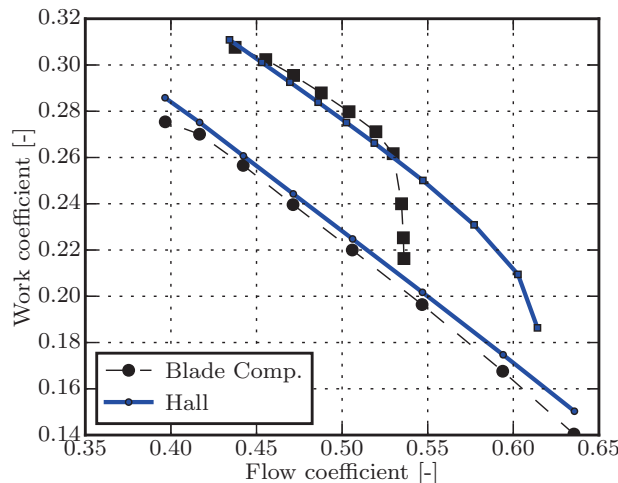


**Figure 2.28:** R4 stage performance map at 50% and 100% RPM. Comparison of Hall baseline model and blade computations.

In the present work, to address these shortcomings, three modifications are added to the model:

- Metal blockage effects are taken into account with the blockage source terms in the governing equations, and by multiplying the pitch of the blade  $s$  by the blockage factor  $b$  in the normal force equation.
- A compressibility correction is added in the normal force definition, that captures the influence of Mach number on lift coefficient.
- Losses are modeled with a simple local skin friction coefficient and an off-design term similar to the one in the lift/drag model.

## Blockage and compressibility correction

To capture the choke mass flow rate, the blockage source terms previously described in section 2.2.2 are added to the equations of motion. For consistency, the pitch of the blade is also multiplied by the blockage factor in the normal force equation, as the thickness of the blade reduces the effective area in a blade passage. In the zero blockage factor limit, the flow would be perfectly guided by the blades, which is consistent with this modification. However, it was found that including the metal blockage source terms globally decreases the work input to the flow. This is not due to a defect in the modeling of metal blockage, but to a limitation of the normal force formulation when compressibility effects become significant. In fact, the magnitude of the normal force is based on the lift coefficient of a thin airfoil at low Mach numbers, but the lift coefficient of an airfoil increases at high subsonic Mach numbers and has a different expression for supersonic flows. To capture the correct amount of work, a compressibility correction is thus added to the normal force model. Using the Prandtl-Glauert correction, the lift coefficient of a thin airfoil for subsonic Mach numbers is:

$$C_L = \frac{2\pi\alpha}{\sqrt{1 - M^2}} \quad (2.38)$$

For supersonic Mach numbers, Ackeret formula gives:

$$C_L = \frac{4\alpha}{\sqrt{M^2 - 1}} \quad (2.39)$$

Both expressions are obtained using linearized forms of the potential equation, which are only valid far from sonic conditions. To avoid the singularity near Mach 1, a blending function that comprises both equations (2.38) and (2.39) is applied to the normal force as a correction factor. The blending function is clipped to a maximum value of 3, as shown in figure 2.29a. It was found that increasing this value did not have a significant impact on the solution. In particular, the area in which the Mach number is close to unity on the R4 fan stage is rather small, as shown in figure 2.29b. This modification gives the following expression for the normal force:

$$f_n = K_{Mach} 0.5 W^2 2\pi \delta \frac{1}{s b |n_\theta|} \quad (2.40)$$

where:

$$K_{Mach} = \begin{cases} \min\left(\frac{1}{\sqrt{1-M_r^2}}, 3\right), & \text{if } M_r < 1 \\ \min\left(\frac{4}{2\pi\sqrt{M_r^2-1}}, 3\right), & \text{if } M_r > 1 \end{cases}$$

Results obtained with the updated model are shown in figure 2.30. The combination of both metal blockage and compressibility correction allows to capture work coefficient at low and high speed and to improve the capture of the choke mass flow rate. As will be shown in the next section, the remaining discrepancy on the latter is partially due to the lack of a loss model in the present computations.

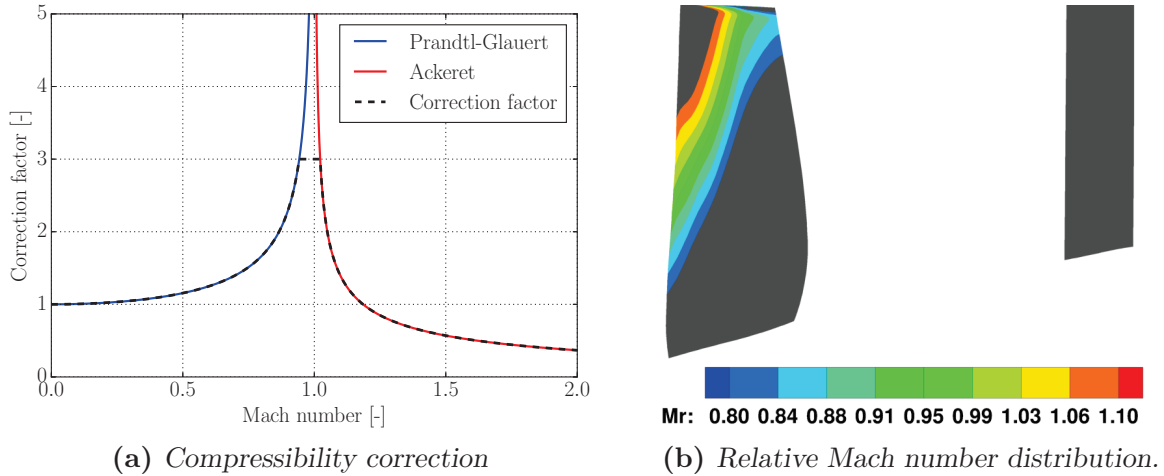


**Figure 2.29:** Compressibility correction applied to the normal force model and contours of tangentially averaged relative Mach number in the R4 fan stage near design.

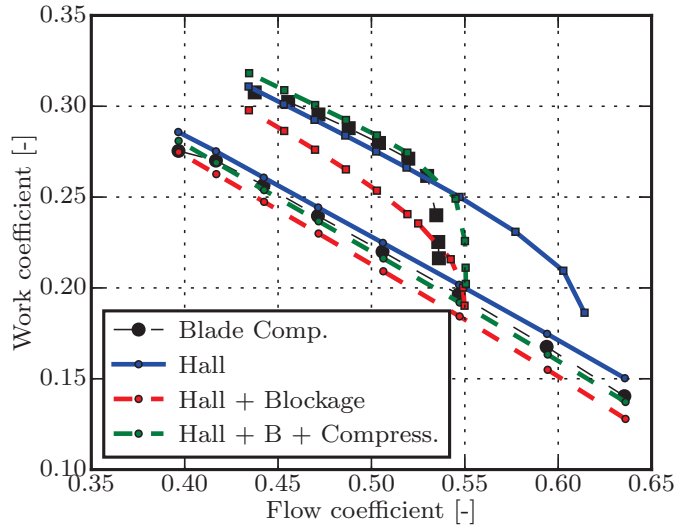


**Figure 2.30:** Performance map of the R4 fan stage (50% and 100% RPM). Metal blockage decreases the work coefficient predicted by Hall's model but including a compressibility correction in the normal force allows to improve the results.

## Loss Modeling

A parallel force formulation consistent with the normal force is sought to generate the loss. Close to maximum efficiency operating conditions, the deviation is small and the flow follows the camber surface. The loss on the blade pressure and suction sides at maximum efficiency is thus estimated using an empirical flat plate local friction coefficient. The off-design loss is computed with a term similar to the one in the lift/drag model. This approach gives the

following relationship for the parallel force:

$$f_p = \frac{0.5W^2}{sb|n_\theta|} (2C_f + \underbrace{2\pi K_{Mach}(\delta - \delta^{\eta_{max}})^2}_{\text{off-design term}}) \quad (2.41)$$

with

$$C_f = 0.0592 Re_x^{-0.2} \quad (2.42)$$

where  $C_f$  is a local friction coefficient, and  $Re_x$  is the local chordwise Reynolds number computed with the local relative velocity:

$$Re_x = \frac{\rho W x}{\mu} \quad (2.43)$$

Obviously,  $\delta^{\eta_{max}}$  is not known a priori. One solution could be to evaluate this term using correlations for the deviation angle at maximum efficiency. In the present work, a first body force computation is run at maximum efficiency. Then, a deviation distribution is extracted from this operating point and used as  $\delta^{\eta_{max}}$  in the next body force computations. This is a fast procedure, as computing an operating point with this model only takes a few minutes. The procedure is illustrated in figure 2.31 where two speed lines are shown, computed with and without the off-design term. Including the parallel force allows to reduce the discrepancy on the choke mass flow rate from 1.6% without any loss to 0.75% with the complete loss model, and to improve the prediction of work coefficient near stall.

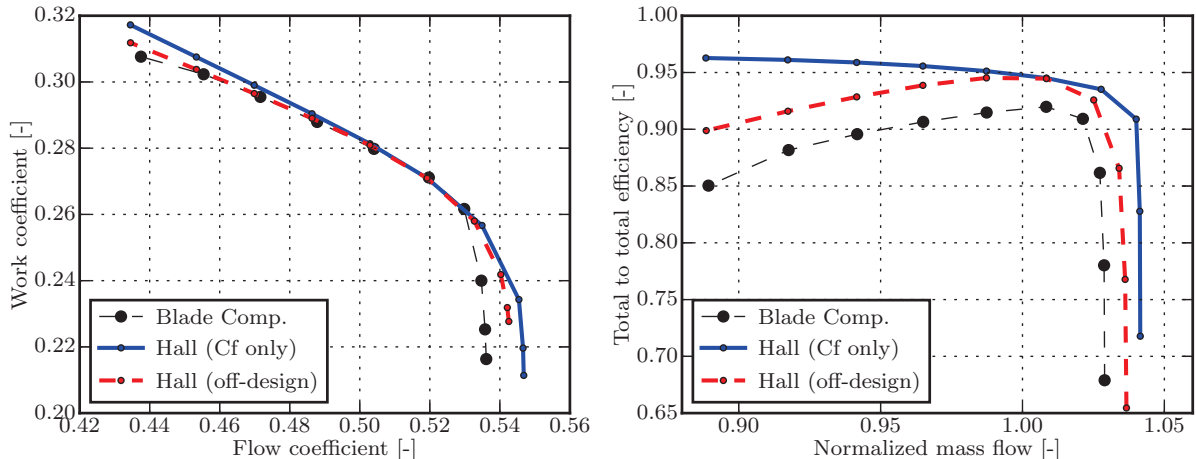


**Figure 2.31:** R4 fan stage 100% RPM speed line. Illustration of the two-step procedure to capture off-design loss with Hall's model.

It should be noted that the off-design term in the parallel force equation differs from the one in the lift/drag model, shown in equation 2.31. In particular the off-design coefficient is equal to  $2\pi K_{Mach}$  versus  $4\pi\sigma$  in the lift/drag model. The reason for this modification is that the magnitude of the normal force in the present model is lower than in the lift/drag model. In fact, the higher the lift coefficient is in the normal force, the faster the flow is turned toward the blade, which decreases the amplitude of the off-design term  $(\delta - \delta^{\eta_{max}})^2$ .

Using the lift/drag model off-design coefficient in the parallel force leads to overestimated losses with the present normal force formulation. It was therefore modified to be consistent with the normal force model.

### Performance map and off-design assessment

Two alternative assumptions can be made about the available knowledge of the fan performance, before the model is used to compute a performance map:

- At a conceptual design level, only the design point is known, and only one  $\delta^{\eta_{max}}$  distribution can be extracted to compute all speed lines.
- In a more advanced design phase, the maximum efficiency mass flow rate may be known for different speed lines, and new  $\delta^{\eta_{max}}$  distributions can be extracted for each speed line.

The performance maps obtained under these two assumptions are shown in figure 2.32. When only the design point  $\delta^{\eta_{max}}$  distribution is used, the efficiency is not well captured at low rotational speeds. In particular, the position of the maximum efficiency is shifted toward lower mass flow rates. When the model can be re-calibrated for each speed line, the prediction of efficiency is substantially improved, as was found with the lift/drag model: both peak and off-design efficiency are well captured at low speed.

Spanwise profiles downstream of the fan stage are shown in figure 2.33. The distributions of work coefficient are well captured in all cases. The distributions of efficiency are well captured near the maximum efficiency operating point at low speed, when an appropriate distribution of  $\delta^{\eta_{max}}$  is available. The efficiency is slightly overestimated at high speed above 60% span, which is notably due to underestimated losses in the supersonic region of the rotor. Near stall, the distributions of efficiency are not captured, which confirms the inability of the loss model to capture the physical sources of off-design losses. In fact, the low-speed off-design loss is mostly localized at the tip of the blade, and is due to flow separation on the shroud. At high speed, a large part of the off-design loss comes from increased shock losses in the rotor and from corner stall in the OGVs, and is localized above mid-span.

A performance map with inlet swirl is shown in figure 2.34. The effect of inlet swirl on work coefficient is well captured. However the model predicts a lower peak efficiency with co-swirl than with counter-swirl. The distributions of work coefficient downstream of the fan stage are well captured, as shown in figure 2.35. As was expected, the distributions of efficiency are not well captured, and in particular the efficiency above 60% span, where the rotor inflow is supersonic, is overestimated.

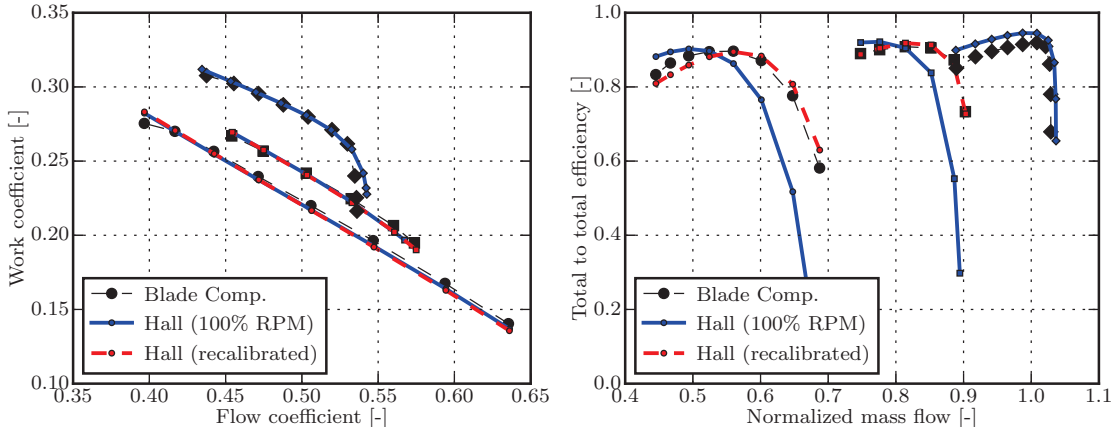


**Figure 2.32:** R4 performance map (50%, 75% and 100% RPM). In blue, a  $\delta^{\eta_{max}}$  distribution is extracted from the design point at 100% RPM and used to compute all speed lines. In red, a new  $\delta^{\eta_{max}}$  distribution is generated for all speed lines, which improves the global accuracy.

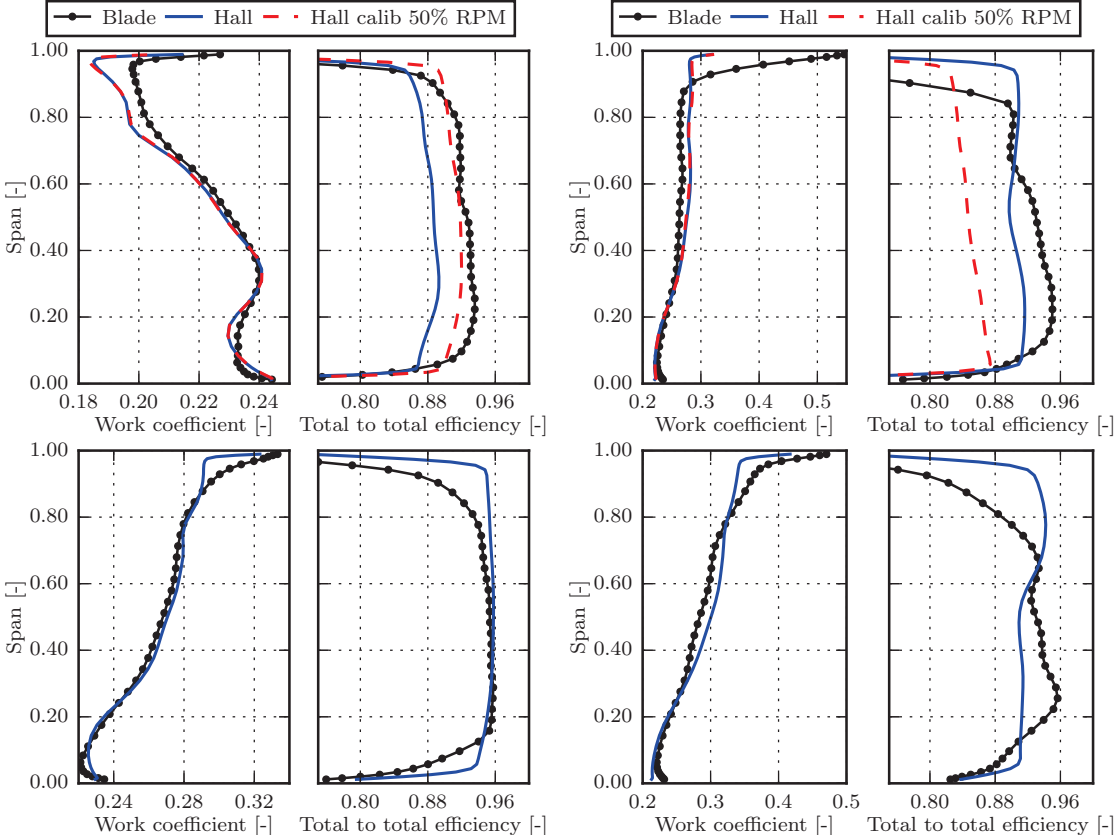


**Figure 2.33:** Spanwise profiles at 50% RPM (top) and 100% RPM (bottom) downstream of the R4 fan stage. Operating points near max efficiency (left) and near stall (right). The model gives encouraging results near maximum efficiency when it can be re-calibrated but profiles of efficiency are not captured near stall.

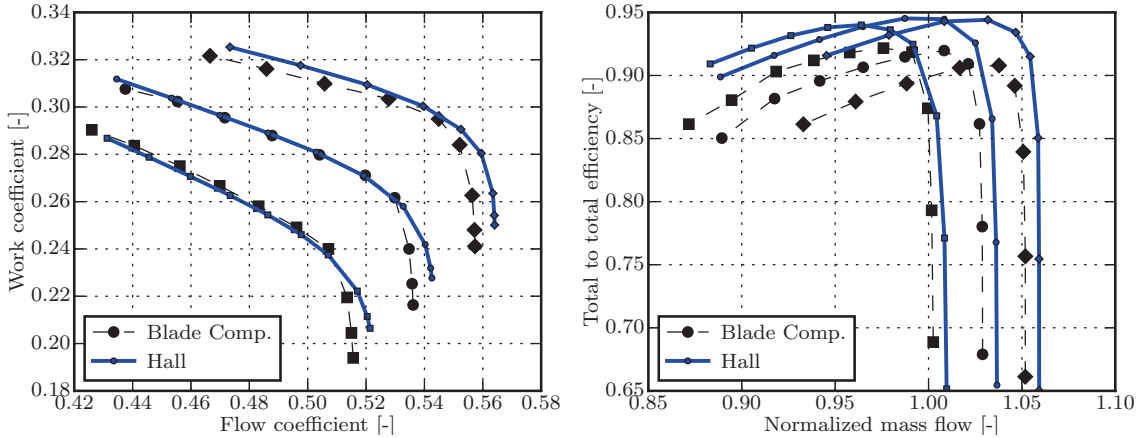


**Figure 2.34:** NASA/GE R4 operating line at 100% RPM, , with  $\pm 5^\circ$  inlet swirl. The global performance is well captured, but the efficiency is in general overestimated.

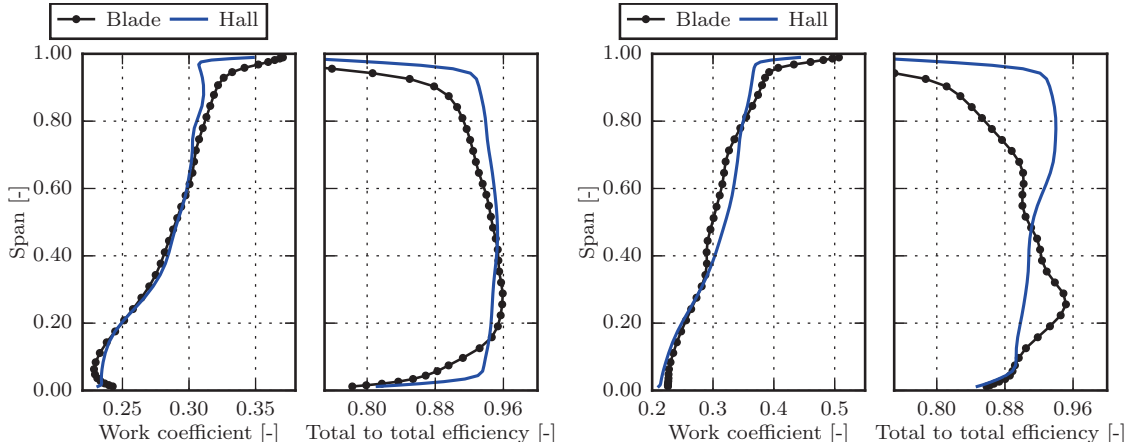


**Figure 2.35:** Spanwise profiles at 100% RPM with  $5^\circ$  inlet counter-swirl downstream of the R4 fan stage. Operating points near max efficiency (left) and near stall (right). As for the lift/drag model, the profile of efficiency near stall is not captured.

## Summary

The final expressions for the normal and parallel force are:

$$f_n = K_{Mach} 0.5 W^2 2\pi \delta \frac{1}{sb|n_\theta|} \quad (2.44)$$

$$f_p = \frac{0.5 W^2}{sb|n_\theta|} (2C_f + 2\pi K_{Mach} (\delta - \delta^{\eta_{max}})^2) \quad (2.45)$$

The model proposed by Hall and extended in the present work to compressible flows gives encouraging results, especially for the prediction of work coefficient which is captured within 5%. The choke mass flow rate is overestimated by 1% at the design speed, which may partially be explained by the lack of a model for the aerodynamic blockage on the blades.

The global efficiency is captured within 5 points at low speed but the local efficiency is overestimated by more than 10 points near the tip of the blade for some operating points at the design rotational speed. The model only requires the definition of the blade geometry, in terms of camber surface and blockage factor, and the knowledge of maximum efficiency mass flow rate(s). As for the lift/drag model, further work on loss modeling is required to obtain a better prediction of the efficiency.

## 2.4 Summary and conclusions

Three explicit body force models were presented in this chapter. The first model is built upon Gong's and Peters' contributions [39, 69] and captures well the design performance of the NASA/GE R4 fan stage. However, several blade computations are required to calibrate the model, the calibration process is not robust, and the model does not capture the off-design efficiency accurately with a local loss formulation. To address these limitations, an improved formulation based on a lift/drag analogy was presented. Only one blade computation is required to calibrate the model, but a manual adaptation of the normal force is necessary to capture the choke mass flow rate accurately. In addition, the off-design component in the parallel force does not capture the physical sources of off-design losses. The third explicit model that was presented is based on Hall's incompressible and inviscid formulation [48], to which a compressible correction and a loss formulation are added. The main asset of this model is that it is solely based on first-principle considerations so that it does not rely on any calibration from blade computations. The model captures the work coefficient of the R4 fan stage within 5% for various operating points, but high-speed and off-design losses are not well modeled. Since both the lift/drag and Hall's models capture the performance of a fan stage for several operating conditions, it is thought that they can be used to capture fan-airframe interactions, although the impact of distortion on fan efficiency may not be well predicted. These questions are explored in the next chapters, where both models are applied to short intake and BLI configurations.

The varying need for calibration of each model should be put into perspective, depending on the targeted application. For instance, if the body force approach is used to design an air intake for a given fan geometry, or to study an aircraft at system level, it is acceptable to use a model that requires input from blade computations, such as the lift/drag model, to reach higher accuracy. On the other hand, at a conceptual design level for the fan, if there is no detailed geometry available, it is useful to have access to a more general approach such as Hall's model. To avoid switching between models for each different application, a future approach could be based on an hybrid formulation, in which optional calibration coefficients could be introduced to increase the accuracy of the model when a detailed knowledge of the fan performance is available. For instance, the calibration process used for the lift/drag model could be applied to Hall's model to improve the design work coefficient and loss predictions.

Although the modeling of the normal force is already satisfying, since the work coefficient is in general well captured by all models, the modeling of the loss constitutes the key difficulty in the body force modeling approach. Further work is thus required to improve this aspect of the method. Future loss models could be based on a large CFD database

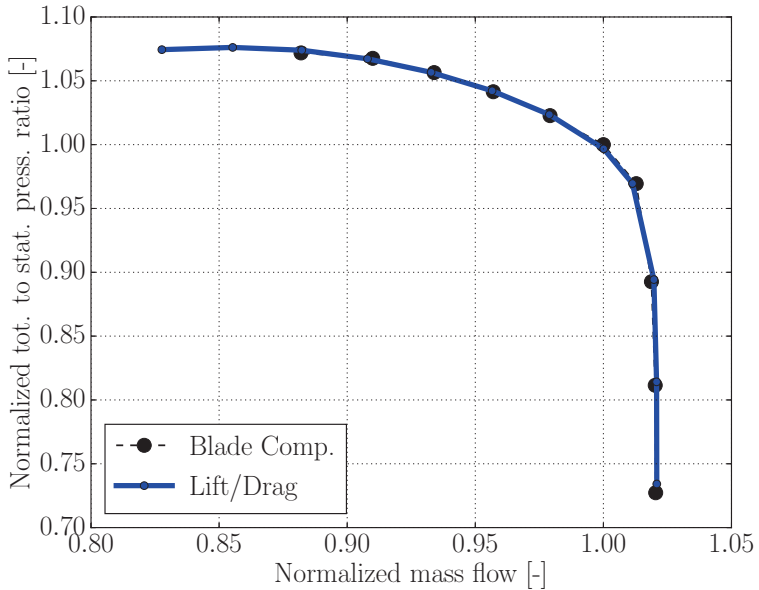


**Figure 2.36:** Total to static pressure ratio in the R4 fan stage (100% RPM). The lift drag model captures the onset of positive slope on the left of the characteristic.

of cascade simulations (see Appendix A), or/and on an improved calibration process from blade computations. Another solution, not explored in the present thesis, could be to base the modeling of the loss on first principles, as is the case in Hall's normal force model. This is an ambitious task, as loss generation mechanisms in turbomachinery are utterly complex and probably impossible to transpose in first-principle-based explicit formulations.

Another important aspect of body force modeling that was set aside in the present work is the modeling of the circumferential stresses, introduced in Appendix B. These stresses were shown in the past to be contributors to aerodynamic blockage and spanwise mixing, the latter being usually modeled with an eddy viscosity as for turbulence closure. While both effects are not dominant in a fan, it may be useful to consider their implementation if the body force approach was used to simulate LPC or HPC stages. Concerning the modeling of aerodynamic blockage, one could consider introducing an additional blockage factor in the equations, that could for instance be modeled with results from cascade simulation. Another solution, adopted by Brand [8], is to apply a correction to the velocity distribution within the blade rows.

A key aspect of the approach that was not assessed in this chapter is the capability of the models to capture the stability limit of the fan stage. In fact it is useful to evaluate the stability margin of the fan for an operation under distorted inflow. A performance map of the R4 fan stage at the design rotational speed, expressed in terms of total-to-static pressure ratio, is shown in figure 2.36. At low mass-flow rates, the lift/drag model captures the onset of positive slope, which is in general associated to the stability limit of a compressor. Numerically, the model fails to converge in this region of the characteristic. Flow separation develops on the shroud in the meridional plane, triggered by the rotor, which leads to the static pressure decrease. A quick sensitivity study showed that the presence of this stall

region is sensitive to the treatment applied on the normal force at the tip (normal force canceled in the tip region, kept constant from a given spanwise location, or directly estimated with the model) and to the values taken by the parallel force. Additional work is required to completely understand in which conditions flow separation occurs, but this preliminary result is encouraging and indicates that the models could also be used to evaluate the stability margin of the fan.

Finally, a last potential application of the approach in the frame of fan-airframe interactions is the evaluation of aeromechanical constraints on the blades, as already reported by Hall [48]. It will be shown in the next section that the models qualitatively capture the IP forces acting on the fan, but the local constraints on the blades and in particular the variation of these constraints when a blade travels around the annulus are not assessed. Gunn et al. [44] showed that, for a transonic fan, the shock structure on the fan blades probably drives the aeromechanical constraints on the blades. Since this shock structure is not captured in body force computations, it is possible that the approach misses the detailed axial distribution of the pressure stresses, but it is thought that it may at least allow to evaluate the global variation of these constraints around the annulus.

# Chapter 3

## Intake–fan interactions on short nacelle configurations

The main objective of this chapter is to demonstrate the ability of the body force models described in chapter 2 to capture fan–intake interactions on short intake configurations, with a focus on the upstream influence of the fan on the air intake. Only the lift/drag model and Hall’s model are kept, as Gong’s model was not found to give better results than the lift/drag model in terms of performance prediction, despite the additional calibration efforts. First the fan geometry is described and the models are applied to the isolated rotor. Then, the fan rotor is placed in three air intakes of varying length, and the impact of inlet length on intake–fan interactions is evaluated with the body force models. In particular, the models are used to assess the fan effect on inlet flow separation and on IP forces at max climb. Finally, the OGVs, the bifurcation and the nozzle are included in the computational domain, to evaluate the potential impact of these elements on the operation of fan and intake, and to assess inlet distortion transfer in the bypass flow. All the results are validated with full annulus unsteady simulations. It is found that both models capture well the upstream influence of the fan on the air intake and the qualitative effect of inlet length on IP forces. Although they are not explored in the present thesis, an example of application of the lift/drag model to crosswind conditions can be found in a publication by Godard et al. [38].

### 3.1 Description and assessment of the fan geometry

The models are applied to a model-scale Turbine Powered Simulator (TPS) fan, designed for experimental purposes. The characteristics of the fan stage are described in table 3.1. First, blade and body-force computations of the isolated rotor were carried out to check the performance prediction of the different models. A performance map at max climb operating conditions, with and without inlet swirl, is shown in figure 3.1. The lift/drag and Hall’s models give similar estimations in terms of global work coefficient. In particular, both models over-estimate the work coefficient and choke mass flow rate with counter swirl. On this geometry, the efficiency is higher with co-swirl than without swirl or with counter-swirl, which is not captured by the models. This is expected, as both model were calibrated based on the peak efficiency operating point from the speed line without swirl, which was assumed

Nb of rotor blades	21
Nb of OGV blades	23
Rotor tip diameter	0.229 m
Rotor hub to tip ratio	0.44
Rotor tip relative Mach number (max climb)	1.26

**Table 3.1:** 9-inch fan stage geometry.

to be the maximum efficiency operating point at this rotational speed. Spanwise profiles of relative error on work coefficient and efficiency downstream of the rotor are shown in figure 3.2. The work coefficient is captured within 10% in all cases, except near the shroud. The efficiency is well captured near design with the lift/drag model, but Hall's model does not capture the losses in the supersonic region of the rotor, which was already observed with the R4 geometry.

The discrepancies are overall more important than on the R4 stage. One key difference between these geometries is the hub to tip ratio, which is higher in the present case. In addition, blockage effects at the tip, due to tip leakage flow, are more important with this geometry as a region of reverse flow appears on the shroud, even at maximum efficiency. This is because the rotational speed at max climb is higher than the design rotational speed for this geometry, which leads to off-design operation near the tip and thus to flow recirculation. Because the hub to tip ratio is higher, the effect of aerodynamic blockage at the tip is more important and the radial distribution of flow coefficient within the blade passage is altered in the blade computation. This is not captured in the body force computations, and the flow angle far from the shroud is therefore not consistent with the one in the blade simulations. For the lift/drag model, one solution to address this limitation is to perform a frozen body force or frozen gradient computation and to calibrate the model from this simulation, following Kerner's force-flow reconciliation concept described in chapter 2. This solution was not adopted here, as it makes the calibration process heavier.

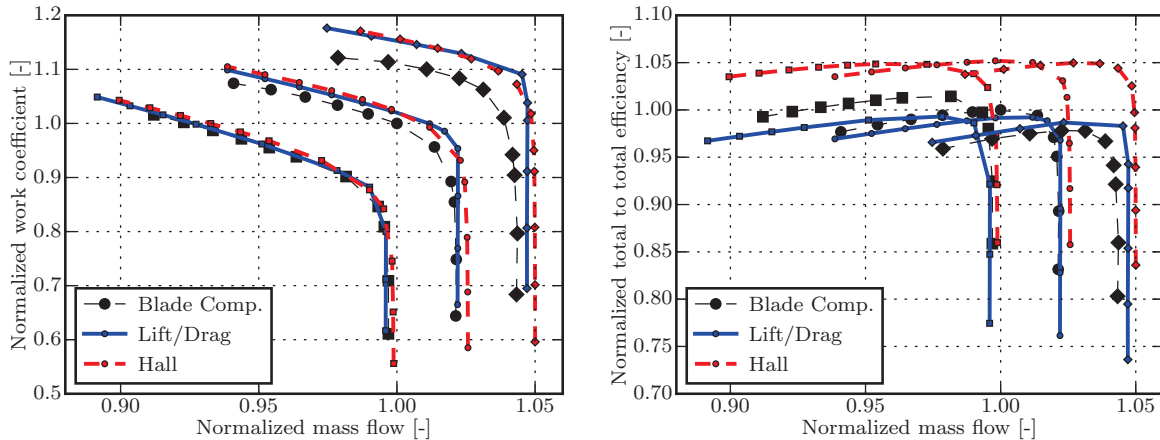


**Figure 3.1:** Performance maps of the fan rotor with 5° positive and negative inlet swirl. The overall work coefficient and rotor efficiency are well captured by the BF models.

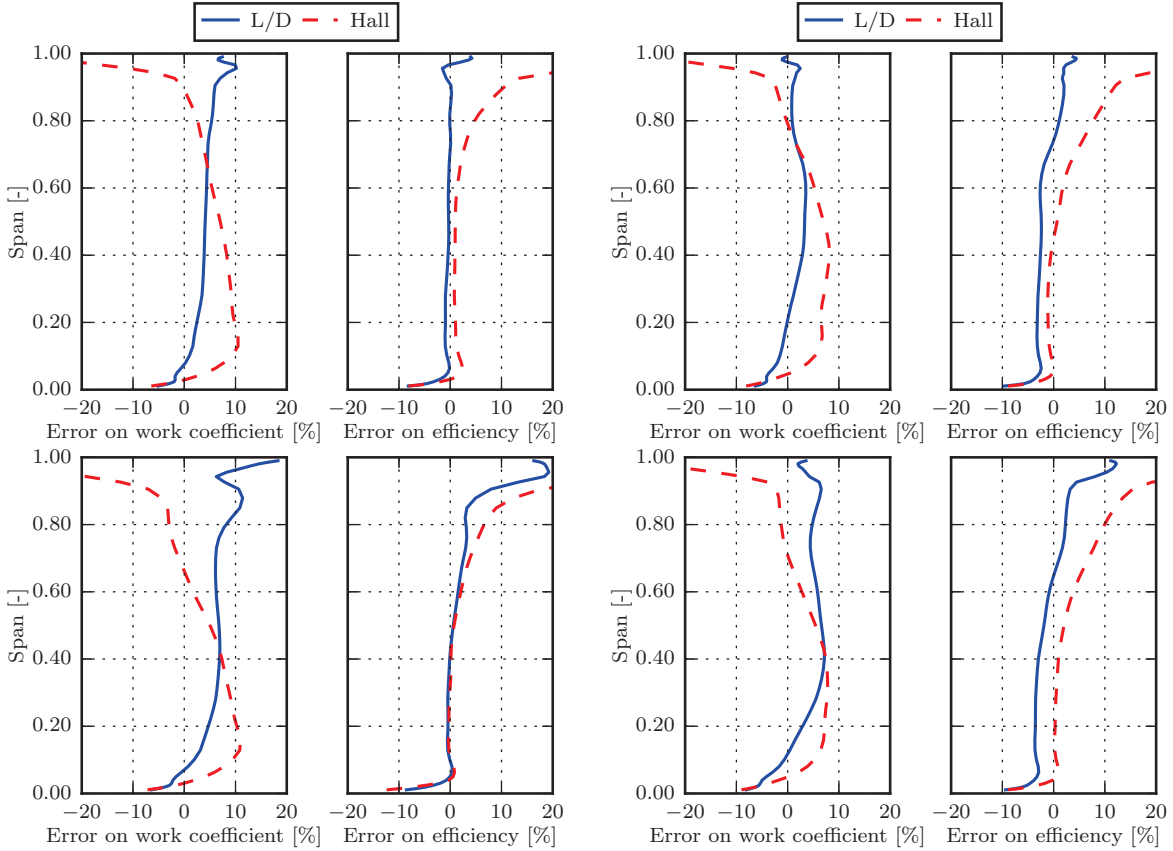


**Figure 3.2:** Spanwise profiles downstream of the fan rotor (relative error as compared to blade computations). Operating point near maximum efficiency (left) and near stall (right) without swirl (top) and with  $5^\circ$  counter-swirl (bottom). The work and efficiency are captured within 10% on most of the span for a wide range of operating points.

## 3.2 Fan–intake interactions at max climb

The rotor geometry described in the previous section is placed in three axisymmetric air intakes of varying length, as illustrated in figure 3.3. The length to diameter ratio of each intake is given in table 3.2. The OGVs are not included in the computational domain and an outlet condition is placed two axial chords downstream of the fan trailing edge. Far field conditions are applied on the outer boundaries of the external domain, and a fixed jet is used downstream of the nacelle. Four sets of computations with increasing angles of attack are carried-out on each geometry:

- Body force computations, with the lift/drag and Hall’s models.
- Full annulus unsteady computations (URANS) of the fan, used for validation.
- Power-Off (P/O) computations, in which the fan effect is not taken into account. These computations allow to highlight the upstream influence of the fan on the air intake.

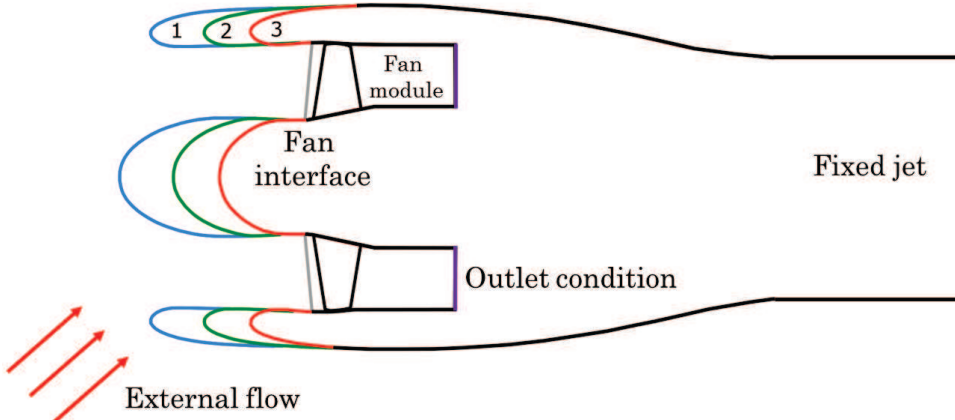


**Figure 3.3:** Illustration of the three intake geometries used to highlight the effect of inlet length on intake-fan interactions.

Intake	1	2	3
$L/D$	0.650	0.450	0.277

**Table 3.2:** Length to diameter ratios of each air intake.

The mesh in power-off computations is the same as in body force computations, and the static pressure at the outlet of the channel is set to obtain the same mass flow rate as in body force and URANS computations. In all the computations, the convective fluxes are determined with a second-order centered scheme with artificial dissipation. Turbulence closure is achieved with the one-equation Spalart-Allmaras model. Body force and power-off computations are conducted with an implicit pseudo-time marching method and a multigrid acceleration on three levels. A non matching interface is used between the external domain and the fan module, so that the same internal mesh can be used for all the air intakes. Full annulus unsteady computations are conducted with a second-order backward difference scheme, with dual-time stepping. The same parameters as in body force and power-off computations are used in the internal loop. A sliding interface is used at the fan face, and, as for body force and power-off computations, the same mesh is used for the fan module in the three intake geometries. More information about the numerical details of the full annulus unsteady computational approach can be found in [41, 33].

For each intake geometry and for each computational approach, some computations are first conducted with a circumferentially uniform inlet flow, then the intake AOA is progressively increased until flow separation occurs inside the air intake. The AOA steps are equal to  $0.5^\circ$  close to the intake stall point. The external Mach number, pressure, and temperature are chosen to be representative of a low-speed, low-altitude flight condition. Because URANS simulations require significant computational power, a special strategy is adopted to compute the flow field at different AOAs. First, computations with only one blade passage and a mixing-plane at the intake-fan interface are conducted for each AOA. Then, the mixing-plane solution in the blade channel is duplicated around the annulus, and the full

annulus unsteady simulations are carried-out in three steps. Five complete rotations with only ten time steps per blade passing period are first conducted, to provide an approximate solution, followed by three complete rotations with sixty time steps per blade passing period. Finally, a last complete rotation is performed with the same time step, during which the flow is averaged in time. This simulation process allows to run all the URANS computations in parallel. Alternatively, if the computations were chained as the AOA is increased, a lot of rotations would be required for the free-stream flow to reach the air intake from external boundaries. However, one potential limitation of this computational method is that some hysteresis may appear if flow separation occurs in the mixing plane computation that would not have occurred in the full annulus unsteady simulation. This highlights another key advantage of the body force method over unsteady approaches, as it allows to carry out the computations sequentially with increasing AOA.

### 3.2.1 Upstream influence: flow field in the air intake

In short intake configurations, the distortion that results from the nacelle angle of attack is not completely removed before the flow reaches the fan face. In particular, the axial velocity is not uniform around the annulus and residual vertical velocity components create regions of co and counter swirl. As a consequence, some redistribution occurs upstream of the fan, which modifies the flow distributions in the air intake and alters the aerodynamics of the intake lips.

#### Flow near the inlet throat

Contours of Mach number in an axial plane near the inlet throat are shown for the intermediate and short intakes in figure 3.4. Although there is almost no difference between power-off and powered computations on the intermediate intake, significant discrepancies are visible on the short intake geometry. Regions of low and high Mach number are circumferentially shifted in the direction opposite to the fan rotation. Furthermore, it can be observed that the minimum Mach number is lower in power-off computations, which is a first indication that the fan reduces the flow velocity distortion in the air intake. These effects are present in URANS computations and well reproduced by both body force models.

The circumferential evolution of the isentropic Mach number on the inlet lips at the same axial location is shown in figure 3.5. The fan reduces the peak-to-peak variations of Mach number on the short intake lips, which is well captured in body force computations. This is another indication that the flow velocity distortion in the air intake is reduced when the fan effect is taken into account. There is almost no effect on the intermediate air intake, and, although this is not shown here, no effect on the long inlet. Finally, the axial evolution of the static pressure on the inner part of the lower intake lip is shown in figure 3.6. The normal shock that appears on the lower lip at high AOA moves upstream when the fan effect is taken into account, and the overspeed is reduced. As a consequence, the shock strength is also reduced, resulting in lower shock losses. The new position and strength of the shock are well captured by the lift/drag and Hall's models.

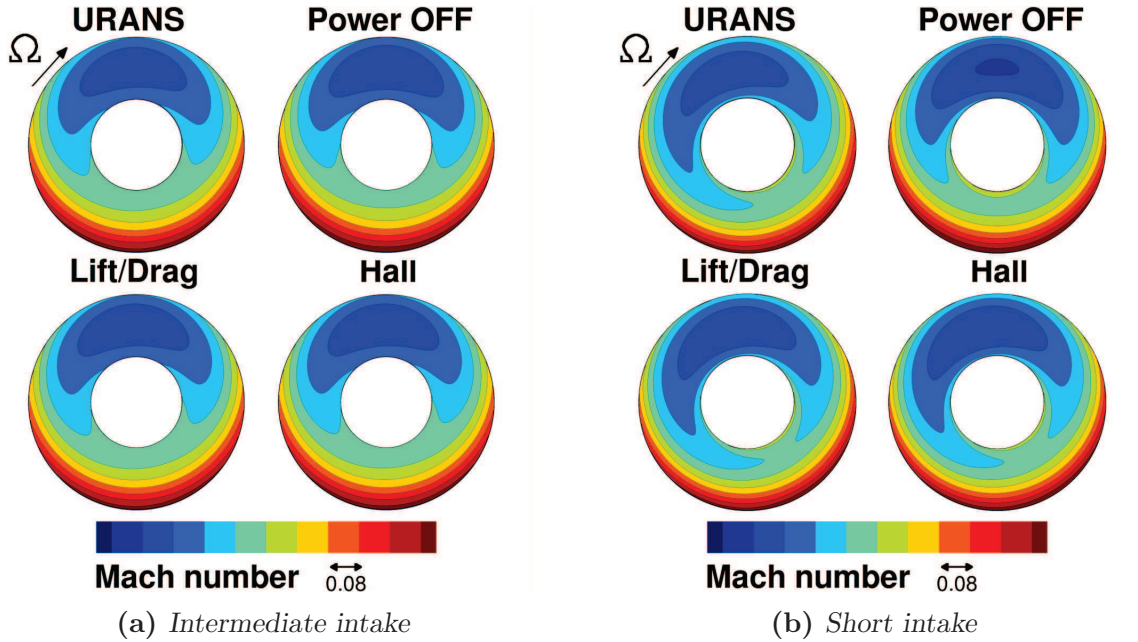


**Figure 3.4:** Contours of Mach number in a plane near the inlet throat.  $AOA_{stall}^{P/O} - 1^\circ$ . The fan-distortion interactions lead to flow redistribution inside the air intake.

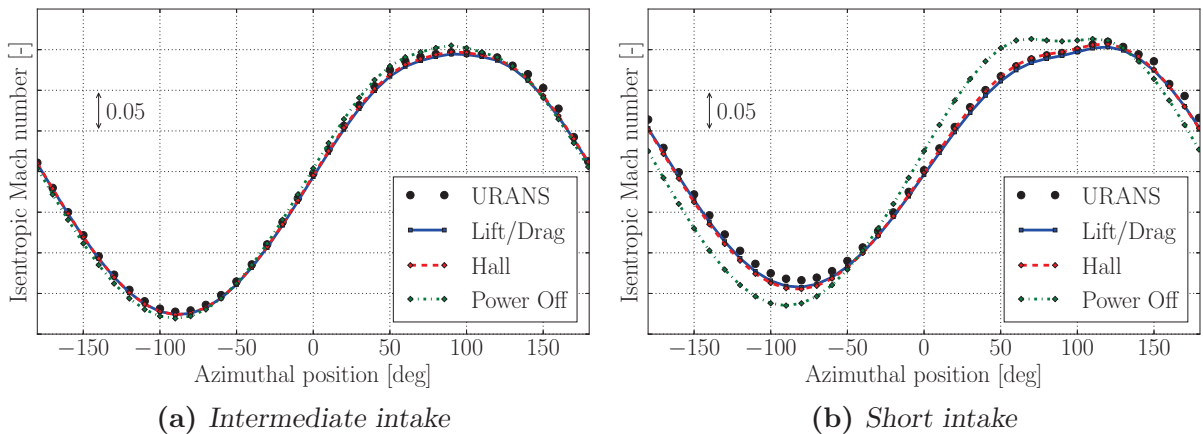


**Figure 3.5:** Circumferential evolution of the isentropic Mach number on the inlet lips, near the inlet throat.  $AOA_{stall}^{P/O} - 1^\circ$ . The static pressure distributions on the intake lips are altered by the fan on the short intake, which is well captured by the BF models.

Flow at the fan face

Contours of Mach number at the fan face are shown in figure 3.7. The redistribution upstream of the fan is visible for both the short and intermediate intakes, although the residual distortion is lower for the latter. The Mach number distortion is slightly attenuated by the fan, which is qualitatively captured by the body force models. The circumferential evolution of absolute and relative Mach numbers and flow angles at mid-span on the short intake are shown in figure 3.8. The relative flow angle is taken relatively to the circumferentially

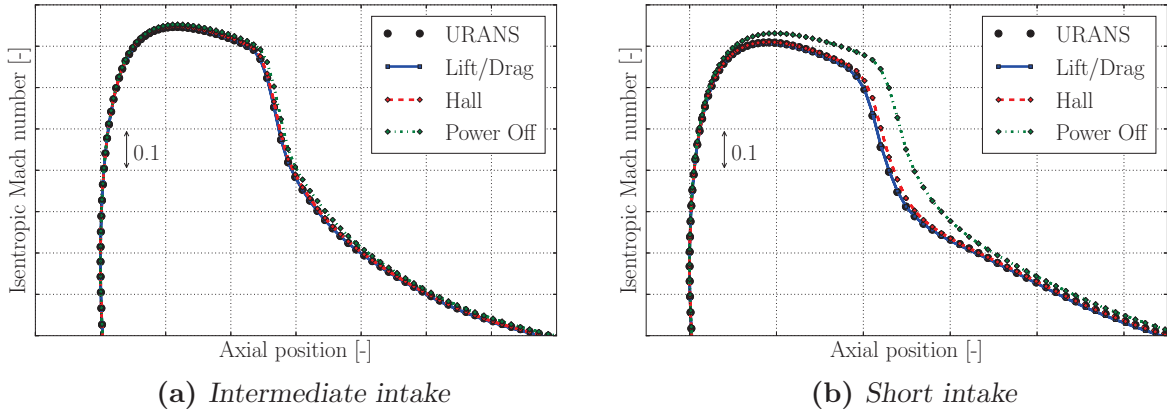


**Figure 3.6:** Axial evolution of isentropic Mach number on the lower lip.  $AOA_{stall}^{P/O} - 1^\circ$ . The position of the shock is moved upstream and its strength reduced in powered computations.

averaged relative flow angle in the URANS blade computation. The circumferential shift due to the fan effect is well visible on these figures. The fan reduces the peak to peak variations of absolute Mach number, but increases the variations of absolute swirl angle. This redistribution is beneficial for the fan, since the variations of relative flow angle are significantly decreased in powered computations. This effect is well captured in the body force computations, which confirms the ability of the models to reproduce the upstream influence of the fan on the intake flow. The upstream influence of the fan is similarly captured on the intermediate and long air intakes, although the peak to peak variations are smaller.

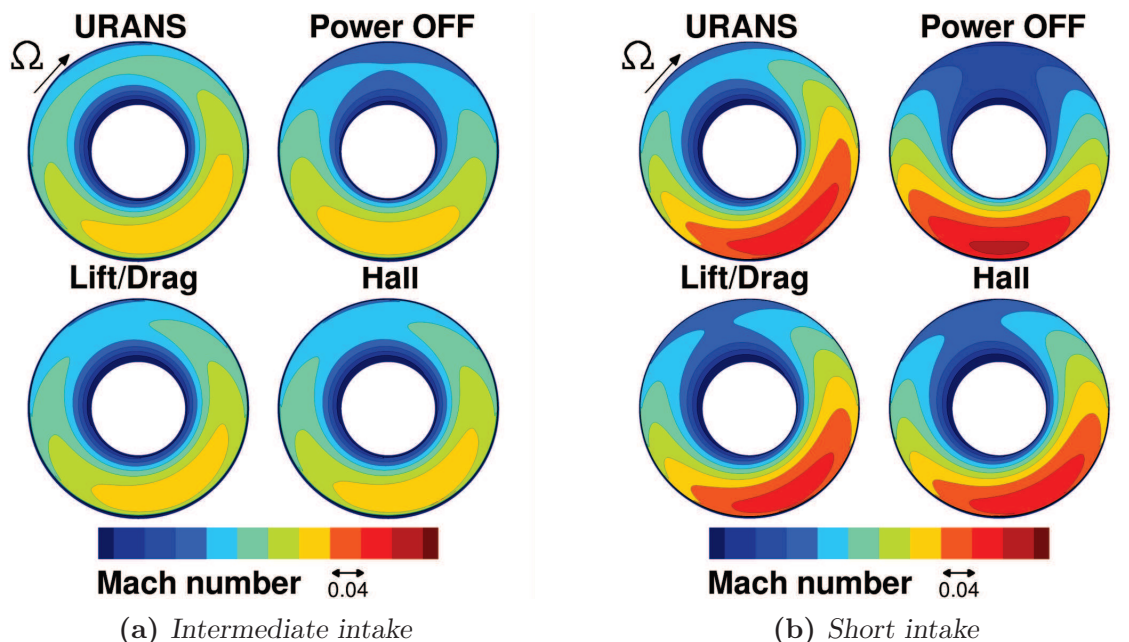


**Figure 3.7:** Contours of Mach number in a plane at the fan face.  $AOA_{stall}^{P/O} - 1^\circ$ . The flow redistribution due to the fan upstream influence is well captured in BF computations.

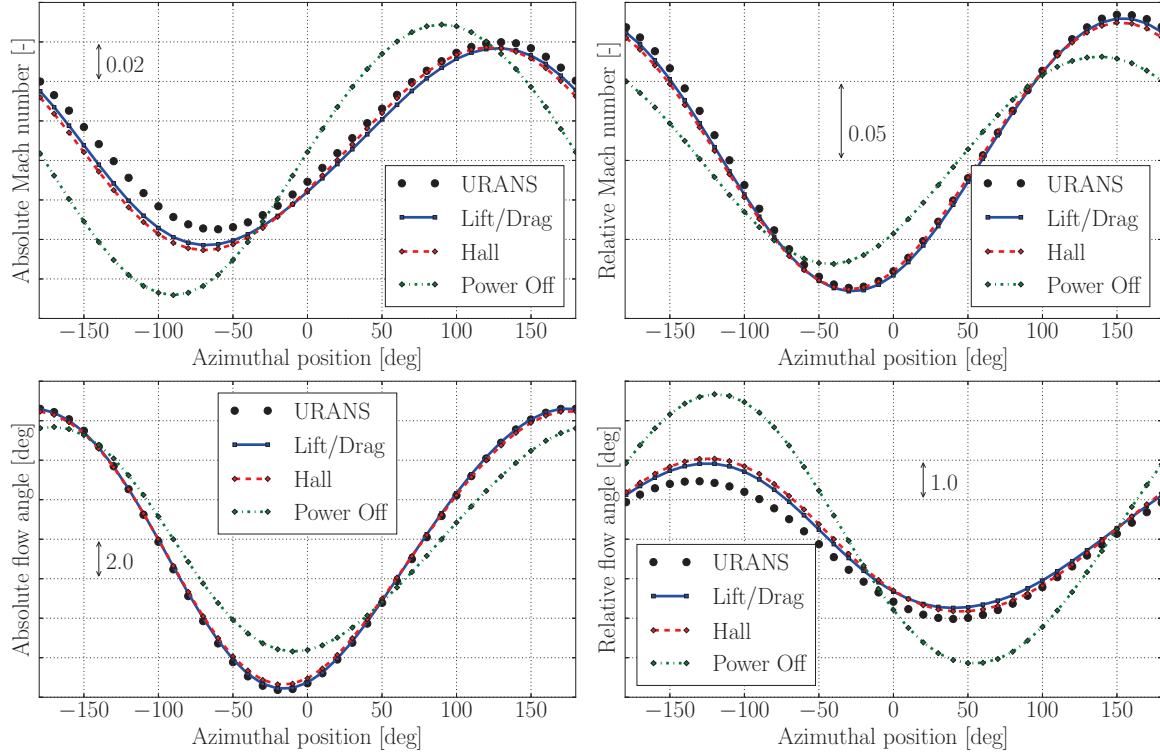


**Figure 3.8:** Circumferential evolution of absolute and relative Mach numbers and flow angles at mid-span at the fan face (short intake).  $AOA_{stall}^{P/O} = 1^\circ$ . The peak-to-peak variations in the relative frame are attenuated by the fan, which is well captured in BF computations.

### 3.2.2 Upstream influence: effect of the fan on inlet flow separation

As explained in chapter 1, the air intake has to be resilient to flow separation in the entire flight envelope of the aircraft. Determining the AOA at which flow separation occurs on the inlet lips is thus especially important. One way to distinguish attached points from separated points is to plot the circumferential distortion index (IDC) at the fan face, defined in equation (1.2), against the AOA. When flow separation occurs, the IDC criteria increases suddenly, which is shown in figure 3.9 for the three intake geometries. The AOA is taken relative to the P/O last attached angle of attack to highlight the beneficial effect of the fan on the occurrence of flow separation. URANS and body force simulations yield the same result: when the fan effect is taken into account, flow separation is delayed by  $0.5^\circ$  in the intermediate air intake and by  $1.5^\circ$  in the short intake. There is no visible effect on the long intake. The body force models capture this effect, in agreement with URANS computations.

Contours of Mach number around the short intake lip and at the fan face for the first AOA for which the intake is stalled in P/O computations are shown in figure 3.10. When the fan effect is taken into account, the boundary layer thickens downstream of the shock on the lower lip, but remains attached thanks to the fan suction. Distributions of isentropic Mach number on the short intake lip are shown in figure 3.11. Because of the flow separation in the power-off computation, the shock moves upstream and its strength is significantly reduced.

The same analysis is now conducted for the first AOA for which the intake is separated

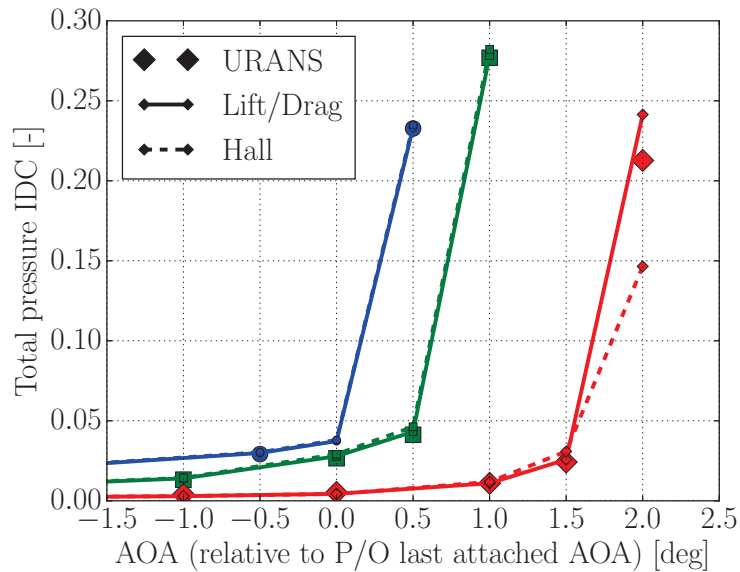


**Figure 3.9:** Circumferential distortion index at the fan face versus air intake AOA for the long (blue), intermediate (green) and short (red) intake. The onset of separation is delayed by  $0.5^\circ$  on the intermediate intake and  $1.5^\circ$  on the short intake in powered computations.

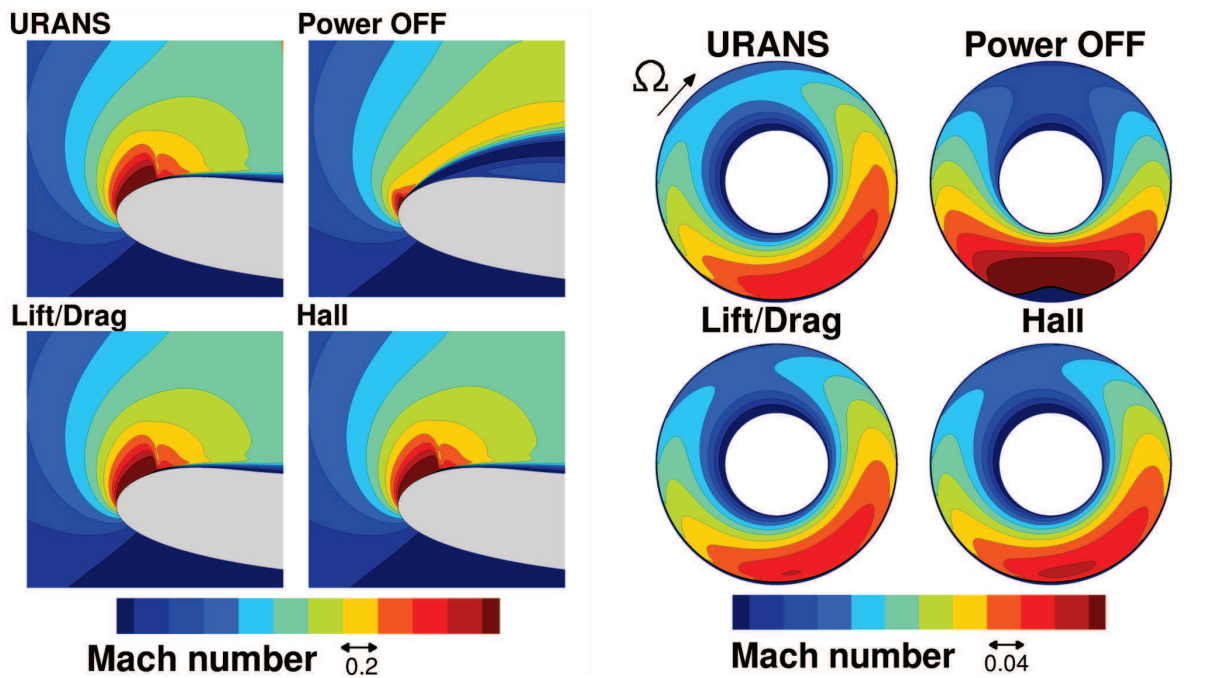


**Figure 3.10:** Contours of Mach number on the lower lip (left) and at the fan face (right) on the short intake.  $AOA_{stall}^{P/O}$ . The flow is separated in the power-off computation but remains attached in URANS and BF computations.

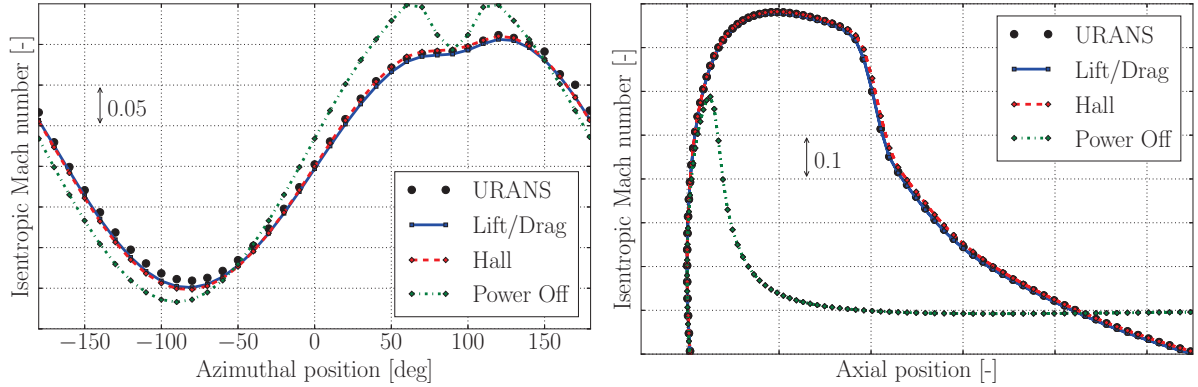


**Figure 3.11:** Circumferential distribution of isentropic Mach number on the short intake lips (left) and axial evolution of isentropic Mach number on the lower lip (right).  $AOA_{stall}^{P/O}$ .

in URANS computations. As shown in figure 3.12, the fan suction decreases the size of the separated region, which is well captured by the lift/drag model, but overestimated by Hall's model. This is the reason for the offset in IDC after flow separation has occurred, which can be observed on the short intake with this model in figure 3.9. The positive effect of the fan on the distortion on the short intake can be quantified with the values taken by the total pressure IDC, with and without the fan effect. The IDC is decreased from 0.33 in the first stalled power-off computation to 0.21 in the first stalled URANS computation. The lift/drag and Hall's models predict values of 0.24 and 0.15 respectively, which is consistent with the previous observations and confirms that the reduction of the size of the stall region with Hall's model is overestimated.

Axial and circumferential distributions of static pressure on the intake lips are shown in figure 3.13. There is a good agreement between URANS and body force computations on the circumferential distribution of static pressure far from the stalled region. The lift/drag model captures well the position of the shock on the lower lip when the intake is stalled, but Hall's model fails to predict this position accurately. Because the amplitude of the stalled region is underestimated, the shock is stronger and the aerodynamics of the intake lip more similar to those before flow separation occurs. It should be noted that the convergence of the computation with Hall's model is poor when flow separation occurs in the air intake, so that it is difficult to evaluate whether these discrepancies are due to the model accuracy or simply to robustness issues.

The positive effect of the fan on the extent of flow separation is only significant on the short intake. Contours of Mach number at the fan face and on the lower lip for the long intake are shown in figure 3.14. The separated region, much larger on the long intake, is slightly attenuated but the total pressure IDC is the same in all cases. This suggests that a beneficial effect of the fan on the extent of the separated region is only present in short intake configurations.

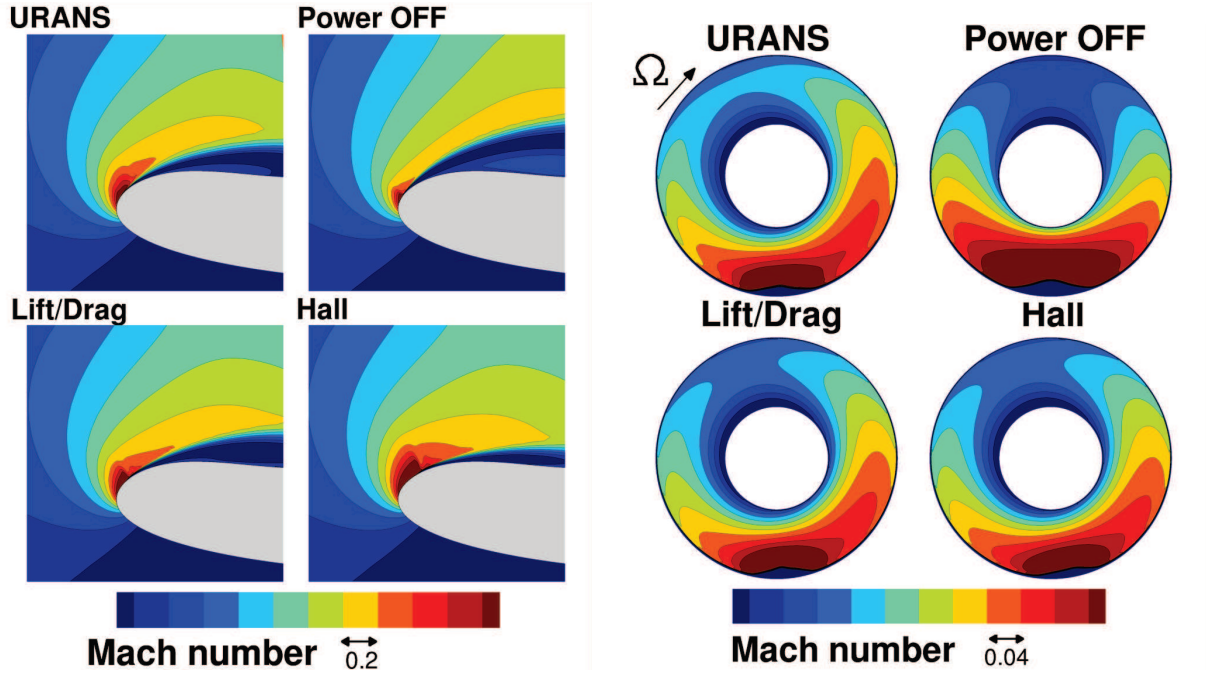


**Figure 3.12:** Contours of Mach number on the lower lip (left) and at the fan face (right) on the short intake.  $AOA_{stall}^{URANS}$ . The size of the separated region is reduced by the fan upstream influence, which is qualitatively captured by the BF models.

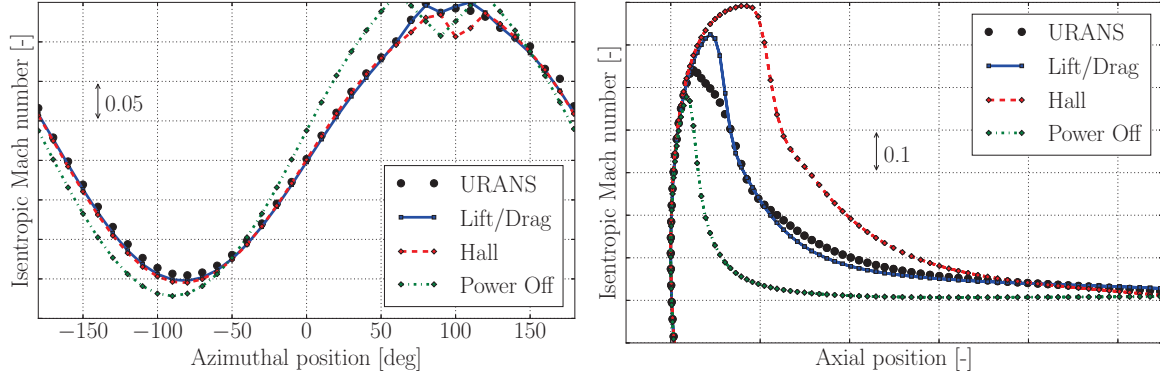


**Figure 3.13:** Circumferential distribution of isentropic Mach number on the short intake lips (left) and axial evolution of isentropic Mach number on the lower lip (right).  $AOA_{stall}^{URANS}$ . The beneficial effect of the fan on the separated region is overestimated by Hall's model.

### 3.2.3 In-plane-forces acting on the fan

In short intake configurations, the flow velocity distortion that results from external angles of attack is not completely suppressed before the flow reaches the fan face. As a consequence, the loading of the blades is not uniform around the annulus, which results in a non-zero force resultant in the plane orthogonal to the rotation axis. This non-zero force contributes to the suppression of the free-stream velocity vertical component across the blades, which

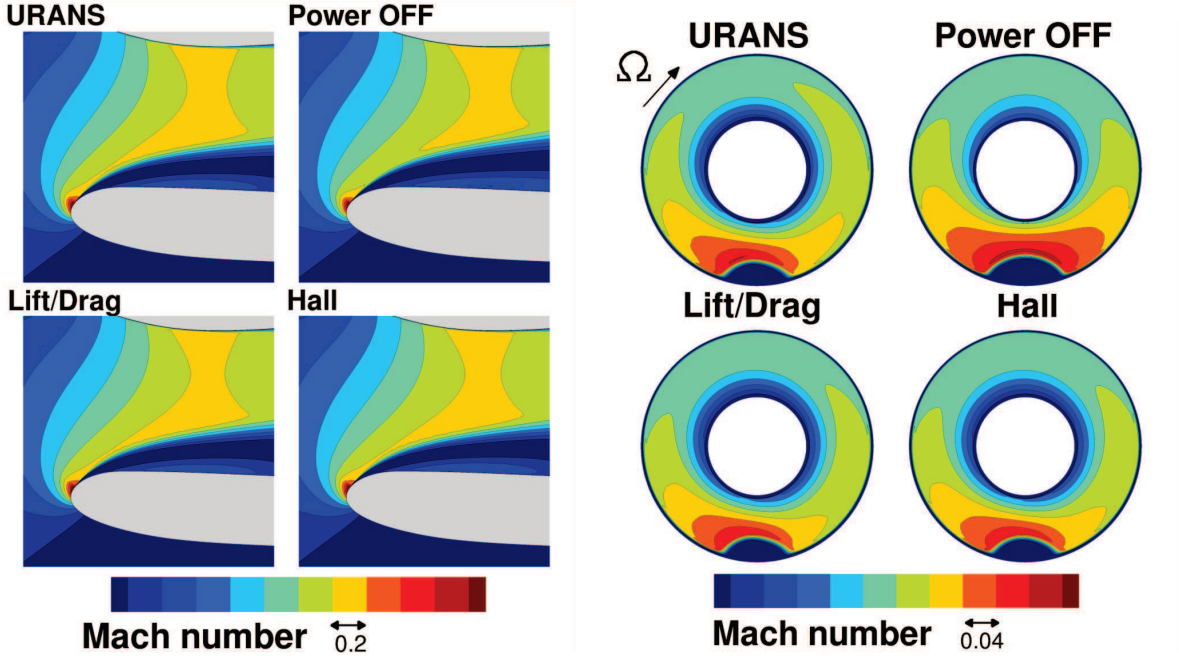


**Figure 3.14:** Contours of Mach number on the lower lip (left) and at the fan face (right) on the long intake.  $AOA = AOA_{stall}^{P/O}$ . The separated region is not affected by the fan.

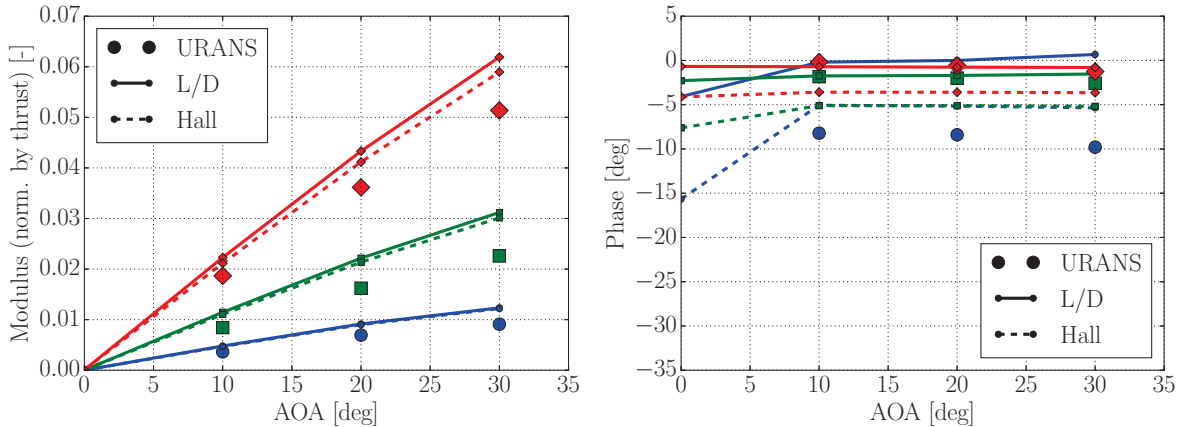


**Figure 3.15:** In-plane forces acting on the fan for the *short* (red), *intermediate* (green) and *long* (blue) intake. The phase is computed relatively to the external flow direction ( $0^\circ$  means that the force is vertical, i.e. aligned with the external flow). The magnitude of the force increases when the air intake is shorter, which is qualitatively captured by the BF models.

is completely done by the intake casing in long nacelle configurations. The modulus and phase of the IP forces acting on the fan blades are shown in figure 3.15. The phase is close to  $0^\circ$  relatively to the external flow direction, which indicates that the IP forces are almost vertical. The modulus of the force is higher in the short intake than in the long one, even at relatively low AOA. Both models qualitatively capture this effect, but with overestimated values for the modulus of the force.

### 3.2.4 Fan-OGV interactions

In all the results presented above, the OGVs are not included in the computational domain. The effect of the OGVs on the intake flow field and on IP forces is evaluated here for the short intake. The internal part of the nacelle was simply extended to allow the inclusion of the OGVs in the fan module. The OGVs geometry was directly included in URANS computations, and modeled in body force computations.

It was found that including the OGVs in the computational domain had no effect on the inlet flow field and on the operating range of the air intake. Flow separation occurs at the same AOA, with and without the OGVs. However, the inclusion of the OGVs slightly alters the magnitude and direction of the IP forces acting on the fan, as shown in figure 3.16. Similar results were obtained by François et al. [34], who showed that aerodynamic interactions between the front stage and the rear stage of a contra-rotating open rotor can alter the direction of IP forces on the front stage, without significant impact on the modulus. Although the impact of the OGVs on the modulus of the force is small, the phase is shifted by more than ten degrees. This effect is also present in body force simulations, but the impact on the modulus is not captured.

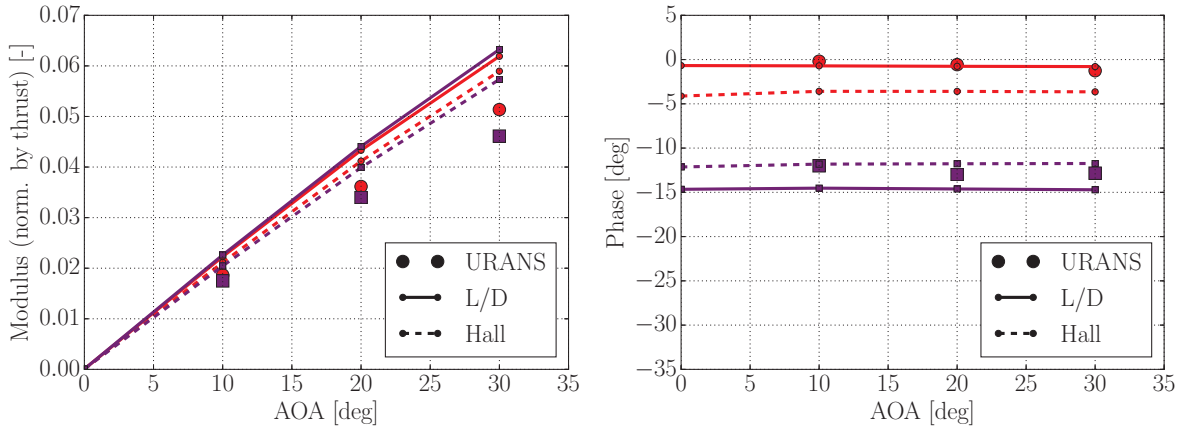


**Figure 3.16:** In-plane forces acting on the fan *with* (purple), and *without* (red) the OGVs. The phase of the force is shifted when the OGVs are included in the simulation.

### 3.2.5 Summary

The aerodynamic interactions between fan and air intake were explored on three intake geometries of varying length to validate the body force formulations proposed in chapter 1. In particular, the upstream influence of the fan on the flow field in the air intake and the effect of inlet distortion on IP forces were evaluated. It was found that the fan has a strong effect on the flow field in the short air intake at high angles of attacks. The presence of the fan modifies the aerodynamic behavior of the intake lips and reduces the circumferential peak-to-peak variations of the relative flow angle at the fan face, although the relative Mach number variations are increased. The fan also has a beneficial effect on the onset of separation, as it delays the angle of attack at which flow separation occurs. When flow separation occurs

in the air intake, the fan slightly decreases the extent of the separated region, and decreases the total pressure IDC at the fan face. These effects are well captured by the body force models, although Hall's model overestimates the beneficial effect of the fan on the extent of the separated region. In terms of robustness, it was also impossible to obtain properly converged results with this model after the occurrence of flow separation.

Finally, it was found that IP forces significantly increase on the short intake for non-zero angles of attack, which is qualitatively captured by the models. The OGVs were included in the computational domain, and it was found that fan-OGV interactions slightly alter the magnitude and direction of the IP forces acting on the fan. The body force models reproduce well the phase variations of IP forces but no effect on the magnitude is captured.

### 3.3 Inclusion of the bifurcation and exhaust in the computational domain

To evaluate the impact of the bifurcation on the inlet flow field, and to assess the distortion transfer through the fan stage, simulations of the complete bypass flow are conducted, using the short intake geometry presented in figure 3.3. This configuration is shown in figure 3.17. There is no lower bifurcation nor core inlet in the computational domain. The core exhaust is taken into account with injection conditions. The computational strategy for URANS computations is kept the same as in section 3.2, although more rotations of the fan are necessary to obtain a time-periodic flow field in the bypass, down to the exhaust. To limit the computational cost of the simulations that are carried out on this configuration, the mesh is coarser than for the intake-fan configurations presented in the previous section. The total mesh size is of about 100 million for the complete configuration, against 80 million for previous intake-fan computations. The body force approach is particularly beneficial for this type of computational domain, in which the convergence of the exhaust flow, including the jet, requires a lot of time steps in unsteady approaches.

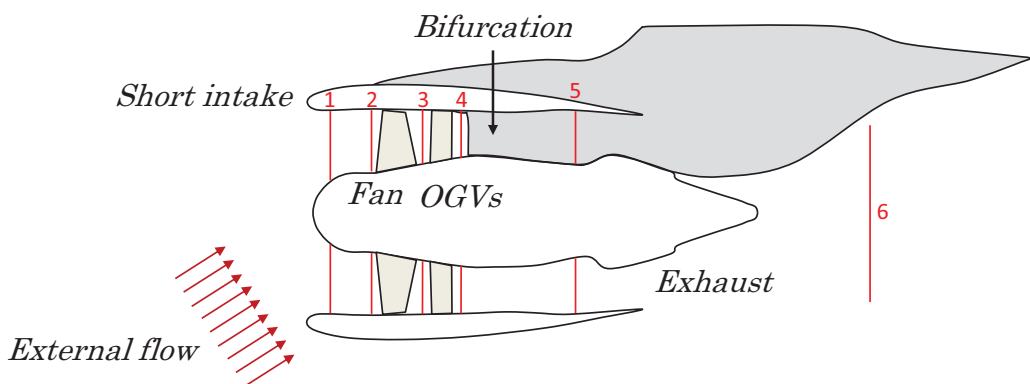


**Figure 3.17:** Sketch of the short intake configuration with fully simulated bypass flow.

### 3.3.1 Effect of the bifurcation on the intake flow field at max climb

In his PhD thesis, Peters [69] found that inlet non uniformities due to the bifurcation potential field were completely decoupled from those due to the external flow field. The main effect of the bifurcation was a local increase of the relative flow angle at the fan inlet. In the present case, the corrected speed of the fan is higher and the fan stage is partially choked: the flow field in the air intake is almost not affected by the bifurcation and the circumferential distributions of relative flow angle at the fan face agree within  $0.5^\circ$ , with and without the bifurcation. The distributions of static pressure on the intake lips are slightly modified when the bifurcation is included, but the effect is small, and can partially be imputed to the modification of the mesh on this configuration. This effect is shown in figure 3.18a.

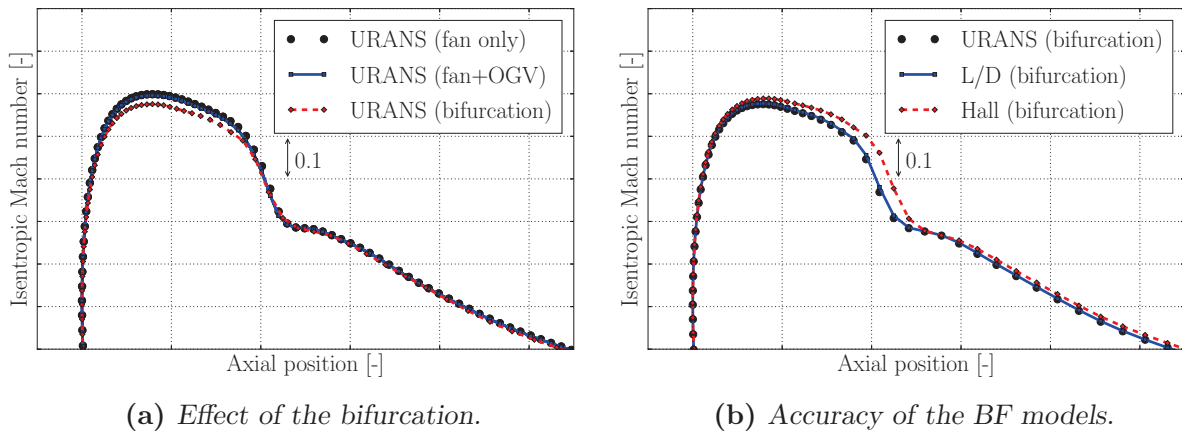


**Figure 3.18:** Axial evolution of the isentropic Mach number on the lower lip. Effect of the bifurcation on the flow field (a) and ability of the models to capture this effect (b).  $AOA = 30^\circ$ .

An indirect consequence of including the entire bypass flow, including the exhaust, in the computational domain is that the mass flow rate in the air intake can not be imposed in the simulation. In the present case, the exhaust is not choked, and the mass flow rate is therefore a result of an equilibrium between work input, losses, and choke mass flow rate in the fan. Underestimated losses at the tip of the rotor blades with Hall's model lead to overestimated mass flow rate, as shown in figure 3.19. Although both body force models capture well the effect of increased angle of attack on the mass flow rate, there is a constant offset of about 0.5% between the mass flow rate predicted with Hall's model and the one in URANS computations. This has a small impact on the intake flow field, and in particular on the distributions of static pressure on the intake lips, as shown in figure 3.18b. The overspeed is higher with Hall's model and as a consequence the shock on the lower intake lip is stronger.

Flow separation occurs at the same AOA as in the simple short intake-fan configuration tested in the previous section, both in URANS computations and with the lift/drag model. However, because the mass flow rate is higher with Hall's model, flow separation occurs  $0.5^\circ$  earlier than with the two other approaches. This highlights the necessity to correctly capture the choke mass flow rate of the fan that is simulated.

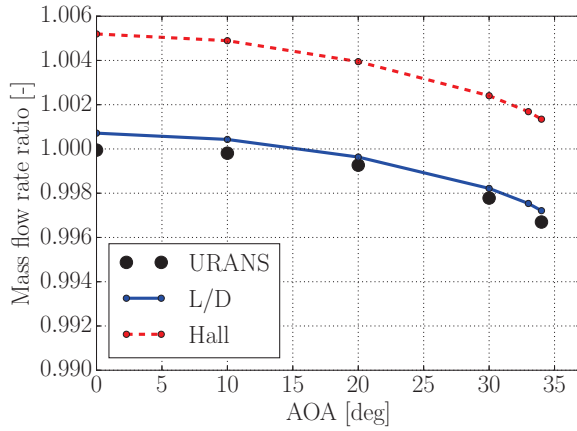


**Figure 3.19:** Effect of increased AOA on the mass flow rate in the air intake with fully simulated bypass flow. The mass flow rate is normalized by the mass flow rate predicted in URANS computations at 0° AOA.

### 3.3.2 Effect of the bifurcation on IP forces

The modulus and phase of IP forces acting on the rotor when the bifurcation is included in the computational domain are shown in figure 3.20. The bifurcation has an important effect on both the modulus and the phase of the forces. In particular, the bifurcation induces non zero IP forces even at zero angle of attack, which is due to the local shift in operating conditions because of the bifurcation potential field. The body force models qualitatively capture the phase and modulus of IP forces that are due to the bifurcation, but they underestimate its effect on the modulus of the forces.

Even if the forces acting on the OGVs in the plane orthogonal to the rotation axis are not as important as those acting on the rotor in terms of structural design, it is nevertheless interesting to evaluate the ability of the body force approach to capture them. As shown in figure 3.21, the forces acting on the OGVs are also very sensitive to the bifurcation. The offset of IP forces on the OGVs when the bifurcation is taken into account is due to the local shift of the fan operating point because of the bifurcation potential field, which induces a region of higher tangential velocities and thus higher turning in the corresponding region of the OGVs. A significant impact on the phase is predicted in URANS computations, which is not captured by the body force models.

### 3.3.3 Distortion transfer in the bypass flow

As explained in section 3.3.1, including the bifurcation does not significantly impact the inlet flow field at high AOA, and Mach number and flow angle distributions at the fan face are consistent with those already shown in figures 3.7 and 3.8. Contours of Mach number and stagnation pressure downstream of the OGVs are shown in figure 3.22. The effect of the bifurcation is well visible, as it induces a region of lower velocities and thus higher static pressure. As a consequence, the operating point of the fan is locally shifted toward higher pressure ratios. The region of the flow where the work input is higher is then convected

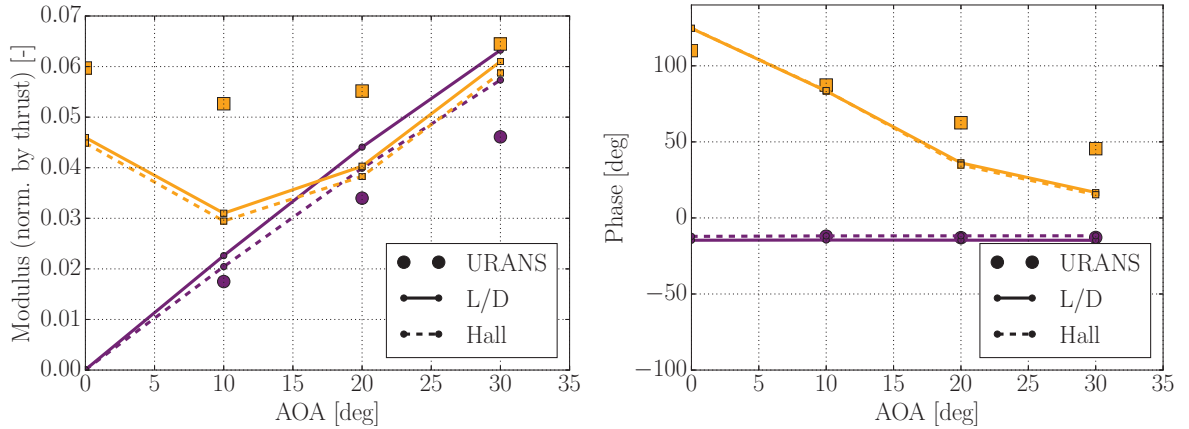


**Figure 3.20:** In-plane forces acting on the fan with (orange), and without (purple) the bifurcation (OGVs included in both cases).

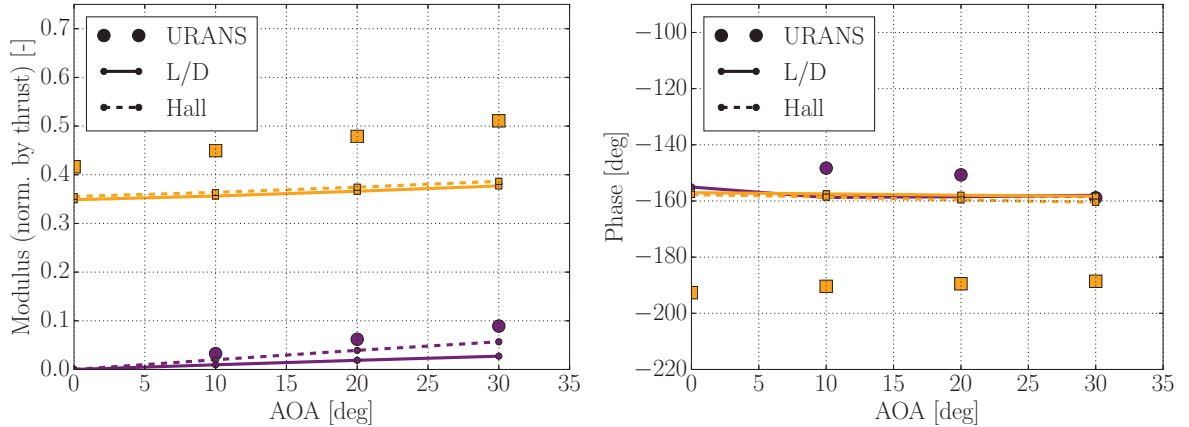


**Figure 3.21:** In-plane forces acting on the OGVs with (orange), and without (purple) the bifurcation. The modulus is normalized by the thrust acting on the OGVs.

by the fan rotation. This effect is combined to the relative flow angle distortion at the fan face, which explains the general asymmetry between the left part and the right part of the annulus.

The circumferential evolution of Mach number and stagnation pressure at 75% span is shown in figure 3.23. A spatial moving average is applied to URANS results to remove blade to blade variations induced by the OGVs wakes. The models capture well the effect of the bifurcation on the stagnation pressure rise and the general asymmetry of the flow. However, the lift/drag model does not capture well the stagnation pressure peak position. This circumferential shift of the maximum stagnation pressure location is already visible between the fan and the OGVs, and could be due to different reasons:

- In URANS computations, the flow is turned past the axial direction in the OGVs, in the region close to the bifurcation. As a consequence, the stagnation point is not located right at the leading edge of the bifurcation, which slightly shifts the bifurcation potential field toward lower azimuthal positions.

- The steady assumption in the present body force implementation may also have an impact on the results. In body force computations, the force field instantaneously responds to flow field variations, whereas in URANS computations, there is some time-lag between operating conditions variations and blade response. In particular, when the blades cross the bifurcation potential field, there is some delay before the flow field in the corresponding blade passages is altered and the consequent increase in stagnation pressure occurs. This assumption is consistent with the fact that the stagnation pressure peak is visible at a lower azimuthal position in URANS computations.

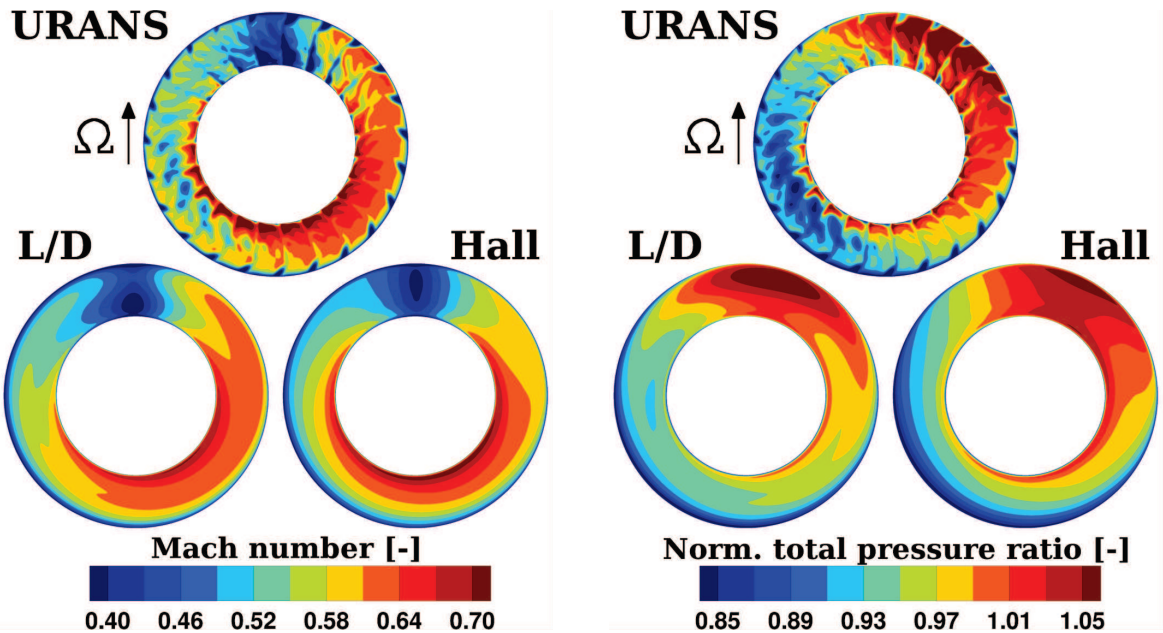


**Figure 3.22:** Contours of Mach number and stagnation pressure downstream of the OGVs (station 4).  $AOA_{stall}^{URANS} = 1^\circ$ . Distortion transfer is qualitatively captured by the models.

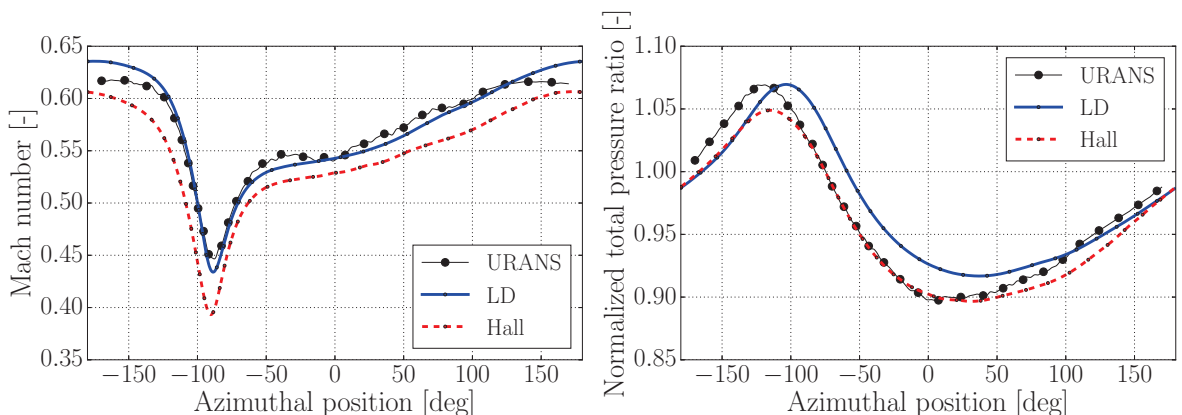


**Figure 3.23:** Circumferential distributions of Mach number and stagnation pressure at 75% span, downstream of the OGVs (station 4).  $AOA_{stall}^{URANS} = 1^\circ$ .

The same analysis is conducted for an operating point in which flow separation has occurred in the air intake. Contours of entropy at the fan face and work coefficient downstream of the rotor are shown in figure 3.24. Flow separation occurs at the same AOA in URANS and lift/drag computations, and half a degree earlier with Hall's model. However, flow separation does not occur at the exact same location in URANS and body force computations, which was not observed when the bifurcation was not included in the computational domain. Downstream of the fan, the stalled region results in locally higher work coefficients. The circumferential position of this region of increased work coefficient is not the same in URANS and body force computations, due to the initial circumferential shift of the stalled region.

Contours of Mach number and stagnation pressure ratio downstream of the OGVs are shown in figure 3.25. The inlet distortion due to flow separation is well attenuated and only a small perturbation of Mach number / stagnation pressure remains. Circumferential distributions of both quantities at 75% span are shown in figure 3.26. The lift/drag model captures well the qualitative effect of the stalled region on the distributions of Mach number and stagnation pressure downstream of the fan stage, however with the same tangential shift as before. With Hall's model, the amplitude of the stalled region is underestimated, resulting in almost no visible perturbations of the flow field downstream of the fan.

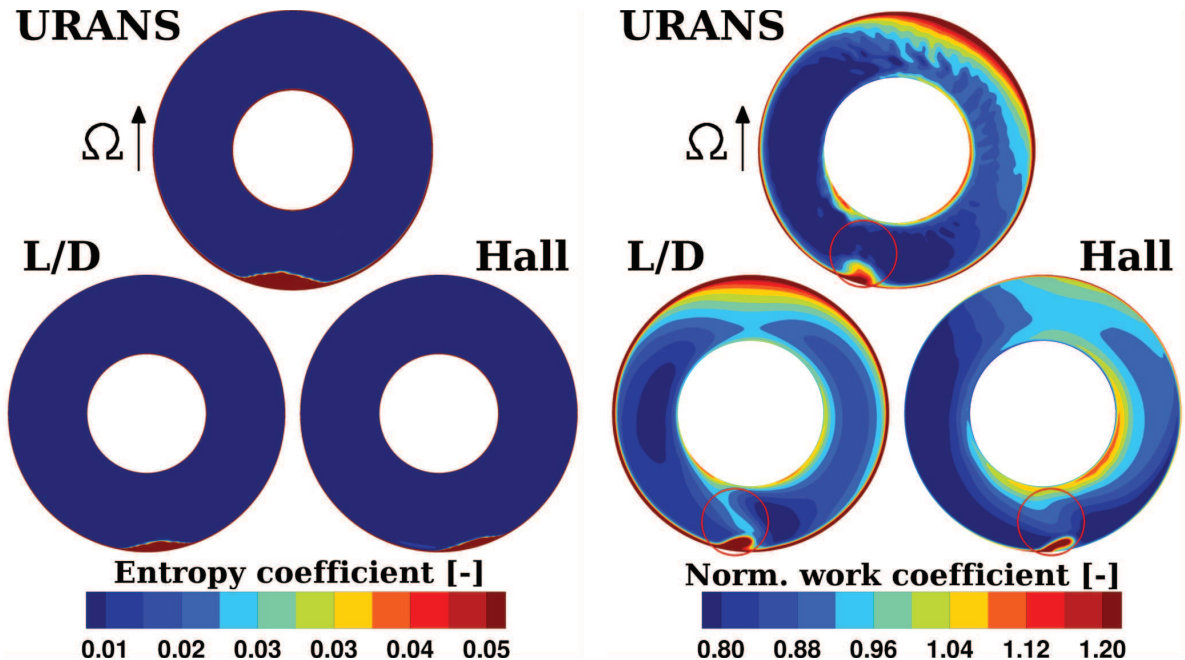


**Figure 3.24:** Contours of entropy at the fan face and work coefficient downstream of the fan rotor (station 3).  $AOA_{stall}^{URANS}$ . The location and amplitude of flow separation varies slightly between URANS and BF computations, but the impact on the work coefficient downstream of the rotor is well captured.

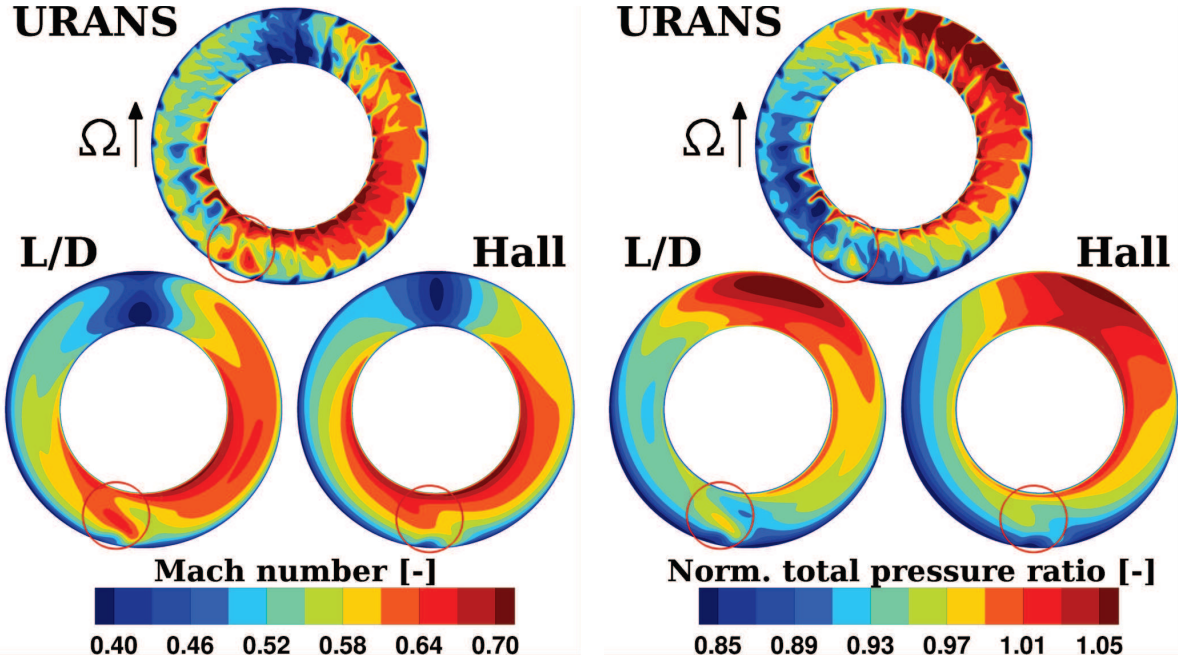


**Figure 3.25:** Contours of Mach number and stagnation pressure downstream of the OGVs (station 4).  $AOA_{stall}^{URANS}$ . The stagnation pressure distortion is attenuated by the fan.

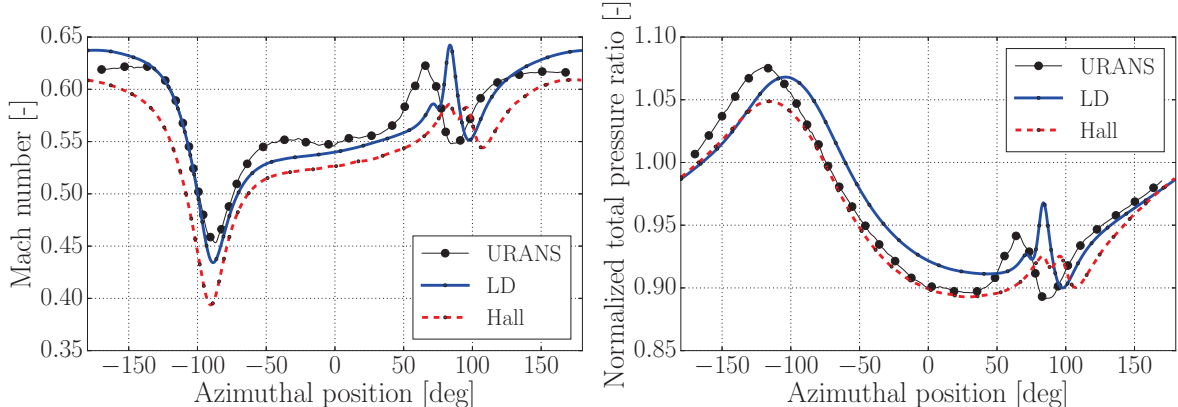


**Figure 3.26:** Circumferential distributions of Mach number and stagnation pressure at 75% span, downstream of the OGVs (station 4).  $AOA_{stall}^{URANS}$ .

### 3.4 Experimental validation

In the frame of research on UHBR engines, wind tunnel tests were conducted by Airbus to experimentally evaluate fan-airframe interactions at high AOA, and in particular to quantify the beneficial effect of the fan on flow separation on short intake configurations. The TPS presented at the beginning of this chapter was used as a test case. To supply power to the fan, a turbine is supplied through the pylon with high pressure flow, and there is thus no core inlet downstream of the fan, as was already shown in figure 3.17. The experimental setup is shown in figure 3.27a.

The TPS was operated with the three axisymmetric air intakes already shown in figure 3.3, which were used in section 3.2 to highlight the impact of inlet length on intake-fan interactions. However, these experiments did not allow to highlight a significant impact of the fan on the shorter air intake, and the last separation-free angle of attack was only increased by  $0.5^\circ$  in the best cases with the shorter intake, against the  $1.5^\circ$  that were found numerically in section 3.2.2. Additional numerical investigations were thus conducted to understand this discrepancy between experimental and numerical results. Here are the main differences between the computations presented in section 3.2.2 and the experiments:

- All the computations presented in that section were conducted without the OGVs and the bifurcation.
- The experiments were in fact conducted with side-slip angles (external flow coming laterally and not vertically), as shown in figure 3.27b.
- The wind tunnel lateral walls were not included in the computational domain.



(a) Photo of the test bench.

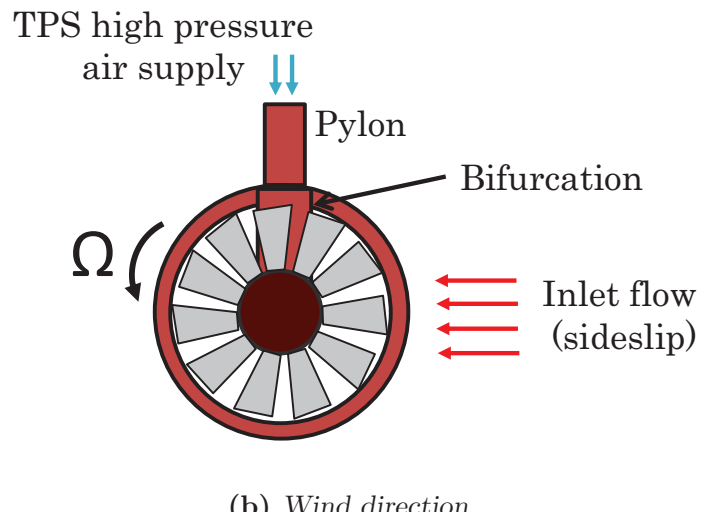
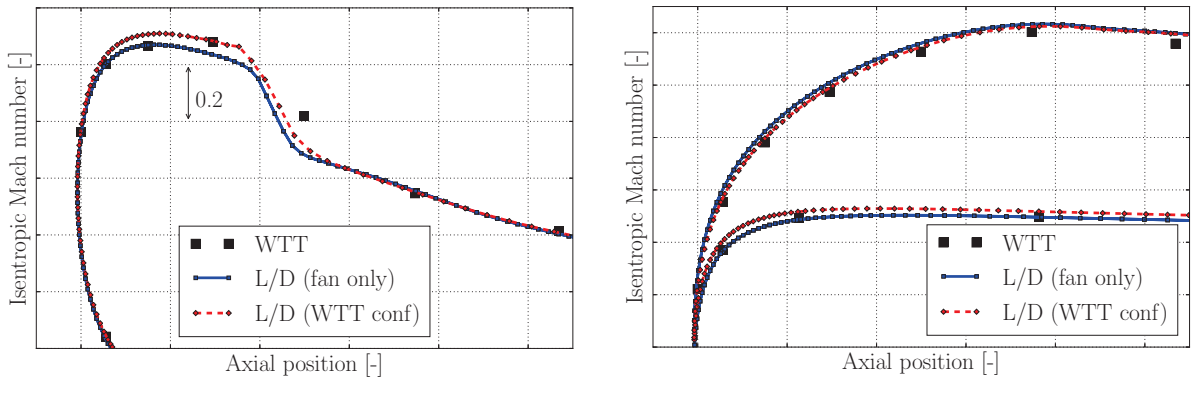


**Figure 3.27:** Experimental setup for the simulation of fan-intake interactions at high AOA.

In the previous section, it was shown that the impact of OGVs and bifurcation on the intake flow field at high angles of attack is not significant, and flow separation occurs at the same angle of attack. However, in the experimental configuration, because the flow field impacts the nacelle from the port side, new interactions may arise because of the interaction between intake, fan, and bifurcation. In particular the fan operates near choke close to the intake lip under the wind, then near stall when it crosses the bifurcation potential field. As a consequence, it is possible that the beneficial effect of the fan is reduced when the flow comes from that direction. URANS results were not available for the complete configuration with lateral wind, and this assumption is therefore assessed using the lift/drag model, whose accuracy was already confirmed in the previous sections.

### 3.4.1 Intake flow field with vertical wind against lateral wind

The evolution of isentropic Mach number on the lower/upper lips relatively to the wind direction is shown in figures 3.28a and 3.28b respectively. Data from the axisymmetric intake-fan computations is compared to data from the complete configuration with lateral wind and from WTT tests. In practice, the shape of the overspeed on the lower lip and the position of the shock are very sensitive to the laminar to turbulent transition. As a consequence, boundary layer trips were used in the experimental campaign to enable a direct comparison between experiments and fully turbulent CFD computations. The distributions of static pressure on the intake lips are slightly shifted on the complete configuration with lateral wind: the overspeed is higher in the complete configuration, resulting in a stronger shock downstream. This effect is rather small, but it brings the CFD results closer to the experimental ones, in terms of shock location and strength.

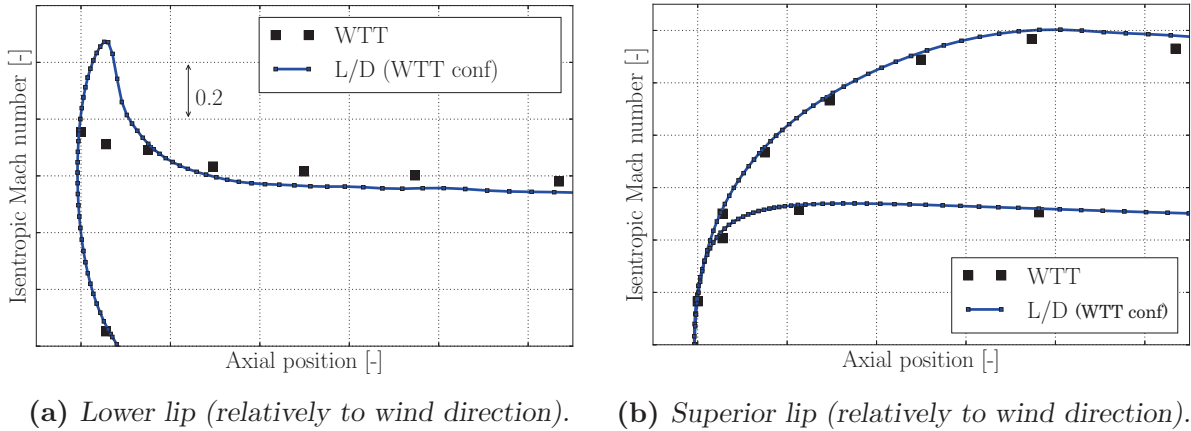


(a) Lower lip (relatively to wind direction). (b) Superior lip (relatively to wind direction).

**Figure 3.28:** Axial evolution of isentropic Mach number on the intake lips (last attached WTT AOA). Comparison between WTT and lift/drag computations.

Although these discrepancies are small, flow separation occurs  $2^\circ$  earlier in the complete configuration with lateral wind in lift/drag computations, whereas no effect of the bifurcation was found with vertical wind. This result suggests that an axisymmetric assumption is not valid to study the resilience of an air intake to flow separation. Although additional computations with the longer air intakes are required to confirm the link between the occurrence of inlet flow separation and the bifurcation, it is likely that this effect contributed to the results obtained during the WTT campaign.

A distribution of isentropic Mach number on the intake lips after flow separation has occurred is shown in figure 3.29. The amplitude of the stalled region seems more important in WTT than in the CFD, as the overspeed is almost completely absent in the former case. This is a limitation of the turbulence model employed in CFD computations (SA), which was already shown to underestimate the spatial extent of the stalled regions in air intake simulations [12]. Although simple turbulence models are in general accurate enough to predict the onset of separation, this experimental result suggests that more accurate turbulence models are needed to assess the interaction of the fan with the stalled region once flow separation has occurred.



(a) Lower lip (relatively to wind direction). (b) Superior lip (relatively to wind direction).

**Figure 3.29:** Axial evolution of isentropic Mach number on the intake lips (first separated AOA in lift/drag computations). Comparison between WTT and lift/drag computations.

### 3.4.2 Effect of bifurcation and flow separation on total pressure rise

During the wind tunnel tests, the TPS was equipped with total pressure rakes placed between the OGVs and the bifurcation, which allowed to evaluate the effect of non uniformities on the stagnation pressure distributions downstream of the fan stage. A comparison between body force computations and WTT results is shown in figure 3.30. Although the general agreement is not excellent, it can be noted that the effect of the bifurcation is well present in WTT. The stagnation pressure peak is located at a lower azimuthal location in the experiments than with the model, which is consistent with what was observed in URANS computations. However, the amplitude of this peak is significantly underestimated by the lift/drag model.

As was shown in the previous sections, after flow separation has occurred, the stalled region results in locally higher work input in the rotor and to a small perturbation of the stagnation pressure field downstream of the OGVs. This effect is well visible in WTT results, as it leads to a local decrease of the total pressure at  $\theta = 0^\circ$ . The model captures well this behavior, although the exact position of this peak may again not be well evaluated.

## 3.5 Summary and conclusions

The main objective of this chapter was to show that the body force modeling approach allows to capture intake-fan interactions on short nacelle configurations. The effect of the fan on the occurrence of flow separation at max climb operating conditions was evaluated for three intakes of varying length, and it was found that the lift/drag model and Hall's model reproduce the intake-fan coupling that is present in full annulus unsteady simulations. In particular, the models capture an increase of the separation-free AOA of  $1.5^\circ$  on the shortest air intake. Once flow separation has occurred, the models capture the beneficial effect of the fan on the spatial extent of the stalled region, although this effect is overestimated with Hall's model.

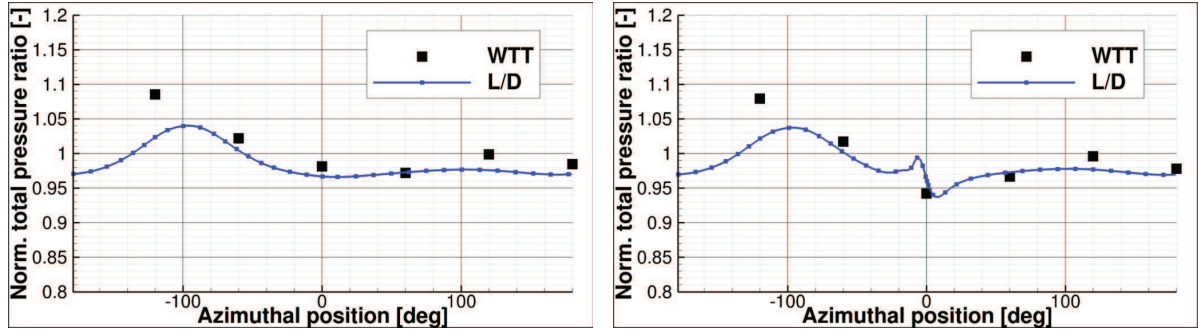


**Figure 3.30:** Circumferential evolution of stagnation pressure at 75% span downstream of the OGVs. Comparison between WTT and lift/drag computations.

As a second step, the impact of inlet non uniformities on IP forces was quantified, and it was found that IP forces increased significantly at high AOA on the short intake configuration. The OGVs and the bifurcation were then included in the computational domain, and it was shown that the effect of the latter is dominant at low AOA, but does not completely add up to the effect of inlet non uniformities at high AOA. The models qualitatively capture the effect of inlet non uniformities, OGVs, and bifurcation on the IP forces acting on the fan, but do not exactly resolve the magnitude and phase of the force.

Next, the ability of the models to capture distortion transfer in the bypass flow was evaluated on the short intake geometry. It was found that the effect of the bifurcation on the stagnation pressure distortion downstream of the fan stage is higher than the effect of the external flow AOA. In particular, the bifurcation locally leads to a significant increase of the stagnation pressure rise. The models do not capture the exact location of the stagnation pressure peak but they qualitatively capture the associated physics. When flow separation occurs, the low momentum region in the intake leads to increased work input, which attenuates the stagnation pressure distortion downstream of the fan stage.

Finally, these inlet–fan–bifurcation interaction features were explored experimentally, but the wind tunnel results did not allow to highlight a significant effect of the fan on flow separation. To understand these experimental results, CFD simulation of the experimental rig were carried-out, without complete success. Although simulating the experimental configuration with lateral wind allows to capture a small effect on the aerodynamic behavior of the intake lips, it is not enough to explain the discrepancies between the wind tunnel test results and the CFD results. Another possible explanation is that the wind tunnel lateral walls altered the intake lips aerodynamics, due to confinement effects. This possibility was not explored in the present work.

Although the preliminary CFD results obtained with this test case are encouraging, the mixed results that were obtained experimentally highlight the difficulty to take advantage of the beneficial effect of the fan on upstream distortion in practice. Further experimental and computational work is thus required to confirm this effect, on more realistic intake/fan geometries, and enable the practical implementation of short intake designs.

# Chapter 4

## Boundary layer ingestion

The purpose of this chapter is to validate the body force models on test-cases representative of BLI configurations. The lift/drag and Hall's models are first applied to the R4 fan stage, already described in chapter 2, with parametric non uniform inflow distributions. Then, the lift/drag model is applied to the “RAPRO” configuration, and used to assess the effect of BLI on the required power to achieve a given thrust. In particular, the link between the amount of ingested aircraft boundary layer and BLI benefits is quantified.

### 4.1 R4 fan stage response to BLI inlet distortion

The purpose of this section is to validate the aerodynamic response of the body force models in presence of stagnation pressure inlet distortion. In particular, the principal redistribution and distortion transfer mechanisms associated to BLI, presented in chapter 1, are highlighted and quantitatively validated against full annulus unsteady simulations. As a second step, the comparison between body force and full annulus simulations focuses on the impact of inlet distortion shape and intensity on IP forces and fan efficiency.

#### 4.1.1 Description of the test case and computational approach

The fan-distortion interaction study is conducted on the R4 fan stage at the nominal rotational speed (100% RPM). Body force results are compared to instantaneous and time averaged full annulus unsteady solutions, further denoted as *URANS computations*. The computational domain is shown in figure 4.1. The inlet domain, including the spinner, is the same in body force and URANS computations. A butterfly topology is used for the spinner, so that there is no singularity in the mesh on the rotation axis. The total number of mesh cells is of about 100 million for URANS against 22 million for body force computations. A slip-wall condition is used on the shroud to convect the inlet stagnation pressure distributions two chords upstream of the fan face.

The five parametric inflow distributions that are shown in figure 4.2 are used as inlet conditions for the fan stage. The vertically stratified distributions are defined using cubic velocity profiles and the wedge distributions are directly defined in terms of stagnation pressure, using bivariate gaussian functions. The characteristics of each distribution are

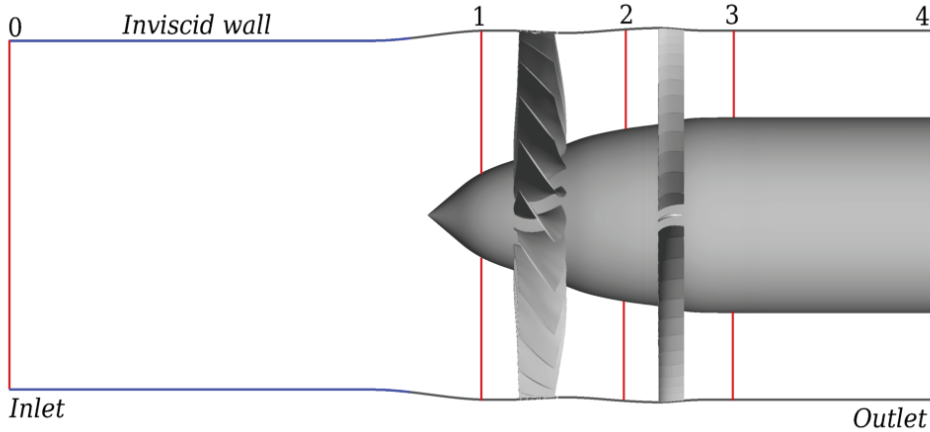


**Figure 4.1:** BLI computational domain for URANS computations.

given in table 4.1. The stagnation temperature is uniform and the inflow velocity is purely axial in all cases. The computations are carried-out for each inlet distribution at the design corrected mass flow rate, within a tolerance of 0.3%. The numerical settings and turbulence model are the same as in chapter 2 (implicit time integration, second order Roe scheme with a Van-Albada limiter, SA turbulence model). URANS computations are initialized from a mixing plane computation without distortion. Eight rotations of the fan (five with ten time steps per blade passing period and three with sixty time steps per blade passing period) are necessary to obtain a periodic solution, then the flow is time-averaged during a ninth rotation. The short length-scale wedge distribution, denoted “Wedge 1” (**W1**) and the long length-scale vertically stratified distribution denoted “Stratified 2” (**S2**) are first selected to conduct a detailed analysis of the flow field upstream and downstream of the fan.

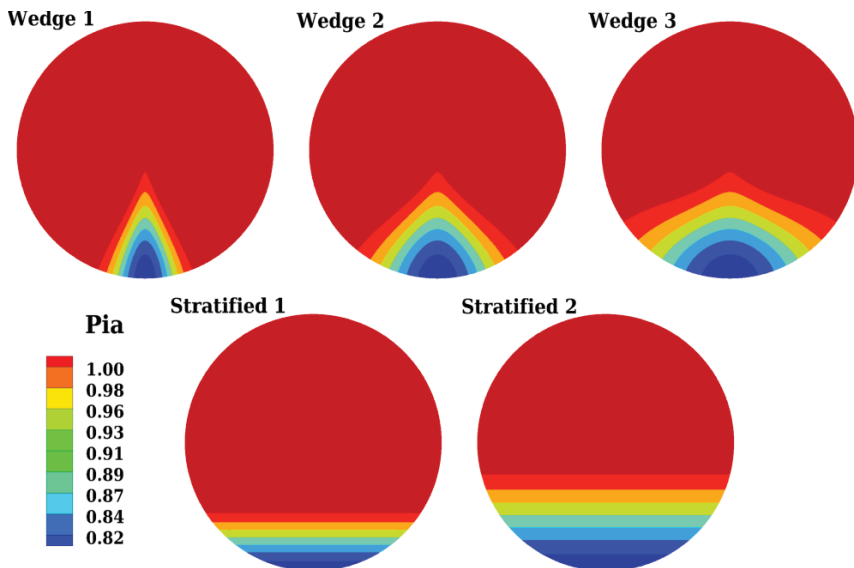


**Figure 4.2:** Parametric inlet distortion patterns: contours of absolute total pressure.

Distribution	Spatial extent	DC60
Wedge 1	40°	0.093
Wedge 2	80°	0.156
Wedge 3	120°	0.179
Strat. 1	30% height	0.112
Strat. 2	50% height	0.173

**Table 4.1:** Inlet distributions characteristics.

#### 4.1.2 Upstream redistribution and distortion transfer

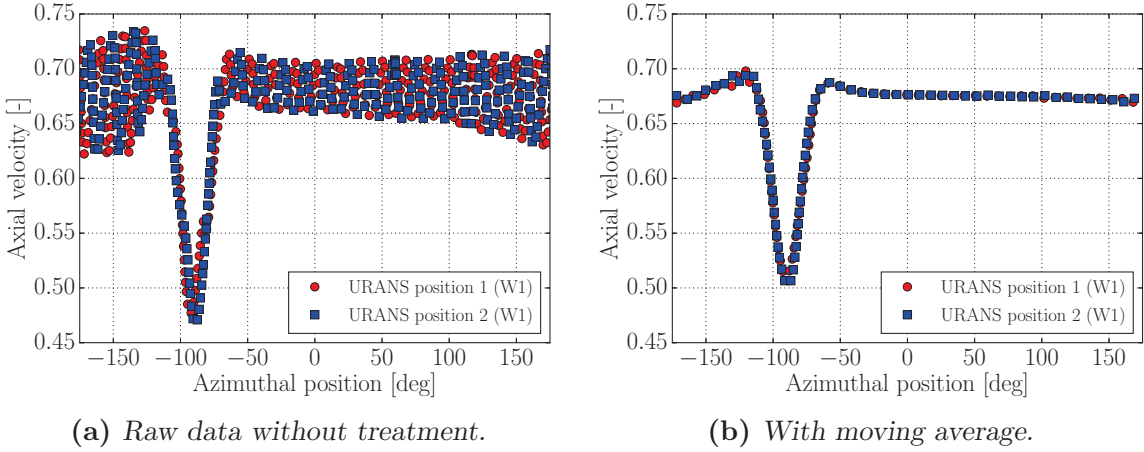
##### Body force models validation methodology

Body force computations are compared to URANS computations for the W1 and S2 inlet distributions. The comparison is based on 2D flow contours on planes orthogonal to the rotation axis extracted at the stations 1, 2 and 3, shown in figure 4.1, and circumferential profiles extracted at 25% and 75% span. Unfortunately, the sliding interface between the inlet domain and the rotor domain was located upstream of station 1, so that time-averaged flow fields could not be computed at this location. Although computing a time-averaged flow field in rotating domains is possible [32, 44], the necessary post-processing tools were not available at the time of this study. The comparison between both approaches at station 1 is thus made using an instantaneous flow solution for the unsteady cases, whereas the comparison at station 2 and 3 is made using time-averaged solutions.

To ease the analysis of circumferential profiles, a spatial moving average is applied to URANS instantaneous solutions at station 1. This treatment is applied over a length of one blade passage, which removes blade to blade variations due to the blades potential effect, as illustrated in figure 4.3. The moving average is shown for two different rotor positions, to ensure that it is not too sensitive to the position of the blades in the circumferential direction. Similar results are indeed obtained for both positions of the rotor, but the axial velocity peak is slightly attenuated in both cases. This is due to the short length scale of the distortion that is used for illustration (Wedge 1), of the order of one to two blade pitches: no attenuation is visible on longer length scale inlet distortions. The same treatment is applied at station 3 to time-averaged URANS results, to remove the blade to blade variations due to OGV wakes. At station 2, the rotor wakes are naturally eliminated during the time-averaging process, so that time averaged data can directly be used without any additional treatment.

The data extracted at each station is used to assess the ability of the body force models to capture all the fan-distortion interactions mechanisms, including upstream redistribution, non-uniform work input, and distortion transfer. Flow redistributions mechanisms are highlighted using distributions of radial and absolute swirl angle at station 1. Then, work input variations are quantified using distributions of work coefficient at station 2. Finally, the distortion transfer is discussed based on distributions of mass flux coefficient  $\Phi$ , defined in equation (4.1), and absolute total pressure, at stations 2 and 3 respectively.

$$\text{Mass flux coefficient: } \Phi = \frac{\rho V_x A_{ref}}{m_{ref}^*} \quad (4.1)$$



(a) Raw data without treatment.

(b) With moving average.

**Figure 4.3:** Effect of the moving average on circumferential profiles of axial velocity. The result does not depend on the position of the rotor blades, but sharp peaks are attenuated.

### Flow field upstream of the rotor (station 1)

The top-to-bottom redistribution occurring upstream of the rotor is illustrated in figure 4.4, where contours of radial flow angle are shown at station 1 for the W1 and S2 distortion cases. A lower static pressure is induced by the rotor in the regions of low-momentum flow, which leads to flow migration from the upper part of the annulus. As a consequence, radial flow angles are higher on the lower part of the annulus. As pointed out by Gunn and Hall [44], the redistribution is completely three dimensional. In particular, streamlines circulate around the spinner, creating regions of positive and negative swirl angle, as shown in figure 4.5. Both radial and swirl angles are well captured in body force computations, which confirms the ability of the models to reproduce the global features of the rotor upstream influence.

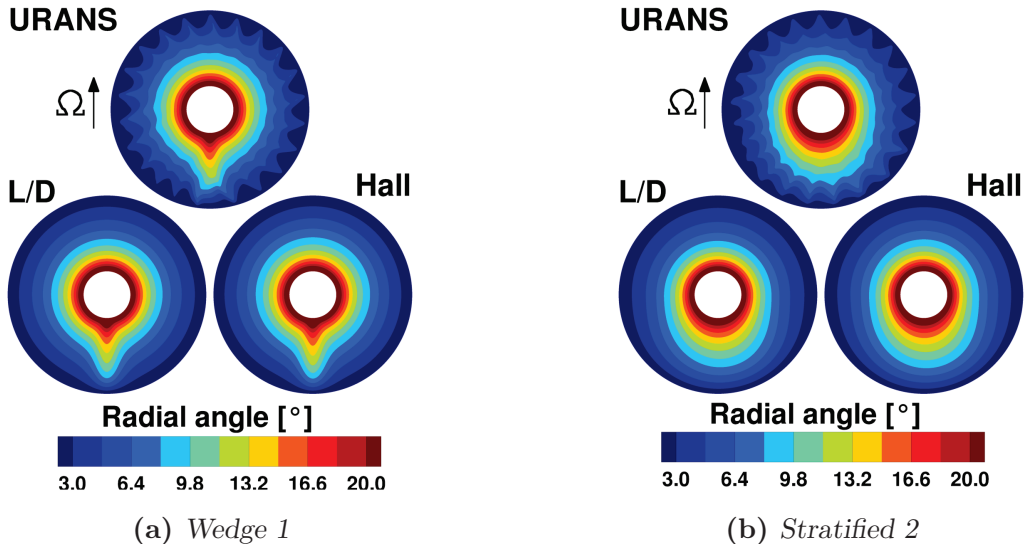


**Figure 4.4:** Contours of radial flow angle at the fan face (station 1). The radial redistribution of the flow upstream of the rotor is well captured by the BF models.

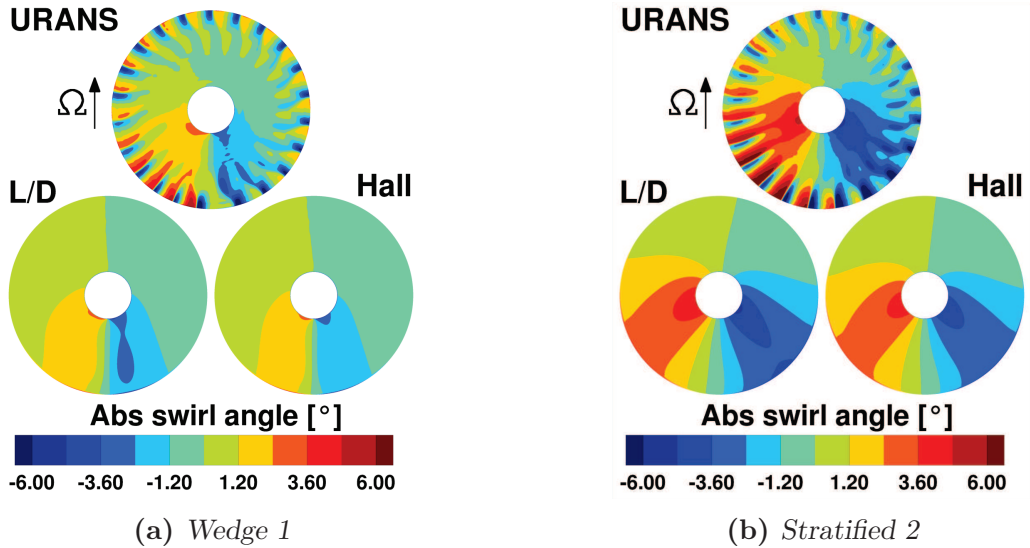


**Figure 4.5:** Contours of absolute swirl angle at the fan face (station 1). The top-to-bottom redistribution of the flow upstream of the rotor is well captured by the BF models.

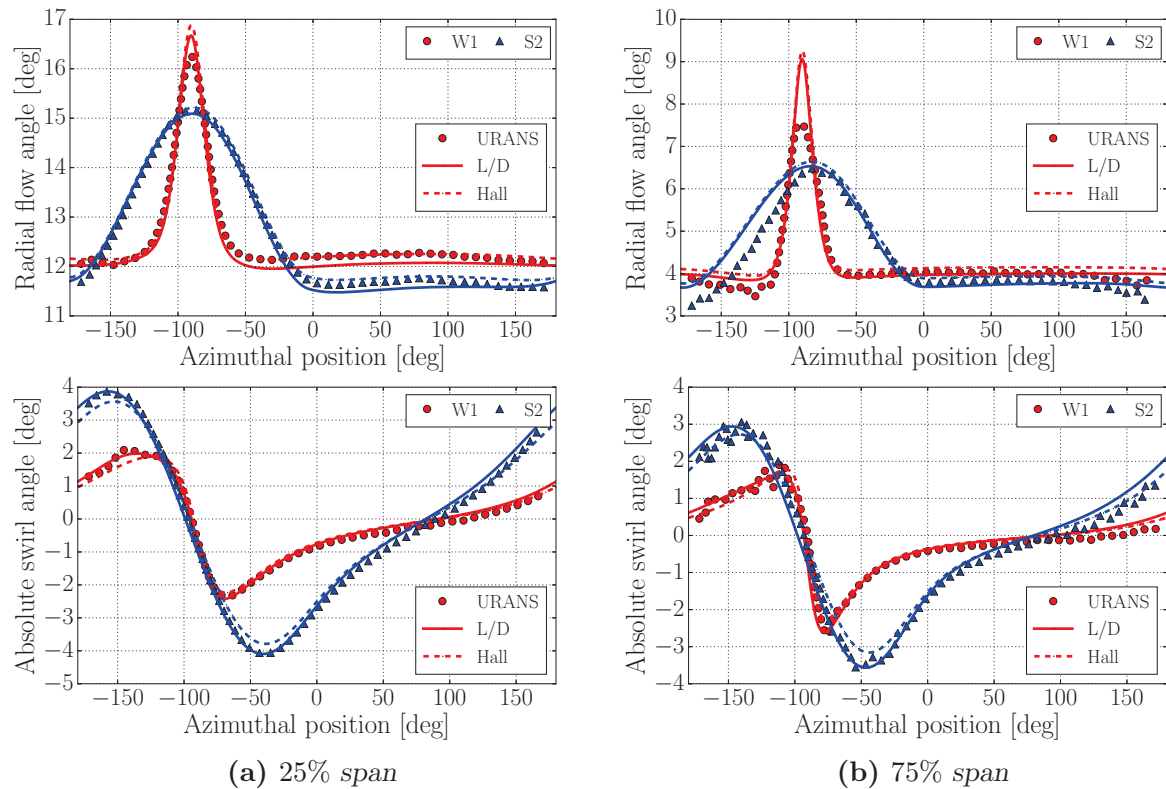


**Figure 4.6:** Circumferential profiles of radial and swirl angles at the fan face (station 1). There is a good quantitative agreement between URANS and body force computations.

The quantitative agreement between body force and URANS results upstream of the fan face is confirmed in figure 4.6, in which circumferential profiles of radial and swirl angles are shown. The flow redistribution is well captured by the two models, although small discrepancies are visible at 75% span, partially due to the effect of the moving average on the peak of radial flow angle in URANS computations. The peak of radial flow angle in the distorted region is lower for the S2 case, whereas swirl angle variations are higher. In fact, in the S2 case, the distorted region occupies most of the lower part of the annulus. As a consequence, a larger amount of fluid migrates from the upper part of the annulus, which causes the higher swirl angle variations. In the W1 case, the redistribution mostly affects the lower part of the annulus, and a large amount of fluid migrates from hub to tip in this region, leading to higher radial flow angles. These effects are well captured by the two body force models, which confirms their ability to capture the details of the upstream redistribution for different inlet distortion patterns.

Circumferential profiles of relative Mach number and relative flow angle are shown in figure 4.7. The range of relative flow angle variations seen by the rotor blades reaches  $5^\circ$  at 25% span and  $7^\circ$  at 75% span, and the relative Mach number is significantly decreased in the distorted region. These operating conditions are perfectly captured by the lift/drag model, and very well captured by Hall's model. This information is especially useful for engine manufacturers, as it can be used to adapt the blades design, for instance to accommodate blade incidence variations.

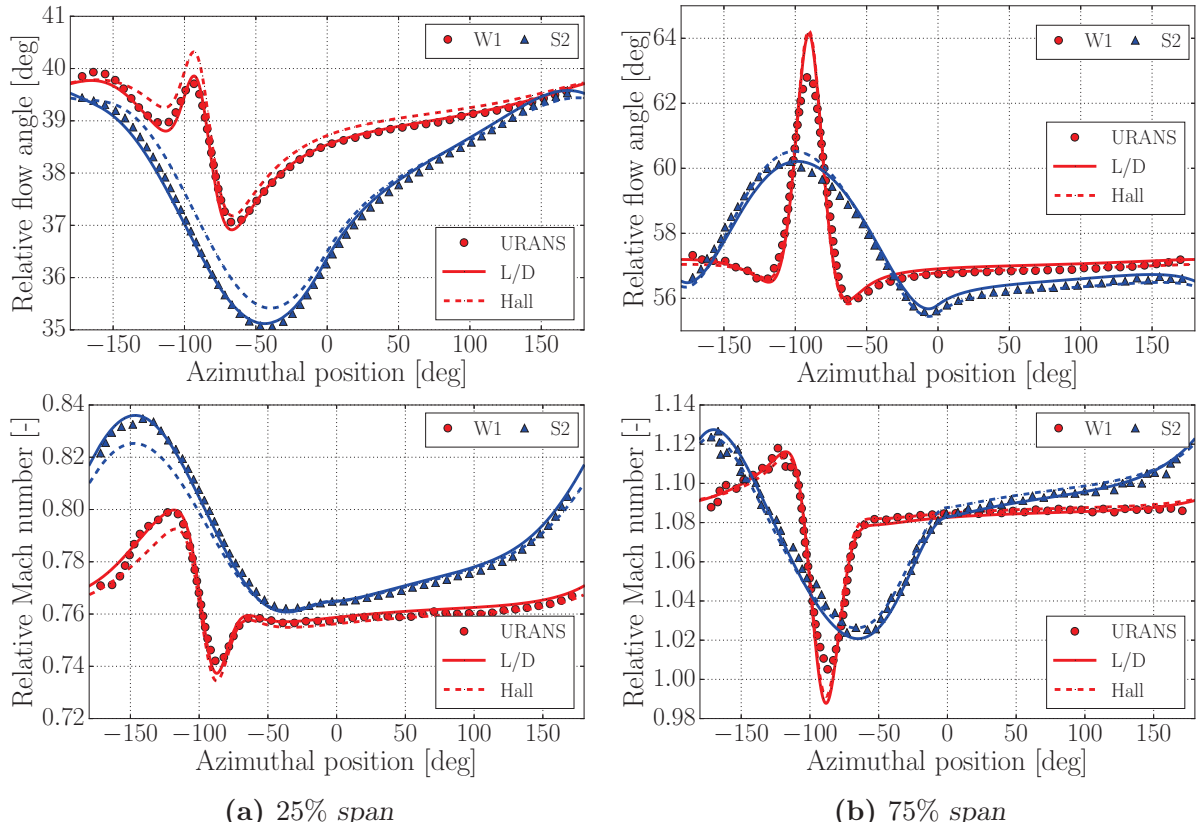


**Figure 4.7:** Circumferential profiles of relative Mach number and flow angle at the fan face.

### Flow field downstream of the rotor (station 2)

As explained in chapter 1, an important feature of the interaction of a fan with distorted inflow is the non uniform work input in the rotor. Regions of low-momentum flow result in locally decreased flow coefficient and thus in higher work coefficient. This is amplified in regions of counter-swirl, and conversely the work input is lower in regions of co-swirl. Distributions of work coefficient are shown in figure 4.8. There is a good agreement between body force and URANS computations on the shape, location, and amplitude of the higher and lower work coefficient regions, convected in the circumferential direction by the fan rotation.

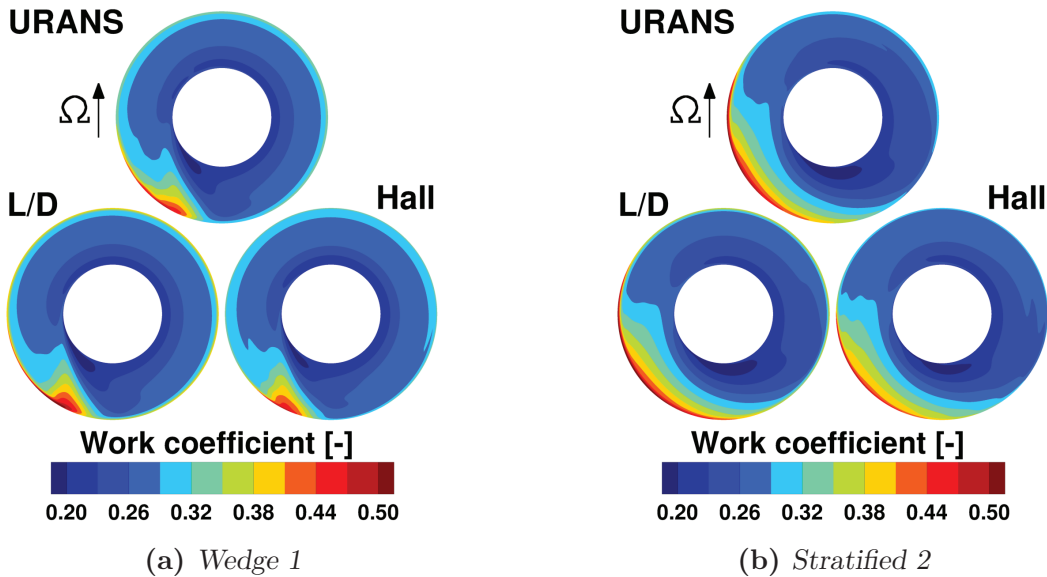


**Figure 4.8:** Contours of work coefficient downstream of the rotor (station 2). The non-uniform work input in the rotor is well captured by the BF models.

Contours of the mass flux coefficient  $\Phi$ , defined in equation (4.1), are shown in figure 4.9. The mass flux distribution is partially a consequence of the redistribution upstream of—and inside—the rotor, but it also results from the non uniform work input in the rotor. In fact, as shown by the continuity equation (4.2), axial variations of mass flux occur in presence of circumferential variations of circumferential momentum. In the present case, those variations are associated to the non uniform work input in the rotor. As a consequence, the circumferential position of the mass flux minimum is not simply convected by the rotor in the direction of the rotation, as is the case for the work coefficient.

$$\frac{\partial \rho V_x}{\partial x} + \frac{1}{r} \frac{\partial r \rho V_r}{\partial r} + \frac{1}{r} \frac{\partial \rho V_\theta}{r \partial \theta} = 0 \quad (4.2)$$

Circumferential profiles of work coefficient and mass flux are shown in figure 4.10. The effect of non-uniform inflow on non-uniform work input is very well captured by the two models and the global shape of mass flux is also well captured, although small discrepancies appear with Hall's model.

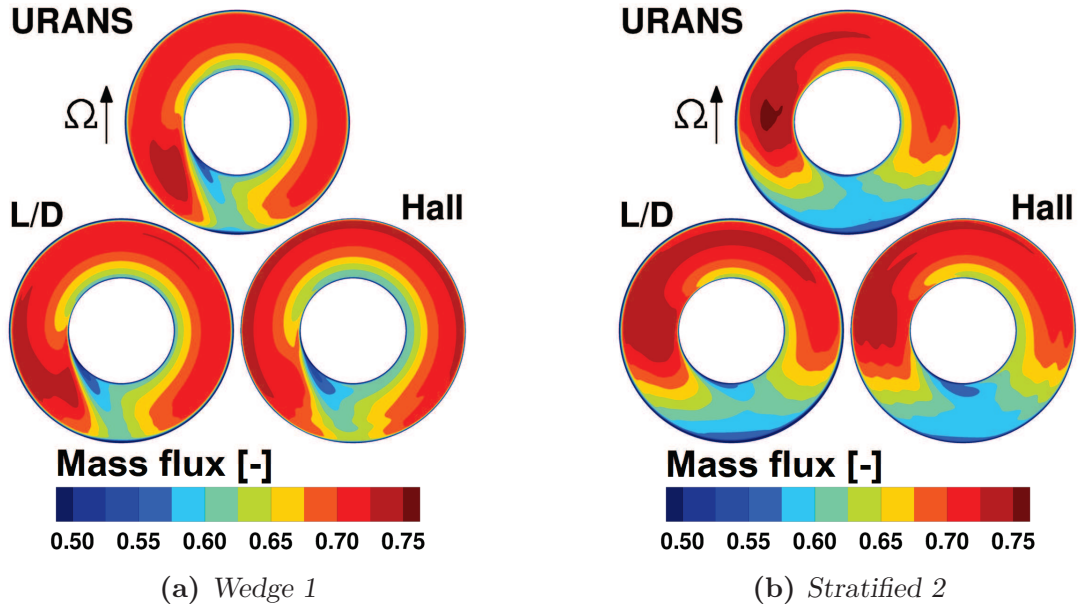


**Figure 4.9:** Contours of mass flux coefficient downstream of the rotor (station 2). The mass flow redistribution in the rotor is well captured by the BF models.

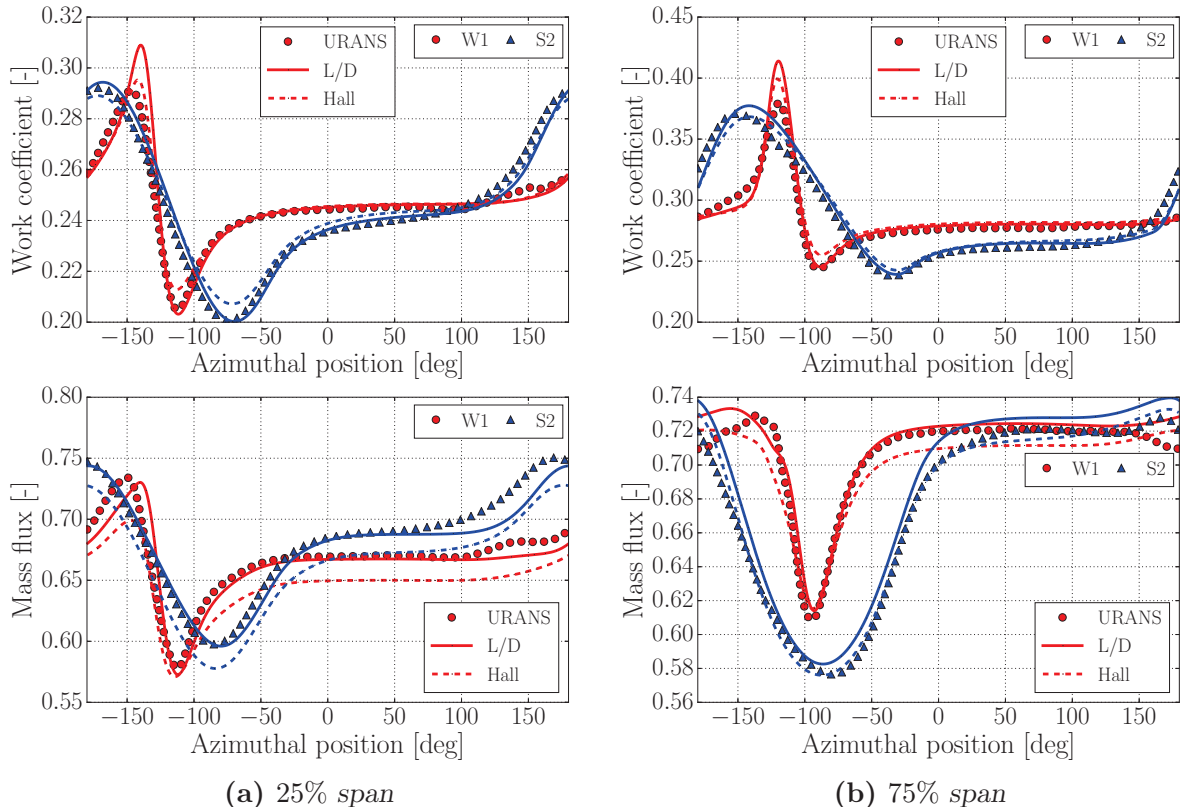


**Figure 4.10:** Circumferential profiles of work coefficient and mass flux coefficient downstream of the rotor (station 2). There is a good quantitative agreement between BF and URANS computations.

## Flow field downstream of the stator (station 3)

As explained by Gunn and Hall [44], there are almost no circumferential variations of the relative flow angle downstream of the rotor, but axial velocity non-uniformities lead to varying absolute swirl angles upstream of the OGVs. In the present cases, swirl angle variations of up to  $4^\circ$  at 25% span and  $8^\circ$  at 75% span are present for the S2 case at station 2. As a consequence, some parts of the OGVs are operating at off-design conditions, leading to increased loss. The distribution of absolute total pressure downstream of the OGVs is therefore a result of the non uniform work input in the rotor, flow convection from rotor to OGVs, and non uniform losses across the OGVs. Contours of total pressure at station 3 are shown in figure 4.11. The two models capture very well the shape of the total pressure downstream of the fan stage. This is confirmed in figure 4.12: the results obtained with the lift/drag model agree well with URANS data, although the total pressure is overestimated at 75% span and underestimated at 25% span. Hall's model captures well the global dynamics of these profiles, but with a non negligible offset at 75% span, due to the underestimated losses in the portion of the rotor operating with supersonic conditions.

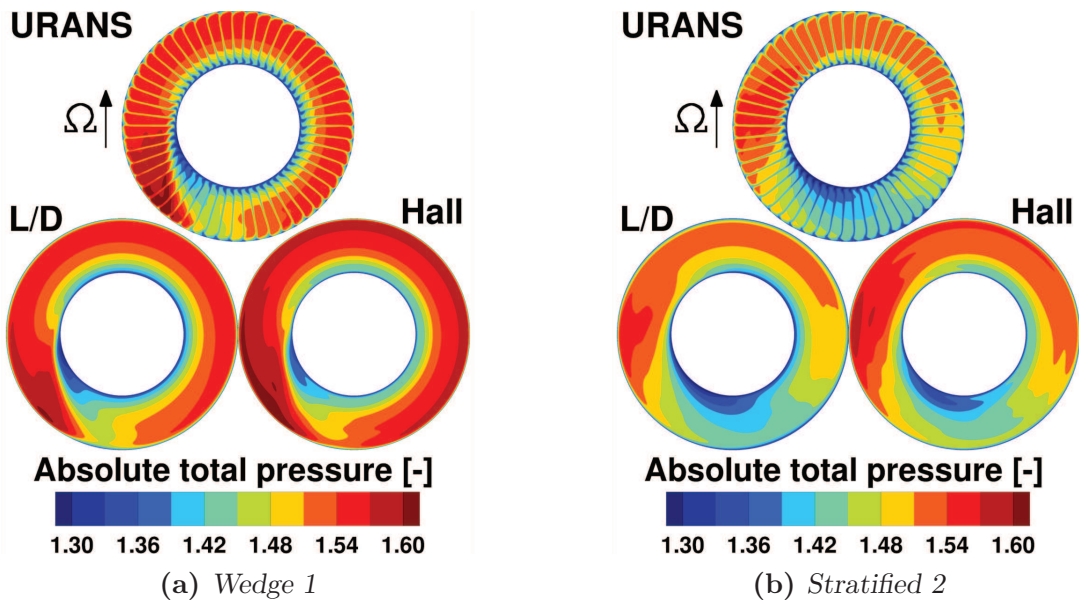


**Figure 4.11:** Contours of absolute total pressure (normalized by clean inlet total pressure) downstream of the OGVs (station 3) for two inlet flow distributions.

## Modal analysis

The body force approach filters high spatial frequencies: local blade to blade details such as the wakes are smeared out in the circumferential direction. In the framework of steady body force computations with inlet distortion, phenomena associated to relatively short length scales, of the order of one blade pitch, may therefore be filtered as well. This potential filtering of the distortion is quantified here using discrete Fourier transforms of circumferential profiles of mass flux at 25% and 75% span from inlet to outlet of the computational domain.

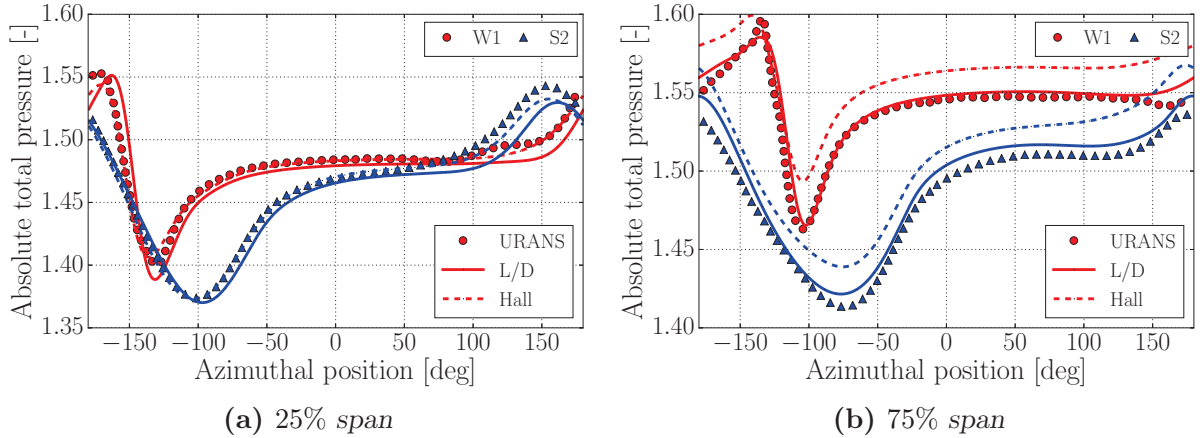


**Figure 4.12:** Circumferential profiles of absolute total pressure (normalized by clean inlet total pressure) downstream of the OGVs (station 3).

An example of spectrum of mass flux at 75% span downstream of the OGVs is shown in figure 4.13. A first peak, localized at low spatial mode numbers is present in URANS and body force computations, corresponding to the distortion frequency content. This first peak is in fact very close to a Gaussian function, as the Fourier transform of a Gaussian function is also a Gaussian function. The two other peaks, only visible in URANS computations, are due to the OGV wakes (spatial modes 54 and 108). The spatial modes that are related to the rotor wakes are not present, since they are eliminated in the time-averaging process. The filtering effect of the body force approach on high spatial mode numbers corresponding to length scales much lower than one blade pitch is thus well visible.

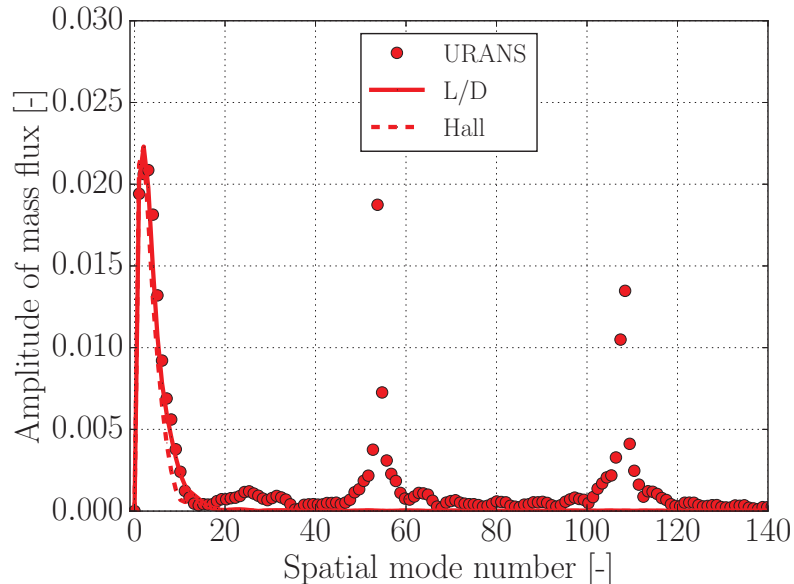


**Figure 4.13:** Discrete Fourier transform of a circumferential profile of mass flux at 75% span downstream of the OGVs (station 3). W1 inlet distortion case.

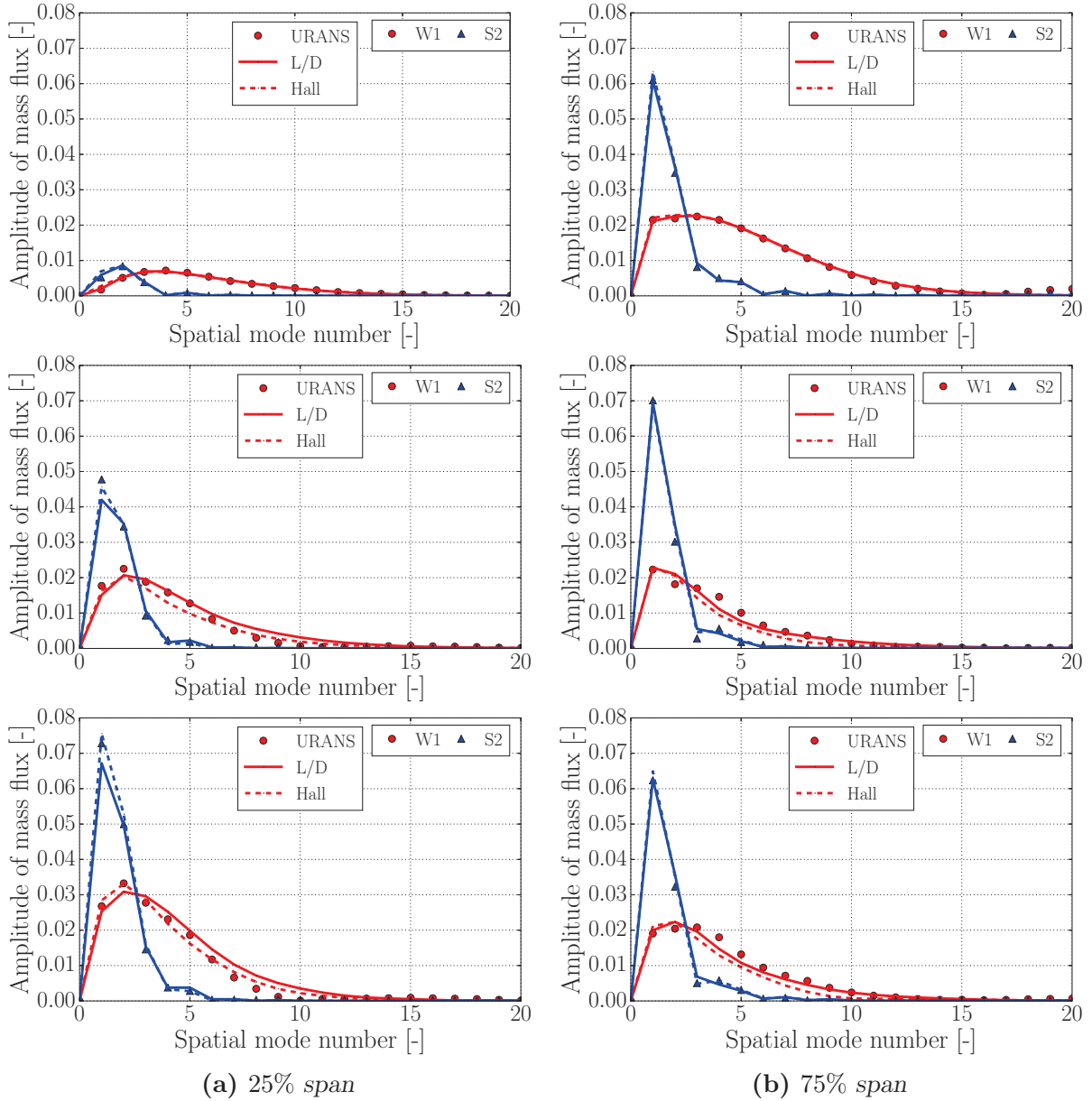


**Figure 4.14:** Discrete Fourier transforms of circumferential profiles of mass flux, from inlet to outlet of the computational domain: stations 1 (top), 2 (middle), 3 (bottom). There is no significant filtering effect in the body force computations.

Fourier transforms of mass flux at stations 1, 2 and 3 are shown in figure 4.14. Spatial mode numbers greater than the number of rotor blades are not shown to focus on the modes related to the inlet distortion. The spatial mode content in the W1 case is much richer than in the S2 case, because it corresponds to a shorter length scale distortion. The effect of the radial redistribution and non uniform work input on the mass flux distortion at the hub is well visible: the amplitude of the modes is very small at 25% span at station 1, but it increases significantly at station 2. This confirms the observation from Gunn and Hall [44]

that the azimuthal distortion is increased near the hub through the rotor. The amplitude of the modes at the hub is higher at station 3 than at station 2, which indicates that the mass flux distortion at the hub is also amplified downstream of the rotor. At 75% span, high spatial mode numbers are well attenuated in the rotor but almost not altered in the OGVs.

Basing the analysis of fan-distortion interactions on Fourier transforms of the spatial signal is an interesting way to highlight distortion transfer mechanisms and to quantify the distortion at any location. The agreement between body force and URANS results is good, and no significant filtering effect is visible in body force computations. This confirms the validity of the steady body force framework, even for relatively short length-scale inlet distortions, which was questioned in chapter 2. Nevertheless, this validity limit should be explored further with spatial mode numbers of the order of the number of blades, as modern fan geometries feature lower rotor blade number: “long” length scales for the R4 could become “short” length scale for these geometries.

### 4.1.3 Parametric study of fan–distortion interactions

The validity of the body force approach was demonstrated in the previous section on two different inlet distortion cases. In this section, a parametric analysis is conducted on the five inlet distortion cases presented in figure 4.2. As a first step, the comparison between URANS and body force computations is approached from a more global perspective, based on the following quantities:

- The energy spectral density of absolute total pressure  $E_{P_i}^*$ , defined in equation (4.3). This quantity is computed by integrating the results given by discrete Fourier transforms on circumferential profiles. The upper limit of the integral is the spatial mode number  $N = 20$  to eliminate frequencies not related to inlet distortion in URANS computations. This metric allows to quantify the intensity of the distortion on a given circumferential profile.
- The circumferential range of the total pressure bucket  $\Delta\theta_{80\%}$  and the circumferential position of the minimum of total pressure  $\theta_{min}$ , defined in figure 4.15.

The objective of this comparison is to check that the body force models capture well the position and intensity of the total pressure distortion, upstream and downstream of the fan stage, for each inflow distribution. In a second step, the impact of each distortion pattern on IP forces and fan efficiency is quantified.

$$E_{P_i}^* = \frac{\sum_0^{20} |\hat{P}_i|^2}{(P_i^{0,max} - P_i^{0,min})^2} \quad (4.3)$$

#### Total pressure distortion intensity and position

The evolution of the distortion intensity  $E_{P_i}^*$  at 25% and 75% span is shown in figure 4.16. As for the mass flux, the distortion intensity increases near the hub and decreases near the shroud across the rotor. However, a large part of this distortion intensity increase is directly due to the non-uniform work input in the rotor, and not to flow redistribution. In fact, the

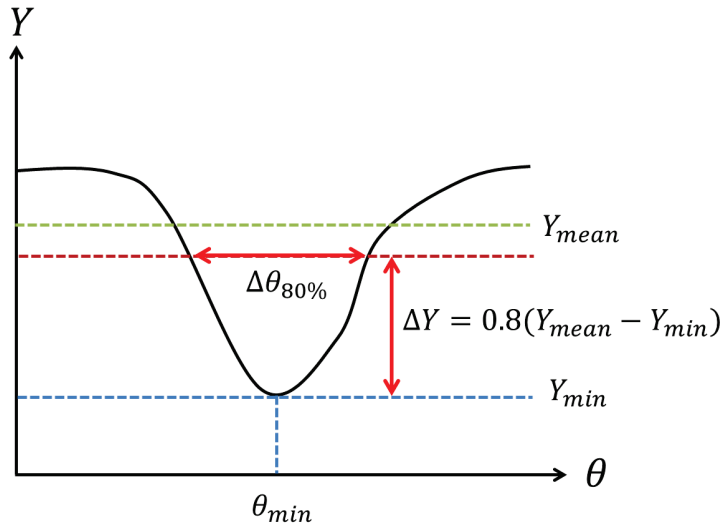


**Figure 4.15:** Definition of the spatial extent of a bucket  $\Delta\theta_{80\%}$  and position of the minimum  $\theta_{min}$ .

distorted area and the regions of co and counter swirl near the hub are responsible for large variations of work coefficient downstream of the rotor, as was shown in figure 4.8, which in turns leads to large variations of total pressure. As opposed to the mass flux, the distortion intensity does not change much downstream of the rotor, which shows that non axisymmetric losses in the OGVs only play a minor role on the final shape of the total pressure distortion. The two body force models capture very well the decrease in distortion intensity at 75% span, but the increase in intensity at 25% span is slightly underestimated for the most distorted cases. It is unclear if this is due to underestimated redistribution effects, or to discrepancies on work coefficient / rotor efficiency.

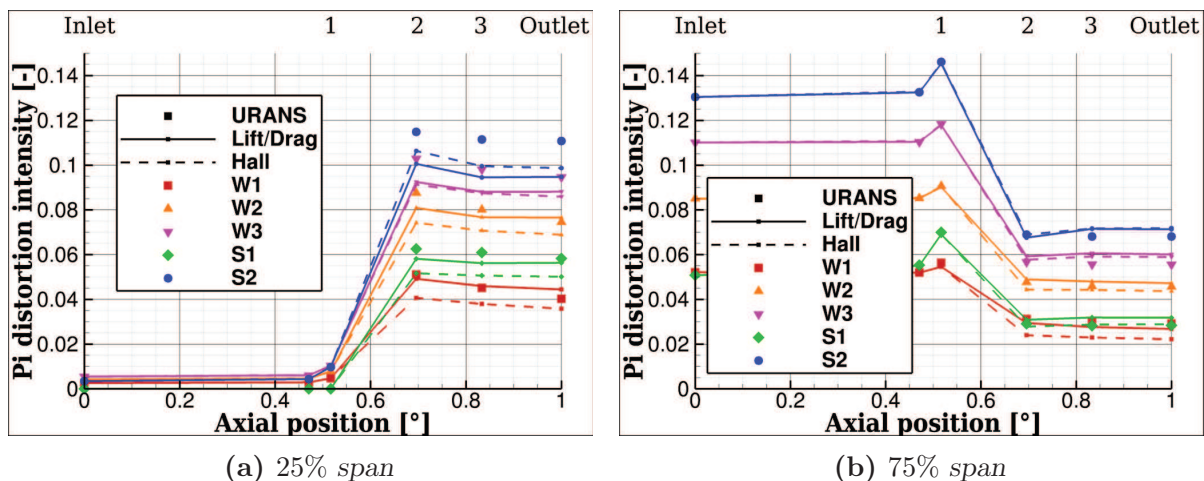


**Figure 4.16:** Distortion intensity  $E_{P_i}^*$  from inlet to outlet for five inlet distortion patterns. The distortion is reduced at 75% span but increased at 25% span, which is well captured by the BF models.

The position of the minimum total pressure point is shown in figure 4.17. This position is not simply the initial position of the lower total pressure at the inlet, convected along the streamlines through the rotor and turned because of the blade rotation. The non uniform work input in the rotor completely alters the total pressure distribution, as was shown in figure 4.11. As a consequence, the position of minimum total pressure downstream of the fan stage is the result of the combined initial total pressure distribution and locations of regions of high/low work input in the rotor. The position of the minimum stagnation pressure point is not directly correlated with the increase/decrease of distortion intensity shown in figure 4.16 (the curves are not set in the same order). In particular, the two vertically stratified cases present significant shifts of this minimum position in the counter rotating direction, which is especially visible at the tip. The two body force models capture well the effect of inlet distortion shape on the evolution of the position of the total pressure minimum, which is consistent with what was shown in figure 4.12 for the W1 and S2 cases.

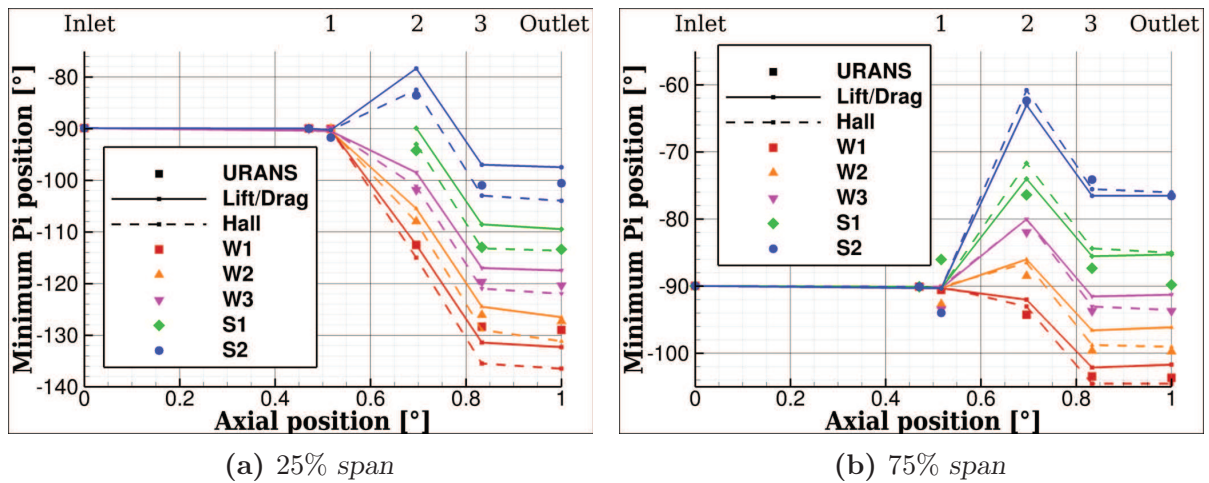


**Figure 4.17:** Position of the total pressure minimum  $\theta_{min}$ , from inlet to outlet for five inlet distortion patterns (decreasing values mean that the minimum goes in the same direction as the fan rotation). There is a good agreement between BF and URANS computations.

The range of the total pressure bucket  $\Delta\theta_{80\%}$  is shown in figure 4.18. This range is taken relatively to the range at inlet, and it could not be computed at 25% span for the S1 case, because the bucket was too shallow. It can be seen that the sharper the initial distortion is, the wider the bucket becomes through the fan stage. The range increases even downstream of the OGVs, which indicates that some circumferential redistribution occurs in this regions. The body force models capture the qualitative evolution of the circumferential range of the total pressure buckets: the curves are set in the right order and their dynamics is consistent with those in URANS computations. In particular, the buckets are not wider than in URANS computations. This shows that the circumferential redistribution, which is limited to one blade pitch in URANS computations in the bladed domains, does not seem to play a major role in body force computations, even though the blades are not physically present.

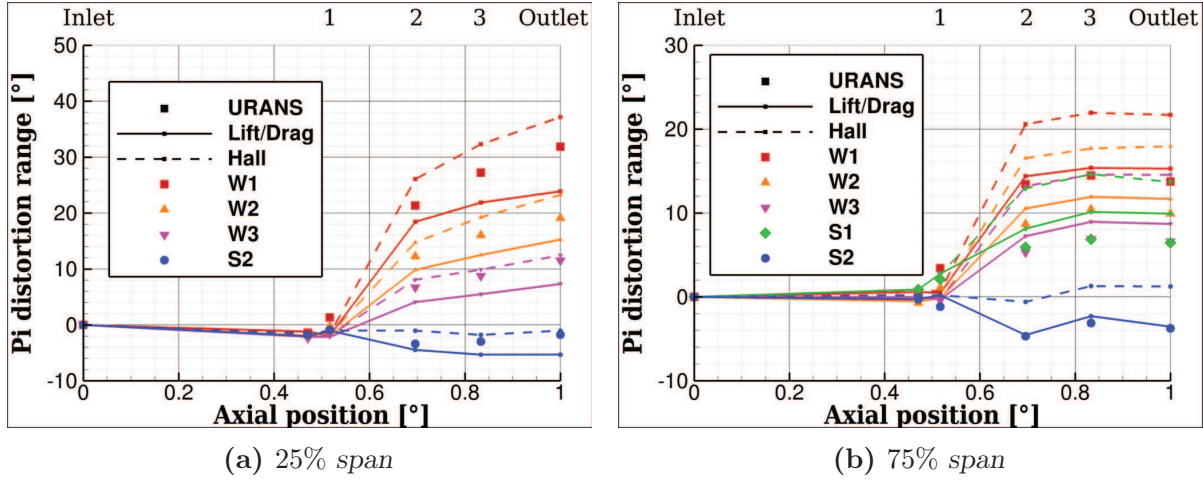


**Figure 4.18:** Relative range of the total pressure bucket  $\Delta\theta_{80\%}$ , from inlet to outlet for five inlet distortion patterns (positive values mean that the bucket is wider than it was at inlet).

### Distortion effect on in-plane forces

The non uniform work input in the rotor under distorted inflow can directly be related to a non uniform static pressure distribution on the blades around the annulus. As a consequence, forces acting in the plane orthogonal to the rotation axis could become significant in BLI configurations. IP forces acting on the rotor and OGV blades are shown in figure 4.19. The modulus of the force is normalized by the thrust on each blade row. The modulus of the force is well correlated to the distortion amplitude, and reaches slightly more than 6% of the thrust on the rotor and 13% of the thrust on the OGVs. The thrust on the OGVs is much lower than on the rotor, so that IP forces on the OGVs are in fact lower. Those values are quantitatively similar to those that were obtained in chapter 3 on the short intake configuration. In the present case, there is no bifurcation included in the computational domain, and, in practice, care should be taken that the effect of the bifurcation on IP forces does not add up to the effect of the inlet distortion. The two body force models capture quite well the qualitative evolution of the modulus of the force on the rotor and on the OGVs with the different inlet distortions. The phase is also well captured, except for the S1 case where a significant discrepancy is visible. The origin of this discrepancy is hard to explain, as the flow field is as well predicted with the S1 distortion as in the other cases by the two models.

### Distortion effect on fan efficiency

One key parameter in BLI configurations is the fan stage efficiency. In fact, to design a BLI aircraft with significant fuel burn benefits, a balance must be found between propulsive efficiency benefits and fan efficiency penalties. The total-to-total isentropic efficiency of the fan was computed at stations 2 and 3, to evaluate the impact of BLI on the losses in the rotor and OGVs. The efficiency decrease was computed relatively to body force and mixing plane computations with clean inlet flow, at the design mass flow rate. A mixing plane computation was thought to be accurate enough to be used as reference for URANS cases,

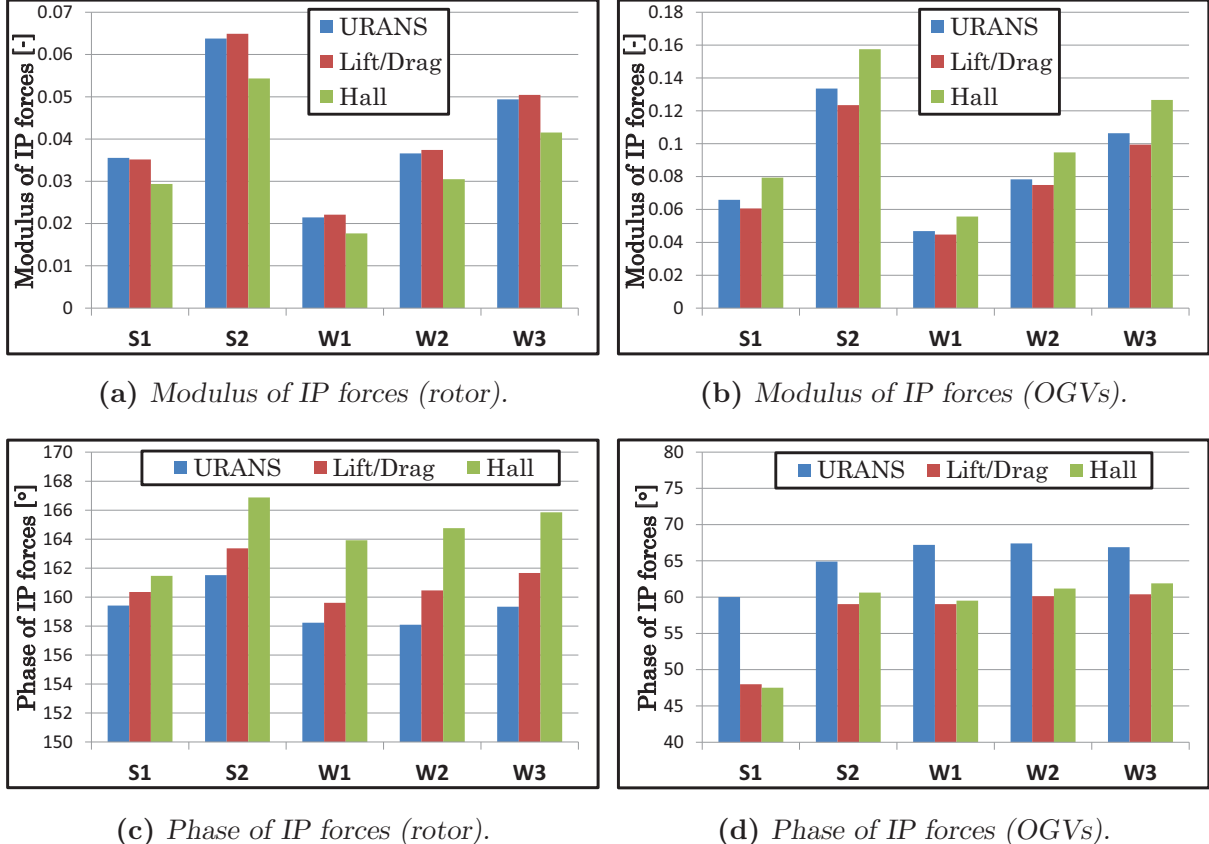


**Figure 4.19:** Modulus normalized by thrust and phase of IP forces acting on the R4 rotor and OGVs (negative phase means the vertical force points downward). The impact of each distortion on the modulus of the force is qualitatively captured by the BF models.

as the axial distance between rotor and stator in the R4 fan stage minimizes rotor/stator interactions. The results are shown in figure 4.20. Efficiency decreases of almost 1.5 points in the rotor and 3.5 points for the fan stage are found for the most distorted case (S2). This is higher than what was found by Gunn and Hall [44], although the global characteristics of the test-case and computational setup are similar. A potential source of differences could be that all computations were compared at the same mass flow rate, corrected by inlet conditions in the present case, against same physical mass flow rate in Gunn and Hall's paper.

The two body force models capture well the qualitative evolution of efficiency with each inlet distortion pattern, although the efficiency decrease is in general underestimated. This is very useful in an airframe design context, as some of the effect of the BLI on the fan performance and thus on the global aircraft performance can be captured. However, it should be kept in mind that the present models do not allow to highlight the exact source of losses, since, as was shown in Chapter 2, the off-design losses are spread along the blade span with the loss formulations in the lift/drag and Hall's models. Hence, the models can not be used as such for fan design, and a more detailed parallel force formulation is needed to capture the location of the increased losses.

It can be noted that fan efficiency penalties do not correlate well with the  $DC_{60}$  criteria, given in table 4.1 for each inflow distribution. In particular, the W3 distortion presents a higher  $DC_{60}$  than the S2 distortion, but the latter leads to higher fan efficiency penalties. This suggests that the  $DC_{60}$  criteria is not really adequate to evaluate the impact of distortion on fan efficiency. A better solution could be to use a criteria similar to the spectral density energy defined in equation (4.3). Although this distortion intensity criteria was only used in a 2D context, one could imagine an extension to 3D by integrating the criteria in the radial direction. One limitation of this criteria is that it requires a sufficient number of total pressure measurements to compute a realistic Fourier transform of the inlet signal, which is difficult in an experimental context.

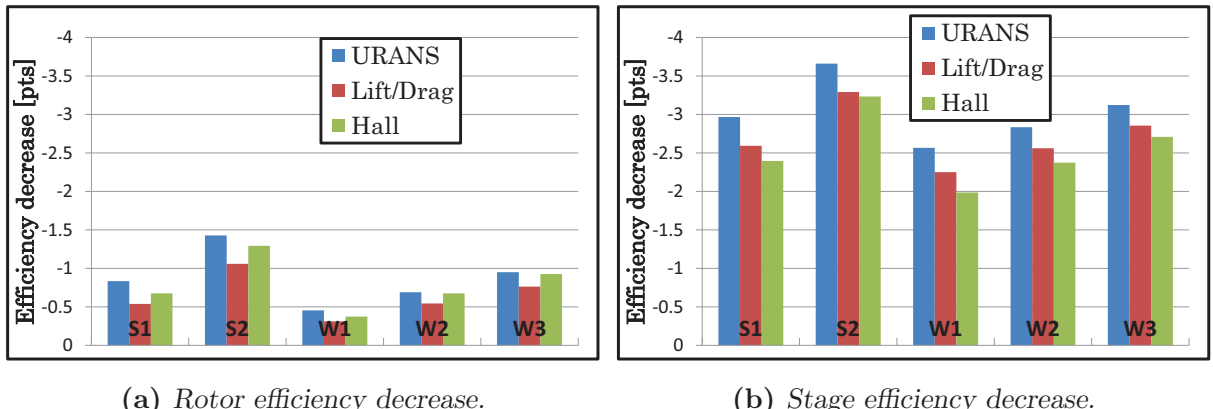


**Figure 4.20:** Efficiency decrease relatively to clean inlet flow. The effect of BLI on the fan stage efficiency is qualitatively captured by the models.

#### 4.1.4 Summary

The lift/drag and Hall's body force models were applied to the R4 fan stage for a range of five parametric inflow distributions with total pressure distortion. The ability of the models to capture the key aerodynamic mechanisms associated to boundary layer ingestion was demonstrated for two of those distributions. In particular, it was shown that the models capture very well the effect of inlet non uniformities on non-uniform work input, and the distortion transfer through the blade rows. Based on a modal analysis, it was shown that the modal content of the distortion was not filtered in the body force computations. However, the minimum distortion length scale was of about two blade pitch, and a similar analysis should therefore be conducted for a distortion of shorter length scales to further confirm this result. Then, a more global analysis was conducted with all the distributions. It was shown that the models capture the qualitative evolution of global flow characteristics such as distortion intensity and position. More importantly, the models qualitatively capture the global change in fan stage efficiency for each inlet distortion pattern. This confirms the validity of the models to study fan-distortion interactions, in an airframe design context. However, additional work is required on the modeling of the loss to enable the localization of the exact source of losses for a given inlet distortion pattern.

## 4.2 RAPRO experiment

### 4.2.1 Description of the RAPRO configuration

To assess the benefits of BLI configurations, an experiment was conducted by ONERA on Airbus' initiative, which allows to link the amount of ingested aircraft boundary layer to the amount of power needed to operate the fan. The experiment consists in a blunt axisymmetric fuselage body that generates a wake, ingested by a fan placed downstream of the body. The experimental set-up is shown in figure 4.21. The nacelle can be moved axially, vertically and laterally to change the portion of fuselage boundary layer ingested by the fan. The power supplied to the fan is measured, as well as the forces and torques applied to the nacelle and fuselage. More information about this experiment can be found in [2].

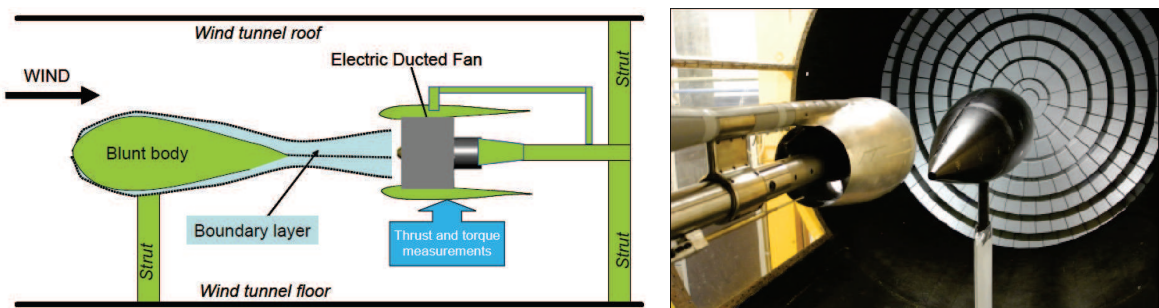


**Figure 4.21:** Sketch of principle and photo of the RAPRO2 experimental set-up (credits ONERA [2])

As illustrated in figure 4.22, several CFD simulations were carried-out to evaluate the BLI benefits on the power required to operate the fan:

- Reference, non BLI computations where the fuselage and nacelle are represented in two separate CFD computations.
- Axisymmetric BLI computations where the nacelle is centered on the fuselage axis.
- Non axisymmetric BLI computations where the nacelle is moved vertically to decrease the amount of ingested boundary layer.

The relative position between engine and fuselage for each case is given in table 4.2. The axial and lateral positions are the same in all cases. Different meshes were used for the nacelle and fuselage and were assembled with the Chimera technique. This approach allowed to change the position of the nacelle relatively to the fuselage without any modification of the different meshes. The fan was modeled with the lift/drag body force model. To evaluate the effect of BLI for different engine operating conditions, computations were realized for varying fan rotational speeds. It is interesting to note that with conventional thrust/drag bookkeeping, ingesting some boundary layer results in decreased fuselage drag and decreased fan thrust. In that case, a positive BLI effect can be observed as the decrease in drag is more important than the decrease in thrust. However, it was shown in the past [27] that methods based on power balance were more adapted to study BLI configurations. As a consequence, for each

rotational speed, the total axial force applied to the nacelle and fuselage was extracted along with the power added to the flow by the fan, allowing to compute the decrease in required power to achieve a given thrust+drag resultant.

Case	$\frac{Z_{axis}^{fus} - Z_{axis}^{fan}}{R_{fan}^{tip}}$
Axisymmetric BLI	0
Non axisymmetric position 1	0.35
Non axisymmetric position 2	0.935

**Table 4.2:** RAPRO, non axisymmetric body force computations: distance between fan and fuselage axis, relatively to the fan radius (greater than one means that the fuselage axis is outside of the fan).

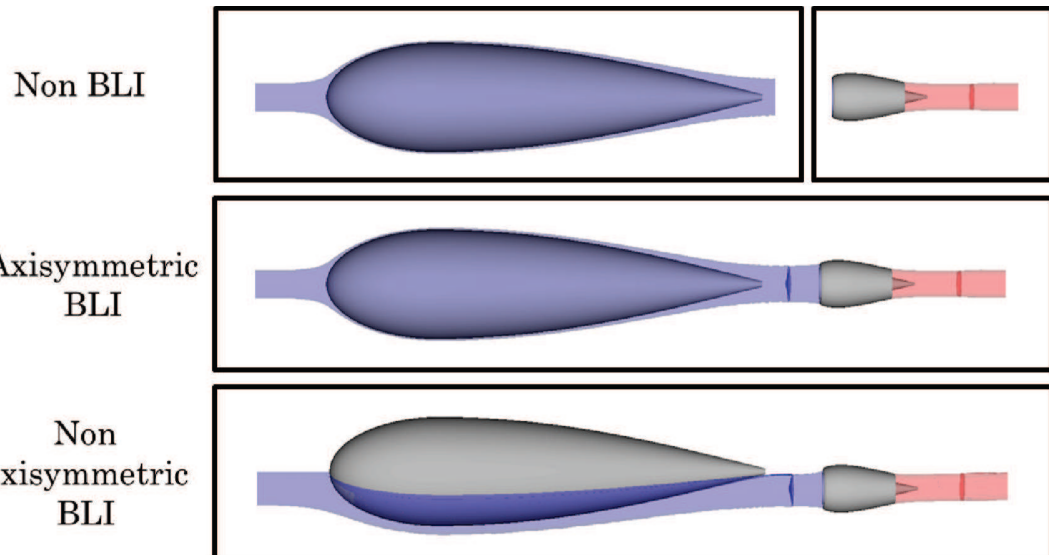


**Figure 4.22:** Illustration of the different types of computations conducted on the RAPRO configuration.

#### 4.2.2 Amount of ingested boundary layer versus power saving

The power savings offered by BLI for the three engine positions described above are shown in figure 4.23. Each curve was obtained for a given engine position by increasing the rotational speed of the fan, which in turns increases the drag+thrust resultant. Unfortunately, experimental data for the non axisymmetric cases were not available when these results were analyzed. These results must be analyzed together with those in figure 4.24 to perfectly understand the evolution of each curve.

For a given thrust+drag resultant, the BLI benefits decrease when the engine is brought further away from the fuselage. In fact, a smaller portion of the fuselage boundary layer is ingested in those cases, which increases the viscous dissipation in the airframe wake and in

the propulsive jet. When the rotational speed is increased, the thrust of the engine is higher and so is the thrust+drag resultant. The mass flow rate inside the engines increases as well, and the streamtube entering the air intake becomes wider upstream of the engines, allowing a larger amount of fuselage boundary layer to be ingested. For the axisymmetric case and for the first engine position, the amount of ingested boundary layer is already high at the lowest rotational speeds. For these cases, increasing the rotational speed primarily leads to an increase of ingested free-stream air, which implies higher propulsive jet penalties and thus decreased BLI benefits. For the second engine position, the relative amount of ingested fuselage boundary layer increases significantly with the rotational speed, which enables an increase of the BLI benefits with the rotational speed.

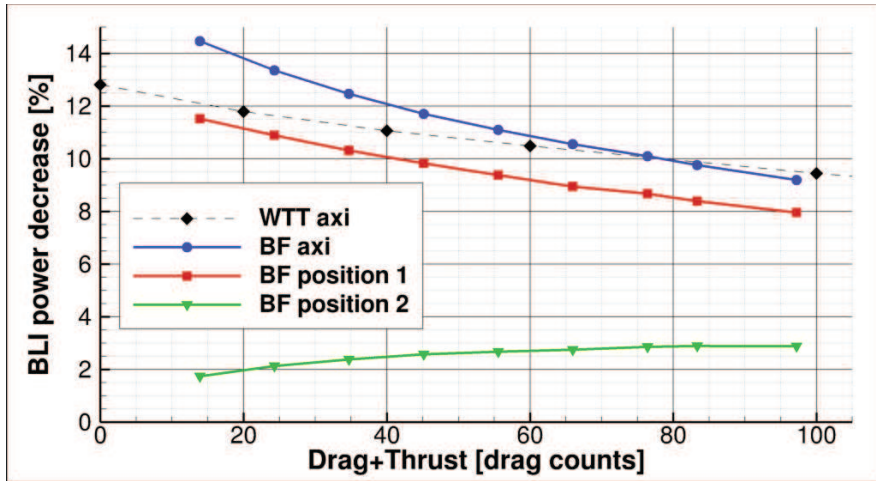


**Figure 4.23:** Experimental measurements (WTT) of power saving against body force computations (lift/drag model).

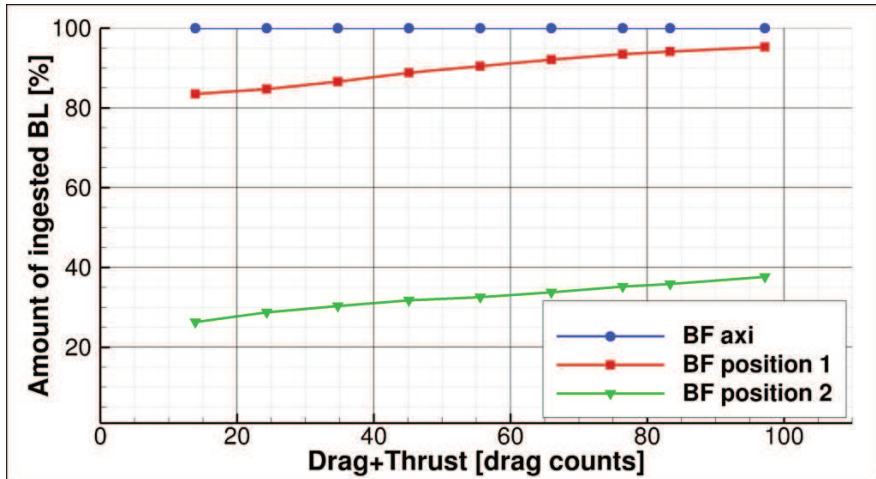


**Figure 4.24:** Portion of ingested fuselage boundary layer in body force computations (lift/drag model). BLI benefits fall to only 2 – 3% when 30% of the fuselage boundary layer is ingested.

The boundary layer ingestion offers fuel burn benefits of more than 10% for the axisymmetric case, in which all the fuselage boundary layer is ingested, against 2% to 3% for the second engine position, for which about one third of the fuselage boundary layer is ingested. The agreement between the body force model and the experiments is qualitative only for the axisymmetric case. The discrepancies with the experimental data may come from the description of the fan: the geometry of the fan used for the wind tunnel tests was not available, and an equivalent fan geometry therefore had to be generated using performance data. In addition, it is possible that the power measured during the tests was not exactly the same as the power added by the fan to the flow, as it was estimated based on the electrical power supplied to the engine.

These results highlight one of the difficulties of designing a BLI aircraft, as the BLI benefits are directly dependent on the amount of airframe boundary layer that can be ingested. In practice, in an ideal case and for a tube and wing configuration, one engine could be placed downstream of the aircraft to ingest all of the fuselage boundary layer, as was for instance proposed in [52] with the STARC configuration. One key advantage of this approach, in addition to the possibility to ingest a large portion of the airframe boundary layer, is that the circumferential component of the distortion at the fan face almost disappears, which could reduce fan efficiency penalties and aeromechanical constraints. However, it is not certain that adding a third engine would allow to maintain the BLI benefits at the system level. Another solution to ingest a large portion of the aircraft boundary layer is to consider distributed propulsion, which is especially attractive in the frame of hybrid or electric aircraft, for which the power distribution may be easier to handle. For this type of configuration, the use of a body force model is even more interesting as the CPU cost of simulations in which the blades are fully modeled directly increases with the number of blade rows that need to be represented. In addition, the use of a surrogate model for rotating blade rows could allow to set-up a coupling between the software that computes the global engine performance and the CFD simulation. One interesting outcome of such a coupling could be, for instance, to automatically adjust the rotational speed to reach a given thrust requirement, while taking into account the power consumption of each blade rows and the induced power requirement on the core.

### 4.3 Summary and conclusion

In this chapter, the body force approach was assessed on two test-cases representative of BLI configurations. The lift/drag model and Hall's model were first applied to the R4 fan stage for a range of five parametric inflow distributions with total pressure distortion. It was shown that both models capture well the aerodynamic features of the fan/distortion interaction, including upstream redistribution, distortion transfer, IP forces, and impact of distortion on fan efficiency. Then, the lift/drag model was applied to the RAPRO configuration, and it was shown that the potential power savings offered by BLI are directly related to the amount of aircraft boundary layer that can be ingested. Both applications demonstrate the need to include a representation of the fan in airframe CFD computations with BLI, and the adequacy of the body force approach for this requirement.

# Summary, conclusions, and ways forward

The main purpose of this thesis was to propose an accurate and robust body force formulation that could be used to design an airframe in a closely coupled engine–airframe configuration. Here are the key elements that summarize the present work:

- First the body force modeling framework was established. The equations that are solved in the domains swept by the fan and OGVs blades are derived from the tangentially averaged NS equations. These equations are simplified, so that only the metal blockage source terms and the blade force remain. The former explicitly depends on the blockage factor and on local flow conditions, but some modeling is required for the latter. The flow is assumed to be quasi-steady, so that steady body force computations can be performed.
- Different procedures to extract body force fields from RANS mixing plane computations were explored. This allows to calibrate a body force model, or to generate a body force database from which the blade force can be interpolated. It was shown that a blade force extraction based on the averaged thermodynamic quantities allows to reproduce the stagnation pressure rise and efficiency of a fan stage more accurately than an extraction based on the blade force average, which only allows to reproduce the forces acting on the blade.
- Three explicit body force formulations were described, that link the blade force to the local blade geometry and to local flow conditions. In all these formulations, the blade force is decomposed into a normal-to-the-flow force that generates turning and a parallel force that generates the losses. The first model is derived from Gong’s and Peters’ contributions. This formulation requires calibration from multiple blade computations and the calibration process is not robust; it was therefore abandoned. The second formulation is built based on a lift and drag analogy and can be calibrated from only one blade computation at maximum efficiency, but it requires manual adaptations of the normal force to capture the choke mass flow rate. The third model does not require any calibration from a-priori blade computations, but is slightly less accurate than the second model.
- The second and third models were applied to an intake–fan interaction test case. Both models capture the upstream influence of the fan on the air intake, which results in increased intake range of operability in terms of AOA. Then, the models were used to

evaluate the distortion transfer inside the bypass flow for high AOAs, and were shown to capture the qualitative physical behavior of the fan due to its interactions with the inlet flow field and with the bifurcation.

- Finally, the models were applied to test cases representative of BLI configurations. As a first step, a detailed assessment of the aerodynamic behavior of a transonic fan stage under parametric inflow distortion patterns was conducted. It was found that the models capture the aerodynamic response of the fan to the inlet distortion, and in particular the fan stage efficiency decrease due to the BLI. As a second step, the second model was applied to the RAPPRO configuration, which allowed to show that the benefits offered by BLI are highly dependent on the amount of boundary layer than can be ingested into the engines.

The overall good agreement that was obtained between body force computations and higher fidelity methods confirms the adequacy of the body force framework. In particular, it was shown that the formulations that are proposed capture the effect of changes in airframe design on fan-airframe interactions. However, further work may be useful to improve the approach:

- One key limitation of the proposed models is that the loss formulations are too simple to capture the details of a fan efficiency decrease because of off-design operation. Some potential avenues of exploration are proposed in Appendix A to address this limitation, but further work is required to clearly define new potential solutions.
- A normal force formulation based on Hall's model but featuring optional calibration coefficients should be developed. Such a formulation would allow to remain consistent between early fan design phases where no detailed geometries are defined and phases in which some detailed computations of the fan are available.
- The adequacy of the body force approach in naturally unsteady configurations (e.g. wing flutter, gusts) was not explored in the present thesis, and only steady-state distortion problems were treated. The body force approach could be used to evaluate the unsteady response of the fan to wing motion, for instance to evaluate unsteady IP forces in pitching nacelles. In these cases, unsteady body force computations with a time-lag model may be required to capture the interaction of the blades with flow perturbations.
- Some additional modeling is required to capture 3D effects on high hub-to-tip ratio geometries. In particular, a spanwise mixing model and an aerodynamic blockage model may enable the use of the models on a larger variety of turbomachines, including LPC compressor stages. For modern fan geometries with low hub-to-tip ratio, it is not thought that these effects are dominant.

One key challenge for research and industry in the years to come is to enable the design of complex products in a multidisciplinary environment. This thesis demonstrates the utility of reduced order models, at a time when lots of efforts are put toward high fidelity approaches such as LES. High fidelity co-simulation is in general too expensive or too complex to be

achieved on realistic industrial cases, and reduced order approaches must be developed to effectively enable a multi-physics design. In particular, in early design phases, methods that are fast and in which the design parameters can easily be modified will always be necessary. Beyond a strict application to aerodynamic design, the body force modeling approach offers an ideal interface between aircraft performance and engine performance and fits perfectly in a model-based environment.

# Bibliography

- [1] J. J. Adamczyk. Model equation for simulating flows in multistage turbomachinery. *ASME Paper*, 85-GT-226, 1985.
- [2] O. Atinault, G. Carrier, R. Grenon, C. Verbecke, and P. Viscat. Numerical and experimental aerodynamic investigations of boundary layer ingestion for improving propulsion efficiency of future air transport. In *Proceedings of 31st AIAA Applied Aerodynamics Conference*, San Diego, CA, June 2013. Paper no. AIAA 2013-2406.
- [3] S. Baralon. *On multistage analysis of transonic compressors : from axisymmetric throughflow time-marching to unsteady three dimensional methods*. PhD thesis, Chalmers university of technology, 2000.
- [4] S. Baralon, U. Hall, and L.-E. Eriksson. Viscous throughflow modelling of transonic compressors using a time-marching finite-volume solver. In *Proceedings of 13th International Symposium on Airbreathing Engines (ISABE)*, Chattanooga, USA, 1997.
- [5] S. Baralon, U. Hall, and L.-E. Eriksson. Validation of a throughflow time-marching finite-volume solver for transonic compressors. In *Proceedings of ASME International Gas Turbine and Aeroengine Congress and Exhibition*, Stockholm, Sweden, June 1998.
- [6] S. Baralon, U. Hall, and L.-E. Eriksson. Evaluation of high-order terms in the throughflow approximation using 3D navier-stokes computations of a transonic compressor rotor. In *Proceedings of ASME International Gas Turbine and Aeroengine Congress and Exhibition*, Indianapolis, Indiana, USA, June 1999.
- [7] B. Benneke. A methodology for centrifugal compressor stability prediction. Master's thesis, Massachusetts Institute of Technology, 2009.
- [8] M. L. Brand. An improved blade passage model for estimating off-design axial compressor performance. Master's thesis, Massachusetts Institute of Technology, 2013.
- [9] L. Cambier, S. Heib, and S. Plot. The ONERA elsA CFD software: input from research and feedback from industry. *Mechanics & Industry*, 14(03):159–174, 2013.
- [10] T. Cao, P. Hield, and P. G. Tucker. Hierarchical immersed boundary method with smeared geometry. In *54th AIAA Aerospace Sciences Meeting*, 2016. AIAA 2016-2130.

- [11] T. Cao, N. R. Vadlamani, P. G. Tucker, A. R. Smith, M. Slaby, and C. T. J. Sheaf. Fan-intake interaction under high incidence. *Journal of Engineering for Gas Turbines and Power*, 139(4), 2017.
- [12] M. Carnevale, F. Wang, J. S. Green, and L. D. Mare. Lip stall suppression in powered intakes. *Journal of Propulsion and Power*, 32(1), 2016.
- [13] K. L. Chan. An assessment of computational procedures for eleven-stage compressor response to inlet distortion. Master's thesis, Massachusetts Institute of Technology, 2003.
- [14] G. T. Chen, E. M. Greitzer, C. S. Tan, and F. E. Marble. Similarity analysis of compressor tip clearance flow structure. *Journal of Turbomachinery*, 113, April 1991.
- [15] R. V. Chima. A three-dimensional unsteady CFD model of compressor stability. In *ASME Turbo Expo 2006: Power for Land, Sea, and Air*, pages 1157–1168. American Society of Mechanical Engineers, 2006.
- [16] R. V. Chima, D. J. Arend, R. S. Castner, and J. W. Slater. CFD models of a serpentine inlet, fan, and nozzle. In *48th AIAA Aerospace Sciences Meeting Including the New Horizons Forum and Aerospace Exposition*, 2010.
- [17] T. J. Choi. Development of an effective computational methodology for multi-stage compressor map generation. Master's thesis, Massachusetts Institute of Technology, 2001.
- [18] Y. Colin. *Simulation numérique de la distortion générée par une entrée d'air de moteur civil par vent de travers*. PhD thesis, Université de Toulouse, 2007.
- [19] H. F. Creveling. Axial-flow compressor computer program for calculating off-design performance. Technical report, NASA, 1968.
- [20] N. A. Cumpsty. *Compressor Aerodynamics*. Krieger Publishing Company, 2004.
- [21] T. Q. Dang. Simulations of propeller/airframe interference effects using an Euler correction method. *Journal of Aircraft*, 26(11), 1989.
- [22] J. Defoe. *Inlet swirl distortion effects on the generation and propagation of fan rotor shock noise*. PhD thesis, Massachusetts Institute of Technology, 2011.
- [23] J. Defoe, A. Narkaj, and Z. Spakovszky. A novel MPT noise methodology for highly-integrated propulsion systems with inlet flow distortion. In *15th AIAA/CEAS Aeroacoustics Conference*, Miami, Florida, May 2009. AIAA 2009-3366.
- [24] J. Defoe, A. Narkaj, and Z. Spakovszky. A body-force-based method for prediction of multiple-pure-tone noise: Validation. In *16th AIAA/CEAS Aeroacoustics Conference*, Stockholm, Sweden, June 2010. AIAA 2010-3747.
- [25] J. D. Denton. Throughflow calculations for transonic axial flow turbines. *Journal of Engineering for Power*, 100(2), 1978.

- [26] J. D. Denton. Loss mechanisms in turbomachines. *Journal of Turbomachinery*, 115:621–656, October 1993.
- [27] M. Drela. Power balance in aerodynamic flows. *AIAA Journal*, 47(7), July 2009.
- [28] M. Drela. Making an extraordinary machine better : the D8 aircraft concept. In *TEDxNewEngland*, 2012.
- [29] G. Dufour and W. Thollet. Body force modeling of the aerodynamics of the fan of a turbofan at windmill. In *Proceedings of ASME Turbo Expo 2016 : Turbomachinery Technical Conference and Exposition*, Seoul, Korea, June 2016. Paper no. GT2016-57462.
- [30] J. F. Escuret and V. Garnier. Numerical simulations of surge and rotating-stall in multi-stage axial-flow compressors. In *AIAA, ASME, SAE, and ASEE, Joint Propulsion Conference and Exhibit, Indianapolis, IN*, 1994.
- [31] J. L. Felder, G. V. Brown, H. D. Kim, and J. Chu. Turboelectric distributed propulsion in a hybrid wing body aircraft. In *Proceedings of the 20th ISABE Conference*, Gothenburg, 12-16 September 2011. Paper no. ISABE-2011-1340.
- [32] V. J. Fidalgo, C. A. Hall, and Y. Colin. A study of fan-distortion interaction within the nasa rotor 67 transonic stage. *Journal of Turbomachinery*, 134(5), 2012.
- [33] G. Fillola, M. L. Pape, and M. Montagnac. Numerical simulations around wing control surfaces. In *24th International Congress of the Aeronautical Sciences*. ICAS, 2004.
- [34] B. François, M. Laban, M. Costes, G. Dufour, and J. F. Boussuge. In-plane forces prediction and analysis in high-speed conditions on a contra-rotating open rotor. *Journal of Turbomachinery*, 136(8), January 2014.
- [35] S. J. Gallimore. Viscous throughflow modeling of axial compressor bladerows using a tangential blade force hypothesis. *Journal of Turbomachinery*, 120(4):662–670, October 1998.
- [36] S. J. Gallimore and N. A. Cumpsty. Spanwise mixing in multistage axial flow compressors : Part 1 - experimental investigation. *ASME Journal of Turbomachinery*, 108:2–9, 1986.
- [37] S. J. Gallimore and N. A. Cumpsty. Spanwise mixing in multistage axial flow compressors: Part 2 - throughflow calculations including mixing. *ASME Journal of Turbomachinery*, 108:10–16, 1986.
- [38] B. Godard, E. D. Jaeghere, N. B. Nasr, J. Marty, R. Barrier, and N. Gourdain. A review of inlet-fan coupling methodologies. In *Proceedings of ASME Turbo Expo 2017 : Turbomachinery Technical Conference and Exposition*, Charlotte, USA, June 2017. Paper no GT2017-63577.

- [39] Y. Gong. *A computational model for rotating stall and inlet distortions in multistage compressors*. PhD thesis, Massachusetts Institute of Technology, 1998.
- [40] Y. Gong, C. S. Tan, K. A. Gordon, and E. M. Greitzer. A computational model for short wavelength stall inception and development in multistage compressors. In *Proceedings of ASME 1998 International Gas Turbine and Aeroengine Congress and Exhibition*, Stockholm, Sweden, 1998.
- [41] N. Gourdain, M. Montagnac, F. Wlassow, and M. Gazaix. High-performance computing to simulate large-scale industrial flows in multistage compressors. *International Journal of High Performance Computing Applications*, 24(4), 2010.
- [42] E. Greitzer, C. Tan, and M. Graf. *Internal flow: concepts and applications*. Cambridge University Press, 2007.
- [43] D. Guegan, F. Julienne, M. Schvallinger, N. Gourdain, M. Gazaix, and M. Montagnac. Three dimensional full annulus unsteady RANS simulation of an integrated propulsion system. In *Proceedings of the 51st AIAA/SAE/ASEE Joint Propulsion Conference, AIAA Propulsion and Energy Forum*, Orlando, FL, July 27-29 2015. Paper no. AIAA 2015-4021.
- [44] E. J. Gunn and C. A. Hall. Aerodynamics of boundary layer ingesting fans. In *Proceedings of ASME Turbo Expo : Turbine Technical Conference and Exposition*, Dusseldorf, Germany, June 16-20 2014. Paper no. GT2014-26142.
- [45] A. Hale, M. Davis, and J. Sirbaugh. A numerical simulation capability for analysis of aircraft inlet-engine compatibility. *J. Eng. Gas Turbines Power*, 3(128):473–148, March 2004.
- [46] A. Hale and W. O’Brien. A three-dimensional turbine engine analysis compressor code (TEACC) for steady-state inlet distortion. *Journal of Turbomachinery*, 120(3):422–430, 1998.
- [47] C. A. Hall, E. Schwartz, and J. I. Hileman. Assessment of technologies for the silent aircraft initiative. *Journal of Propulsion and Power*, 25(6), 2009.
- [48] D. K. Hall. *Analysis of Civil Aircraft Propulsors with Boundary Layer Ingestion*. PhD thesis, Massachusetts Institute of Technology, 2015.
- [49] D. K. Hall, E. M. Greitzer, and C. S. Tan. Analysis of fan stage design attributes for boundary layer ingesting propulsion. In *Proceedings of ASME Turbo Expo 2016 : Turbomachinery Technical Conference and Exposition*, Seoul, Korea, June 2016. Paper no. GT2016-57808.
- [50] E. Hsiao, M. Naimi, J. P. Lewis, K. Dalbey, Y. Gong, and C. Tan. Actuator duct model of turbomachinery components for powered-nacelle Navier-Stokes calculations. *Journal of Propulsion and Power*, 17(4):919–927, 2001.

- [51] C. Hughes, R. Jeracki, R. Woodward, and C. Miller. Fan noise source diagnostic test - rotor alone aerodynamic performance results. In *8th AIAA / CEAS Aeroacoustics Conference and Exhibit*, Breckenridge, Colorado, June 2002. AIAA 2002-2426.
- [52] R. Jansen, C. Bowman, and A. Jankovsky. Sizing power components of an electrically driven tail cone thruster and a range extender. In *Proceedings of the 16th AIAA Aviation Technology, Integration and Operations Conference*, Washington, D.C., 2016. Paper no 2016-3766.
- [53] W. G. Joo and T. P. Hynes. The application of actuator disks to calculations of the flow in turbofan installations. *Journal of turbomachinery*, 119(733), October 1997.
- [54] J. Kerner. An assessment of body force representations for compressor stall simulation. Master's thesis, Massachusetts Institute of Technology, 2010.
- [55] H. Kim and M.-S. Liou. Flow simulation of N3X hybrid wing-body configuration. In *Proceedings of 51th AIAA Aerospace Sciences Meeting*, 2013. AIAA 2013-0221.
- [56] G. Kiwada. Development of a body force description for compressor stability assessment. Master's thesis, Massachusetts Institute of Technology, 2008.
- [57] C. C. Koch and L. H. Smith. Loss sources and magnitudes in axial-flow compressors. *Journal of Engineering for Power*, 1976.
- [58] A. P. Kottapalli. Development of a body force model for centrifugal compressors. Master's thesis, Massachusetts Institute of Technology, 2013.
- [59] M. J. Larkin and P. S. Schweiger. Ultra high bypass nacelle aerodynamics : Inlet flow-through nacelle high angle of attack distortion test. Technical Report 189149, NASA, 1992.
- [60] S. Lieblein. Aerodynamic design of axial-flow compressors - experimental flow in two dimensional cascades. Technical report, National Advisory Committee for Aeronautics. Lewis Flight Propulsion Lab; Cleveland, OH, United States, 1955.
- [61] S. Liodice, P. G. Tucker, and J. Watson. Modelling of coupled open rotor engine intakes. In *Proceedings of 48th AIAA Aerospace Sciences Meeting*, January 2010. AIAA 2010-840.
- [62] F. Marble. *Three Dimensional Flow in Turbomachines*, volume X of *High Speed Aerodynamics and Jet Propulsion*, pages 83–166. Princeton Univesity Press, 1964.
- [63] C. O. Marquez and A. Stuermer. Validation of actuator disk simulations of CROR propulsion systems at low-speed flight conditions. In *Proceedings of 30th AIAA Applied Aerodynamics Conference*, New Orleans, Louisiana, June 2012. AIAA 2012-2787.
- [64] M. Meinel and G. O. Einarsson. The flowsimulator framework for massively parallel CFD applications. In *PARA 2010 conference: state of the art in scientific and parallel computing*, 2010.

- [65] F. Moens and P. Gardarein. Numerical simulation of the propeller/wing interactions for transport aircraft. In *Proceedings of 19th AIAA Applied Aerodynamics Conference*, Anaheim, CA, 2001. AIAA 2001-2404.
- [66] W. Ning and L. He. Computation if unsteady flows around oscillating blades using linear and nonlinear harmonic euler methods. *Journal of Turbomachinery*, 120(3), July 1998.
- [67] R. Owens., K. Hasel, and D. Mapes. Ultra high bypass turbofan technologies for the twenty-first century. In *26th Joint Propulsion Conference*, 1990. AIAA 1990-2397.
- [68] A. A. Patel. Assessment of a body force representation for compressor stability estimation. Master's thesis, Massachusetts Institute of Technology, 2009.
- [69] A. Peters. *Ultra-short nacelles for low fan pressure ratio propulsors*. PhD thesis, Massachusetts Institute of Technology, 2014.
- [70] A. Peters, Z. S. Spakovszky, W. K. Lord, and B. Rose. Ultra-short nacelles for low fan pressure ratio propulsors. *Journal of Turbomachinery*, 137(2), 2015.
- [71] A. P. Plas, M. A. Sargeant, V. Madani, D. Crichton, E. M. Greitzer, T. P. Hynes, and C. A. Hall. Performance of a boundary layer ingesting (BLI) propulsion system. In *Proceedings of 45th AIAA Aerospace Sciences Meeting and Exhibit*, Reno, Nevada, January 2007. AIAA 2007-450.
- [72] G. Pullan and J. J. Adamczyk. Filtering mixing planes for low reduced frequency analysis of turbomachines. In *ASME Turbo Expo 2016*, Seoul, South Korea, June 13–17 2016. Paper no GT2016-57380.
- [73] A. Purwanto, T. Deconinck, S. Vilmin, E. Lorrain, and C. Hirsch. Efficient prediction of nacelle installation effects at take-off conditions. In *9th European Turbomachinery Conference*, Istanbul, Turkey, March 21-25 2011.
- [74] G. A. Reichstein. Estimation of axial compressor body forces using three-dimensional flow computations. Master's thesis, Massachusetts Institute of Technology, 2009.
- [75] W. B. Roberts, G. K. Serovy, and D. M. Sandercock. Modeling the 3-d flow effects on deviation angle for axial compressor middle stages. *Journal of Engineering for Gas Turbines and Power*, 1986.
- [76] W. B. Roberts, G. K. Serovy, and D. M. Sandercock. Design point variation of three-dimensional loss and deviation for axial compressor middle stages. *Journal of Turbomachinery*, 110(4), 1988.
- [77] D. Rutherford and M. Zeinali. Efficiency trends for new commercial jet aircraft. Technical report, International Council on Clean Transportation, 2009.
- [78] Y. Sadoudi. *Numerical simulation of Fan/Nacelle interaction under crosswind conditions*. PhD thesis, Université de Toulouse, 2016.

- [79] J. Sans, J. Brouckaert, and S. Hiernaux. Experimental and numerical investigations of the solidity effect on a linear compressor cascade. In *ASME Turbo Expo 2015 : Turbine Technical Conference and Exposition*, Montreal, Canada, June 15-19 2015. Paper no. GT2015-43204.
- [80] G. Sharma, L. Zori, S. Conell, and P. Godin. Efficient computation of large pitch ratio transonic flow in a fan with inlet distortion. In *ASME Turbo Expo 2013 : Turbine Technical Conference and Exposition*, San Antonio, Texas, June 3-7 2013. Paper no. GT2013-95059.
- [81] W. Z. Shen and J. N. Sorensen. Actuator surface model for wind turbine flow computations. In *Proceedings of the 2007 EWEC conference*, Milan, 2007.
- [82] J.-F. Simon. *Contribution to throughflow modelling for axial flow turbomachines*. PhD thesis, Universite de Liege, 2007.
- [83] J. Sorensen and W. Z. Shen. Numerical modeling of wind turbine wakes. *Journal of Fluids Engineering*, 124:393–399, 2002.
- [84] W. A. Sorensen. A body force model for cavitating inducers in rocket engine turbopumps. Master’s thesis, Massachusetts Institute of Technology, 2014.
- [85] A. Spurr. The prediction of 3D transonic flow in turbomachinery using a combined throughflow and blade-to-blade time marching method. *International Journal of Heat and Fluid Flow*, 2(4):189–199, 1980.
- [86] W. Thollet, G. Dufour, F. Blanc, and X. Carbonneau. Body force modeling for aerodynamic analysis of air intake-fan interactions. In *Proceedings of the 50th 3AF conference on applied aerodynamic*, Toulouse, France, April 2015.
- [87] J. C. Tyacke, M. Mahak, and P. G. Tucker. Large-scale multifidelity, multiphysics, hybrid reynolds-averaged navier-stokes/large-eddy simulation of an installed aeroengine. *Journal of Propulsion and Power*, 32(4), 2016.
- [88] A. Uranga, M. Drela, E. Greitzer, N. Titchener, M. Lieu, N. Siu, A. Huang, G. M. Gatlin, and J. Hannon. Preliminary experimental assessment of the boundary layer ingestion benefit for the D8 aircraft. In *52nd Aerospace Sciences Meeting*, pages 13–17, National Harbor, MD, 2014. Paper no. AIAA 2014-0906.
- [89] T. K. Walker III. The development and requirements of a body force database from two-dimensional and streamline curvature calculations. Master’s thesis, Massachusetts Institute of Technology, 2009.
- [90] D. L. Whitfield and A. Jameson. Euler equation simulation of propeller-wing interaction in transonic flow. *Journal of Aircraft*, 21(11), 1984.
- [91] L. Wiart, O. Atinault, J.-C. Boniface, and R. Barrier. Aeropropulsive performance analysis of the nova configurations. In *Proceedings of the 30th congress of the International Council of the Aeronautical Sciences (ICAS)*, Daejeon, Korea, September 2016.

- [92] L. Xu. Assessing viscous body forces for unsteady calculations. *ASME Journal of Turbomachinery*, 125, July 2003.
- [93] F. M. Zadeh, J.-Y. Trepanier, and E. Petro. Development and validation of a new boundary condition for intake analysis with distortion. *International Journal of Aerospace Engineering*, 2013(284206), 2013.

# Appendix A

## Loss modeling for compressor cascades

This appendix describes a study that aims at improving the modeling of the loss in axial compressor cascades. CFD computations are run on parametric cascade geometries to evaluate the loss, which is then correlated against the cascades geometrical parameters. Although no model is proposed, this study could constitute a basis for future work.

### A.1 Motivation and objective

An accurate modeling of the loss and hence an accurate formulation for the parallel force is required to capture the performance of a blade row under distorted inflow. In fact, the loss alters the velocity distributions, affects the work coefficient, reduces the choke mass flow rate and drives the efficiency. All the loss formulations proposed in the previous section are based on a simple drag relationship in which the drag coefficient modeling is very limited: it does not explicitly depend on the blade geometry and has thus to be recalibrated for each new case. Furthermore, the different physical mechanisms that generate the loss are not considered separately, but included into this bulk drag coefficient. In past contributions, losses in turbomachinery blade rows were often divided into three categories:

- Profile loss, due to the boundary layers on the blade walls. Correlations for this loss were often based on two-dimensional cascade tests.
- Endwall loss or secondary loss, which arises due to the interactions of the blades with the hub and shroud boundary layers.
- Tip leakage loss, generated by the leakage of the flow in clearances between blades and endwalls.

To these three categories should be added the shock loss. This loss can hardly be estimated on 2D cascade profiles as it is highly dependent on 3D effects such as leading edge sweep. As explained by Denton [26], this breakdown of the loss is over-simplified, as it is difficult to evaluate how independent each loss component is from the others. Many correlations

have been used in the framework of mean-line or throughflow modeling to estimate the loss. However, most of them suffer from two main limitations:

- These correlations are usually based on global variables, such as Diffusion Factor or blade incidence [19, 57, 76]. They must therefore be applied along streamlines, which are subject to large radial and tangential shifts in a fan operating under distorted inflow, and usually not available during the computation in most CFD solvers. A local loss formulation is preferable to enable a direct estimation of efficiency under distorted inflow.
- Most of those correlations are based on “simple” profile geometries, such as NACA profiles. Modern fan geometries are made of custom profiles and use 3D effects to reduce the loss. Each manufacturer has therefore its own proprietary correlations to evaluate the loss on their geometries.

While previous loss correlations were mostly based on experiments, from which the amount of available local data is in general limited, it is thought that a large database of cascade CFD computations may allow developing a local formulation. One difficulty is that the loss in cascades can be affected by many geometrical and operating parameters. The objective of the present study is to propose a relevant parametric cascade study and to find some correlations between the loss and these parameters, which could constitute a basis for an explicit, local, loss model.

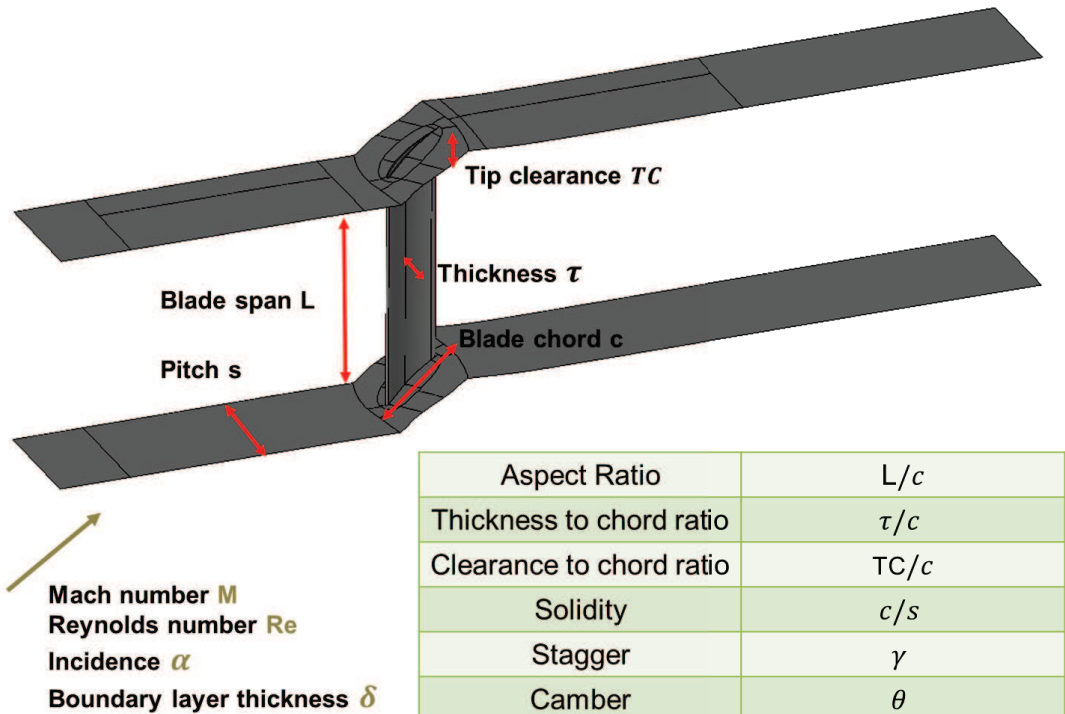


**Figure A.1:** Illustration of the parametric linear cascade geometry.

## A.2 Parametric linear cascades generation

A procedure was developed to generate and mesh parametric linear cascade geometries. First, a 2D blade profile is defined using circular arc camberlines and a NACA 4 digits thickness distribution. The parameters for this 2D profile are:

- Stagger
- Camber
- Solidity (chord to pitch ratio)
- Maximum thickness to chord ratio

Then the 2D blade profile is extruded to get a 3D prismatic blade (no twist). The following parameters are used to perform the extrusion:

- Aspect ratio
- Tip clearance to chord ratio

Finally, CFD computations are run on these geometries, with the following independent flow parameters:

- Mach number
- Reynolds number
- Incidence
- Inlet boundary layer thickness to chord ratio

The cascade parameters are illustrated in figure A.1. In the present study, there are ten parameters that can potentially affect the loss. Some parameters such as the camber and thickness distributions or 3D treatments are not considered. To control the inlet boundary layer thickness to chord ratio, all cascade computations were launched using a parametric inlet velocity profile for which the boundary layer thickness was specified. Then, the boundary layer was convected toward the blade using slip wall conditions on the hub and shroud up to a few percent chord upstream of the leading edge.

## A.3 Construction of loss metrics and loading parameter

Because the cascade geometries presented in the previous section are purely 2D, it is easier to separate the loss in several component, as was done in previous studies:

- The 2D profile loss that occurs at midspan

- The additional 3D loss that occurs near the hub, because of the interaction of the blade with the endwall.
- The additional 3D loss that occurs near the shroud, because of the tip clearance.

If each loss component is modeled independently from the others, it may allow to capture most of the loss mechanisms occurring in a real geometry. Because of a lack of time to study each loss separately, only the loss at the tip of the blade was assessed in the present work. It was thought that the process used to evaluate and correlate this loss to geometrical and flow parameters could be extended to the 2D profile loss and to the loss occurring near the hub. Moreover, it is the only loss that is affected by all the parameters described in the previous section, including tip clearance. In the next sections, loading and loss metrics are defined, then correlated against each other for a set of geometrical and flow parameters.

### A.3.1 Loss metrics

Some metrics describing the amount and distribution of the 3D loss at the tip are needed. Because the purpose of this parametric cascade study is to find some correlation to model the parallel force, the parametric cascade results are averaged in the pitchwise direction. The mass averaged entropy is a useful loss metric candidate, as it is not frame-dependent and as it can directly be used to compute the parallel force using equation (2.6).

To extract a parallel force from blade computations, Brand [8] chose to distribute the loss evenly from leading to trailing edge using a “mean” entropy gradient, already described in equation (2.15), to smooth the loss distribution. This can be a good approximation near the design point and at mid-span, where the entropy may vary almost linearly from leading to trailing edge. Contours of local entropy gradient and mean entropy gradient are shown in figure A.2. It is worth noticing that the entropy can decrease along averaged meridional streamlines, which is due to its transport by secondary flows in the 3D blade simulation. In particular, the entropy is lower in the tip gap at the trailing edge of the blade than it is at the leading edge. The center of the region where the loss is the highest travels from the shroud to lower radii, with an almost linear trajectory. Similar results were obtained by Chen et al. [14], concerning the tangential trajectory of the tip leakage vortex.

Given the shape of this vortex trajectory, it is unlikely that a completely local model can be used to capture the 3D loss at the tip. In particular, the spanwise position of the vortex at a given axial location depends on its previous spanwise positions. As a first step, only the bulk entropy production in the tip is therefore evaluated. Using the distributions of mass averaged entropy, a mean entropy gradient across the blade is computed using the leading and trailing edges entropy values:

$$\frac{\Delta S}{\Delta m} = \frac{S_{TE} - S_{LE}}{c \cos \gamma} \quad (\text{A.1})$$

where  $c$  and  $\gamma$  are the chord and the stagger of the cascade, respectively. This extraction is done at constant span, neglecting streamline shifts due to 3D effects. Then, to evaluate the total amount of entropy that needs to be added to the flow for a given set of parameters, this

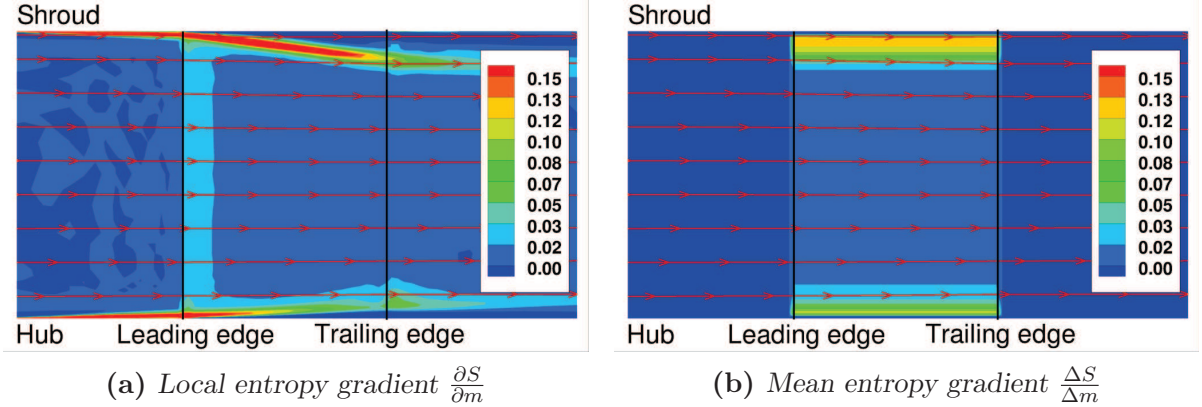


**Figure A.2:** Meridional contours of pitch-averaged entropy gradients. The red lines are streamlines computed with the pitch-averaged axial and radial velocities.

entropy gradient is integrated along the span, using a mass weighting based on the velocities at the trailing edge of the blade:

$$\overline{\Delta S_{3D}} = \frac{\int \rho V (\Delta S - \Delta S_{2D}) dr}{\int \rho V dr} \quad (\text{A.2})$$

The  $\Delta S_{2D}$  parameter is taken at midspan, where the cascade loss is purely 2D, as shown in figure A.3. Finally, the spanwise area contaminated by the 3D losses is extracted:

$$\Delta R_{3D} = R_{tip} - R_{(\Delta S = \Delta S_{2D})} \quad (\text{A.3})$$

With the knowledge of both quantities, it is possible to input the right amount of losses into the flow on the correct fraction of the span.

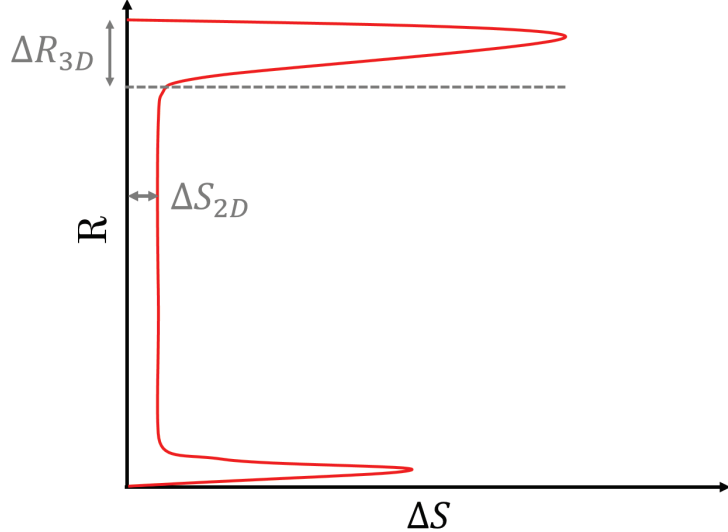


**Figure A.3:** Spanwise distribution of entropy downstream of the cascade blade.

Following what is done in similarity analysis, non-dimensional scaling parameters are built on these metrics. A preliminary analysis conducted with a given set of geometrical and operating parameters but with varying chord showed that the  $\Delta R_{3D}$  parameter scaled almost exactly with the chord. This seems consistent with the fact that the tip vortex trajectory is almost linear along the axial direction. This allows to define a first non-dimensional loss extent metric:

$$H_{3D} = \frac{\Delta R_{3D}}{c} \quad (\text{A.4})$$

In practice, a version of  $\Delta R_{3D}$  built with the local entropy gradient may scale very well with the axial position from the leading edge. The second metric is a loss coefficient denoted  $\xi_{3D}$  and is computed as:

$$\xi_{3D} = \frac{T_0 \Delta S_{3D}}{\sqrt{\sigma} W_0^2} \quad (\text{A.5})$$

where the 0 subscript denotes inlet conditions.

### A.3.2 Loading metric

As will be shown in the next section the values taken by the normal force are a good indicator of the amount of tip loss in a blade row. The normal force is thus extracted from the pitch-averaged cascade solutions using the following equations:

$$f_\theta = \frac{W_m}{r} \frac{\partial r V_\theta}{\partial m} \quad (\text{A.6})$$

$$fp_\theta = T \frac{\partial S}{\partial m} \frac{W_m}{W} \frac{W_\theta}{W} \quad (\text{A.7})$$

$$f_n = -(f_\theta - fp_\theta) \frac{W}{W_m} \quad (\text{A.8})$$

Then a loading factor is defined as:

$$f_n^* = \frac{f_n s \sqrt{\sigma}}{W^2} \quad (\text{A.9})$$

The  $\sqrt{\sigma}$  factor in this loading factor improves the correlation of the loss. The use of the normal force is appropriate, as it is a parameter directly available in body force simulations. Physically, it is a good indicator of the difference of static pressure across the blade, which was shown to drive the tip leakage loss [26]. This loading factor can be computed locally, which is desired in the targeted loss model, but this is not compatible with the bulk loss parameters that were defined previously. To remain consistent with these loss parameters, a global version of the loading factor has to be defined. A simple way to do this is to compute the average of the loading factor along the blade chord. The discrete version of this mean loading factor can be computed with the following equation:

$$\bar{f}_n^* = \frac{1}{n_i} \sum_{i=1}^{n_i} f_n^* \quad (\text{A.10})$$

where  $n_i$  is the number of points from leading to trailing edge in the axial direction.

### A.3.3 Local vs global metrics

Both the loss and loading metrics described in the previous section are based on an integration of local variables, and are thus “global”. This is not compatible with the targeted loss model, that should be completely local. One solution to simplify the modeling process and to use these global metrics is to compute the loss coefficient *per* circumferential sector, as shown in figure A.4. The mean loading factor is extracted near the tip of the blade for each circumferential sector and used to compute the corresponding loss coefficient and loss extent in this circumferential sector. The main limitation of this simplification are that the tangential shift of the streamlines within the blade row is neglected, and that it is restricted to structured meshes. Another solution to make the model more local could be to compute the loss coefficient and the loss extent at each axial station, using the loading coefficient at the same axial location near the tip (i.e. no integration), but this would remove the spatial coherence of the contaminated area along the blade chord.

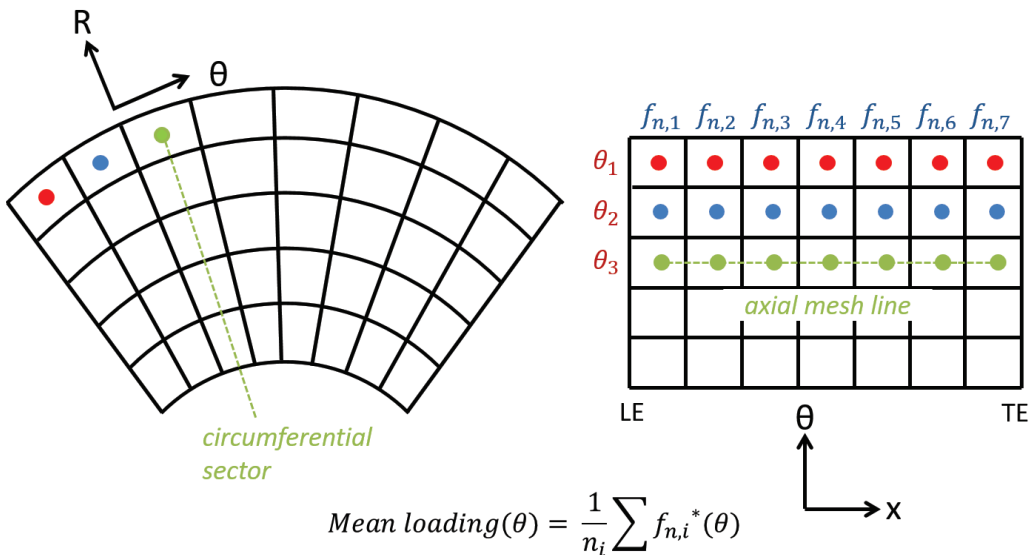


**Figure A.4:** Computation of a mean loading coefficient on a circumferential sector in a body force computation. A mean loading coefficient can be computed at the tip for each circumferential sector, and the corresponding loss can be applied on the desired fraction of the span from leading to trailing edge, on the same sector.

## A.4 Correlation of loss metrics against the loading parameter

### A.4.1 Effect of aspect ratio

The effect of aspect ratio was assessed by examining 3D loss distributions on identical 2D blade geometries with aspect ratios ranging from 1.2 to 2. Spanwise profiles of entropy downstream of the cascade blades for 3 different aspect ratios are shown in figure A.5. It can be seen that the local profiles of entropy are not modified by changes in aspect ratio, although the impact of the 3D loss on the overall loss decreases when the aspect ratio increases. This observation confirms that the relevant length scale for studying the 3D loss is the chord of the blade, which was already reported in [14, 20].

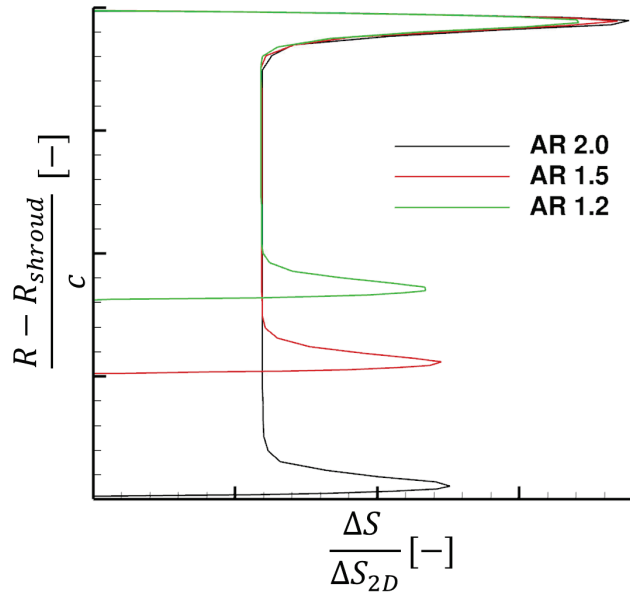


**Figure A.5:** Effect of aspect ratio on the 3D loss.

### A.4.2 Effect of camber, stagger, and solidity

Several CFD computations were run, varying the camber, the stagger, and the solidity of the cascade geometry. The range of parameters used for these computations is shown in table A.1. The results for the loss coefficient  $\xi_{3D}$  are shown in figure A.6a. An encouraging, almost linear, correlation appears between the defined loss coefficient and the mean loading factor, with data dispersion at  $\bar{f}_n^* = 1$  of about  $+/-5\%$ . It should be noted that obtaining this correlation was only possible using the  $\sqrt{\sigma}$  factor in both the loss coefficient  $\xi_{3D}$  and loading factor  $f_n^*$ , which reminds of Carter's deviation rule and previous body force modeling work [22, 39]. Figure A.6b shows the  $H_{3D}$  factor plotted against the mean loading. The “stair-case” aspect of this plot is due to the radial resolution of the meshes employed for this study: the 3D loss extent captured in 3D computations “jumps” from one value to another with jumps corresponding to the radial extent of a meridional mesh cell. Both figures show

that it seems possible to capture changes in stagger, camber, and solidity with the loss metrics and with the loading parameter defined previously.

Mach number	0.3
Reynolds number	$10^6$
Incidence	$-8^\circ$ to $+8^\circ$
Aspect ratio	1.0
Thickness to chord ratio	0.03
Tip clearance to chord ratio	0.0005
Solidity	1.2 to 2.4
Stagger	$0^\circ$ to $60^\circ$
Camber	$10^\circ$ to $30^\circ$

**Table A.1:** Preliminary cascade computations parameters.

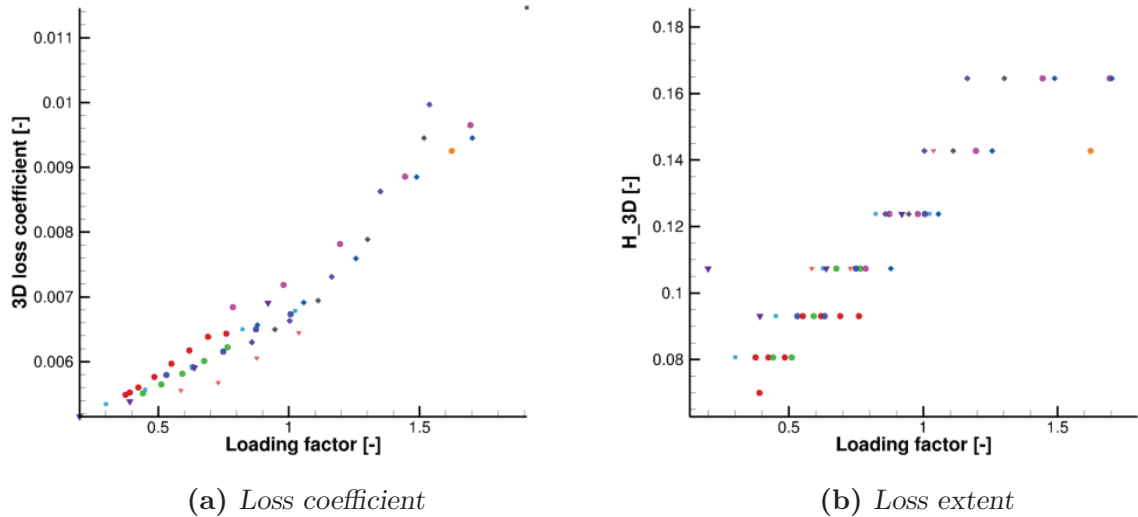


**Figure A.6:** Loss coefficient  $\xi_{3D}$  and loss extent  $H_{3D}$  against mean loading factor  $\bar{f}_n^*$  for a range of camber, stagger, and solidity. A correlation seems to emerge between the loss metrics and the loading metric.

#### A.4.3 Effect of thickness

The effect of thickness to chord ratio on the 3D loss is shown in figure A.7. The thickness to chord ratio has a significant effect on the 3D loss coefficient value, although it does not impact its slope. This indicates that the effect of thickness to chord ratio is completely decoupled from the effect of blade loading:

$$\xi_{3D} = F \left( \bar{f}_n^*, \frac{\tau}{c} \right) \quad (\text{A.11})$$

The effect on the loss extent is hard to determine because of the poor resolution of this parameter.

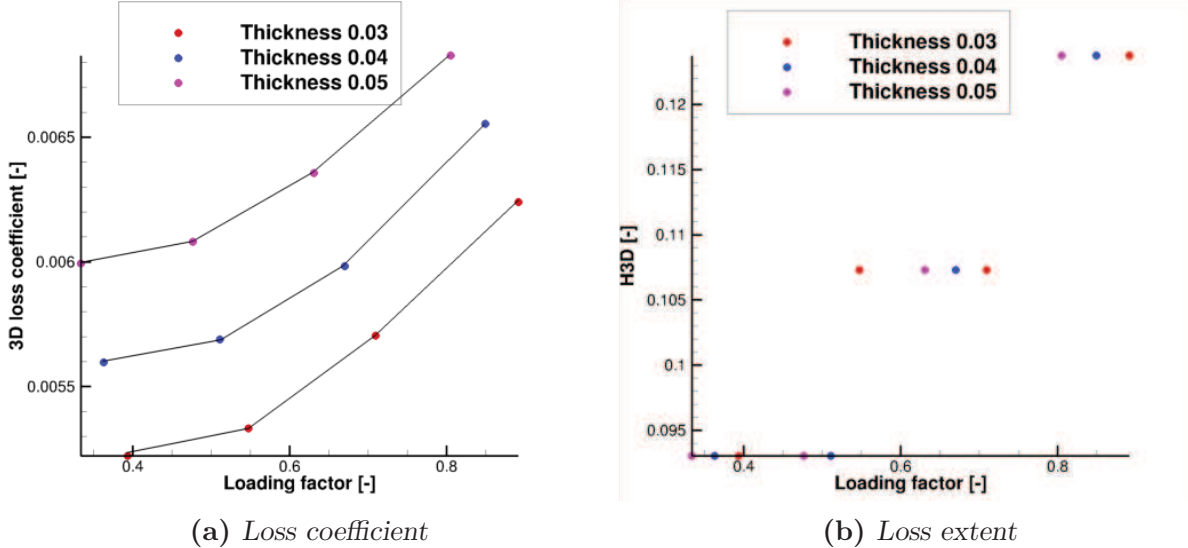


**Figure A.7:** Loss coefficient  $\xi$  and loss extent  $H_{3D}$  against mean loading factor  $\bar{f}_n^*$  for three different thickness to chord ratios. The effect of thickness is decoupled from the effect of the loading.

#### A.4.4 Effect of tip clearance

The effect of tip clearance to chord ratio on the 3D loss is shown in figure A.8. The tip clearance impacts both the values and slope of the loss coefficient, which means that the effect of tip clearance is coupled with the effect of the loading:

$$\xi_{3D} = F \left( \bar{f}_n^*, \frac{\tau}{c}, \frac{TC}{c} \otimes \bar{f}_n^* \right) \quad (\text{A.12})$$

where  $\otimes$  is an unknown operator that combines two quantities. Again, the effect on the loss extent is hard to evaluate, but it seems that the  $H_{3D}$  parameter also increases with the tip clearance to chord ratio.

#### A.4.5 Effect of Mach number

The effect of Mach number on the 3D loss is shown in figure A.9. There is no effect of Mach number to be seen between  $M = 0.3$  and  $M = 0.5$ , but a significant change of the shape and values taken by the loss coefficient can be observed at  $M = 0.7$ , possibly due to transonic effects. The effect of the Mach number on the loss extent seems to be small. Although the data here is very limited, it is therefore likely that the Mach number will mainly have some impact on the 3D loss coefficient.

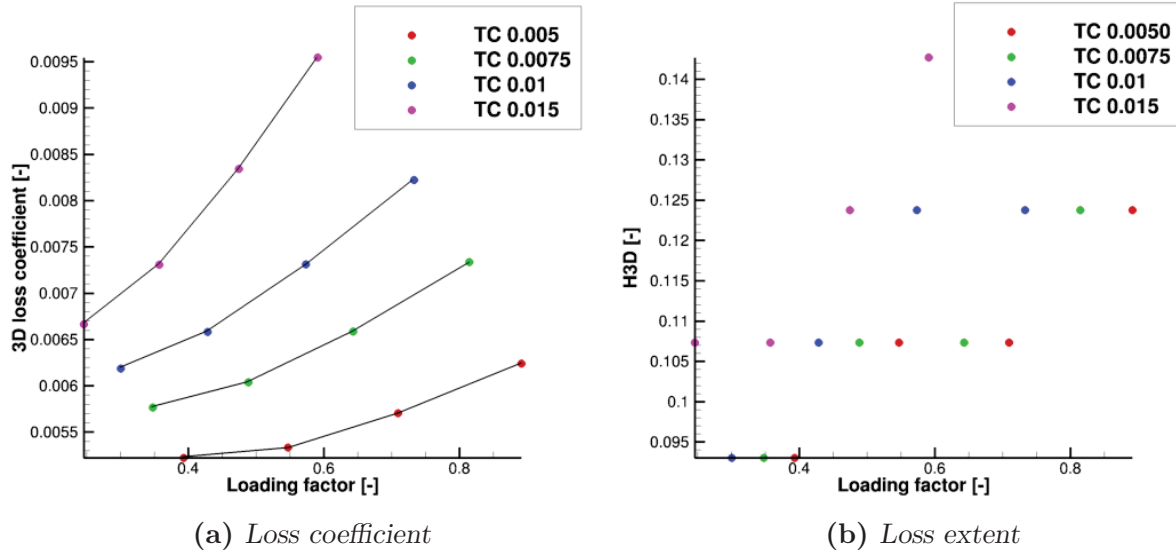


**Figure A.8:** Loss coefficient  $\xi_{3D}$  and loss extent  $H_{3D}$  against mean loading factor  $\bar{f}_n^*$  for four different tip clearance to chord ratios. The effect of tip clearance is coupled with the effect of the loading.

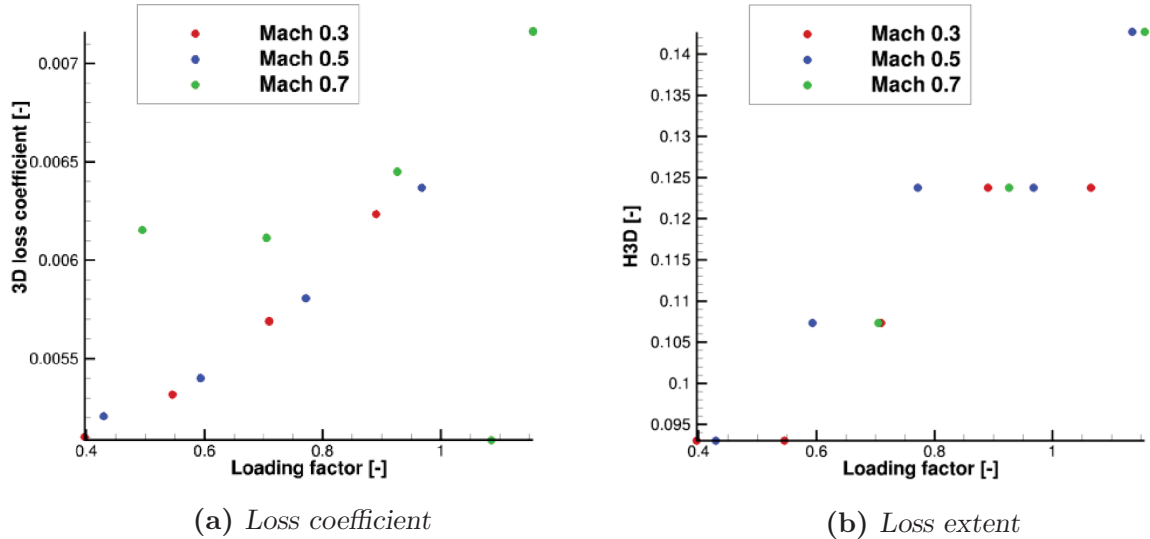


**Figure A.9:** Loss coefficient  $\xi$  and loss extent  $H_{3D}$  against mean loading factor  $\bar{f}_n^*$  for four Mach numbers. There is a significant effect of the Mach number on the loss coefficient at  $M = 0.7$ .

#### A.4.6 Other effects

The two remaining parameters that have not been studied here are the Reynolds number and the boundary layer thickness. While it is thought that the effect of the Reynolds number should be negligible compared to other effects, the effect of the boundary layer thickness

raises uncertainties. In past correlations, this effect was often included (see [75] for instance) but for a final application in which the endwall friction was not directly computed as it is the case here. Two questions can therefore be asked:

- Does the boundary layer thickness only impact the endwall losses that are already captured in the body force computation, or does it alter the interactions of the endwall flow with the blade and should therefore be taken into account in the correlations ?
- How to separate (i) the losses due to the endwall that are already resolved in the body force computations from (ii) the 3D losses that are due to the interactions of the blade with the endwalls and that are not resolved in body force computations ?

As specified above, the boundary layer thickness was imposed at the inlet of the computational domain using parametric velocity profiles. However, even with this approach, it was difficult to keep the boundary layer thickness as specified at the inlet, as some numerical diffusion occurred between the inlet and the blade leading edge, altering the radial velocity distribution. To effectively separate the endwalls losses already captured in body force computations and the 3D losses, a solution could be to take the difference between the circumferentially averaged flow field from bladed computations and the equivalent axisymmetric body force computation without any parallel force. This way, only the 3D losses due to the interaction of the blade with the endwall would remain.

## A.5 Summary and way forward

Here is a summary of what was learned in this section:

- A loading parameter and two loss metrics that enclose the total entropy generation due to 3D losses at the tip of the blade were proposed.
- The loss metrics are functions of the loading parameter, thickness to chord ratio, tip clearance to chord ratio and Mach number.
- The loss metric  $H_{3D}$  suffers from a lack of spanwise resolution in the 3D and meridional meshes on which the tangential average is performed.

This information is far from enough to effectively lead to a parallel force formulation. The main finding is that the tip loss can be correlated using the knowledge of the normal force and some geometrical parameters in the body force computation, but it is unclear how exactly the loss should be computed (local vs global) and distributed in the computational domain. The same uncertainty arises concerning the loss at the intersection between blade and endwall. It is thought that the 2D profile loss may be easier to correlate, as it is affected by fewer parameters, but the normal force may not be a good loading metric in that case. Another possible limitation of the present approach concerns the modeling of the loss due to leading edge bow shocks. In fact, this loss is very sensitive to 3D effects such as leading edge sweep, and to the blade thickness at the leading edge. Using NACA profiles will not allow to be representative of the loss occurring with more realistic blade profiles, tailored

for supersonic flows. In addition, it should be kept in mind that the accuracy of the results that could be obtained with the present approach is very dependent on the accuracy of the CFD cascade simulation, which is limited in a RANS context. For instance it was found by Sans et al. [79] that the off-design loss in cascades was not well estimated with a RANS code, but a good agreement with experimental data was obtained with LES. To alleviate these limitations, the model could be produced using the cascade database correlations and one or several realistic fan blade geometries, for which experimental data is available. The correlations would be useful to identify what are the parameters driving the loss, and the model could then be established based on quantitatively more accurate results.

Another potential outcome of the present study is the development of a model for aerodynamic blockage, which was neglected in the present thesis. In high pressure compressors for instance, the aerodynamic blockage on the endwall is strongly affected by corner flow separation and by tip leakage flow, not captured in body force simulations. As a consequence, the velocity distributions along the span are significantly altered, which has a direct impact on the work input. In that case, capturing the aerodynamic blockage is thus especially important.

## Appendix B

# Circumferentially averaged Navier Stokes Equations

### B.1 Derivation of the equations

The Navier-Stokes equations in cylindrical coordinates can be written :

$$\frac{\partial \rho}{\partial t} + \frac{\partial \rho V_x}{\partial x} + \frac{\partial r \rho V_r}{r \partial r} + \frac{\partial \rho V_\theta}{r \partial \theta} = 0 \quad (\text{B.1})$$

$$\frac{\partial \rho V_x}{\partial t} + \frac{\partial(\rho V_x V_x + P - \tau_{xx})}{\partial x} + \frac{\partial r(\rho V_x V_r - \tau_{xr})}{r \partial r} + \frac{\partial(\rho V_x V_\theta - \tau_{x\theta})}{r \partial \theta} = 0 \quad (\text{B.2})$$

$$\frac{\partial \rho V_r}{\partial t} + \frac{\partial(\rho V_x V_r - \tau_{xr})}{\partial x} + \frac{\partial r(\rho V_r V_r + P - \tau_{rr})}{r \partial r} + \frac{\partial(\rho V_r V_\theta - \tau_{r\theta})}{r \partial \theta} = \frac{\rho v_\theta v_\theta + P - \tau_{\theta\theta}}{r} \quad (\text{B.3})$$

$$\frac{\partial \rho V_\theta}{\partial t} + \frac{\partial(\rho V_x V_\theta - \tau_{x\theta})}{\partial x} + \frac{\partial r(\rho V_r V_\theta - \tau_{r\theta})}{r \partial r} + \frac{\partial(\rho V_\theta V_\theta + P - \tau_{\theta\theta})}{r \partial \theta} = \frac{-\rho V_r V_\theta + \tau_{r\theta}}{r} \quad (\text{B.4})$$

$$\frac{\partial \rho e_t}{\partial t} + \frac{\partial(\rho h_t V_x - \vec{\tau}_x \cdot \vec{v} + q_x)}{\partial x} + \frac{\partial r(\rho h_t V_r - \vec{\tau}_r \cdot \vec{v} + q_r)}{r \partial r} + \frac{\partial(\rho h_t V_\theta - \vec{\tau}_\theta \cdot \vec{v} + q_\theta)}{r \partial \theta} = 0 \quad (\text{B.5})$$

where

$$\tau_{xx} = \frac{2}{3} \mu \left( 2 \frac{\partial V_x}{\partial x} - \frac{\partial r V_r}{r \partial r} - \frac{\partial V_\theta}{r \partial \theta} \right) \quad \tau_{rr} = \frac{2}{3} \mu \left( 2 \frac{\partial r V_r}{r \partial r} - \frac{\partial V_x}{\partial x} - \frac{\partial V_\theta}{r \partial \theta} \right) - 2 \mu \frac{V_r}{r}$$

$$\tau_{\theta\theta} = \frac{2}{3} \mu \left( 2 \frac{\partial V_\theta}{r \partial \theta} - \frac{\partial V_x}{\partial x} - \frac{\partial r V_r}{r \partial r} \right) + 2 \mu \frac{V_r}{r} \quad \tau_{xr} = \mu \left( \frac{\partial V_r}{\partial x} + \frac{\partial V_x}{\partial r} \right)$$

$$\tau_{x\theta} = \mu \left( \frac{\partial V_\theta}{\partial x} + \frac{\partial V_x}{r \partial \theta} \right) \quad \tau_{r\theta} = \mu \left( \frac{\partial V_\theta}{\partial r} + \frac{\partial V_r}{r \partial \theta} - \frac{V_\theta}{r} \right)$$

$$q_x = -k \frac{\partial T}{\partial x} \quad q_r = -k \frac{\partial T}{\partial r} \quad q_\theta = -k \frac{\partial T}{r \partial \theta}$$

For any quantity denoted  $f$ , the average of  $f$  in the tangential direction is defined by :

$$\bar{f} = \frac{1}{\theta_s - \theta_p} \int_{\theta_p}^{\theta_s} f d\theta$$

These equations are tangentially averaged between two blades using Leibniz's integral rule, which gives the following relationship for the temporal, axial and radial derivatives in bladed regions [82] :

$$\frac{\overline{\partial f}}{\partial i} = \frac{\partial b \bar{f}}{\partial i} - \frac{1}{\theta_s - \theta_p} \left[ f \frac{\partial \theta}{\partial i} \right]_p^s \quad (\text{B.6})$$

where the subscripts  $s$  and  $p$  denote the suction side and the pressure side of the blade respectively.  $b$  is the blockage factor defined by :

$$b = \frac{\theta_s - \theta_p}{2\pi/Z}$$

For tangential derivatives, we can commute the integral and differential sign, such that :

$$\frac{\overline{\partial f}}{\partial \theta} = \frac{1}{\theta_s - \theta_p} \int_{\theta_p}^{\theta_s} \frac{\partial f}{\partial \theta} d\theta = \frac{1}{\theta_s - \theta_p} [f]_p^s$$

Finally, the Favre averaging is used for velocity components and energy:

$$\widetilde{V}_x = \frac{\overline{\rho V_x}}{\overline{\rho}}$$

such that :

$$\overline{\rho} \cdot \widetilde{V}_x = \overline{\rho} \frac{\overline{\rho V_x}}{\overline{\rho}} = \overline{\rho V_x}$$

## Density equation

Since the axial and radial velocities are equal to zero on the blade walls, the second term in equation (B.6) vanishes for axial and radial derivatives :

$$\frac{\overline{\partial \rho V_x}}{\partial x} = \frac{\partial b \overline{\rho V_x}}{\partial x}$$

The tangential velocity on the blade walls is equal to  $r\Omega$ . Therefore, we have :

$$\frac{\partial b \overline{\rho}}{\partial t} - \frac{\Omega(\rho_s - \rho_p)}{\theta_s - \theta_p} + \frac{\partial b \overline{\rho V_x}}{\partial x} + \frac{\partial r b \overline{\rho V_r}}{\partial r} + \frac{r \Omega(\rho_s - \rho_p)}{r(\theta_s - \theta_p)} = 0$$

Which directly leads to :

$$\frac{\partial b \overline{\rho}}{\partial t} + \frac{\partial b \overline{\rho V_x}}{\partial x} + \frac{\partial r b \overline{\rho V_r}}{\partial r} = 0$$

(B.7)

## Axial momentum equation

In the axial momentum equation, since the axial velocity appears in almost all the equation terms, the only terms contained in axial and radial derivatives that are not equal to zero on the blade walls are the pressure and the shear stress components. Therefore, we have :

$$\frac{\partial b\overline{\rho V_x}}{\partial t} + \frac{\partial b\overline{\rho V_x V_x + P - \tau_{xx}}}{\partial x} - \frac{[(P - \tau_{xx})\frac{\partial \theta}{\partial x}]_p^s}{\theta_s - \theta_p} + \frac{\partial r b\overline{\rho V_x V_r - \tau_{xr}}}{r \partial r} - \frac{[(-r\tau_{xr})\frac{\partial \theta}{\partial r}]_p^s}{r(\theta_s - \theta_p)} + \frac{[(-\tau_{x\theta})]_p^s}{r(\theta_s - \theta_p)} = 0$$

which can be written :

$$\boxed{\frac{\partial b\overline{\rho V_x}}{\partial t} + \frac{\partial b\overline{\rho V_x V_x + P - \tau_{xx}}}{\partial x} + \frac{\partial r b\overline{\rho V_x V_r - \tau_{xr}}}{r \partial r} = b(f_x^{inv} + f_x^{visc})} \quad (\text{B.8})$$

where :

$$f_x^{inv} = \frac{[P\frac{\partial \theta}{\partial x}]_p^s}{\theta_s - \theta_p} \quad f_x^{visc} = \frac{[-\tau_{xx}\frac{\partial \theta}{\partial x} - \tau_{xr}\frac{\partial \theta}{\partial r} + \tau_{x\theta}/r]_p^s}{\theta_s - \theta_p}$$

Defining  $\theta_m = \frac{\theta_s + \theta_p}{2}$ , the inviscid component of the axial blade force can be written :

$$f_x^{inv} = \frac{P_s \frac{\partial(\theta_m + \frac{\Delta\theta}{2})}{\partial x} - P_p \frac{\partial(\theta_m - \frac{\Delta\theta}{2})}{\partial x}}{\theta_s - \theta_p}$$

with  $\Delta\theta = (\theta_s - \theta_p)$ , which leads to :

$$\boxed{f_x^{inv} = \frac{(P_s - P_p)}{\theta_s - \theta_p} \frac{\partial \theta_m}{\partial x} + \frac{(P_s + P_p)}{2b} \frac{\partial b}{\partial x}} \quad (\text{B.9})$$

In the viscous component, the viscous stress tensor applied to the vector normal to the blade surface appears, ie the friction vector :

$$\boxed{f_x^{visc} = \frac{\tau_{px}^s + \tau_{px}^p}{r(\theta_s - \theta_p)}} \quad (\text{B.10})$$

Extracting the blockage factor from the derivatives gives (the blockage factor does not depend on time) :

$$\begin{aligned} \frac{\partial \overline{\rho V_x}}{\partial t} + \frac{\partial \overline{\rho V_x V_x + P - \tau_{xx}}}{\partial x} + \frac{\partial r \overline{\rho V_x V_r - \tau_{xr}}}{r \partial r} &= (f_x^{inv} + f_x^{visc}) \\ &\quad - \frac{1}{b} \overline{\rho V_x V_x + P - \tau_{xx}} \frac{\partial b}{\partial x} - \frac{1}{b} \overline{\rho V_x V_r - \tau_{xr}} \frac{\partial b}{\partial r} \end{aligned}$$

## Radial momentum equation

The radial momentum equation behaves as the axial momentum equation :

$$\frac{\partial b\overline{V_r}}{\partial t} + \frac{\partial b\overline{V_x V_r - \tau_{xr}}}{\partial x} - \frac{[(-\tau_{xr})\frac{\partial \theta}{\partial x}]_p^s}{\theta_s - \theta_p} + \frac{\partial r b\overline{V_r V_r + P - \tau_{rr}}}{r b \partial r} - \frac{[r(P - \tau_{rr})\frac{\partial \theta}{\partial r}]_p^s}{r(\theta_s - \theta_p)} + \frac{[(-\tau_{r\theta})]_p^s}{r(\theta_s - \theta_p)} = \frac{\rho v_\theta v_\theta + P - \tau_{\theta\theta}}{r}$$

which yields :

$$\boxed{\frac{\partial b\overline{V_r}}{\partial t} + \frac{\partial b\overline{V_x V_r - \tau_{rx}}}{\partial x} + \frac{\partial r b\overline{V_r V_r + P - \tau_{rr}}}{r \partial r} = b \frac{\rho v_\theta v_\theta + P - \tau_{\theta\theta}}{r} + b(f_r^{inv} + f_r^{visc})} \quad (\text{B.11})$$

where :

$$f_r^{inv} = \frac{[P\frac{\partial \theta}{\partial r}]_p^s}{\theta_s - \theta_p} \quad f_r^{visc} = \frac{[-\tau_{xr}\frac{\partial \theta}{\partial x} - \tau_{rr}\frac{\partial \theta}{\partial r} + \tau_{r\theta}/r]_p^s}{\theta_s - \theta_p} \quad (\text{B.12})$$

As for axial momentum, the force components can be written :

$$\boxed{f_r^{inv} = \frac{(P_s - P_p)\partial \theta_m}{\theta_s - \theta_p} + \frac{(P_s + P_p)\partial b}{2b} \frac{\partial b}{\partial r}} \quad \boxed{f_r^{visc} = \frac{\tau_{pr}^s + \tau_{pr}^p}{r(\theta_s - \theta_p)}} \quad (\text{B.13})$$

Extracting the blockage factor from the derivatives gives :

$$\frac{\partial \overline{\rho V_r}}{\partial t} + \frac{\partial \overline{\rho V_x V_r - \tau_{rx}}}{\partial x} + \frac{\partial r \overline{\rho V_r V_r + P - \tau_{rr}}}{r \partial r} = \frac{\rho v_\theta v_\theta + P - \tau_{\theta\theta}}{r} + (f_r^{inv} + f_r^{visc}) - \frac{1}{b} \frac{\partial b}{\partial r} \frac{\partial b}{\partial x} - \frac{1}{b} \frac{\partial b}{\partial r} \frac{\partial b}{\partial r}$$

## Tangential momentum equation

In the tangential momentum equation, the tangential velocity is not equal to zero on the blade walls, which leads to :

$$\frac{\partial b\overline{V_\theta}}{\partial t} - \frac{r\Omega^2(\rho_s - \rho_p)}{\theta_s - \theta_p} + \frac{\partial b\overline{V_x V_\theta - \tau_{x\theta}}}{b \partial x} - \frac{[(-\tau_{x\theta})\frac{\partial \theta}{\partial x}]_p^s}{\theta_s - \theta_p} + \frac{\partial r b\overline{V_r V_\theta - \tau_{r\theta}}}{r b \partial r} - \frac{[-r\tau_{r\theta}\frac{\partial \theta}{\partial r}]_p^s}{r(\theta_s - \theta_p)} + \frac{[(\rho V_\theta V_\theta + P - \tau_{\theta\theta})]_p^s}{r(\theta_s - \theta_p)} = \frac{-\rho V_r v_\theta + \tau_{r\theta}}{r}$$

This leads to :

$$\boxed{\frac{\partial b\overline{\rho V_\theta}}{\partial t} + \frac{\partial b\overline{\rho V_x V_\theta - \tau_{x\theta}}}{\partial x} + \frac{\partial r b\overline{\rho V_r V_\theta - \tau_{r\theta}}}{r\partial r} = b\frac{\overline{-\rho V_r v_\theta + \tau_{r\theta}}}{r} + b(f_\theta^{inv} + f_\theta^{visc})} \quad (\text{B.14})$$

where :

$$f_\theta^{inv} = \frac{-[P]_p^s}{r(\theta_s - \theta_p)} \quad f_\theta^{visc} = \frac{\left[-\tau_{x\theta}\frac{\partial\theta}{\partial x} - \tau_{r\theta}\frac{\partial\theta}{\partial r} + \tau_{\theta\theta}/r\right]_p^s}{\theta_s - \theta_p} \quad (\text{B.15})$$

or :

$$\boxed{f_\theta^{inv} = \frac{P_p - P_s}{r(\theta_s - \theta_p)}} \quad \boxed{f_\theta^{visc} = \frac{\tau_{p\theta}^s + \tau_{p\theta}^p}{r(\theta_s - \theta_p)}}$$

This can be rewritten :

$$\begin{aligned} \frac{\partial \overline{\rho V_\theta}}{\partial t} + \frac{\partial \overline{\rho V_x V_\theta - \tau_{x\theta}}}{\partial x} + \frac{\partial r \overline{\rho V_r V_\theta - \tau_{r\theta}}}{r\partial r} &= \frac{\overline{-\rho V_r v_\theta + \tau_{r\theta}}}{r} + (f_\theta^{inv} + f_\theta^{visc}) \\ &\quad - \frac{1}{b} \overline{\rho V_x V_\theta - \tau_{x\theta}} \frac{\partial b}{\partial x} - \frac{1}{b} \overline{\rho V_r V_\theta - \tau_{r\theta}} \frac{\partial b}{\partial r} \end{aligned}$$

## Energy equation

The heat flux are considered to be equal to zero on the blade walls. In addition, all the terms containing a radial or axial velocity component vanish on the walls.

$$\begin{aligned} \frac{\partial b\overline{\rho e_t}}{\partial t} - \frac{\Omega [\rho e_t]_p^s}{\theta_s - \theta_p} + \frac{\partial b(\overline{\rho h_t V_x - \vec{\tau}_x \cdot \vec{v} + q_x})}{b\partial x} - \frac{r\Omega \left[-\tau_{x\theta}\frac{\partial\theta}{\partial x}\right]_p^s}{\theta_s - \theta_p} \\ + \frac{\partial br(\overline{\rho h_t V_r - \vec{\tau}_r \cdot \vec{v} + q_r})}{br\partial r} - \frac{r\Omega \left[-\tau_{r\theta}\frac{\partial\theta}{\partial r}\right]_p^s}{\theta_s - \theta_p} + \frac{r\Omega [\rho e_t + P - \tau_{\theta\theta}]_p^s}{r(\theta_s - \theta_p)} = 0 \end{aligned}$$

which can be written :

$$\boxed{\frac{\partial b\overline{\rho e_t}}{\partial t} + \frac{\partial b(\overline{\rho h_t V_x - \vec{\tau}_x \cdot \vec{v} + q_x})}{\partial x} + \frac{\partial br(\overline{\rho h_t V_r - \vec{\tau}_r \cdot \vec{v} + q_r})}{r\partial r} = br\Omega(f_\theta^{inv} + f_\theta^{visc})} \quad (\text{B.16})$$

or :

$$\begin{aligned} \frac{\partial \overline{\rho e_t}}{\partial t} + \frac{\partial (\overline{\rho h_t V_x - \vec{\tau}_x \cdot \vec{v} + q_x})}{\partial x} + \frac{\partial r(\overline{\rho h_t V_r - \vec{\tau}_r \cdot \vec{v} + q_r})}{r\partial r} &= r\Omega(f_\theta^{inv} + f_\theta^{visc}) \\ &\quad - \frac{1}{b} \overline{\rho V_x h_t - \vec{\tau}_x \cdot \vec{v}} \frac{\partial b}{\partial x} - \frac{1}{b} \overline{\rho V_r h_t - \vec{\tau}_r \cdot \vec{v}} \frac{\partial b}{\partial r} \end{aligned}$$

## B.2 Blade force and blockage contribution

As shown above, the axial and radial components of the blade force can be divided in two components. The total blade force is therefore divided in two components :

- the first one is orthogonal to the blade camber surface and provides flow turning
- the second one is parallel to the blockage gradient and represents the pressure forces acting on the flow due to section variations.

As the static pressure on the walls are not directly computed in the throughflow approach, most throughflow solvers approximate the second term by :

$$\frac{P_s + P_p}{2} = \bar{P}$$

This leads to the apparition of the terms  $P \frac{\partial b}{\partial x}$  and  $P \frac{\partial b}{\partial r}$  in the axial and radial momentum equations, which cancel the pressure contribution in the blockage source term of these equations. It is not clear however if this term must be accounted for when correlating body forces to the loads distribution on the blades, for the computation of IP forces for instance.

## B.3 Blade camber surface and metal angles definition

As most body force models require distributions of the blade metal angles (camber and lean), the definition of the camber surface must be clarified. While not the most “natural” way to define the camber surface, the averaging process of the RANS equations allows to propose a simple relationship between the camber surface and the pressure/suction sides :

$$\theta_m = \frac{\theta_s + \theta_p}{2} \quad (\text{B.17})$$

This is the definition of the camber surface to which the blade force due to the static pressure is orthogonal. While consistent with the averaged form of the RANS equations, this definition of the blade camber surface also allows an easy extraction from a given blade geometry. In the present case, circular arcs were plotted at each meridional body force grid cell center locations. When two intersections with the blade were found, the location of the camber surface corresponding to the cell center axial and radial coordinate could then be easily retrieved. Then, the blade camber angle  $\beta_m$  and lean angle  $\lambda_m$  were computed using a second order finite difference method on the body force meridional grid:

$$\beta_m = \arctan(r \frac{\partial \theta_m}{\partial x}) \quad (\text{B.18})$$

$$\lambda_m = \arctan(r \frac{\partial \theta_m}{\partial r}) \quad (\text{B.19})$$

One difficulty appears with this approach when applied to the R4 fan stage, near the tip of fan rotor blades. In fact, the camber angle does not monotonically decrease from leading

to trailing edge, but instead increases near the leading edge, reaches a maximum near mid-chord and then decreases until the trailing edge. One issue with these distributions is that the body force models in which the flow is brought toward the blade camber surface fail to capture the real turning of the flow in these regions. To address this issue, new distributions of blade metal angle were computed, based on the spanwise distributions at the leading and trailing edges of the rotor blades. “Ideal” circular arc distributions of camber angle were computed for each spanwise location (i.e. the camber angle varies linearly from leading to trailing edge), and the final distribution was computed by taking the minimum value between this ideal distribution and the real one. This modification of the blade camber is shown in figure B.1. The new blade camber angle can only decrease from leading to trailing edge at the tip, while capturing the increased camber at the trailing edge at lower spanwise locations.

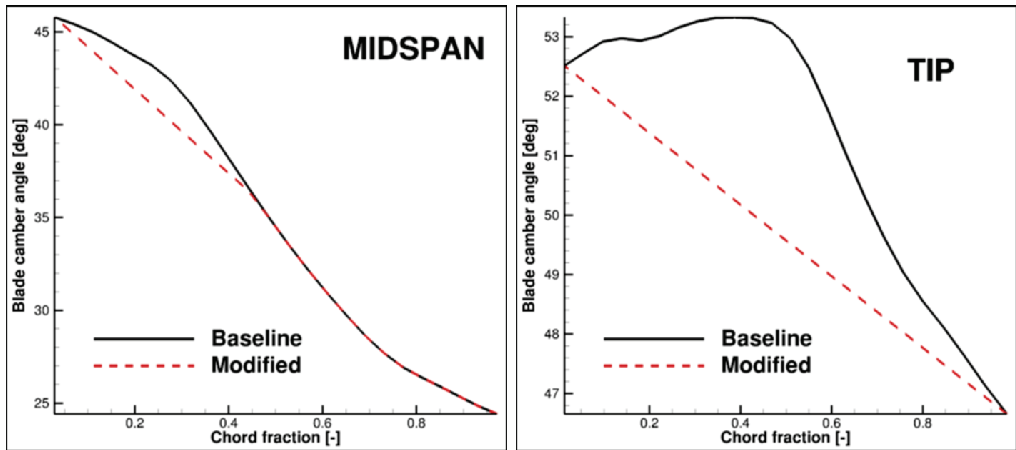


**Figure B.1:** Distributions of blade metal angle from leading to trailing edge on the R4 fan rotor, taken at constant span. Comparison of the blade metal angle directly computed from the camber surface definition in equation (B.17) and of a corrected distribution based on the leading and trailing edge angles.

The new distribution of blade camber angle was used along with the initial distribution of lean angle for Gong’s model. However, for Hall’s model, in which information about the camber surface is needed in terms of normal vectors, the following formula were used to retrieve the normal vector distributions from the modified blade camber angle distributions:

$$n_x = \frac{\beta_m}{|\beta_m|} \sqrt{\frac{\tan(\beta_m)^2}{1 + \tan(\beta_m)^2 + \tan(\lambda_m)^2}} \quad (\text{B.20})$$

$$n_\theta = -\frac{n_x}{\tan \beta_m} \quad (\text{B.21})$$

$$n_r = -n_\theta \tan \lambda_m \quad (\text{B.22})$$

The main effect of this modification is that it increases the work input on the upper part of the blade, and the choke mass flow rate.

## B.4 Circumferential stresses

In all equations presented above, each conservative variable can be seen as the superimposition of an axisymmetric flow field with a tangentially varying flow field, ie for a given quantity  $f$  :

$$f = \bar{f} + f'$$

with  $\bar{f}' = 0$  by definition. Therefore, for two quantity  $f$  and  $h$  we have :

$$\bar{f}\bar{h} = \overline{(\bar{f} + f')(\bar{h} + h')} = \bar{f}\bar{h} + \bar{h}\bar{f}' + \bar{f}\bar{h}' + \bar{f}'\bar{h}' = \bar{f}\bar{h} + \bar{f}'\bar{h}'$$

For instance, in the axial momentum equation we have :

$$\frac{\partial b\bar{\rho}\bar{V}_x}{\partial t} + \frac{\partial b(\bar{\rho}\bar{V}_x\bar{V}_x + \bar{P} - \bar{\tau}_{xx} + \bar{\rho}\bar{V}'_x\bar{V}'_x)}{\partial x} + \frac{\partial rb(\bar{\rho}\bar{V}_x\bar{V}_r - \bar{\tau}_{xr} + \bar{\rho}\bar{V}'_x\bar{V}'_r)}{r\partial r} = b(f_x^{inv} + f_x^{visc})$$

The circumferential stresses  $\bar{V}'_x\bar{V}'_x$  and  $\bar{V}'_x\bar{V}'_r$  appear, which account for the effect of the tangential fluctuations on the average flow. Similarly, the circumferential stresses  $\bar{V}'_r\bar{V}'_r$ ,  $\bar{V}'_\theta\bar{V}'_\theta$ ,  $\bar{V}'_x\bar{V}'_\theta$ ,  $\bar{V}'_r\bar{V}'_\theta$ , and  $\bar{V}'_x\bar{H}'$ ,  $\bar{V}'_r\bar{H}'$  appear in the other momentum equations and in the energy equation respectively. These terms, which are supposed to be responsible for phenomena such as radial mixing [3, 82], are sometimes accounted for with an eddy viscosity model as for turbulence closure. For instance, Baralon [3] uses an algebraic formula for the eddy viscosity :

$$\mu_c = \rho l^2 \sqrt{\left(\frac{\partial V_x}{\partial r}\right)^2 + \left(\frac{\partial V_r}{\partial r}\right)^2 + \left(\frac{\partial V_\theta}{\partial r}\right)^2}$$

where  $l$  is the mixing length, computed with a near-wall mixing length model near the hub and shroud, with a Von-Karman constant equal to 0.41, and chosen equal to one fourth of the pitch in the core flow.

# Appendix C

## Body force interpolation from database

This section discusses the use of a database from which body forces can be interpolated, which can be particularly interesting for data sharing between engine and airframe manufacturer, as it does not directly involve the details of the geometry of the blades. More detailed findings about the approach can be found in a conference publication related to the present work [86]. Although encouraging results were obtained, this path was abandoned due to its cost and lack of robustness in an industrial context. The key elements of the approach are given below, the reasons for its lack of robustness are discussed, and potential ways forward are given to improve the method.

As explained in section 2.1.5, it is possible to retrieve the blade force from a database generated with blade computations. Two different approaches can be envisioned. The first approach is to generate a database of gradients of the thermodynamic quantities to which the blade forces are related, such as the tangential velocity and entropy gradients. A response surface can be generated to relate these gradients to local flow conditions, then the body forces can be recovered using Marble’s formula. This approach was presented as “semi-explicit” in section 2.1.5, as the computation of the body forces is based on physical considerations, but the gradients of thermodynamic quantities are themselves not modeled. A more direct approach is to directly interpolate body forces from a database of body force fields.

This second approach was assessed on a 9 inch fan rotor, which will be described with more details in chapter 3. CFD computations of the blade were conducted for several operating points at a given rotational speed, with and without inlet swirl and for varying outlet conditions. Then, body force fields were extracted from these computations using the Blade Force Average approach, along with relative Mach number and relative flow angle distributions. For each meridional point, a first order bivariate polynomial was then sought for each body force component ( $x, r, \theta$ ):

$$\vec{f} = \vec{A}_0 M_r + \vec{A}_1 \beta + \vec{A}_2 \quad (\text{C.1})$$

A performance map obtained with this method is shown in figure C.1. The performance is well captured far from choke, even for operating points with inlet swirl, but the choke mass flow rate is overestimated. A good way to improve these results could be to use the

thermodynamics-based approach to generate the body force database, which was shown to yield better results than the BFA in section 2.3.2. Good results were also obtained with an application of the model to an intake–fan interaction test case: the interpolated body force approach quantitatively captured the effect of the fan on inlet flow separation and qualitatively captured IP forces.

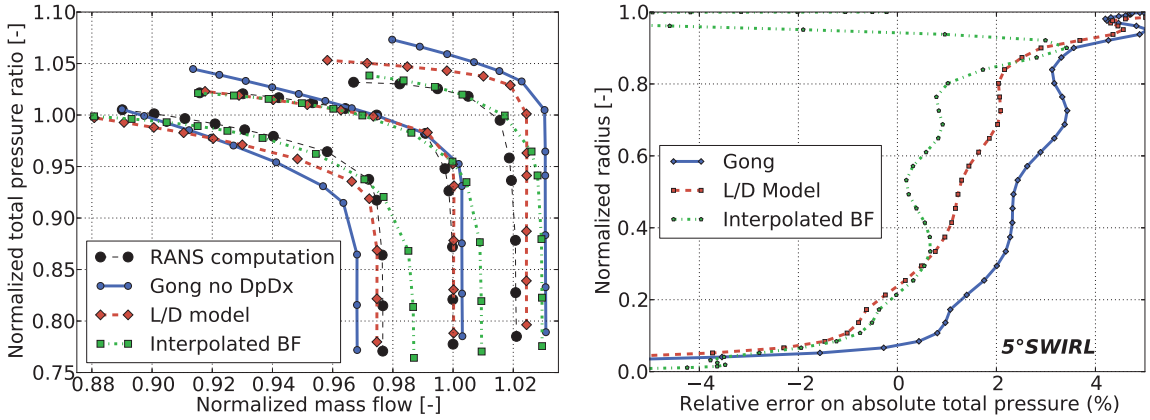


**Figure C.1:** Performance map of a 9 inch TPS rotor at maximum rotational speed, with  $\pm 5^\circ$  inlet swirl and no inlet swirl (left) and radial profile for an operating point near stall with  $+5^\circ$  inlet swirl (from [86]). The interpolated body force approach is compared to Gong’s model and to the lift/drag model.

Despite these encouraging results, the approach suffers from a lack of robustness:

- A large number of blade computations is needed to generate the body force database. Using too few operating points leads to failure in fitting a polynomial that does not produce large errors.
- The polynomial fitting is realized at each meridional grid point. This yields good results far from the endwalls and near the leading edge of the blade, where the blade forces and flow variations are usually well correlated. However, the fitting often fails near the endwalls where non linear phenomena occur and near the trailing edge of the blade where the blade force and relative flow field variations with operating conditions are small.
- This approach does not provide any natural mechanisms to make the computation stable. With the previously proposed models, perturbations are naturally damped as the normal force brings the flow toward the blade. Here, perturbations may be amplified depending on the local form of the polynomial found in the fitting procedure. This also prevents the use of higher order polynomial for which this amplification is even stronger.
- To make the method more robust and obtain more accurate results, the “Force–Flow reconciliation” concept of Kerner [54] had to be used. In fact, a body force simulation never matches all the averaged quantities from a blade computation. Several “frozen”

body force simulations therefore had to be performed and the interpolation procedure was conducted using the Mach number and relative flow angle distributions from these simulations.

Because of this lack of robustness, it was difficult to obtain converged results for a rotor alone, and even more difficult for a rotor-stator configuration, especially at high rotational speeds. To make this approach more viable in an industrial context, it may be useful to consider the following elements:

- **What should be interpolated:** The approach presented above built a polynomial for each spatial component of the blade force  $(x, r, \theta)$ . Given the results of section 2.3.2, it is possible that building the interpolating function for the normal and parallel force would increase the accuracy of the method.
- **Choice of variables:** Some flow variables must be chosen to perform the interpolation. It is thought that a bivariate interpolation is necessary to capture the effect of changes in operating conditions on the blade force. The relative Mach number and relative flow angle are good candidates, but one issue is that the relative flow angle does not vary much after 30 – 50% chord.
- **How to interpolate:** One key point is that the approach used to interpolate the body forces within the database must be both accurate and robust. Rather than polynomials, functions with better physical meaning can be sought, or more precise approaches, for instance based on Radial basis functions, can be used. The interpolation procedure should eliminate the “inappropriate” data that may appear due to localized phenomena such as flow separation or due to poor convergence of the blade computations.
- **How to extrapolate:** The approach often failed to converge for operating conditions too far from the range of available data. This means that the available data should either be large enough to avoid this phenomenon, or that some specific extrapolation techniques must be used. This was addressed by Brand on a similar approach by reducing the order of the polynomial fit outside of the range of available data [8].
- **Spatial coherence:** In the present work, nothing was done to ensure the spatial coherence of the fitting polynomials between too adjacent points on the meridional grid. Although this coherence should be naturally captured if the extracted flow fields and body force distributions are continuous, some discontinuity may occur because of the interpolation process.

## Appendix D

### Endwall treatment for Hall's model

While the proposed formulation for the normal force in Hall's model gives accurate results far from the endwall where the flow can be approximated as 2D, some additional modifications are necessary to correctly capture the turning in the vicinity of the endwalls. Figure D.1 shows spanwise profiles of deviation angle and work coefficient at the trailing edge of the R4 fan rotor, near the hub. It can be seen in this figure that the body force model does not capture the overturning in this region, which can notably be explained by the fact that the normal component of the body force vanishes in the boundary layer, due to the dependence on the  $W^2$  term. A similar behavior can be seen in the OGVs where the overturning is not captured in the hub and shroud boundary layers. Finally, a similar issue can be observed near the rotor tip gaps, where the undeturning is not captured by the model.

Capturing these endwall effects may be of particular importance for low aspect ratio turbomachines, although the impact on the overall performance is very low for a fan. However, a wrong behavior was observed on the R4 geometries, for which non physical flow separation occurred on the hub in body force computations, in the vicinity of the OGVs and for highly loaded cases (high RPM and high pressure ratio). The analysis of the flow field revealed that the occurrence of flow separation was likely to be due to the wrong behavior of the model in the boundary layer, and in particular to the low work input in this region. Additional computations were run with just the OGVs, using inlet profiles extracted from blade computations, and flow separation still occurred. This suggests that the occurrence of flow separation is also due to the vanishing of the normal force near the endwall in the OGVs.

Past contributions [82, 35] tried to model the blade force near the endwalls using a simple approach. Their initial assumption was that the radial gradient of the blade walls static pressure was low in the endwall boundary layer, which implied that the blade force could only vary slowly or remain constant in these regions. They therefore applied a constraint on the tangential component of the normal force, which was held constant or for which the radial gradient was clipped to a given value.

These ideas were put to the test on the R4 geometry. First, the tangential component of the normal force was kept constant on a given fraction of the span. The main challenge with that approach is that the other components of the normal force need to be recomputed to keep the final force normal to the flow and avoid non physical losses. If the relative flow field is almost tangential and if the tangential force component that is being duplicated is not small enough, the recomputed axial component of the normal force can become very large

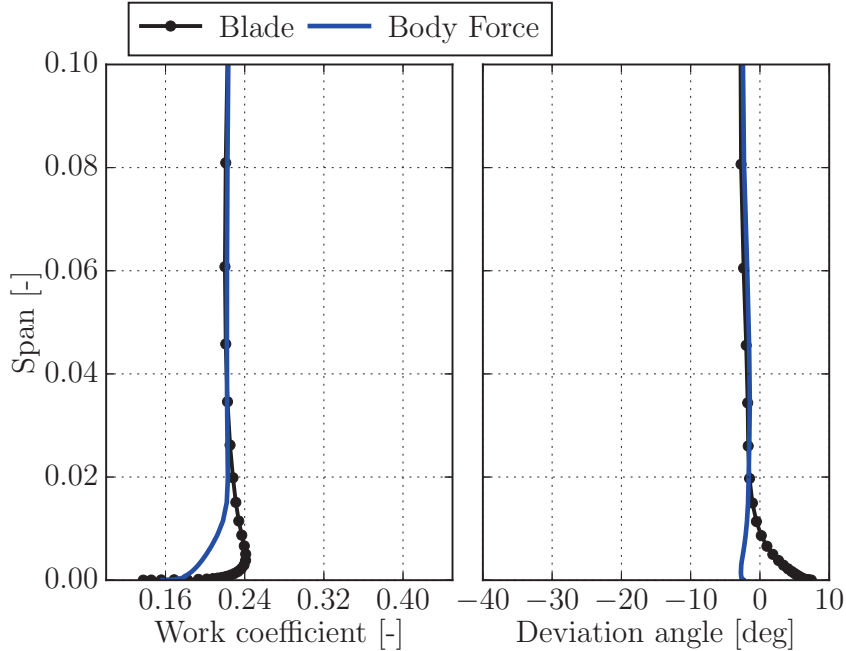


**Figure D.1:** Spanwise profiles of work coefficient and deviation angle near the hub, downstream of the R4 fan rotor. Comparison of Hall's model with blade computations at the design operating point.

which leads to instabilities. The same approach was employed, working directly with the normal force magnitude, but it led to an overestimated overturning and it did not remove the occurrence of flow separation. Limiting the radial gradient of the normal force also gave mixed results, with flow separation still occurring and with a high sensitivity to the chosen clipping value for the gradient.

A simple workaround was found to avoid separation, although its physical validity may be contested. The idea of this workaround is to help the low momentum flow crossing the rotor and OGVs by canceling the pressure gradient in the boundary layer. The source terms  $S_{\partial p \partial x}$  and  $S_{\partial p \partial r}$  defined in equations D.1 and D.2 are added to the axial and radial momentum equations respectively. The edge boundary layer velocity  $W_{edge}$  is taken at an arbitrary reference span between 2% and 5% along radial mesh lines.

$$S_{\partial p \partial x} = \left[ 1 - \left( \frac{W}{W_{edge}} \right)^2 \right] \frac{\partial P}{\partial x} \Big|_{edge} \quad (D.1)$$

$$S_{\partial p \partial r} = \left[ 1 - \left( \frac{W}{W_{edge}} \right)^2 \right] \frac{\partial P}{\partial r} \Big|_{edge} \quad (D.2)$$

These additional source terms are only activated in the boundary layer when  $W$  is small enough, due to the dependence on  $\left( \frac{W}{W_{edge}} \right)^2$ . If flow separation occurs, the low momentum fluid is sucked inside the blades and the flow reattaches. The term was not used for rotor tip

gaps, where the normal force was simply set to zero to capture some of the underturning in this region. The main default of this workaround is that it prevents from capturing the real thickening of the boundary layer that may occur in the OGVs for highly loaded conditions.

Another solution could be to add an offset  $\delta_0$  to the computed deviation in normal force equation within the boundary layer, to increase the work input near the hub and decrease it near the shroud. To compute this offset, one of the deviation models used in streamline curvature solvers could be used, such as those used in [82].



# THÈSE

**En vue de l'obtention du**

## **DOCTORAT DE L'UNIVERSITÉ DE TOULOUSE**

**Délivré par :**

Institut Supérieur de l'Aéronautique et de l'Espace

---

**Présentée et soutenue par :**  
**William THOLLET**

**le** mardi 18 juillet 2017

**Titre :**

Modélisations simplifiées de turbomachines pour l'analyse par la simulation  
des installations motrices complexes d'avions

Body force modeling of fan-airframe interactions

---

**École doctorale et discipline ou spécialité :**

ED MEGeP : Dynamique des fluides

**Unité de recherche :**

Équipe d'accueil ISAE-ONERA EDyF

**Directeur(s) de Thèse :**

M. Xavier CARBONNEAU (directeur de thèse)  
M. Guillaume DUFOUR (co-directeur de thèse)

**Jury :**

M. Zoltan SPAKOVSKY, Professeur Massachusetts Institute of Technology - Président  
M. Tony ARTS, Professeur Von Karman Institute for Fluid Dynamics - Rapporteur  
M. Florian BLANC, Ingénieur Airbus Opérations SAS  
M. Xavier CARBONNEAU, Professeur ISAE-SUPAERO - Directeur de thèse  
M. Guillaume DUFOUR, Professeur Associé ISAE-SUPAERO - co-Directeur de thèse  
M. Cesare HALL, Professeur Associé University of Cambridge  
M. Paul TUCKER, Professeur University of Cambridge - Rapporteur

## Résumé

Les futurs concepts d'avion seront sujets à de fortes interactions aérodynamiques entre les soufflantes des moteurs et la cellule de l'avion. Pour concevoir de tels avions, des méthodes numériques rapides et précises qui permettent de reproduire et de comprendre ces interactions sont nécessaires. Ce travail de thèse étudie une méthode de simulation des turbomachines, souvent appelée la méthode "body force", dans laquelle les étages de pales sont remplacés par des termes sources qui reproduisent la déviation de l'écoulement et les pertes. Il est démontré dans la thèse que cette méthode de calcul permet de capturer de manière efficace les interactions entre une soufflante et son environnement, sur des configurations d'entrée d'air courte et sur des configurations à ingestion de couche limite.

Les termes sources en question sont en général divisés en une force normale à l'écoulement, qui produit la déviation, et une force parallèle à l'écoulement, qui génère les pertes. Une hiérarchie de modèles dont la complexité est variable est proposée dans la thèse. Différents modèles de la littérature sont évalués, et des améliorations sont proposées. Une nouvelle formulation basée sur une analogie avec la portance et la traînée d'une aile d'avion est développée. Le principal défaut des approches plus anciennes était leur manque de généralité, qui nécessitait l'utilisation de coefficients d'étalonnage empiriques. Cette limite est partiellement résolue avec la nouvelle formulation. Pour améliorer la précision de la méthode, des termes sources permettant de prendre en compte le blocage métallique des pales sont également ajoutés aux équations de transport. Ces termes sources additionnels permettent notamment d'améliorer la prédiction du débit de blocage et de l'échange de travail sur des géométries transsoniques.

Cette nouvelle formulation est appliquée à des configurations d'entrée d'air courte et à des configurations à ingestion de couche limite. Les résultats sont validés à l'aide de simulations instationnaires de la soufflante sur  $360^\circ$  et parfois avec des données expérimentales. Il est démontré que l'approche permet de reproduire les interactions entre la soufflante et l'entrée d'air lorsque celle-ci est raccourcie. En particulier, la nouvelle formulation reproduit l'effet amont de la soufflante sur l'entrée d'air, qui permet de retarder l'apparition d'un décollement interne lorsque l'entrée d'air est mise en incidence. Le modèle capture également les efforts transversaux qui agissent sur la soufflante du fait de la distribution non-uniforme du chargement sur les pales. Ensuite, il est démontré que le modèle reproduit la redistribution qui a lieu en amont de la soufflante sur des configurations à ingestion de couche limite, ainsi que le transfert de la distorsion à travers les étages de pales. Enfin, le modèle est appliqué à un cas-test simple permettant d'évaluer les bénéfices de l'ingestion de couche limite sur la consommation de carburant. Il est alors démontré que des bénéfices substantiels ne peuvent être obtenus que si une quantité suffisante de couche limite est ingérée par la soufflante.

# Table des matières

<b>Introduction</b>	<b>4</b>
<b>1 Revue des interactions avion-soufflante</b>	<b>6</b>
<b>2 Modélisation de turbomachines par termes sources</b>	<b>10</b>
<b>3 Interactions entre la soufflante et l'entrée d'air sur une configuration à entrée d'air courte</b>	<b>14</b>
<b>4 Ingestion de couche limite</b>	<b>18</b>
<b>Conclusion</b>	<b>21</b>

# Table des figures

1.1	Fonctionnement d'une entrée d'air par forte incidence. . . . .	7
1.2	Fonctionnement d'une entrée d'air par vent de travers. . . . .	7
1.3	Illustration des phénomènes de redistribution dans une soufflante ingérant de la couche limite. (Adapté depuis [4]). . . . .	9
2.1	Illustration du facteur de blocage et de la décomposition de la force de la pale. . . . .	11
2.2	NASA/GE R4 : champs de performance à 100% RPM, $+/-5^\circ$ swirl en entrée. . . . .	12
2.3	Profils radiaux en aval de l'étage soufflante (100% RPM) avec $5^\circ$ inlet de contre-swirl en entrée. Points de fonctionnement proche rendement max. (gauche) et proche pompage (droite). . . . .	13
3.1	Illustration des trois entrées d'air utilisées pour mettre en évidence l'effet potentiel de la soufflante. . . . .	14
3.2	Indice de distortion circonférentielle en fonction de l'incidence pour une entrée d'air <b>courte</b> (rouge), <b>intermédiaire</b> (vert) et longue (bleue). L'incidence est comptée relativement à l'incidence de décollement lorsqu'aucun effet de la soufflante n'est pris en compte. . . . .	15
3.3	Contours de nombre de Mach sur la lèvre inférieure de l'entrée d'air (gauche) et devant la soufflante (droite) sur l'entrée d'air courte. $AOA_{stall}^{P/O}$ . . . . .	16
3.4	Efforts IP agissant sur la soufflante pour une entrée d'air <b>courte</b> (rouge), <b>intermédiaire</b> (vert) and longue (bleue). . . . .	16
3.5	Contours de nombre de Mach et de pression totale en aval des OGVs. . . . .	17
4.1	Domaines de calcul pour le premier cas-test BLI. . . . .	18
4.2	Distribution du coefficient de travail en aval du rotor (station 2) pour deux distributions de pression totale en entrée du domaine de calcul. . . . .	19
4.3	Diminution du rendement relativement à un écoulement uniforme. . . . .	20
4.4	Schéma de principe et photo du montage expérimental de la configuration RAPRO2 (crédits ONERA [1]) . . . . .	20
4.5	Mesures expérimentales (WTT) des bénéfices de la BLI comparés à des résultats issus de calculs body force. . . . .	21

# Liste des symboles

## Abbréviations

CFD	Computational Fluid Dynamics
RANS	Reynolds Averaged Navier-Stokes
URANS	Unsteady Reynolds Averaged Navier-Stokes
OGV	Outlet Guide Vane
BLI	Boundary Layer Ingestion
AOA	Angle of Attack
RPM	Rotation Par Minute
IP	In-Plane
WTT	Wind Tunnel Test
IDC	Indice de Distortion Circomférentielle
MFR	Mass Flow Rate

## Coordonnées

$x, y, z$	Coordonnées cartésiennes
$x, r, \theta$	Coordonnées cylindriques
$n, p$	Normal et parallèle à l'écoulement

## Symboles Grecs

$\alpha$	Angle d'attaque
$\beta$	Angle relatif
$\beta_m$	Angle de cambrure des pales
$\delta$	Ecart flux profil
$\eta$	Rendement
$\Omega$	Vitesse de rotation
$\sigma$	Solidité

## Symboles Romain

$\vec{f}$	Force par unité de masse
$\vec{F}$	Force par unité de volume
$\vec{V}$	Vitesse absolue
$\vec{W}$	Vitesse relative
$\rho$	Densité
$P$	Pression statique
$P_i$	Pression totale
$M$	Nombre de Mach
$Re$	Nombre de Reynolds
$C_f$	Coefficient de friction
$b$	Facteur de blocage
$s$	Distance aube à aube
$c$	Corde
$h$	Distance aube à aube avec calage
$\vec{n}$	Vecteur normal au squelette
$R$	Rayon

## Indices et Exposants

$a$	absolue
$r$	relatif
$P/O$	Power-Off

# Introduction

Ce document est un résumé en Français des travaux de thèse dont le manuscrit principal est rédigé en Anglais. Chaque chapitre de ce manuscrit principal est résumé en quelques pages, tout en incluant les éléments les plus importants tels que certaines des figures ou des équations.

Il peut être démontré que le rendement propulsif des avions civils peut être amélioré en augmentant le diamètre de la soufflante des moteurs et en réduisant son taux de compression. Cependant, l'intégration de tels moteurs, dont l'encombrement devient significatif, est problématique, notamment en raison de l'accroissement de la masse et de la traînée de toute l'installation motrice. Le poids et la traînée de la nacelle peuvent par exemple être réduits en considérant des entrées d'air plus courtes, mais ceci conduit à de nouvelles interactions aérodynamiques entre celles-ci et les soufflantes. Des configurations d'avion innovantes, utilisant le principe de l'ingestion de couche limite (BLI), peuvent être envisagées, mais là encore de fortes interactions aérodynamiques entre l'avion et les soufflantes apparaissent.

Il s'agit là de deux exemples concrets de configurations d'avion civil pour lesquelles de fortes interactions aérodynamiques entre soufflantes et cellule de l'avion doivent être prises en compte dans le processus de design de cette dernière. Ce travail de thèse porte sur la modélisation d'étages de turbomachines à l'aide de termes sources, dans le but de reproduire des interactions avion-moteur à faible coût. Dans un premier temps, les principaux phénomènes d'interaction aérodynamiques entre un avion et ses moteurs sont décrits. Ensuite, les méthodes développées au court de ce travail de thèse pour capturer ces interactions sont développées et validées sur une configuration de soufflante isolée. Le troisième chapitre de cette thèse montre l'application de ces méthodes à un cas d'interaction de soufflante avec une entrée d'air courte. Pour finir, la capacité de ces méthodes à capturer l'aérodynamique d'une soufflante ingérant de la couche limite et les bénéfices de cette dernière sur la consommation de carburant sont évalués.

# Chapitre 1

## Revue des interactions avion-soufflante

Ce chapitre décrit les interactions aérodynamiques entre la soufflante d'un moteur et la cellule de l'avion, qui peuvent être rencontrées sur des configurations de nacelle à entrée d'air courte, ou sur des configurations à ingestion de couche limite. Le rôle principal de l'entrée d'air est de fournir à la soufflante un écoulement adéquat, à la bonne vitesse, et avec des niveaux de distorsion les plus faibles possibles. Ceci est particulièrement difficile pour deux types de conditions :

- Lorsque l'avion doit rapidement gagner de l'altitude, pour éviter un obstacle par exemple, l'incidence de l'avion est importante et le débit de fonctionnement du moteur est élevé. Dans ces conditions, un décollement peut survenir sur la lèvre inférieure de l'entrée d'air et mettre en danger le bon fonctionnement du moteur. Par conséquent, les entrées d'air sont toujours conçues de manière à ce qu'aucun décollement ne survienne dans la plage d'opération de l'avion et du moteur à basse altitude. Ce type de phénomènes est illustré sur la figure 1.1.
- Lorsque l'avion est au sol et en présence de fortes rafales de vent, la nacelle peut parfois être sujette à de forts vents de travers. Dans ces conditions, l'entrée d'air est décollée lorsque le débit à travers la soufflante est trop faible ou trop important, et il existe une plage de débit dans laquelle le fonctionnement de l'entrée d'air est sain, c'est-à-dire sans décollement. Il est important que cette plage de fonctionnement soit la plus large possible pour éviter qu'un décollement ne soit présent en amont de la soufflante pour des vitesses de rotation élevées. Dans le cas contraire, des instabilités aéromécaniques peuvent survenir et endommager la soufflante. Le comportement d'une entrée d'air par vent de travers est illustré sur la figure 1.2.

Pour limiter le poids et la traînée de la nacelle sur les futurs moteurs à très haut taux de dilution, de nouveaux concepts de nacelles compactes sont actuellement étudiés. En particulier, une solution pour diminuer l'encombrement de la nacelle est d'utiliser une entrée d'air plus courte et plus fine. Cependant, maintenir une plage de fonctionnement sain avec ce type d'entrée d'air est loin d'être trivial. En effet, les lèvres de l'entrée d'air étant plus fines et plus courtes, il devient particulièrement difficile d'adapter la courbure de l'écoulement par de fortes incidences ou par vent de travers, et donc d'éviter qu'un décollement ne survienne. Néanmoins, un constat encourageant a été mis en avant dans de nombreuses publications,

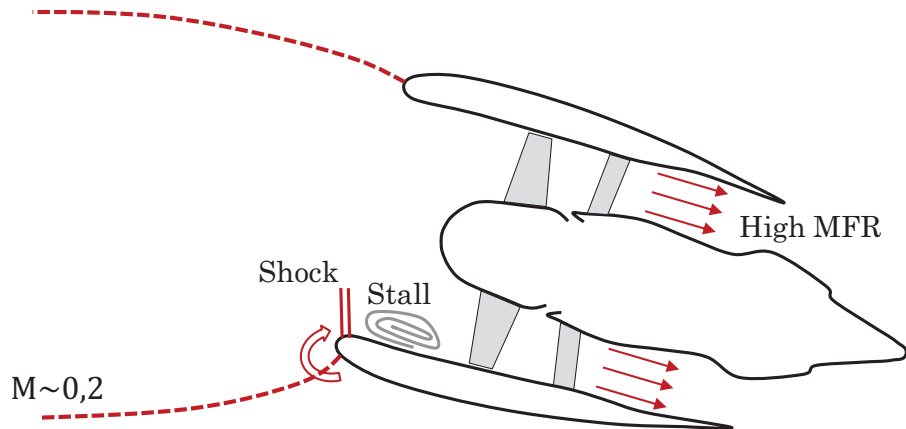


**Figure 1.1 – Fonctionnement d'une entrée d'air par forte incidence.**

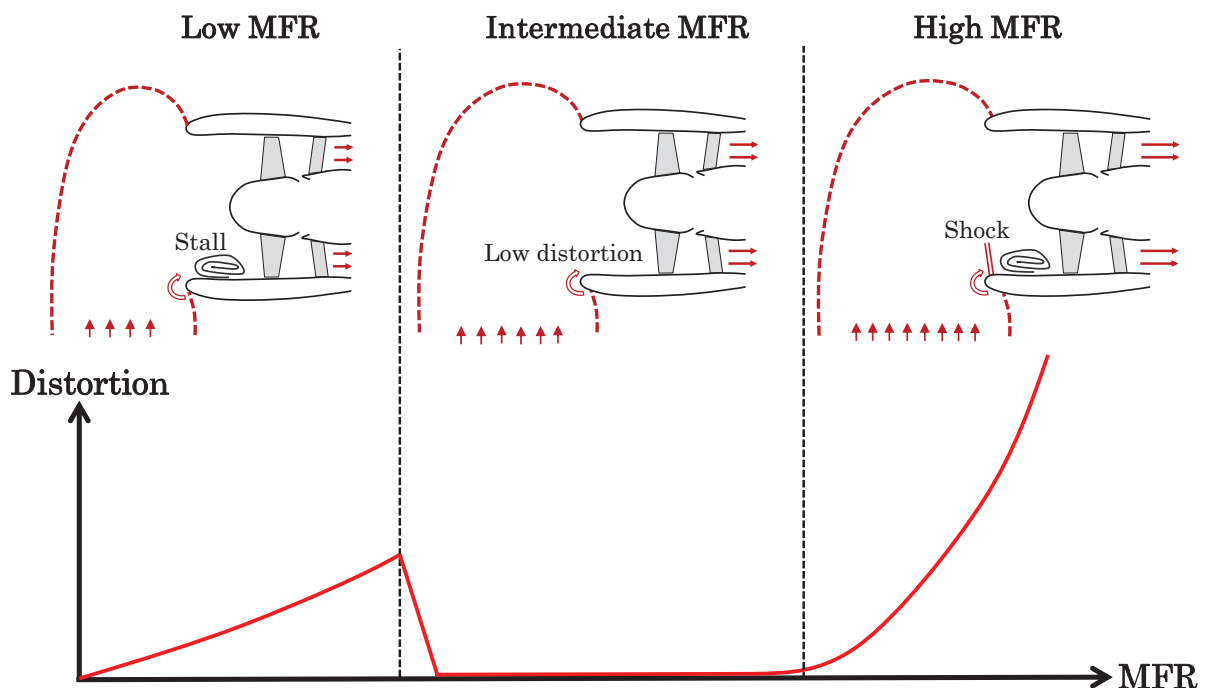


**Figure 1.2 – Fonctionnement d'une entrée d'air par vent de travers.**

dans lesquelles il a été démontré que la soufflante a un effet bénéfique sur l'entrée d'air lorsque celle-ci est raccourcie. En particulier, un élargissement de la plage de fonctionnement sain de ces entrées d'air a pu être constaté, lorsque l'effet de la soufflante était pris en compte.

Des méthodes numériques permettant de prendre en compte cet effet sont alors désirables si l'on souhaite permettre la conception d'entrée d'air plus courtes.

Sur le long terme, de nouveaux concepts disruptifs d'avions sont étudiés. En particulier, un concept particulièrement encourageant est celui de l'ingestion de couche limite. L'idée de ce concept est de rapprocher les moteurs de l'avion pour leur permettre d'ingérer la couche limite qui se développe sur le fuselage et/ou sur les ailes. Un gain significatif sur la consommation de carburant est possible sur ce type de configuration, notamment grâce à une réduction des pertes visqueuses dans les jets propulsifs et dans les sillages de l'avion. La principale difficulté pour mettre en pratique ce genre de configurations est que le fonctionnement de l'avion et du moteur sont fortement couplés. Les soufflantes des moteurs ont un effet non négligeable sur les distributions de pression statique sur le fuselage et sur les ailes, ce qui conduit à une modification de la traînée et de la portance de l'avion. Réciproquement, l'ingestion de la couche limite de l'avion par les soufflantes se traduit par des conditions d'entrée qui ne sont plus uniformes pour celles-ci. En pratique, ceci se traduit par une diminution du rendement de la soufflante, et donc par une augmentation de la consommation de carburant. Fort heureusement, les gains potentiels offerts par l'ingestion de couche limite sont largement supérieurs aux pertes dues à la baisse de rendement de la soufflante. Néanmoins, il est primordial de minimiser cette baisse de rendement, tout en prenant en compte l'effet des soufflantes sur l'aérodynamique de l'avion. L'aérodynamique d'une soufflante avec des conditions d'entrées non uniformes a été étudiée à plusieurs reprises par le passé. Les principales caractéristiques des écoulements en question sont les suivantes :

- La soufflante a un effet amont très important, qui se traduit en pratique par une redistribution de l'écoulement avant que celui-ci n'atteigne les pales de la soufflante. Des portions de l'écoulement dans lesquelles la pression totale est la plus élevée migrent vers les régions où la pression totale est plus faible, ce qui en pratique se traduit par de fortes composantes de vitesse tangentielles et radiales en amont de la soufflante.
- L'apport de travail à l'écoulement dans le rotor est plus important dans les régions dans lesquelles la vitesse est plus faible, ce qui tend à réhomogénéiser l'écoulement en aval. En revanche, du fait de la redistribution de l'écoulement en amont et au travers de la soufflante, les niveaux de distorsion ont tendance à augmenter dans les régions proches du moyeu. Le rendement dans le rotor diminue du fait de l'éloignement local du point de fonctionnement par rapport au point nominal. Des décollements surviennent en bout de pale, lorsque celles-ci traversent les zones où la pression totale est la plus faible.
- Les perturbations de vitesse résiduelles en aval du rotor se traduisent par des incidences variables sur les pales des redresseurs, ce qui conduit à des décollements de coin au niveau du moyeu et du carter, et donc à des pertes supplémentaires.

La redistribution de l'écoulement en amont et dans le rotor est illustrée sur la figure 1.3. Du fait de la complexité de ces phénomènes aérodynamiques, il est nécessaire d'utiliser des modèles suffisamment représentatifs pour prendre en compte ce type d'interactions. De manière générale, l'approche la plus fidèle pour calculer un écoulement de ce type est la simulation instationnaire des pales sur  $360^\circ$ . Cependant, en pratique, le coût de ce genre de simulation est prohibitif pour des boucles quotidiennes de conception. Bien qu'il existe des méthodes moins coûteuses, par exemple basées sur des hypothèses chorochroniques, ces méthodes souffrent en général d'autres défauts, telle qu'une multiplication de leur complexité

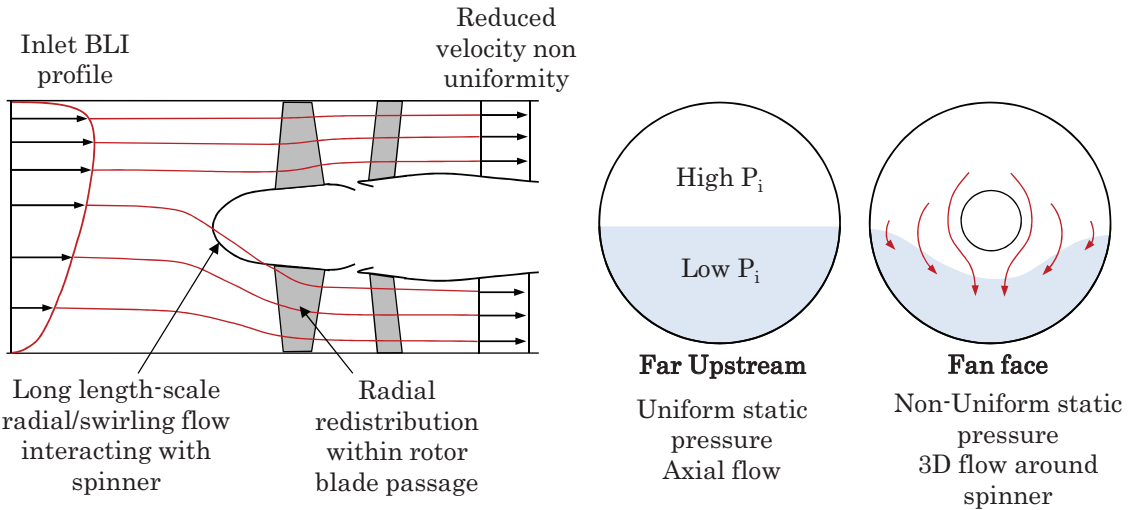


**Figure 1.3 – Illustration des phénomènes de redistribution dans une soufflante ingérant de la couche limite. (Adapté depuis [4]).**

lorsque plusieurs étages de pales doivent être simulés, qui ne les rendent pas plus adéquates. Pour ces raisons, ce travail de thèse s'est concentré sur des méthodes d'ordre réduit, moins coûteuses, qui sont développées et testées dans les chapitres suivants.

# Chapitre 2

## Modélisation de turbomachines par termes sources

Ce chapitre présente tout d'abord une revue des méthodes à faible coût utilisées dans la littérature pour représenter un étage de pales de turbomachines. Ces méthodes sont divisées en plusieurs catégories :

- Les méthodes "Throughflow" axisymétriques basées sur les équations de l'équilibre radial ou sur les équations de Navier-Stokes moyennées dans la direction tangentielle. Ces méthodes sont en général utilisées en phase de conception des turbomachines.
- Les méthodes de type Disque d'Action, dans lesquels les étages de pales sont représentés par un disque de discontinuité à travers lequel l'écoulement subit un saut de pression et de température totales.
- Les méthodes "Throughflow" non axisymétriques, dans lesquelles des termes sources sont ajoutés aux équations de Navier-Stokes pour représenter l'effet des pales sur l'écoulement.

Sur la base de la revue bibliographique, cette thèse se concentre sur cette troisième catégorie de méthodes, qui semble la plus adéquate pour la représentation des interactions avion-moteur. En particulier, des méthodes "explicites" sont étudiées, dans lesquelles les termes sources représentant les forces appliquées par les pales sur l'écoulement sont une fonction explicite de l'écoulement. Le modèle le plus utilisé dans la littérature est le modèle de Gong [3], qui a notamment été appliqué à plusieurs reprises à des cas d'interaction entrée d'air soufflante [7, 6]. Dans ce travail de thèse, les termes sources reproduisant l'effet des pales sont divisés en deux contributions :

- Des termes sources appliqués aux équations de la quantité de mouvement et de l'énergie, qui permettent de prendre en compte la déviation de l'écoulement, les pertes, et l'échange de travail. La déviation est en générale capturée en appliquant une force normale à l'écoulement dans le repère relatif, et les pertes sont capturées à l'aide d'une force parallèle à l'écoulement. Ceci est illustré sur la figure 2.1a
- Des termes sources présents dans chaque équation, qui permettent de prendre en compte le blocage métallique dans un passage de pales. Plus particulièrement, la réduction de section dans les passages de pales est modélisée à l'aide d'un terme d'ajout ou de réduction de masse, proportionnel au gradient du facteur de blocage  $b$ , défini sur la figure 2.1b

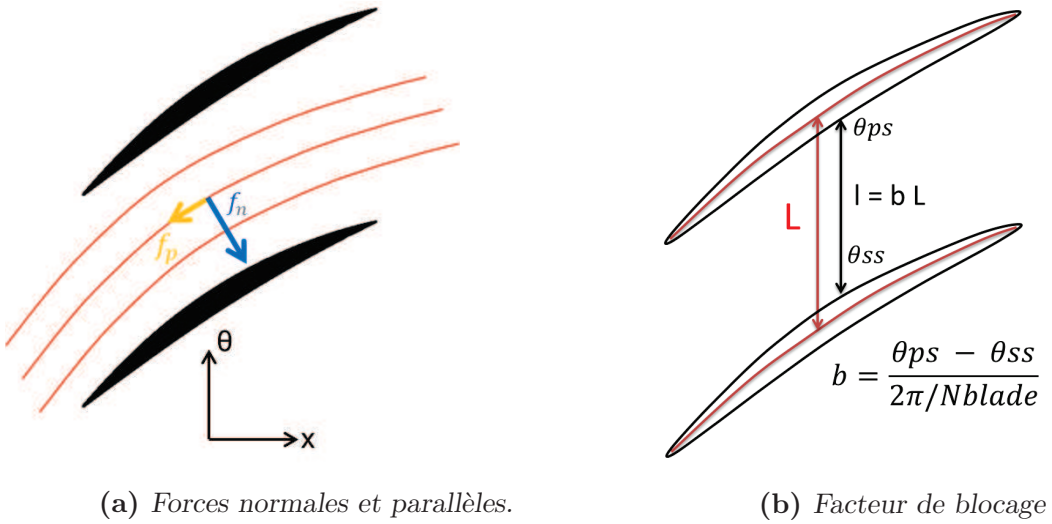


**Figure 2.1 – Illustration du facteur de blocage et de la décomposition de la force de la pale.**

Les termes sources de blocage métallique sont dérivés de manière analytiquement exacte. En revanche, les termes sources reproduisant la déviation et les pertes doivent être calculés à l'aide d'un modèle tel que le modèle de Gong. Ce dernier est appliqué à un étage de soufflante isolé, dans laquelle les conditions d'entrée sont uniformes. Plusieurs limitations du modèle sont mises en évidence, notamment sa forte dépendance à des coefficients d'étalonnage, qui peuvent être évalués à l'aide de données expérimentales ou de calculs avec plan de mélange. Quelques tentatives sont faites pour améliorer le modèle, qui permettent notamment d'améliorer sa robustesse et sa capacité à prédire le débit de blocage dans l'étage de la soufflante. Cependant, le processus d'étalonnage à mettre en œuvre pour pouvoir utiliser le modèle est jugé trop lourd et trop coûteux pour être industriellement viable.

Par conséquent, de nouveaux modèles de déviation et de pertes sont développés. Deux formulations sont présentées. La première est construite en utilisant une analogie avec la portance et la traînée d'une aile d'avion. Ce modèle nécessite toujours des coefficients d'étalonnage, mais ceux-ci sont beaucoup plus simples à calculer que pour le modèle de Gong. Les résultats donnés par le modèle, en termes de performance de l'étage de soufflante, sont très encourageants. En particulier, le modèle prédit correctement l'échange de travail à la traversée du rotor, et il prédit également le rendement global de l'étage, et ce même pour des points de fonctionnement off-design. La force normale à l'écoulement, qui produit la déviation, et la force parallèle à l'écoulement, qui produit les pertes, sont données dans les équations (2.1) et (2.2) respectivement.  $C(x)$  est une fonction permettant d'améliorer la prédiction du débit de blocage, qui doit être réglée manuellement.  $\beta_0$ ,  $\beta^{\eta_{max}}$  et  $K_p^{\eta_{max}}$  sont des coefficients d'étalonnage qui peuvent être obtenus en utilisant des résultats issus de calculs avec plan de mélange moyennés azimuthalement.

$$f_n = \frac{2\pi\sigma}{h} W^2 (\beta - C(x)\beta_0) \quad (2.1)$$

$$f_p = \frac{K_p^{\eta_{max}} + 2\pi\sigma(\beta - \beta^{\eta_{max}})^2}{h} W^2 \quad (2.2)$$

Le deuxième modèle est construit sur la base du travail de Hall [5], qui avait proposé dans sa thèse un modèle de déviation ne nécessitant pas de coefficients d'étalonnage, mais cependant limité à des écoulements incompressibles. Le modèle est ici corrigé à l'aide d'un coefficient de compressibilité et un modèle de pertes lui est ajouté. Le modèle final ne nécessite aucun étalonnage, mais il parvient néanmoins à capturer de manière précise l'échange de travail et les pertes dans l'étage de la soufflante. Les équations du modèle sont numérotées (2.3) et (2.4).  $K_{Mach}$  est un coefficient de compressibilité basé sur la correction de compressibilité de Prandtl-Glauert pour les écoulements subsoniques et sur la formule d'Ackeret pour les écoulements supersoniques.  $C_f$  est un coefficient de frottement obtenu à l'aide d'une relation empirique permettant d'évaluer le frottement sur une plaque plane, sans gradient de pression.  $\delta^{\eta_{max}}$  est une distribution de la déviation au point de rendement maximal.

$$f_n = K_{Mach} 0.5 W^2 2\pi \delta \frac{1}{sb|n_\theta|} \quad (2.3)$$

$$f_p = \frac{0.5 W^2}{sb|n_\theta|} (2C_f + 2\pi K_{Mach}(\delta - \delta^{\eta_{max}})^2) \quad (2.4)$$

Un exemple d'application de ce dernier modèle à un étage de soufflante (rotor-stator) isolé est montré dans les figures 2.2 et 2.3. Ces figures montrent des champs de performance de la soufflante (NASA R4) et des profils radiaux en aval du stator. Le modèle capture très bien l'échange de travail au sein du rotor, et ce pour plusieurs conditions d'entrées et de sorties. Le modèle de pertes ne permet pas de capturer de manière précise le rendement. En particulier, le rendement maximum est surestimé, ce qui est principalement dû à une sous-estimation des pertes liées au chocs au bord d'attaque du rotor.

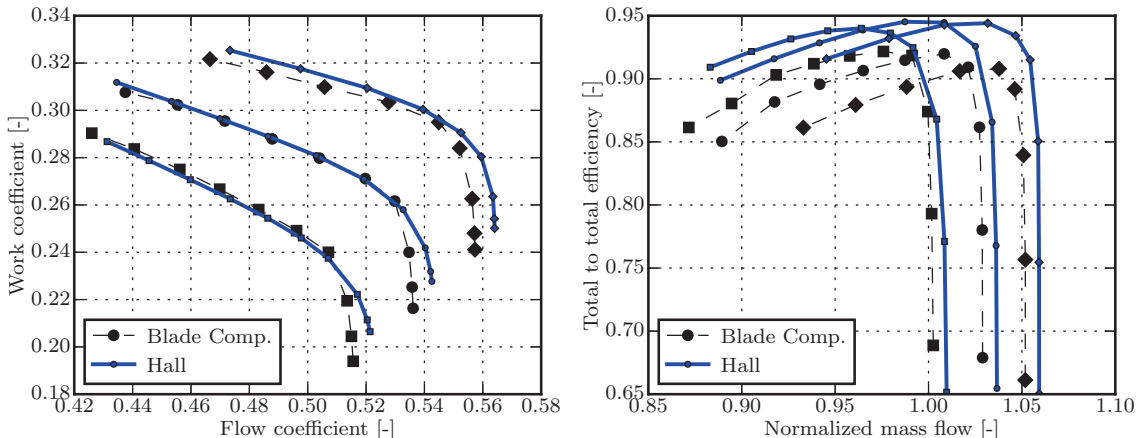


**Figure 2.2 – NASA/GE R4 : champs de performance à 100% RPM,  $+/-5^\circ$  swirl en entrée.**

De manière générale, la modélisation des pertes constitue la principale difficulté dans la construction des modèles de pale. Les pertes dans des étages de turbomachines sont particulièrement difficile à évaluer, et ce même lorsque la géométrie des pales est directement

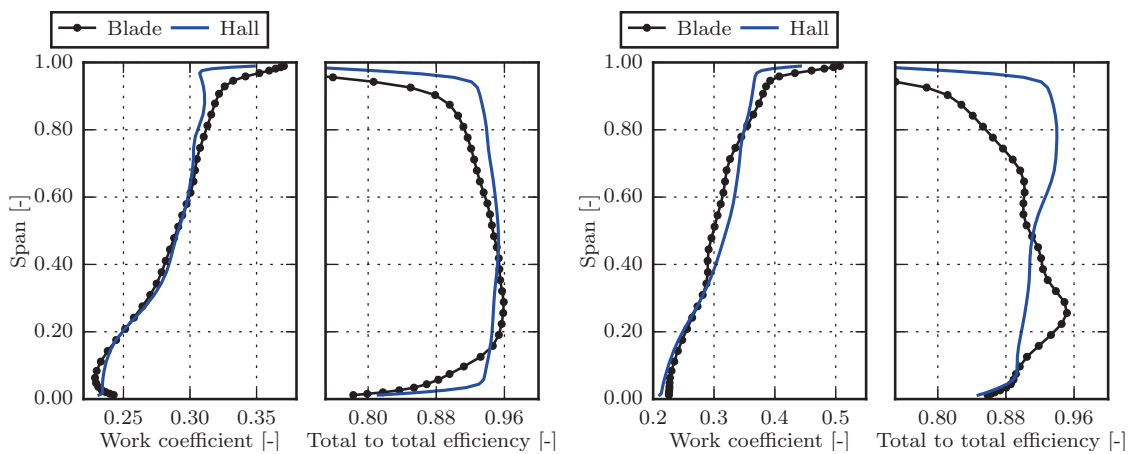


**Figure 2.3 – Profils radiaux en aval de l'étage soufflante (100% RPM) avec 5° inlet de contre-swirl en entrée. Points de fonctionnement proche rendement max. (gauche) et proche pompage (droite).**

inclue dans la simulation plutôt que modélisée. De futurs travaux pourraient donc se focaliser sur ces aspects, pour tenter d'améliorer la prédiction des pertes et donc du rendement des étages de pale en présence de distortion.

# Chapitre 3

## Interactions entre la soufflante et l'entrée d'air sur une configuration à entrée d'air courte

Ce chapitre présente l'application des deux modèles présentés dans le chapitre 2 à une configuration d'entrée d'air courte. Pour mettre en évidence les interactions qui peuvent apparaître lorsque l'entrée d'air est raccourcie, un étage de soufflante est placé dans trois entrées d'air axisymétriques de longueur différentes, présentant les mêmes caractéristiques de résistance au décollement par vent de travers et par fortes incidences. Ces géométries sont illustrées sur la figure 3.1. Des simulations instationnaires de la soufflante sur  $360^\circ$  sont réalisées pour valider les résultats donnés par les modèles body force.

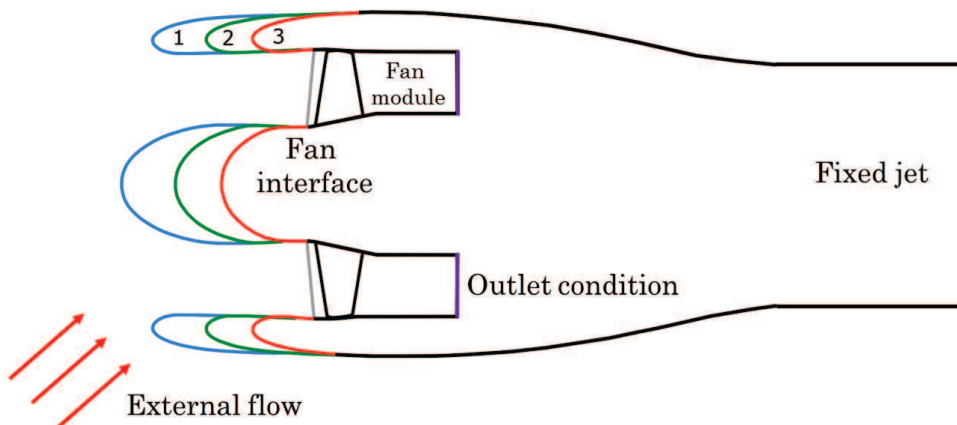
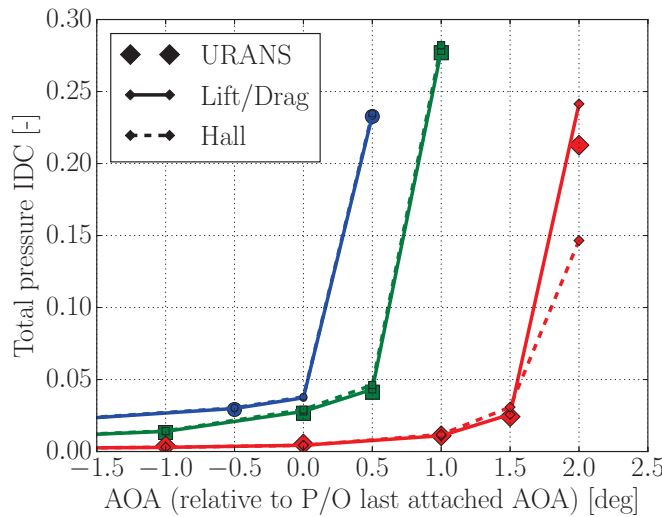


Figure 3.1 – Illustration des trois entrées d'air utilisées pour mettre en évidence l'effet potentiel de la soufflante.

Il est montré que, sur cette configuration, les interactions aérodynamiques entre la soufflante et l'entrée d'air permettent de retarder l'apparition d'un décollement à fortes incidence. Cet effet est visible sur l'entrée d'air la plus courte uniquement, comme le montre la figure 3.2. Cette figure montre l'évolution de l'indice de distortion circonférentielle en amont de la

soufflante lorsque l'incidence de la nacelle augmente. Ce critère de distortion permet notamment de mettre en évidence l'apparition d'un décollement dans l'entrée d'air, qui se traduit par une augmentation soudaine des niveaux de distortion en amont de la soufflante. Des résultats très similaires sont obtenus avec les calculs instationnaires et les calculs body force, basés sur les deux modèles présentés précédemment.



**Figure 3.2 – Indice de distortion circonférentielle en fonction de l'incidence pour une entrée d'air courte (rouge), intermédiaire (vert) et longue (bleue).** L'incidence est comptée relativement à l'incidence de décollement lorsqu'aucun effet de la soufflante n'est pris en compte.

Ces résultats sont confirmés par des visualisations de l'écoulement dans l'entrée d'air, telles que celle montrée dans la figure 3.3. Ces visualisations sont obtenues en comparant des calculs instationnaires avec des calculs body force, ainsi que d'autres simulations dénotées "Power-Off", dans lesquelles aucun effet de la soufflante n'est pris en compte. On voit sur ces visualisations que lorsque l'effet de la soufflante n'est pas capturé, un décollement apparaît plus tôt dans l'entrée d'air la plus courte. Dans les calculs instationnaires et body force, l'écoulement reste attaché plus longtemps, ce qui permet d'étendre la plage de fonctionnement de la nacelle. Quantitativement, le bénéfice de la soufflante est relativement faible puisqu'il n'atteint que 1.5°. Des travaux supplémentaires sont donc requis pour démontrer cet effet sur d'autres configurations du même type, et pour être capable de le valider expérimentalement.

Dans un second temps, la capacité des modèles à capturer les efforts agissant sur la soufflante dans le plan orthogonal à l'axe de rotation est évalué (efforts IP). Ces efforts, en général négligeables pour une entrée d'air longue, peuvent devenir significatifs avec une entrée d'air courte, du fait de la répartition non uniforme du chargement sur les pales le long de la circonference. Ceci est montré dans la figure 3.4. L'amplitude de la force IP est beaucoup plus élevée sur l'entrée d'air la plus courte, ce qui est qualitativement capturé par les modèles body force. La phase n'est elle presque pas affectée par la longueur de l'entrée d'air.

Pour finir, les modèles sont appliqués à une configuration de nacelle à entrée d'air courte, dans laquelle la bifurcation et la tuyère sont également simulées. L'idée de cette dernière

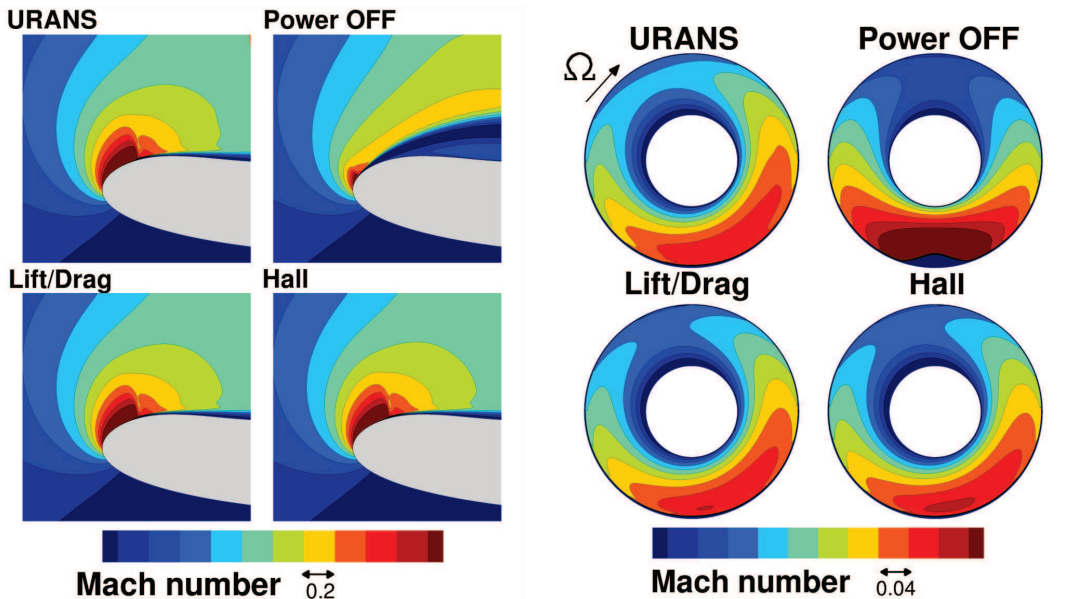


**Figure 3.3 – Contours de nombre de Mach sur la lèvre inférieure de l’entrée d’air (gauche) et devant la soufflante (droite) sur l’entrée d’air courte.  $AOA_{stall}^{P/O}$ .**

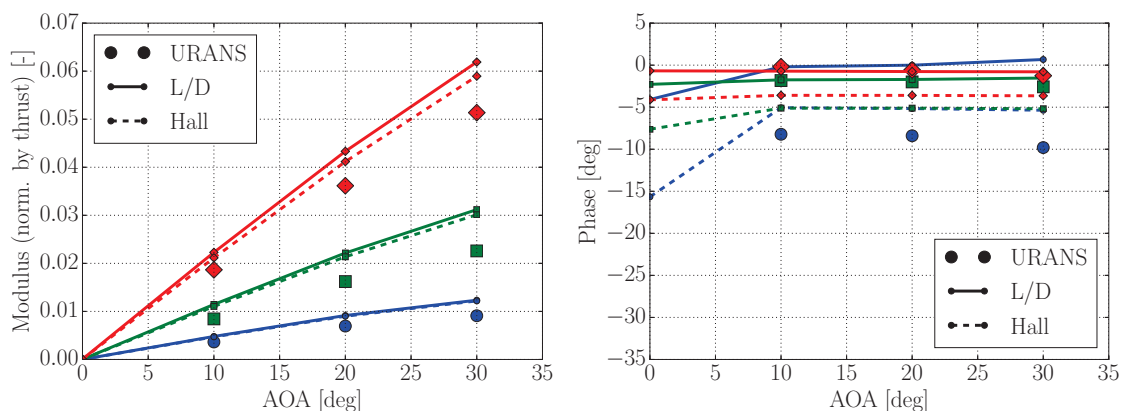


**Figure 3.4 – Efforts IP agissant sur la soufflante pour une entrée d’air courte (rouge), intermédiaire (vert) and longue (bleue).**

application est notamment d’évaluer l’effet de la bifurcation sur les efforts IP et sur la répartition d’échange de travail dans la soufflante. Le transfert de la distortion due aux conditions d’entrée non-uniformes et à la bifurcation est également évalué. Il est démontré que les modèles body force capturent de manière satisfaisante l’effet de la distortion sur les distributions de nombre de Mach et de pression totale en aval de l’étage de la soufflante (figure 3.5). De légers écarts sont visibles, notamment en ce qui concerne la position azimutale de la zone dans laquelle la pression totale est plus élevée.

Les résultats obtenus dans ce chapitre sont globalement satisfaisants. Les modèles body force capturent très bien l’effet potentiel de la soufflante sur les distributions d’écoulement dans l’entrée d’air, et en particulier l’effet de la soufflante sur l’angle d’incidence auquel

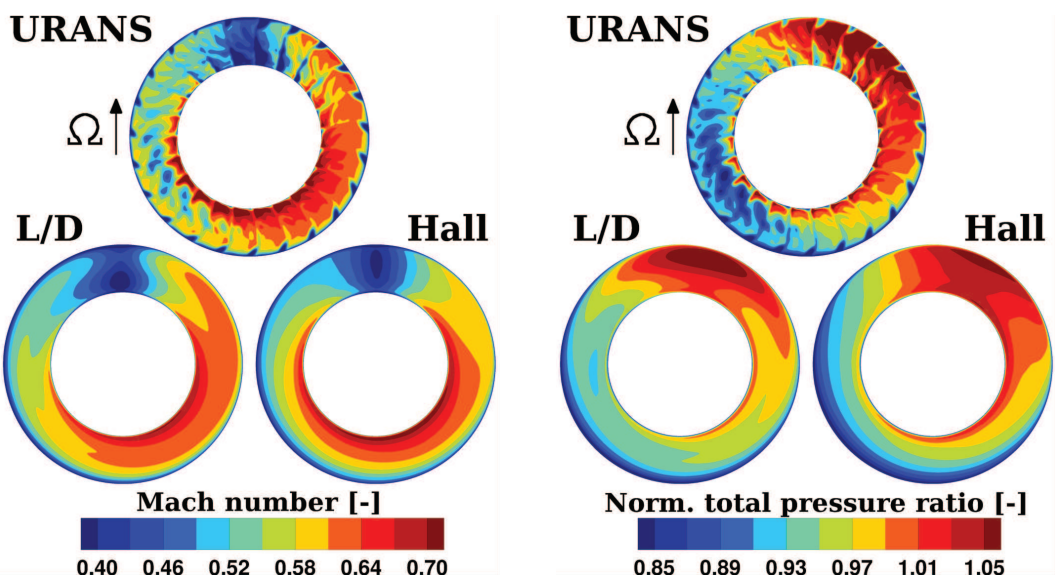


**Figure 3.5 – Contours de nombre de Mach et de pression totale en aval des OGVs.**

un décollement survient dans l'entrée d'air. Les modèles permettent également d'évaluer les efforts IP sur la soufflante, ainsi que le transfert de la distortion jusqu'à la tuyère secondaire.

# Chapitre 4

## Ingestion de couche limite

Dans ce chapitre, les modèles body force décrits dans les chapitres précédents sont appliqués à deux cas tests représentatifs de configurations BLI. Dans un premier temps, les modèles sont appliqués à une géométrie de soufflante avec OGVs. Les calculs sont réalisés sur  $360^\circ$  avec des conditions d'entrée paramétriques, représentatives de conditions BLI. Le domaine de calcul est montré sur la figure 4.1. La distribution imposée en entrée est convectée deux cordes en amont du bord d'attaque de la soufflante, en utilisant des conditions de paroi glissante jusqu'à cette position. Le but de ces simulations est de démontrer que les approches body force capturent le comportement aérodynamique de la soufflante lorsque les conditions d'entrées ne sont pas uniformes. En particulier, l'étude se concentre sur les phénomènes de redistribution de l'écoulement en amont et au sein de la soufflante, ainsi que sur l'effet de la distortion sur la répartition de l'échange de travail dans le rotor.

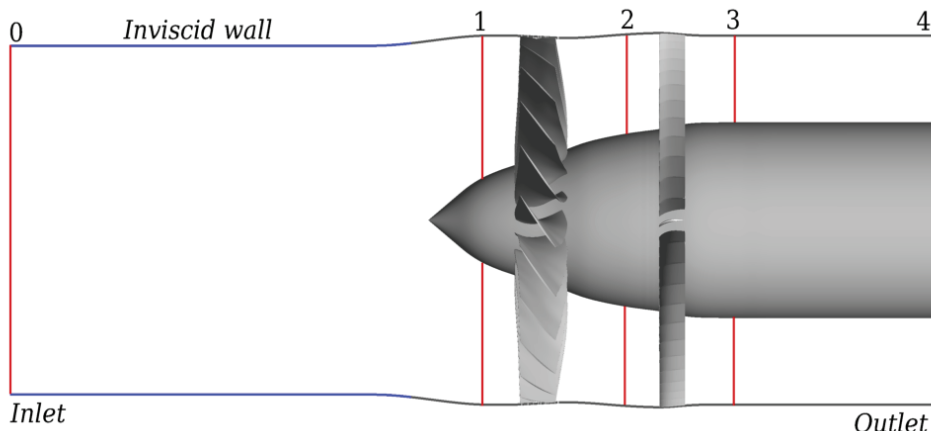
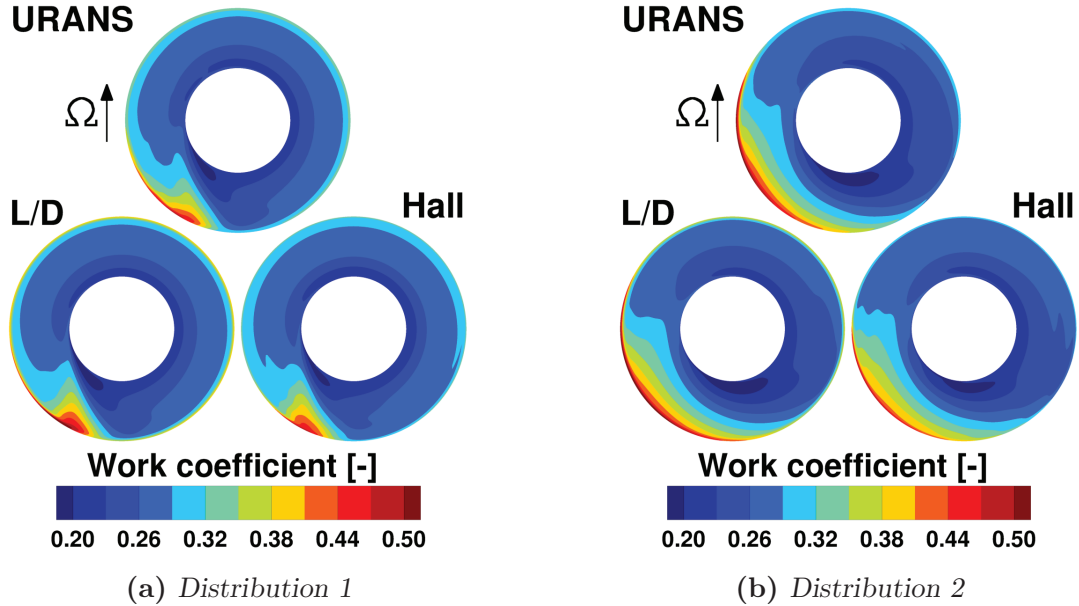


Figure 4.1 – Domaines de calcul pour le premier cas-test BLI.

Les modèles capturent très bien les différents phénomènes aérodynamiques résultant de l'interaction de la soufflante avec la distortion. Les phénomènes mis en évidence dans d'autres contributions ([2, 4]) sont bien retrouvés avec ces simulations. En particulier, l'effet potentiel de la soufflante se traduit par une redistribution significative de l'écoulement en amont du rotor, qui conduit à de fortes migrations de fluide depuis les zones où la pression totale est élevée vers les zones où la pression totale est plus faible. Ceci peut être observé à l'aide de

distributions d'angles radiaux et tangentiels en amont du rotor, plus élevés dans les régions où la migration de fluide est plus importante. Du fait de la distortion en amont du rotor, l'échange de travail n'est pas uniforme ce qui conduit à des distributions de coefficient de travail telles que celles montrées sur la figure 4.2.

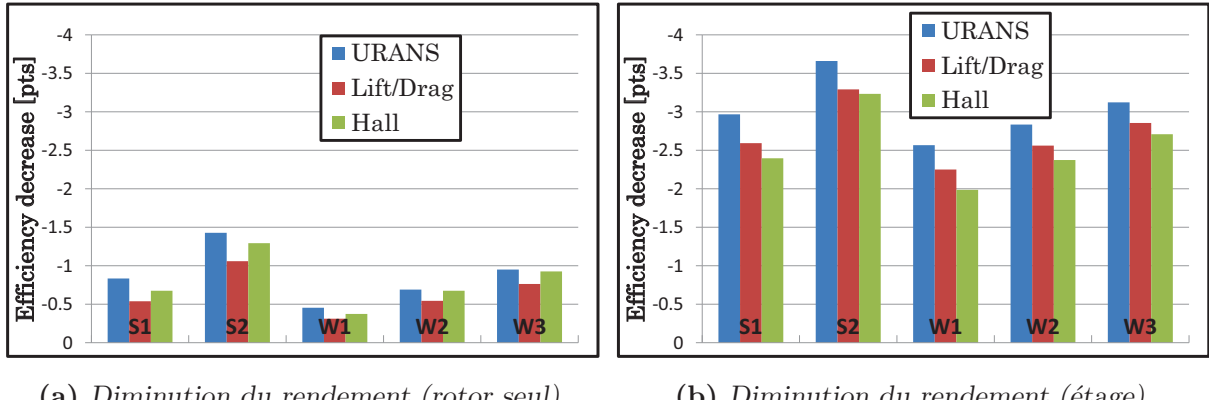


**Figure 4.2 – Distribution du coefficient de travail en aval du rotor (station 2) pour deux distributions de pression totale en entrée du domaine de calcul.**

Le comportement aérodynamique des modèles est validé de manière détaillée sur la base de deux distributions de pression totale distinctes. Dans un second temps, une étude paramétrique est réalisée, sur la base de cinq distributions imposées en entrée. Des critères globaux mono-dimensionnels sont construits et mesurés à différentes positions axiales pour valider les modèles :

- Un critère d'intensité de distortion
- Un critère de position de la distortion
- Un critère d'étendue de la distortion

Il est démontré que les modèles capturent bien l'intensité et la position de la distortion, mais des écarts significatifs sont observés concernant son étendue en aval des OGVs. Pour finir, la baisse de rendement de la soufflante associée à un fonctionnement dans des conditions non uniformes est évaluée. Ceci est montré sur la figure 4.3, où l'on peut voir la baisse de rendement dans le rotor et dans l'étage de la soufflante pour les cinq distributions de pression totale utilisées. Les modèles ne capturent pas les niveaux absolus de la différence de rendement entre les écoulements distordus et un écoulement uniforme, mais la dynamique globale de cette baisse de rendement est elle bien capturée. Ceci montre que ces modèles peuvent être utilisés dans un contexte de conception de la cellule de l'avion, puisqu'ils permettront, une fois couplés à un modèle moteur, d'évaluer la performance du moteur et donc de l'avion complet.



(a) Diminution du rendement (rotor seul).

(b) Diminution du rendement (étage).

Figure 4.3 – Diminution du rendement relativement à un écoulement uniforme.

Pour terminer, le modèle lift/drag est appliqué à la configuration "RAPRO", pour laquelle des données expérimentales sont disponibles. Cette configuration, présentée en figure 4.4, permet de relier les bénéfices offerts par l'ingestion de couche limite à la quantité de couche limite qui peut effectivement être ingérée par les moteurs. Une nacelle est placée en aval d'un corps solide produisant de la traînée. La position de la nacelle relativement à ce corps peut être modifiée pour changer la quantité de couche limite qui est ingérée par le moteur.

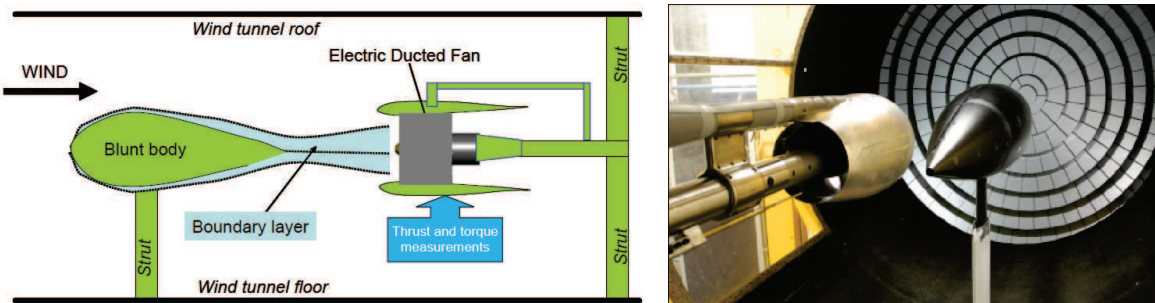
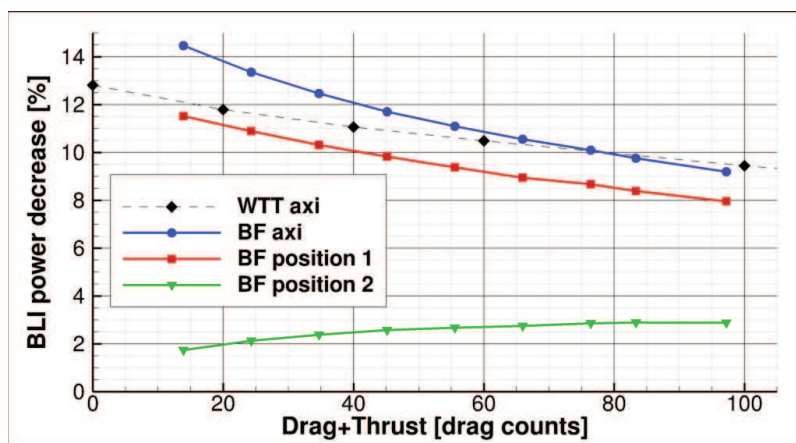


Figure 4.4 – Schéma de principe et photo du montage expérimental de la configuration RAPRO2 (crédits ONERA [1])

L'effet de l'ingestion de couche limite sur la réduction de la puissance nécessaire pour produire une certaine poussée est montré sur la figure 4.5. Des calculs body force sont réalisés pour trois positions relatives de la nacelle par rapport au corps produisant de la traînée, incluant une position dite "axisymétrique", dans laquelle le moteur ingère toute la couche limite de ce corps. La quantité de couche limite ingérée sur les positions 1 et 2 diminue, au fur et à mesure que l'axe de rotation du moteur est éloigné de celui du corps solide. On voit clairement sur ce graphe que des bénéfices substantiels peuvent être obtenus lorsque toute la couche limite du corps est ingérée par les moteurs, mais que ces bénéfices décroissent rapidement lorsque la fraction de couche limite ingérée diminue.



**Figure 4.5** – Mesures expérimentales (WTT) des bénéfices de la BLI comparés à des résultats issus de calculs body force.

Ces deux applications permettent de démontrer que les modèles développés sont parfaitement adaptés à l'étude des interactions avion-moteur dans un cadre de conception aérodynamique de la cellule de l'avion. La première application permet de montrer que les modèles capturent de manière précise le comportement aérodynamique de la soufflante et son effet sur les éléments de l'avion environnant. La seconde application permet de montrer que les modèles peuvent être utilisés pour évaluer la performance de l'avion d'un point de vue Système.

# Conclusion

Le but principal de cette thèse était de démontrer la pertinence de l'approche body force dans un contexte de design aérodynamique de la cellule de l'avion, lorsque de nouvelles interactions apparaissent entre l'avion et ses moteurs. Pour ce faire, plusieurs modèles disponibles dans la littérature ont d'abord été testés sur des configurations simplifiées, et leurs limitations mises en évidence. Sur la base de ces premiers résultats, de nouveaux modèles ont été développés, avec l'objectif d'obtenir une approche à la fois précise et robuste. Ces nouveaux modèles ont ensuite été appliqués à plusieurs cas-tests, comprenant notamment une entrée d'air courte et deux cas-test représentatifs d'une configuration à ingestion de couche limite. Les résultats obtenus ont permis de montrer que l'approche capture très bien l'effet amont de la soufflante, mais qu'elle peut également être utilisée pour évaluer l'écoulement en aval de l'étage de la soufflante ou pour évaluer des effets d'installation sur son rendement et donc sur la performance globale de l'avion. Bien que d'autres travaux soient nécessaires pour rendre la méthode encore plus fiable, la concordance générale qui a pu être observée entre les résultats issus de calculs body force et ceux issus de méthodes plus fidèles démontrent que la méthode est parfaitement adaptée à ce cadre de travail.

# Bibliographie

- [1] O. Atinault, G. Carrier, R. Grenon, C. Verbecke, and P. Viscat. Numerical and experimental aerodynamic investigations of boundary layer ingestion for improving propulsion efficiency of future air transport. In *Proceedings of 31st AIAA Applied Aerodynamics Conference*, San Diego, CA, June 2013. Paper no. AIAA 2013-2406.
- [2] V. J. Fidalgo, C. A. Hall, and Y. Colin. A study of fan-distortion interaction within the nasa rotor 67 transonic stage. *Journal of Turbomachinery*, 134(5), 2012.
- [3] Y. Gong. *A computational model for rotating stall and inlet distortions in multistage compressors*. PhD thesis, Massachusetts Institute of Technology, 1998.
- [4] E. J. Gunn and C. A. Hall. Aerodynamics of boundary layer ingesting fans. In *Proceedings of ASME Turbo Expo : Turbine Technical Conference and Exposition*, Dusseldorf, Germany, June 16-20 2014. Paper no. GT2014-26142.
- [5] D. K. Hall. *Analysis of Civil Aircraft Propulsors with Boundary Layer Ingestion*. PhD thesis, Massachusetts Institute of Technology, 2015.
- [6] E. Hsiao, M. Naimi, J. P. Lewis, K. Dalbey, Y. Gong, and C. Tan. Actuator duct model of turbomachinery components for powered-nacelle Navier-Stokes calculations. *Journal of Propulsion and Power*, 17(4) :919–927, 2001.
- [7] A. Peters. *Ultra-short nacelles for low fan pressure ratio propulsors*. PhD thesis, Massachusetts Institute of Technology, 2014.